



## TECHNICAL REPORT

ARL-TR-97-1  
3 March 1997

Copy Number 3

### Control of Acoustic Cavitation with Application to Lithotripsy

Technical Report under Grant N00014-89-J-1109  
and  
ARL:UT IR&D Program

19970716 115

Michael R. Bailey

DTIC QUALITY INSPECTED 2

Prepared for: Office of Naval Research  
ONR 331 • 800 North Quincy Street • Arlington, VA 22217-5660

---

Approved for public release:  
Distribution unlimited.

---

# UNCLASSIFIED

REPORT DOCUMENTATION PAGE			Form Approved OMB No. 0704-0188
Public reporting burden for this collection of information is estimated to average 1 hour per response, including the time for reviewing instructions, searching existing data sources, gathering and maintaining the data needed, and completing and reviewing the collection of information. Send comments regarding this burden estimate or any other aspect of this collection of information, including suggestions for reducing this burden, to Washington Headquarters Services, Directorate for Information Operations and Reports, 1215 Jefferson Davis Highway, Suite 1204, Arlington, VA 22202-4302, and to the Office of Management and Budget, Paperwork Reduction Project (0704-0188), Washington, DC 20503.			
1. AGENCY USE ONLY (Leave blank)	2. REPORT DATE	3. REPORT TYPE AND DATES COVERED	
	3 Mar 97	Technical	
4. TITLE AND SUBTITLE	5. FUNDING NUMBERS		
CONTROL OF ACOUSTIC CAVITATION WITH APPLICATION TO LITHOTRIPSY (Technical Report under Grant N00014-89-J-1109 and ARL:UT IR&D Program)	PE 61153 N, G N00014-89-J-1109 and ARL:UT IR&D Program		
6. AUTHOR(S)	8. PERFORMING ORGANIZATION REPORT NUMBER		
Michael R. Bailey	ARL-TR-97-1		
7. PERFORMING ORGANIZATION NAMES(S) AND ADDRESS(ES)	9. SPONSORING/MONITORING AGENCY NAME(S) AND ADDRESS(ES)		
Applied Research Laboratories The University of Texas at Austin P.O. Box 8029 Austin, Texas 78713-8029	Office of Naval Research ONR 331 800 North Quincy Street Arlington, VA 22217-5660		
Independent Research and Development Program Applied Research Laboratories The University of Texas at Austin P.O. Box 8029, Austin, Texas 78713-8029			10. SPONSORING/MONITORING AGENCY REPORT NUMBER
11. SUPPLEMENTARY NOTES Ph.D. Dissertation of Michael R. Bailey			
12a. DISTRIBUTION/AVAILABILITY STATEMENT Approved for public release: Distribution unlimited.		12b. DISTRIBUTION CODE	
13. ABSTRACT (Maximum 200 words) Control of acoustic cavitation (sound-induced bubble activity) is the subject of this dissertation. Application is to clinical lithotripsy where cavitation contributes to kidney stone comminution and tissue damage. An electrical spark at the near focus of an underwater ellipsoidal reflector was the acoustical source, as in the Dornier HM3 lithotripter. Experiments were done with rigid reflectors, pressure-release reflectors, and pairs of reflectors sharing a common focus and a controlled delay between sparks. Since a bubble hit by a single shock pulse can grow profoundly and then collapse violently, our hypothesis was that a second pulse timed to arrive during the collapse phase would intensify the ultimate collapse. Experiments and numerical calculations confirmed the hypothesis. Pitted by bubble collapses, aluminum foil placed along the reflector axis recorded the spatial cavitation field. Tempered collapse was also discovered; a sufficiently short delay between two pulses or a change in order of the positive and negative phases of a single pulse stifled bubble growth. Early collapse was detected acoustically. Computations of bubble radius and collapse pressure reinforced the observations. Finally, two reflectors facing each other produced highly localized, intense cavitation.			
14. SUBJECT TERMS cavitation two-pulse lithotripsy pressure-release ellipsoidal reflector		15. NUMBER OF PAGES 198	
		16. PRICE CODE	
17. SECURITY CLASSIFICATION OF REPORT UNCLASSIFIED	18. SECURITY CLASSIFICATION OF THIS PAGE UNCLASSIFIED	19. SECURITY CLASSIFICATION OF ABSTRACT UNCLASSIFIED	20. LIMITATION OF ABSTRACT

## ACKNOWLEDGEMENTS

Thanks are due Robin Cleveland for taking it upon himself to make me graduate.

Thanks are due Dr. Blackstock for encouraging me to do my own thing and for putting me in touch with the right people to help me do it. Some of those people in addition to Robin are Larry Crum and the APL group and Dr. Carstensen, Diane Dalecki, and the RCBU group. Thanks are due Mark Hamilton for his support; I didn't see him often, just when I needed a fix of positive energy. I also thank Dr. Blackstock, Dr. Crum, and Dr. F. Michael Pestorius for providing funding though ONR, NIH#DK43881, and ARL IR& D, respectively. I want to thank Lewis Thompson and Bob Rogers for preventing me from electrocuting myself, and Don Artieschoufsky and company for watching out for me while I was in the machine shop.

Then of course thanks to my family for making my project seem important when I needed to justify still being a student. Thanks are due Tricia Savage for preventing my project from getting too important and for pushing me to finally stop being a student.

May 1997

## Contents

<b>Acknowledgments</b>	<b>ii</b>
<b>List of Figures</b>	<b>vii</b>
<b>Abstract</b>	<b>xix</b>
<b>Preface</b>	<b>xxi</b>
<b>Chapter 1 Introduction</b>	<b>1</b>
1.1 Theory . . . . .	2
1.2 Experiment . . . . .	4
1.2.1 Sources . . . . .	5
1.2.2 Cavitation measurement . . . . .	6
1.2.3 Control of cavitation . . . . .	7
1.3 Dissertation map . . . . .	7
1.3.1 Map of Chapter 2 . . . . .	8
1.3.2 Map of Chapter 3 . . . . .	9
1.3.3 Map of Chapter 4 . . . . .	10
1.3.4 Map of Chapter 5 . . . . .	11
<b>Chapter 2 The Gilmore equation, its numerical implementation, and explorative calculations of the use of a second acoustic pulse to control cavitation behavior of a bubble</b>	<b>12</b>
2.1 Development of the Gilmore equation of bubble dynamics . . . . .	13
2.1.1 Statement of the problem . . . . .	13
2.1.2 Equations used as a basis for the model . . . . .	14
2.1.3 Outline of the derivation of the Rayleigh-Plesset equation . . . . .	16
2.1.4 Limits of the Rayleigh-Plesset equation . . . . .	17
2.1.5 General additions to the Rayleigh-Plesset equation and applicability of the Gilmore equation to lithotripsy . . . . .	18

2.1.6	Outline of the derivation and description of the Gilmore equation	18
2.1.7	Summary of the Gilmore equation	20
2.2	Numerical solution of the Gilmore equation	21
2.2.1	Solution algorithm	21
2.2.2	Measured waveforms as inputs to the code	22
2.3	Benchmarking our numerical code	24
2.3.1	Goal and method of benchmarking	24
2.3.2	Benchmarking against Church <sup>5</sup>	24
2.3.3	Church's waveform as input to the code	25
2.3.4	Benchmarking against Ding and Gracewski <sup>8</sup> and Ding and Gracewski pulses as inputs to the code	26
2.4	Explorative Gilmore code predictions with idealized triangular pulses and sequences of two pulses	28
2.4.1	Single unipolar pulse – what are the important parameters in the model?	29
2.4.2	Exploration of a bubble response to a sequence of two unipolar pulses	33
2.4.3	Exploration of a bubble response to a sequence of two bipolar pulses	36
2.5	Summary	43
<b>Chapter 3</b>	<b>Experimental setup</b>	<b>44</b>
3.1	General setup	44
3.1.1	Tank and water	46
3.1.2	Positioning system	48
3.1.3	Spark sources	48
3.1.4	Ellipsoidal reflectors	49
3.2	Modified or alternative configurations	53
3.2.1	Seattle dual spark systems	53
3.2.2	Austin experimental configuration	54
3.2.3	Indianapolis clinical lithotripter	56

3.3	Measurement configuration . . . . .	56
3.3.1	Direct pressure measurement . . . . .	56
3.3.2	PCD . . . . .	60
3.3.3	Aluminum foil detectors . . . . .	62
<b>Chapter 4 Results</b>		<b>66</b>
4.1	Acoustic fields of rigid and pressure-release reflectors . . . . .	67
4.1.1	Acoustic waveforms of rigid and pressure-release reflectors . . . . .	67
4.1.2	Uncertainty in recorded waveforms . . . . .	77
4.1.3	Peak pressure mappings – rigid and pressure-release reflectors . .	81
4.2	Acoustic pressure amplitude and cavitation – rigid reflector . . . . .	85
4.2.1	Acoustic amplitude and charging potential . . . . .	85
4.2.2	Computed bubble response and charging potential . . . . .	85
4.2.3	Measured bubble response and charging potential . . . . .	86
4.2.4	Comparison of theory and experiment . . . . .	90
4.2.5	Simultaneous measurement with the PCD and foil . . . . .	90
4.2.6	More interpretation of the PCD signal . . . . .	91
4.3	Cavitation fields of rigid and pressure-release reflectors . . . . .	94
4.3.1	Measured cavitation field of a rigid reflector . . . . .	95
4.3.2	Interpretation of the cavitation field of a rigid reflector . . . . .	97
4.3.3	Measured cavitation field of a pressure-release reflector . . . . .	101
4.4	Quantification of surface pitting by single reflectors and dual reflector confocal arrangements. . . . .	107
4.4.1	Pit depth with pressure-release and rigid reflectors . . . . .	108
4.4.2	Confocal pair consisting of a pressure-release reflector and a rigid reflector . . . . .	113
4.4.3	Cavitation by a sequence of two pulses produced by a confocal pair of rigid reflectors . . . . .	126
4.5	Simultaneous PCD and foil measurement . . . . .	142
4.5.1	Bubble dynamics versus interpulse delay–part I . . . . .	142
4.5.2	Bubble dynamics versus interpulse delay–part II . . . . .	159

4.6	Pair of rigid reflectors facing each other . . . . .	163
4.7	Applications-related results . . . . .	167
4.7.1	In vitro measurement of a modified clinical lithotripter . . . . .	167
4.7.2	In vivo measurement of a modified clinical lithotripter . . . . .	170
4.7.3	In vitro measurement of a partially modified clinical lithotripter . . . . .	171
4.7.4	Miscellaneous measurements with the experimental lithotripter .	176
<b>Chapter 5 Discussion and Applications</b>		<b>179</b>
5.1	Summary of numerical results . . . . .	179
5.2	Summary of experimental results . . . . .	180
5.3	Applications . . . . .	180
5.3.1	Intensified, tempered and localized cavitation – applications to research and safer lithotripsy . . . . .	181
5.3.2	Applications in progress . . . . .	182
5.3.3	General method for application . . . . .	183
<b>Appendix A Directivity</b>		<b>184</b>
<b>Appendix B Peak pressure with rigid and pressure-release reflectors</b>		<b>187</b>
<b>Bibliography</b>		<b>189</b>
<b>Vita</b>		<b>196</b>

## List of Figures

1.1 Recreations of Church's <sup>5</sup> (a) modeled lithotripter waveform and (b) predicted radial response of a bubble. Initial bubble radius $R_0$ is $3 \mu\text{m}$ . . . . .	3
1.2 Schematic of focusing by an ellipsoidal reflector. All reflected ray paths are equidistant. Their contributions sum to a strong signal. The direct wave which traveled the shorter distance $r_0$ is not focused and is negligibly weak. . . . .	5
2.1 Recreations of Church's <sup>5</sup> (a) modeled lithotripter waveform and (b) predicted radial response of a bubble to the waveform in (a). Initial bubble radius $R_0$ was $3 \mu\text{m}$ , and peak pressure of the waveform in (a) was $p^+ = 1000 \text{ bar}$ . . . . .	27
2.2 Sequence of pulses used by Ding and Gracewski. <sup>8</sup> . . . . .	28
2.3 Comparison of driving acoustic pulses (left) and bubble radial pulsation versus time (right) calculated with the Gilmore formulation: (a) positive (black) and negative (grey) $10 \text{ MPa}$ , $1 \mu\text{s}$ duration pulses, (b) $-100 \text{ MPa}$ (black) and $-10 \text{ MPa}$ (grey) $1 \mu\text{s}$ duration pulses, and (c) $10 \mu\text{s}$ (black) and $1 \mu\text{s}$ (grey) duration, $-10 \text{ MPa}$ pulses. Positive pulses have little effect on the static bubble. Duration and amplitude of the negative pulse have a very strong effect on the maximum pressure created within the bubble, with duration's effect being slightly stronger. ( $R_{\text{init}} = 2 \mu\text{m}$ in all cases.) . . . . .	30

2.4 Comparison of driving acoustic pulses (left) and bubble radial pulsation versus time (right) calculated with the Gilmore formulation: (a) tenfold decrease (black) and increase (grey) in fall time of -10 MPa, 1 $\mu$ s duration acoustic pulse, (b) tenfold increase in bubble size, 20 $\mu$ m (black) and 2 $\mu$ m (grey). Pulse fall time has little effect on the bubble dynamics. Both large and small bubbles grow and collapse in nearly the same span of time, but the small bubble exhibits larger relative changes in size and higher internal collapse pressure. . . . .	31
2.5 Two pulse results: (a) positive-then-negative-pressure pulse (black) has nearly identical bubble response to that with a single negative pulse (grey); (b) a sequence of a negative-pressure pulse and a time-delayed half-amplitude positive pressure pulse reduces ("stifles") and increases ("kicks") collapse pressure in the bubble, depending on interpulse delay $\tau$ ; (c) a sequence of a negative pressure pulse and a time-delayed, half-amplitude negative-pressure pulse increases ("bounces") and reduces ("catches") collapse pressure in the bubble. . . . .	34
2.6 Peak pressure $P_{\max}$ in the bubble versus interpulse delay $\tau$ for (a) negative-pressure pulse then half-amplitude positive-pressure pulse and (b) negative-pressure pulse then half-amplitude negative-pressure pulse sequences. Interpulse delays that reduce or increase $P_{\max}$ exist for both (a) and (b). . . . .	37
2.7 Four bipolar pulse sequences: (a) negative-positive then positive-negative ( $np - pn$ ), (b) negative-positive then negative-positive ( $np - np$ ), and (c) positive-negative then negative-positive ( $pn - np$ ). . . . .	38
2.8 The positive-negative then negative-positive ( $pn - np$ ) pressure pulse sequence has either (a) the negative pressure dominate (half-amplitude positive), which looks like Fig. 2.6(b), or (b) the positive pressure dominate (150%-amplitude positive), which has a result nearly identical to Fig. 2.6(a). . . . .	39

2.9 The positive-negative then positive-negative ( $pn - pn$ ) "stifles" the bubble growth and collapse with short delays $\tau$ between the bipolar pulses and "kicks" the collapse when the second pulse arrives as the bubble, responding to the first pulse, collapses. . . . .	40
2.10 Effect of pulse strength in the positive-negative then positive-negative ( $pn - pn$ ) pressure pulse sequence: (a) half-amplitude positive pulse and full-amplitude negative pulse "catches" the collapsing bubble. A slightly longer delay and the positive pulse is able to "kick" the collapse; (b) nearly equal amplitude positive and negative phases yield large regions of interpulse delay time for "stifling" and "kicking"; (c) a double strength positive and the collapse is always "kicked." . . . . .	41
2.11 A four-pulse sequence roughly mimicking a lithotripter pulse: both a stifling region and a kicking region are present. . . . .	42
3.1 Schematic and nomenclature of electrode and ellipsoidal reflector. . . . .	45
3.2 Schematic of the experimental lithotripter and the added second spark generator and reflector. It was necessary to use the membrane hydrophone in deionized water. The small tank contained the deionized water. Walls of the small tank contained large acoustically transparent windows made of polyethylene membrane. . . . .	47
3.3 Photograph of a rigid reflector and a pressure-release reflector. . . . .	50
3.4 Both halves of the pressure-release insert placed within rigid reflector. .	52
3.5 One half of the pressure-release insert placed within rigid reflector. . .	52
3.6 Bird's eye view of the Austin confocal arrangement of a rigid and a pressure-release reflector. Electronics are in the tank but above the water level. The capacitors are white. The brass bullet shapes on the black holders are the open-air triggers. Aluminum foil is positioned at $f_2$ , which is indicated with a white star. . . . .	55
3.7 Dornier HM3 lithotripter (used for research) at Methodist Hospital, Indianapolis, Indiana. . . . .	57

3.8 Schematic of Sonic Industries reference shock wave hydrophone (actual size). The thickness of the frame is 6 mm, and of the PVdF membrane is 25 $\mu$ m. . . . .	59
3.9 Confocal arrangement of lithotripter and passive cavitation detector (PCD). . . . .	60
3.10 Sketch of (a) aluminum foil on plastic frame on V-shaped holder, (b) top view of foil and holder positioned at $f_2$ of the reflector, and (c) side view of foil and holder positioned at $f_2$ of the reflector. . . . .	64
4.1 Acoustic waveform produced by a pressure-release reflector and calculated numerically by Cleveland and Averkiou. <sup>53</sup> . . . . .	69
4.2 Acoustic field of rigid-reflector <i>S</i> (actual size) measured with SI membrane hydrophone. . . . .	70
4.3 Acoustic field of pressure-release reflector <i>C</i> (actual size) measured with SI membrane hydrophone. . . . .	71
4.4 Side-by-side comparison of axial pressure mappings produced by a rigid reflector and a pressure-release reflector. . . . .	74
4.5 Side-by-side comparison of transverse pressure mappings produced by a rigid reflector and a pressure-release reflector. . . . .	75
4.6 Rigid-reflector waveform measured with SI membrane and waveform, negative phase lengthened to correct for shortening by membrane hydrophone, as measured by Staudenraus and Eisenmenger. <sup>48</sup> . . . . .	78
4.7 Side-by-side comparison of pressure-release reflector axial pressure mappings with SI membrane and NTR needle. The needle records weaker negative pressures. . . . .	80
4.8 Axial and transverse peak pressure mappings for rigid (grey) and pressure-release (black) reflectors. Each point is the mean of ten sparks. Standard deviation lines are shown and capped with x's (rigid) or +'s (pressure release). The -6 dB region is long and narrow for both. . . . .	82

4.9	Axial and transverse peak pressure mappings normalized to the peak peak pressure along each curve. Each point is the mean of ten sparks. Standard deviation lines are shown and capped with x's (rigid) or +'s (pressure release). The -6 dB region for the pressure-release reflector (black) is nearly half as long and wide as that of the rigid reflector (grey). . . . .	83
4.10	Pressure waveforms for four lithotripter-charging potentials. . . . .	86
4.11	Peak positive and negative pressures for four lithotripter-charging potentials. . . . .	87
4.12	R-T curves calculated with Gilmore code for waveforms at four charging potentials. . . . .	88
4.13	Signals measured with the passive cavitation detector (PCD) for four lithotripter-charging potentials. . . . .	89
4.14	Bubble duration (a) calculated with Gilmore code and measured with PCD and bubble internal collapse pressure (b) calculated with Gilmore code. . . . .	91
4.15	PCD signal and statistics with and without aluminum foil at $f_2$ . . . . .	92
4.16	Transverse cavitation field of rigid reflector measured with PCD, aluminum foil, and high speed video camera. Dimensions are actual size. The top plot is the transfer function of the PCD. Video images were borrowed from Church <i>et al.</i> <sup>67</sup> . . . . .	96
4.17	Axial cavitation field of rigid reflector measured with PCD and aluminum foil. Dimensions are actual size. . . . .	98
4.18	A sequence of four video frames taken at 3000 frames/second: (a) lithotripter spark discharge occurs, and a few ambient bubbles or dirt reflect the flash, (b) broad streak of broad bubbles 150 $\mu$ s after the arrival of the acoustic pulse, (c) off-axis bubbles have collapsed; thin stripe on axis still collapsing, and (d) no bubbles appear after collapse. Video images were borrowed from Church <i>et al.</i> <sup>67</sup> . . . . .	100

4.19 A comparison of foil pitting after (a) one spark and (b) ten sparks in a rigid reflector. Note the broadening of the pit path, which results from creating bubbles with successive shots and variation in position of the focus between successive sparks (magnified 2.5 times). . . . . 102

4.20 From top to bottom: waveform measured at  $f_2$  of a pressure-release reflector, bubble R-T curve predicted with Gilmore code, and shock waves radiated by bubble collapse and recorded by the PCD, which was focused at  $f_2$ . Arrows show the relative time scales of each plot. Note no collapse, delayed by hundreds of microseconds, is either measured or predicted with the pressure-release reflector. . . . . 103

4.21 Comparison of pitting by ten sparks in a (a) rigid reflector and (b) pressure-release reflector (magnified 2.5 times). . . . . 105

4.22 Map of pitting by ten sparks produced by a pressure-release reflector (magnified 2 times). Pit path is hourglass shaped. . . . . 106

4.23 Worm's eye view of the Austin two spark configuration. Both reflectors were angled so they shared the same  $f_2$ . Each foil was placed at  $f_2$  along the axes of the reflectors. The pressure-release reflector on the right was replaced with a rigid reflector in some experiments. . . . . 109

4.24 Foil pitted with pressure-release reflector, profilometer comparison of pitted and unpitted section of foil, and histogram pixel color distribution as indirect measure of pitting. . . . . 110

4.25 Foil pitted with rigid reflector. Profilometer measurement shows deeper larger pits with the rigid reflector than with the pressure-release reflector (see previous figure), and histogram has a higher standard deviation. . . 112

4.26 Comparison of numerically calculated maximum pressure within the bubble. The pressure-release reflector produced a lower pressure than did the rigid reflector. However, a confocal pair of a rigid reflector and a pressure-release reflector in which the pulse from the rigid reflector was delayed by 5  $\mu$ s yielded the highest pressure. The result illustrates kicking because the delayed pulse increased the collapse pressure. . . . 114

4.27 Pitting produced by a spark in pressure-release reflector and a spark delayed by  $5 \mu\text{s}$  in the rigid reflector. Pitting is seen in the center of the foil at  $f_2$  and along the centerline between the reflectors. The pits are deep and large. . . . . 117

4.28 Pitting produced by spark in pressure-release reflector and a spark delayed by  $8 \mu\text{s}$  in the rigid reflector. Pitting is seen in the center of the foil at  $f_2$  and along the centerline between the reflectors. Results are similar to those of Fig. 4.27, but the pitting has moved up and to the left. Foils in both figures show additional deep pitting created by the pressure-release-then-rigid-reflector sequence. . . . . 118

4.29 Kicking with the pressure-release-rigid reflector sequence. Three foils in which the pressure-release reflector was fired first. Intensified pitting is noted in the center ( $f_2$ ) of the foil. . . . . 119

4.30 Lines of constant interpulse delay superimposed on foil. Intensified pitting occurred at an interpulse delay of  $5 \mu\text{s}$ . Reduced pitting occurred around  $\tau = 0$ , where the pulses canceled each other and stifled bubble growth. . . . . 120

4.31 Pit depth (a) and diameter (b) are plotted for the pressure-release reflector alone, rigid reflector alone, and both reflectors fired in sequence with the rigid reflector delayed no more than  $8 \mu\text{s}$ . The sequence produced the deepest pits. . . . . 122

4.32 Pitting produced by spark in rigid reflector and a spark delayed by  $2 \mu\text{s}$  in the pressure-release reflector. No pitting along the centerline is observed. Pitting is reduced in the focal region. . . . . 123

4.33 Stifling with the rigid-pressure-release reflector sequence. Three foils in which the rigid reflector was fired first. Tempered pitting is noted in the center ( $f_2$ ) of the foil. . . . . 125

4.34 Calculated radius-time curve for one pulse (a) and the bubble's maximum internal pressure for a sequence of two pulses plotted versus inter-pulse delay (b). Times are normalized to bubble cycle for the one pulse. The arrow in (a) indicates a delayed arrival of a second pulse and in (b) the corresponding pressure increase for the kicked bubble. The grey line in (b) indicates the collapse pressure with a single pulse. . . . .	128
4.35 Worm's eye view of the Austin confocal rigid reflectors. Both reflectors were angled so they shared the same $f_2$ . Each foil was placed at $f_2$ along the axes of the reflectors. . . . .	129
4.36 Pitting produced by a spark in the right rigid reflector and a spark delayed by 300 $\mu$ s in the left rigid reflector. Two thin crossed rigid-reflector pit paths are seen. No area of intensified or mitigated pitting appeared. . . . .	130
4.37 Pitting produced by a spark in the right rigid reflector and a spark delayed by 190 $\mu$ s in the left rigid reflector. The first path was broadened when the second pulse kicked the off-axis bubbles. Pit depth also increased because of the kick. . . . .	132
4.38 Pitting produced by a spark in the right rigid reflector and a spark delayed by 92 $\mu$ s in the left rigid reflector. The first path was broadened when the second pulse kicked the off-axis bubbles. However, on axis the bubbles were kicked only weakly because the second pulse was early in the bubble period. Pits were not as deep as with the 190- $\mu$ s delay. . . . .	133
4.39 Foils subjected to a two-pulse sequence produced by a confocal pair of rigid reflectors. The right path is wider for decreasing time delay of the pulse from the left reflector. Histograms indicate increasing number and depth of pits. . . . .	135
4.40 Foils subjected to a two-pulse sequence produced by a confocal pair of rigid reflectors. The right path is narrower and the pits shallower for decreasing time delay of the pulse from the left reflector. Histograms indicate decreasing number and depth of pits. . . . .	136

4.41 Photograph borrowed from Crum <sup>69</sup> of a microjet of water through a cavitating bubble. Bubble diameter is about 2 mm. . . . .	137
4.42 Measured (a) pit depth, (b) number of white pixels in foil image, (c) standard deviation of histogram of foil image, and (d) pit path width versus delay between pulses produced by two confocal rigid reflectors. . . . .	138
4.43 Pitting produced by a spark in the right rigid reflector and a spark delayed by 0 $\mu$ s in the left rigid reflector. A streak of deep pits is apparent along the centerline between the beams. No pitting occurred along the axis of either reflector. . . . .	140
4.44 Foils subjected to two pulses produced by a pair of rigid reflectors. Pulses arrived simultaneously. The crossing beam paths do not appear at all. A long, deep narrow path of pits appears on the centerline. Many white pixels in the histograms indicate deep pits. . . . .	141
4.45 PCD detection (a) of two separate bubble cycles with 800- $\mu$ s delay between sparks in rigid reflectors. The first cycle is $450 \pm 100 \mu$ s. Numerical prediction (b) for second pulse delayed by 8/5ths of the initial bubble cycle. . . . .	144
4.46 Foils pitted by a single shot with a single rigid reflector. The location of the PCD focus is indicated and was 1.5 mm off the axis. The measured collapse cycle is $450 \pm 100 \mu$ s. The PCD was on the axis of the other reflector, and the other collapse cycle was $550 \pm 100 \mu$ s. . . . .	146
4.47 Pulse sequence used in numerical calculations. Peak pressure amplitude of the first pulse is 28 MPa, and peak pressure amplitude of the second pulse is 35 MPa. In this example, interpulse delay $\tau$ is 10 $\mu$ s. . . . .	147
4.48 Foil (a) and PCD (b) measurement with 700- $\mu$ s delay between sparks in rigid reflectors and the corresponding numerical prediction (c). Two cycles are resolved. The collapse of the first was lost in the electrical noise of the second spark in the PCD data. . . . .	148
4.49 Narrow pit path and two edge wave pit paths. . . . .	149

4.50 Foil (a) and PCD (b) measurement with 600- $\mu$ s delay between sparks and the corresponding numerical calculation (c). Two cycles are resolved. The collapse of the first is detectable in the electrical noise of the second spark in the PCD data. . . . .	150
4.51 Foil (a) and PCD (b) measurement with 500- $\mu$ s delay between sparks and the corresponding numerical prediction (c). The second pulse kicked the collapse in the first bubble cycle. No second cycle was measured or calculated. . . . .	152
4.52 Foil (a) and PCD (b) measurement with 400- $\mu$ s delay between sparks and the corresponding numerical prediction (c). The second pulse kicked the collapse in the first bubble cycle. No second cycle was measured or calculated. . . . .	153
4.53 Foil (a) and PCD (b) measurement with 300- $\mu$ s delay between sparks and the corresponding numerical prediction (c). The second pulse kicked the collapse in the first bubble cycle. No second cycle was measured or calculated. . . . .	154
4.54 Foil (a) and PCD (b) measurement with 200- $\mu$ s delay between sparks and the corresponding numerical prediction (c). The second pulse forced the early collapse in first bubble cycle, but intensification is negligible. No second cycle was measured or calculated. . . . .	157
4.55 Foil (a) and PCD (b) measurement with 100- $\mu$ s delay between sparks and the corresponding numerical prediction (c). The second pulse stifled the collapse in first bubble cycle. No second cycle was measured or calculated. . . . .	158
4.56 Foil detection (a), PCD measurement (b), and numerical calculation (c) of simultaneous pulses. PCD was located on the centerline just in front of $f_2$ . Huge pitting, one long bubble cycle, and big collapse pressures are in agreement. Foil data were corrupted by a delayed additional spark in the first reflector, which made the streak along axis 1 where the simultaneous pulses had not produced pits. . . . .	161

4.57 Foil detection (a), PCD measurement (b), and numerical calculation (c) of simultaneous pulses. PCD was located 6 mm off axis 1 and on axis 2 behind $f_2$ . Foil data were corrupted by a delayed additional spark in the first reflector, which made the streak along axis 1 where the simultaneous pulses had not produced pits. No pitting (as measured before the inadvertent pulse), no long bubble cycle, and weak collapse pressures are in agreement. . . . .	162
4.58 One hundred and eighty degree configuration of two rigid reflectors. Foil was placed at $f_2$ . Spark gaps were connected in series. . . . .	164
4.59 Foils pitted: (a) single spark in reflector $Q$ and (b) simultaneous sparks in two rigid reflectors ( $R$ and $Q$ ) facing each other. The simultaneous sparks cancel most of the long streak of pits seen in (a) and intensify a short region along and across the beams at $f_2$ . . . . .	166
4.60 Detection of pitting solely normal to the two beam paths of simultaneously fired pulses. . . . .	167
4.61 No observable pitting produced by two sparks in one bowl and $\sim 2-4 \mu\text{s}$ apart. The second pulse stifles the bubble growth caused by the first. . . .	168
4.62 Photograph of the pressure-release mask $D$ inserted in the reflector of the Dornier HM3 lithotripter. . . . .	168
4.63 Waveform measured with pressure-release masks (a) placed over Dornier HM3 brass reflector and unmodified Dornier HM3 reflector. Both waveforms contain a strong positive phase. The total positive pressure excursion in (a) is greater. Peak negative pressures in (a) are less than -18 MPa. . . . .	169
4.64 With a rigid reflector and 18 kV charging potential, the waveform measured with an encapsulated (ktech) membrane <i>in vivo</i> behind the kidney. Peak amplitude of the positive pressure phase is 14.4 MPa, and peak amplitude of the negative pressure phase is -2.5 MPa. The waveform has the same shape as <i>in vitro</i> measurements. . . . .	172

4.65 With a pressure-release reflector and 18 kV charging potential, the waveform measured with an encapsulated SI membrane <i>in vivo</i> behind the kidney. Peak amplitude of the positive pressure phase is 3 MPa, and peak amplitude of the negative pressure phase is -2.3 MPa. The waveform has the same shape as <i>in vitro</i> measurements. . . . .	173
4.66 Photograph of half of the pressure-release mask <i>D</i> inserted in the reflector of the Dornier HM3 lithotripter. . . . .	174
4.67 Waveform measured with half a pressure-release mask placed within the Dornier HM3 brass reflector. The waveform characteristic of the pressure-release reflector is seen first, followed by that of the rigid reflector. The pressure-release reflector is smaller, so the travel path (time) is shorter. . . . .	175
4.68 Foil placed halfway in the water normal to the water's surface. Increased cavitation damage is observed where splashing occurred at the water-air interface. . . . .	177
4.69 PCD detection of collapse of the plasma bubble created at $f_1$ by the spark. The experimental configuration was two confocal rigid reflectors 90° apart and an interspark delay of 300 $\mu$ s. The collapse at each $f_1$ was detected. . . . .	178
<b>A.1 Distortion of rigid-reflector waveform by hydrophone directivity. . . . .</b>	<b>185</b>
<b>A.2 Peak pressure recorded versus angle between aperture axis and hydrophone normal. . . . .</b>	<b>186</b>
<b>B.1 Highest positive amplitude waveforms recorded in the experimental lithotripter with rigid and pressure-release reflectors. . . . .</b>	<b>188</b>

**CONTROL OF ACOUSTIC CAVITATION WITH APPLICATION TO  
LITHOTRIPSY**

**ABSTRACT**

Michael Rollins Bailey, Ph.D.

The University of Texas at Austin, 1997

Supervisor: David T. Blackstock

Control of acoustic cavitation, which is sound-induced growth and collapse of bubbles, is the subject of this dissertation. This technology can be applied to extracorporeal shock wave lithotripsy (ESWL), used to treat kidney stones. Cavitation is thought to help comminute stones yet may damage tissue.

Can cavitation be controlled? The acoustic source in a widely used clinical lithotripter is an electrical spark at the near focus of an underwater ellipsoidal reflector. To control cavitation, we used rigid reflectors, pressure-release reflectors, and pairs of reflectors aligned to have a common focus and a controlled delay between sparks. Cavitation was measured with aluminum foil, which was placed along the axis at the far focus of the reflector(s). Collapsing bubbles pitted the foil. Pit depth measured with a profilometer provided a relative measure of cavitation intensity. Cavitation was

also measured with a focused hydrophone, which detected the pressure pulse radiated in bubble collapse. Acoustic pressure signals produced by the reflectors were measured with a PVdF membrane hydrophone, digitally recorded, and input into a numerical version of the Gilmore equation [F. R. Gilmore, "The growth or collapse of a spherical bubble in a viscous compressible liquid," Rep#26-4, California Institute of Technology, Pasadena (1952), pp. 1-40.]. Maximum pressure produced in a spherical bubble was calculated and employed as a relative measure of collapse intensity.

Experimental and numerical results demonstrate that cavitation can be controlled by an appropriately delayed auxiliary pressure pulse. When two rigid-reflector pulses are used, a long interpulse delay (150-200  $\mu$ s) of the second pulse "kicks" the collapsing bubble and intensifies cavitation. Foil pit depth and computed pressure that were three times single pulse values were obtained. Conversely, a short delay (< 90  $\mu$ s) "stifles" bubble growth and weakens cavitation. A single pressure-release reflector time-reverses the rigid-reflector waveform – a positive pressure spike *follows* a shallow negative phase – and thus inherently stifles cavitation.

Additional configurations and waveforms were explored, and localization of an intensified cavitation region surrounded by a tempered cavitation region was realized. The general methods of control and their specific implementations provide tools for assessment of cavitation's role in, and for improvement of, ESWL.

## Preface

This report is adapted from the doctoral dissertation of the same title by Michael R. Bailey. Mr. Bailey began his graduate studies in the Department of Mechanical Engineering in August 1991. He received a master's degree in May 1994, and will receive his doctoral degree in May 1997.

The research was done primarily at Applied Research Laboratories (ARL:UT), The University of Texas at Austin. Some of the research was performed elsewhere. During brief periods in March and May 1996 Bailey made measurements at Indiana University Medical Center, Indianapolis, Indiana, in the laboratory of Dr. A. P. Evan. Bailey also made measurements and calculations during the summer of 1996 in Dr. L. A. Crum's group at Applied Physics Laboratory (APL), University of Washington, Seattle, Washington. Support for the work carried out at ARL:UT came from the Office of Naval Research (ONR) under Grant N00014-89-J-1109, and from the IR&D Program of ARL:UT. Scientific Officer for ONR was Dr. L. E. Hargrove. Support for the work carried out in Indianapolis and at APL came from National Institutes of Health Grant DK 43881.

The current address for Mr. Bailey is Applied Physics Laboratory, University of Washington, 1013 N.E. 40th Street, Seattle, Washington 98105-6698.

David T. Blackstock  
Supervisor

This page intentionally left blank.

# Chapter 1

## Introduction

Extracorporeal shock wave lithotripsy (ESWL) is used to break kidney stones into fragments. Fragmentation ("communition" in medical usage) is caused, either directly or indirectly, by a powerful pressure pulse produced by a large focusing transducer (a spark-driven ellipsoidal reflector in this study). The clinical goal is to maximize kidney stone communiton while minimizing kidney tissue damage. One indirect mechanism by which the lithotripter pulse causes damage to stones and/or tissue is acoustic cavitation, i.e., bubble action excited by the pulse. Whether acoustic cavitation is the most important mechanism is yet to be proven. But it may be possible to assess the role of cavitation and to improve ESWL by intensifying and/or tempering cavitation. Experimental and numerical demonstrations of methods that dramatically affect cavitation yet do not affect peak positive or negative acoustic pressure are the subject of this paper.

The work started in February 1992 with a challenge to the author by L. A. Crum<sup>1\*</sup> to produce a two-pulse sequence of a negative-pressure pulse followed by a positive-pressure pulse. At the time the author was working with E. L. Carstensen and D. T. Blackstock<sup>2</sup> to remove the first pulse in a sequence of a positive-pressure pulse followed by a negative-pressure pulse. According to Crum's idea, a bubble grows as the negative-pressure pulse passes, and then the bubble collapses as surrounding water fills the void. A second positive-pressure pulse, Crum speculated, helps accelerate the collapse. The author aligned two spark-driven ellipsoidal reflectors – one pressure release and the other rigid – so that both focused sound at the same point. Müller<sup>3</sup> had previously measured a strong nearly unipolar negative-pressure pulse using a pressure-release reflector, and Müller<sup>3</sup> and Coleman and Saunders<sup>4</sup> had previously obtained a strong positive pressure spike (with a weaker negative pressure tail) by using a rigid reflector. A controlled delay between sparks in our two reflectors was added, and two pulse

---

\*Reference found in the bibliography.

sequences investigated. Experiments turned out to be interesting, at which point a numerical model, popular in the lithotripsy community, was adopted. The model was used first to investigate the behavior and parameter space of sequences of two idealized pulses such as the sequence Crum suggested and then to predict results that were compared to experimental results.

### 1.1 Theory

Lithotripters (please understand “lithotripter” and “lithotripsy” in this dissertation to mean exclusively the extracorporeal shock wave variety) produce a focused acoustic pulse in liquid. In clinical use, a patient is placed in or against the liquid with the kidney stone at the lithotripter focus, and the liquid, often water, acts as a coupling agent to transmit sound through the patient’s body to the stone. When measured at the focus in water without a patient present, the pressure pulse is 5-10  $\mu\text{s}$  long and consists of a sharp positive spike followed by a long shallow negative tail. Figure 1.1(a) shows an idealized example.

The acoustic pulse creates and excites bubbles at the focus. Church<sup>5</sup> used the Gilmore-Akulichev formulation of bubble dynamics<sup>6,7</sup> to predict bubble response to the model lithotripter pulse shown in Fig. 1.1(a). The pulse upon which the model pulse was based was obtained with a spark-driven rigid reflector. Church found the bubble to grow and collapse in a single cycle 50 times longer than the model duration of the pulse (see Fig. 1.1(b)). The bubble initially contracts under the high pressure of the pressure spike. Then the bubble expands as pressure surrounding the bubble drops below ambient in the negative pressure tail. The forward drive of the bubble gives the surrounding water momentum that keeps the water moving outward and the bubble expanding long after the negative pressure phase of the acoustic pulse, the driving force, has ended. When the outward flow stops, only the overexpanded, low-pressure gas bubble exists; there is no driving pressure. The water naturally fills the space occupied by the bubble. The water now gains inward inertia as it rushes toward the center of the bubble. In the final stage, the bubble is suddenly compressed sufficiently to become stiff, and the water slams to a halt. The sudden halt sends a shock wave back outward through the water.

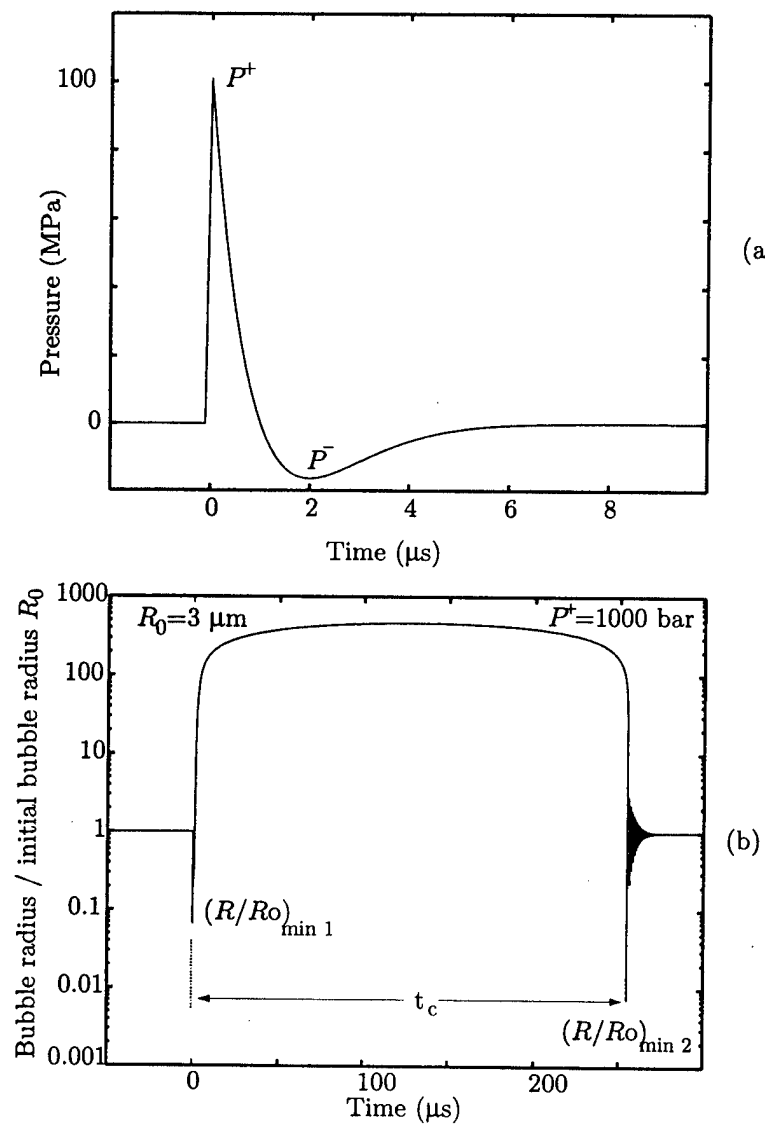


Figure 1.1: Recreations of Church's<sup>5</sup> (a) modeled lithotripter waveform and (b) predicted radial response of a bubble. Initial bubble radius  $R_0$  is  $3 \mu\text{m}$ .

The shock wave, a pressure pulse radiated into the liquid, provides one way the bubble can cause damage to stones and tissue. Another is for the bubble to collapse asymmetrically, as it tends to do near the surface of an object, such as a kidney stone or tissue. In asymmetric collapse, water can form a high-speed jet that blasts into stone or tissue. Our theoretical model is only for a spherical bubble in an infinite liquid (i.e., no stones or tissue near the bubble and no jets through the bubble). However, the bubble's maximum internal pressure, which is calculated by means of the model, is an indication of the energy concentration and therefore destructive power of the bubble. Destructive power, represented by the maximum collapse pressure in the bubble, is here used to gauge "cavitation intensity."

Ding and Gracewski,<sup>8</sup> using a modification of Church's pulse and the Gilmore-Akulichev model, numerically demonstrated that addition of a second pulse can increase the pressure in the bubble. By extension the bubble then has the potential to do more damage. Their motivation was to model bubble response to the positive-then-negative pulse sequence and the isolated negative-pressure pulse with which Carstensen *et al.*<sup>9</sup> and Bailey *et al.*<sup>2</sup> had experimentally worked. They did not attempt to change the pulse amplitude or shape. In work unrelated to lithotripsy, Moss *et al.*<sup>10</sup> proposed the extra kick of an auxiliary pressure spike to obtain thermonuclear fusion in a bubble.

In this dissertation, the Gilmore-Akulichev model and measured acoustic waveforms are used to show that a second pulse may either reduce or increase the maximum pressure in the bubble depending on the time delay between pulses. Order of magnitude changes in collapse pressure are calculated. For all the complicated codes and equations, the physical basis is very simple. If a delayed positive-pressure pulse catches the bubble in collapse, the pulse gives the bubble an extra kick that accelerates and intensifies the collapse. If the positive-pressure pulse catches the bubble early in its growth, growth is stifled and the ensuing collapse is weaker.

## 1.2 Experiment

Different sound sources are employed by different lithotripters, but all sources create more or less the pulse described above.<sup>4</sup> In this investigation, the interaction of the

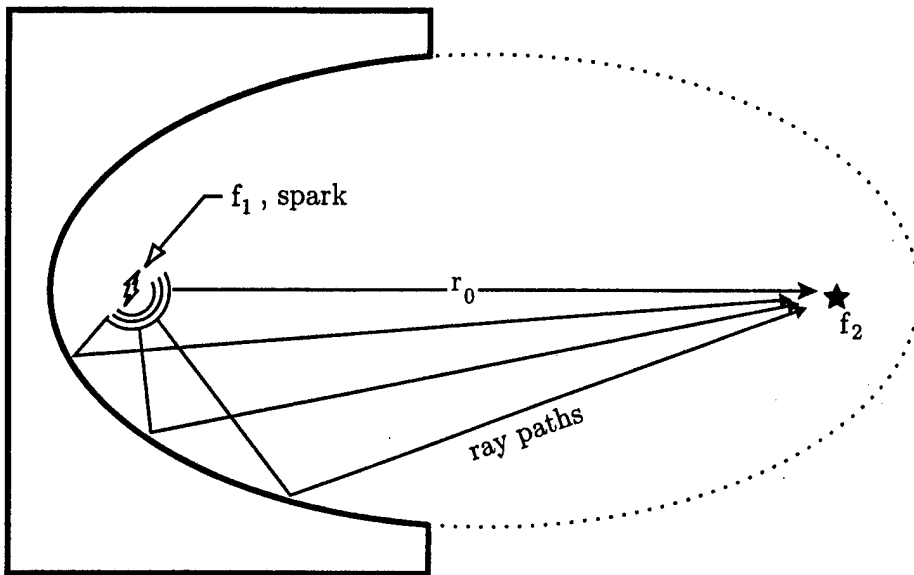


Figure 1.2: Schematic of focusing by an ellipsoidal reflector. All reflected ray paths are equidistant. Their contributions sum to a strong signal. The direct wave which traveled the shorter distance  $r_0$  is not focused and is negligibly weak.

AS-97-2

pulse with the bubble is more important than the means of generating the pulse. Nevertheless, the sources do not differ greatly from those used in clinical lithotripters, and new arrangements of sources are, therefore, directly applicable to lithotripsy. Measurement techniques developed also apply to clinical lithotripsy.

### 1.2.1 Sources

Like the clinical Dornier HM3 lithotripter,<sup>11</sup> the sources in our investigation use an underwater spark to make the sound pulse and an ellipsoidal reflector to focus it. Figure 1.2 illustrates how sound rays emanating from a spark at the near focus  $f_1$  of the ellipsoid are focused at the far focus  $f_2$ . At  $f_2$ , direct sound that travels along the path  $r_0$  is negligible compared with the focused sound.

The following variations on the conventional HM3-style source were used in this study:

1. Pressure-release ellipsoidal reflector.
2. Pair of ellipsoidal reflectors, either both rigid or one rigid and one pressure release. The pair were aligned to focused at the same spot. The timing between the pair of sparks was controlled and varied as was the angle between the reflector pair. Angles 80°, 90°, and 180° were considered.
3. Single ellipsoidal reflector driven by a sequence of two sparks.
4. Half and half single reflector. One reflector was essentially divided in half. The cutting plane was along, not perpendicular to, the major axis of the ellipsoid. In one half was inserted a shell in the shape of a quarter ellipsoid, which shared the same foci with the original ellipse but had smaller dimensions.

### 1.2.2 Cavitation measurement

Cavitation at the focus of a lithotripter has previously been detected and measured. Coleman *et al.*<sup>12</sup> placed aluminum foils at  $f_2$  of a Dornier HM3 lithotripter, normal to the reflector axis. Pits created in the foil were shown to be evidence of cavitation activity. By constructing a box containing shelves of foil and subjecting the box to many lithotripter shots, they created a map of the cavitation field. Lifshitz *et al.*<sup>13</sup> demonstrated a statistical method of quantifying the intensity of the cavitation seen in digital images of pitted foil.

A new foil technique is described in this paper. One shot is used per foil, not several, and foils are placed along the axis of the reflector, not perpendicular to it. The new alignment gives an axial and lateral map of the cavitation field for each shot. The new alignment also does not trap bubbles convected by radiation pressure, because radiation pressure is tangential to the foil in the new alignment. Number of white pixels and standard deviation of the histogram of the shades of the pixels in digital images of the pitting are compared to direct profilometer measurement of pit depth, and profilometer results are used as a relative measure of cavitation intensity.

Coleman *et al.*<sup>14,15</sup> used a focused hydrophone as another means of cavitation detection. The hydrophone measures the pressure pulse emitted in cavitation collapse.

A map of the cavitation field is created by scanning with the hydrophone and recording many shots.

A hydrophone much like that of Coleman *et al.* was built for our experiments. It is referred to in this paper as the passive cavitation detector (PCD). The design was not greatly altered. However, effort was made to calibrate the PCD, which the Coleman group did not report doing.<sup>16</sup>

### 1.2.3 Control of cavitation

The new reflectors and reflector arrangements and new and old measurement techniques were used to demonstrate experimental control of cavitation. A positive-pressure pulse, or the positive pressure phase of a pulse, that arrives as the bubble starts to grow stifles growth and forces a weak collapse. Pits on the foil are smaller and shallower. "Stifling" was found to occur when the pressure-release reflector was used by itself and also when the time delay between sparks was short in the reflector pair arrangement (two rigid reflectors). On the other hand, positive-pressure pulse "kicks" the bubbles when it arrives as the bubbles are collapsing. The result is deeper pits in the aluminum foil. Because, in the reflector pair configurations, interpulse delay depends on the precise location around the focus, localized regions of deep pits surrounded by shallow pits were obtained. PCD results show time of collapse and agree with numerically predicted collapse times. The combination of foil pitting, passive cavitation detection, and numerical predictions demonstrate that cavitation can be controlled. They also provide a description of the bubble dynamics involved.

## 1.3 Dissertation map

Here a map of the dissertation is presented. Theory is discussed first. The goal is to demonstrate how a sequence of two pressure pulses may be used to control cavitation. The experimental procedure is next. The new reflectors, sources, and reflector pairs as well as new techniques for detecting and measuring cavitation are introduced. Results are then presented. Numerical and experimental evidence of bubble duration and collapse violence are in agreement, and control of cavitation is demonstrated. Lastly,

results and contributions are summarized, applications described, and future work discussed.

### 1.3.1 Map of Chapter 2

In Chapter 2 our theoretical model is described, its numerical implementation explained, the implementation benchmarked against other codes, and bubble response to two pulses explored. The goal in the chapter is to describe the numerical tool and use it to explore bubble response to two pressure pulses. The tool is used to approximate the radial response of a spherical bubble as a function of time and to calculate the pressure in the bubble. The single bubble response to a pulse or a two pulse sequence is a model of the individual bubbles in our experiments. Although new results are explored, numerical results to be compared with the experiment are not presented in this chapter. Such results appear in Chapter 4.

Modeling a cloud of bubbles or bubbles impacting aluminum foil is beyond the scope of our model. But the pressure in a single bubble is calculated for a single acoustic pulse and for sequences of two pulses. The procedure parallels our experiments. A relative increase in pressure, which is caused by, for example, a specific two pulse sequence, indicates intensified cavitation. Just as in the experiments, an increase in pit depth in foil, which is again caused by a specific two pulse sequence, demonstrates intensified cavitation.

The model is presented in this chapter. Some illustrative calculations are made here, but they are with simplified waveforms. The calculations demonstrate the general effects of two pulses on a bubble without the complications added by using more complex waveforms that more accurately model the pulses used in experiments.

Chapter 2 proceeds as follows:

In Sec. 2.1 an outline of the deviations of the Rayleigh-Plesset equation of bubble dynamics and our theoretical model, the Gilmore equation, are given. The Gilmore equation allows for compressibility of the liquid surrounding the bubble, and the Rayleigh-Plesset does not. Inclusion of compressibility makes the Gilmore equation better suited to application to lithotripsy research.

The numerical implementation of the model is discussed in Sec. 2.2. The algorithm to solve the Gilmore equation and thus the radius of a single spherical bubble as a function of time is described. Descriptions of pressure waveforms, pulses, are inputs to the code that drives the bubble. The radial response versus time is a response to the time varying pressure produced by the pulse. The algorithm that permitted use, as inputs, of pressure waveforms, which were measured with a hydrophone and digitized on an oscilloscope, is addressed.

In Sec. 2.3, our code is benchmarked against other codes, those of Church<sup>5</sup> and Ding and Gracewski.<sup>8</sup> To compare to others' results, their waveforms are used rather than waveforms measured by our hydrophone. Church and Ding and Gracewski used analytic descriptions of a lithotripter pulse.

In Sec. 2.4, the bubble's radial response to sequences of two pulses is explored. The calculations are new. Pressure pulses used are simple triangle pulses (not measured or analytically described lithotripter waveforms). Simple pulses permitted exploration of the parameter space of the single bubble, single pulse system, and the single bubble, two pulse system without the complications added by more complex waveforms. First, for a single pulse, bubble size and the properties of the pulse that affect bubble response are investigated and ranked. The two most important properties are found to be amplitude and duration. No attempt is made, therefore, to vary other properties. Second, sequences of two triangle pulses are investigated. Amplitude and time-delay of the second pulse are investigated. The concepts of "kicking" (intensification of the bubble collapse) and "stifling" (tempering the bubble collapse by stunting bubble growth) are defined and illustrated. Third, sequences of bipolar pulses made up of triangle pulses are investigated. Bipolar pulses better represent the pulses produced by the experimental spark-driven reflectors. Kicking and stifling are numerically predicted for bipolar pulses.

### 1.3.2 Map of Chapter 3

In Chapter 3, the experiments are described. How cavitation was created and controlled is described first. Then how cavitation was measured and how control was observed are discussed.

Water tank, water, spark generator, positioners, and reflectors, which together make up the experimental lithotripter, are discussed in Sec. 3.1. The heart of the system is a spark at the near focus of an ellipsoidal reflector. The spark produces sound, which is reflected and focused by the reflector. Two types of reflectors, rigid (brass) and pressure release (polyurethane foam), were used.

In Sec. 3.2 modifications to the basic single spark source/single reflector arrangement are discussed. First, one arrangement of two reflectors is described. Each reflector had at its near focus a spark source, and both reflectors shared the same second focus. The time delay between sparks was varied. Second, another arrangement of two reflectors is addressed. In the second arrangement, the angle between the reflectors was varied. Angles  $80^\circ$ ,  $90^\circ$ , and  $180^\circ$  were considered. Third, experimental modifications to a clinical Dornier HM3 lithotripter are discussed.

Measurement techniques are described in Sec. 3.3. The PVdF membrane hydrophone used to record the focused acoustic field produced by the lithotripter, new techniques to record and measure cavitation-induced pits in aluminum foil, and the PCD used to detect sound radiated by bubble collapse are described in detail.

### 1.3.3 Map of Chapter 4

Results are presented in seven sections in Chapter 4. Numerical and measured results appear together.

In Sec. 4.1, the acoustic fields of the rigid and pressure-release reflectors are described. Waveforms and mappings of peak amplitudes are presented. Rigid and pressure release reflectors are compared.

Section 4.2 presents a comparison of bubble duration as predicted by the numerical code and as measured by the PCD. The rigid reflector was used, and the electrical potential of the spark generator was varied. The duration of the bubble cycle increased with electrical potential. Good agreement between numerical and measured results provides a solid basis for more complicated experiments discussed later in the chapter.

In Sec. 4.3, the cavitation fields of the rigid and pressure-release reflectors are described. Numerical predictions made with measured acoustic waveforms and measurements made with the PCD are presented. Foil data are also presented. Rigid and

pressure-release reflectors are compared.

Section 4.4 shows results of the study of collapse intensity as a function of delay between two pulses. Pit depth measured on aluminum foil is compared to numerical calculation of the maximum pressure within the model bubble. Intensified and tempered cavitation is demonstrated, as is localization of an intensified region.

In the results shown in Sec. 4.5, the measurements in Sec. 4.4 are repeated with emphasis on measuring the time history of the bubble. Time history recorded with the PCD is compared with numerical prediction of the bubble growth and collapse cycle. Agreement is good. Stifling and kicking are demonstrated, and the experimental results support the model's description of the bubble dynamics involved.

Measurements with the confocal reflectors facing each other are presented in Sec. 4.6. The 180° configuration was designed to shrink the localized region of intensified cavitation. Stifling with two sparks in one reflector is also reported.

In Sec. 4.7, results directed toward clinical studies are reported. *In vivo* and *in vitro* measurements with modifications to a Dornier lithotripter are presented.

#### **1.3.4 Map of Chapter 5**

Results are discussed and summarized in Chapter 5. Specific applications to clinical lithotripsy and lithotripsy research are presented. The section includes a proposal of future work.

## Chapter 2

### The Gilmore equation, its numerical implementation, and explorative calculations of the use of a second acoustic pulse to control cavitation behavior of a bubble

Nowhere in this dissertation is an attempt made to calculate the behavior of the complicated, multi-bubble cavitation field of a lithotripter or to theoretically predict damage to stones. What is calculated is the radius as a function of time  $R(t)$  of a single bubble and the pressure in the gas within the bubble when the bubble is driven by an acoustic pulse or sequence of two pulses. Relative increase in calculated pressure is shown in Chapter 4 to correspond well to relative increase in experimentally determined damage.

The Gilmore equation was adopted as our bubble dynamics model. The equation is described in terms of its modifications to the Rayleigh-Plesset equation in Sec. 2.1. The Gilmore equation is not derived. The model's relevance to lithotripsy studies is addressed in Church<sup>5</sup> and has been accepted by a number of others.<sup>18,8</sup> For our purposes the model was used as a tool to investigate the use of a second pulse to control the cavitation behavior of a bubble.

The numerical algorithm used to solve the equation is addressed in Sec. 2.2. The input is an analytic or digital description of an acoustic pressure pulse or pulse sequence and the output is the radius-time curve of the bubble and the pressure inside the bubble. Four input types were used in this study. Two were analytical descriptions of lithotripter pulses to benchmark our implementation against others. Benchmarking is discussed in Sec. 2.3. The third type consisted of simple triangle pulses for purposes of exploring two pulse sequences in general. Explorative results with triangle pulses are included in Sec. 2.4. The fourth type included waveforms measured with a hydrophone and digitized with an oscilloscope. Results with the measured waveforms are presented in Chapter 4, alongside the measurements.

The point of Sec. 2.4 is to explore bubble response to a sequence of two pulses.

This section alone in the chapter contains new and original work. The exploration is a half step between our simple physical concept that a second pulse can “kick” the collapsing bubble and the necessarily more complicated investigation using two spark-driven ellipsoidal reflectors. The calculations in the section give validation to the “kicking” idea, describe the regions of parameter space where “kicking” occurs, and demonstrate other effects caused by addition of a second pulse.

## 2.1 Development of the Gilmore equation of bubble dynamics

The Gilmore equation is not derived, but after a description of the problem, the assumptions and derivations of the Rayleigh-Plesset and Gilmore equations are outlined. The Gilmore equation differs only in that a compressible liquid is considered. Applicability to lithotripsy is addressed. For a more thorough discussion of the Gilmore equation’s applicability to lithotripsy, see Church.<sup>5</sup>

### 2.1.1 Statement of the problem

The physical problem is one of a single bubble in an infinite liquid under a time-dependent applied pressure (our pulse or pulses). What is the radius of the bubble as a function of time? The assumptions are:

1. a single bubble exists in an infinite medium
2. the bubble remains spherical at all times
3. conditions are spatially uniform inside the bubble
4. the initial radius of the bubble  $R_0$  is much less than the wavelength (pulse duration) of the acoustic excitation
5. no body forces (i.e., no gravity) act on the bubble
6. bulk viscous effects can be ignored
7. the bubble is initially at equilibrium

8. gas content is constant in the bubble (i.e., no diffusion, mass transfer, or evaporation across the bubble wall)
9. the gas within the bubble behaves as an ideal gas
10. flow in the liquid around the bubble is isentropic.

The last two assumptions are not required in the derivation but were used to define terms necessary in the evaluation of the Gilmore equation. In regard to assumption 6, Poritsky<sup>17</sup> followed a similar approach to what we use below but included an account for liquid viscosity. He found that effects of liquid viscosity manifest themselves through the boundary condition and not through the Navier-Stokes equations. Since viscosity in the bulk liquid has been neglected, the assumption of isentropic liquid flow may also be made. In the following, development is based on that of Prosperetti,<sup>19</sup> but Young,<sup>20</sup> Leighton,<sup>21</sup> and Akulichev<sup>7</sup> have similar developments.

All quantities refer to the liquid except  $p_g$ , which is the pressure in the gas. Radial distance  $R(t)$  refers to the position of the liquid gas interface, which for lack of a better phrase is often referred to as the bubble wall. Capital letters by convention refer to quantities in the liquid evaluated at the bubble interface.

### 2.1.2 Equations used as a basis for the model

The following equations uniquely model the motion of the liquid around the bubble. Enthalpy  $h$  of the liquid (actually the difference between the enthalpy at a point distance  $r$  away from the center of the bubble and the enthalpy far from the bubble), given by

$$h = \int_{p_\infty}^{p(r,t)} \frac{1}{\rho} dp , \quad (2.1)$$

and sound speed  $c$  in the liquid given by

$$c = \left( \frac{dp}{d\rho} \right)^{\frac{1}{2}} |_{s=\text{constant}} , \quad (2.2)$$

where  $p$  and  $\rho$  are pressure and density of the liquid. Both pressure and density in general depend on position  $r$  and time  $t$ . The pressure of the liquid far from the bubble is  $p_\infty$  and is the sum of the acoustic  $p_a(t)$  and hydrostatic  $p_0$  pressure of the liquid.

Note  $p_\infty$  means far from the bubble but within the same sound field as the bubble. Pressure of the liquid distance  $r$  from the bubble center is  $p(r, t)$ ;  $p(R, t)$  is therefore pressure of the liquid at the bubble interface. Entropy of the liquid is  $s$ .

The fundamental equations used in modeling liquid motion are conservation of mass

$$\frac{1}{\rho} \left( \frac{\partial \rho}{\partial t} + u \frac{\partial \rho}{\partial r} \right) + \frac{\partial u}{\partial r} = 0 , \quad (2.3)$$

and conservation of momentum

$$\frac{\partial u}{\partial t} + u \frac{\partial u}{\partial r} = - \frac{1}{\rho} \frac{\partial p}{\partial r} , \quad (2.4)$$

where  $u$  is liquid particle velocity that has been assumed to be entirely in the radial direction. The two equations describe a relationship between velocity  $u$  and pressure  $p$  of the liquid. When pressure on the bubble changes, the fluid moves. If the liquid surrounding a bubble moves one way, the bubble expands. If it moves the other the bubble contracts. With the inclusion of the velocity potential  $\phi$  where  $u = \frac{\partial \phi}{\partial r}$ , the mass and continuity equations can be recast as, respectively,

$$\frac{\partial^2 \phi}{\partial r^2} + \frac{1}{c^2} \left( \frac{\partial h}{\partial t} + \frac{\partial \phi}{\partial r} \frac{\partial h}{\partial r} \right) = 0 , \quad (2.5)$$

and

$$\frac{\partial \phi}{\partial t} + \frac{1}{2} \left( \frac{\partial \phi}{\partial r} \right)^2 + h = 0 . \quad (2.6)$$

Equation 2.6 is the Bernoulli integral.

The physical interpretation of the mass/momentum system of equations is obscured but only slightly. Pressure, now, enters through  $c$  and  $h$ , and  $\phi$  is directly related to  $u$ . Therefore,  $h$  and  $c$  are our driving forces and  $\phi$  represents the bubble motion.

The first boundary conditions at the bubble interface  $r = R(t)$  is simply a restatement of the definition of  $\phi$  and states that the bubble interface moves with the liquid. The mathematical expression is

$$\frac{\partial \phi}{\partial r} = U , \quad (2.7)$$

where  $U = u(R, t) = \frac{dR}{dt}$ . The conventional use of capital letters to denote quantities at the boundary on the liquid side is followed. Only in the case of mass transfer through the wall is the boundary condition in error (see Prosperetti<sup>19</sup>). The second boundary

condition is a statement of the force balance across the bubble interface. The condition is

$$p_g(R, t) = p(R, t) + 2\sigma/R + 4\mu U/R , \quad (2.8)$$

where  $\mu$  is the shear viscosity coefficient of the liquid and  $\sigma$  is surface tension. At the interface,  $p(R, t)$  is the pressure in the liquid side, and  $p_g$  is the pressure in the gas. Again,  $p(R, t)$  encompasses the acoustic pulse as well as the hydrostatic pressure, and since uniform properties have been assumed in the gas,  $p_g$  is the gas pressure anywhere inside the bubble.

Here, an ideal gas in the bubble is assumed; pressure in the gas within the bubble  $p_g$  is given by

$$p_g = \left( p_0 + \frac{2\sigma}{R_0} \right) \left( \frac{R_0}{R} \right)^{3\gamma} , \quad (2.9)$$

where  $\gamma$  is the ratio of specific heats of the gas. Isentropic flow in the gas strictly must also be assumed, but the assumption of spatially uniform properties may cover this assumption.

Equations 2.5, 2.6, 2.7, and 2.8 describe the radial motion of the single bubble model when pressure in the liquid  $p(r, t)$  is prescribed, but further approximations are made to proceed further. Here, the path to the Rayleigh-Plesset equation diverges from that to the Gilmore equation. To obtain the Rayleigh-Plesset equation, an incompressible liquid ( $c \rightarrow \infty$  and  $\rho = \text{constant}$ ) is assumed. Gilmore approximated the compressibility of the liquid.

### 2.1.3 Outline of the derivation of the Rayleigh-Plesset equation

The path to the Rayleigh-Plesset equation is discussed (for a history of the equation see Young<sup>20</sup>). With the incompressibility assumption, equations of conservation of mass and conservation of momentum take the forms

$$\frac{\partial^2 \phi}{\partial r^2} = 0 , \quad (2.10)$$

and

$$\frac{\partial \phi}{\partial t} + \frac{1}{2} \left( \frac{\partial \phi}{\partial r} \right)^2 + \frac{p(R, t) - p_\infty}{\rho} = 0 , \quad (2.11)$$

where  $h$  reduces to  $\frac{1}{\rho}(p(R, t) - p_\infty)$  and is the only driving force in the equation. A solution to Eq. 2.10 is

$$\phi = -R^2 \frac{U}{r} . \quad (2.12)$$

Substitution of Eqs. 2.8 and 2.12 into Eq. 2.11 yields the Rayleigh-Plesset equation for the radial motion of the bubble interface,

$$R \frac{dU}{dt} + \frac{3}{2} U^2 = \frac{1}{\rho} (p(R, t) - p_\infty) . \quad (2.13)$$

The liquid is incompressible. Surface tension and viscosity enter through a boundary condition at the bubble wall and are included in  $p_g$ . In this form the equation equates inertial energy on the left with work done by a pressure difference on the right. The pressure difference occurs between the pressure at the bubble interface, which is gas pressure minus surface tension and a term due to viscosity, and the pressure far from the bubble, which is the sum of the hydrostatic pressure and the applied acoustic field. Here, a glimpse of why compressibility of the liquid (which is neglected in the Rayleigh-Plesset equation) is important may be made. The difference in pressure at the bubble and far from the bubble drives the bubble. Both are time varying. But a change in one must propagate through the fluid to affect the other. In an incompressible fluid the travel is instantaneous. But a real compressible fluid introduces a lag due to a finite sound speed. The lag and therefore compressibility becomes increasingly important the faster the bubble wall moves. For a different and more physical derivation, see Apfel.<sup>22</sup>

#### 2.1.4 Limits of the Rayleigh-Plesset equation

The Rayleigh-Plesset equation works well as long as the velocity of the bubble wall is small compared with the sound speed of the fluid. For a good portion of many bubble cycles, this stipulation holds. Approximations to address compressibility of the liquid therefore only address final stages of strong collapse or very early stages of abrupt growth. Inclusion of compressibility adds a dissipation mechanism, sound radiation from the bubble, which tempers the suddenness of the extreme motions.

Herring,<sup>23</sup> Trilling,<sup>24</sup> Flynn,<sup>25</sup> and others made models which included compressibility but assumed a constant sound speed in the liquid. The assumption restricted

application to cases where  $U \ll c$ , the linear sound speed. Gilmore<sup>6</sup> used the Kirkwood-Bethe<sup>26</sup> approximation, which sets the speed of acoustic waves equal to the sum of the local sound speed in the liquid and the liquid velocity. The Gilmore model is, therefore, not restricted to cases where  $U \ll c_0$ . For this reason, the Gilmore equation has been chosen for lithotripsy studies.

### **2.1.5 General additions to the Rayleigh-Plesset equation and applicability of the Gilmore equation to lithotripsy**

In general what was said about the incompressibility assumption is true about other assumptions in the model: the assumptions remove mechanisms of energy dissipation (e.g., heat conduction) from the model. This means that the calculated pressure in the bubble is an upper limit approximation of the true pressure. However, we are interested in relative changes in the pressure, not absolute pressures. In addition, the duration of the bubble is of interest. Duration, too, is affected little by the assumptions, since dissipation plays its greatest role when the bubble moves most quickly (i.e., only as the bubble just begins to grow or to be in its final stages of collapse). The time over which bubble wall speed is a factor is brief compared with the duration of the collapse cycle. Church<sup>5</sup> gives a detailed account and shows that the factors neglected by the Gilmore equation play little role in the cavitation field of a lithotripter. He finds, however, that compressibility is a big factor. Vokurka,<sup>27</sup> Ayme,<sup>28</sup> and Young<sup>20</sup> discussed the applicability of the Gilmore equation to situations in which the bubble collapses slowly and in which it collapses very suddenly. In fact, in descriptions of numerical comparisons of the Gilmore equation and the exact Navier-Stokes equations, the description "surprisingly accurate" said of the Gilmore equation comes up surprisingly often.<sup>29,20,7</sup>

### **2.1.6 Outline of the derivation and description of the Gilmore equation**

The Gilmore equation is an appropriate stopping point for lithotripsy research in a line of increasingly sophisticated approximations to liquid compressibility. Of the common models, it is the first one designed to be valid for bubble wall speeds equal to or greater than the sound speed.

Two approximations in addition to the seven listed above are used to derive and implement the Gilmore equation. The first is the Kirkwood-Bethe hypothesis,<sup>26</sup> which states that the speed at which a pressure disturbance travels is a function of liquid motion. Specifically, the Kirkwood-Bethe hypothesis states that for spherical waves of finite-amplitude, the product of the radial coordinate  $r$  and the velocity potential  $\phi$  propagates with a velocity equal to the sum of the local sound velocity  $c$  and the liquid velocity  $u$ . Gilmore<sup>6</sup> used a form of Eqs. 2.5, 2.6, 2.7, and 2.8, the Kirkwood-Bethe hypothesis, and a mathematical approach known as the method of characteristics to obtain the Gilmore equation,

$$R \left(1 - \frac{U}{C}\right) \frac{dU}{dt} + \frac{3}{2} \left(1 - \frac{U}{3C}\right) U^2 = \left(1 + \frac{U}{C}\right) H + \frac{U}{C} \left(1 - \frac{U}{C}\right) R \frac{dH}{dR} , \quad (2.14)$$

where again by convention capital letters are used to denote quantities to be evaluated at the bubble interface. The terms on the left are again inertial terms, and those on the right represent the work done by the pressure difference at the bubble and far from the bubble. The impetus that drives the bubble, acoustic pressure, enters through  $C$  and  $H$ , which are functions of pressure. Corrections to the Rayleigh-Plesset equation are proportional to  $\frac{U}{C}$ . At slow interface speeds, the corrections are small, and in the case of an empty bubble, the Gilmore equation can be reduced to a form similar to that taken by the Rayleigh-Plesset equation.

In the second approximation, pressure dependence on density  $\rho$  is approximated by a modified Tait equation:<sup>30,31</sup>

$$p = A(\rho/\rho_0)^n - B , \quad (2.15)$$

where  $A$ ,  $B$ , and  $n$  are empirical constants and  $\rho_0$  is the equilibrium density of the liquid. Included in the approximation is the assumption of isentropic liquid flow. The approximation was inaccurate for the short time periods when pressure in the liquid exceeded  $10^4$  MPa.<sup>5</sup> The modified Tait equation was used to calculate the enthalpy,

$$H = \int_{p_\infty(t)}^{p(R,t)} \frac{dp}{\rho} = \frac{nA^{1/n}}{(n-1)\rho_0} \{ [p(R,t) + B]^{\frac{n-1}{n}} - [p_\infty(t) + B]^{\frac{n-1}{n}} \} , \quad (2.16)$$

and sound speed,

$$C = \frac{dp}{d\rho} = [c_0^2 + (n-1)H]^{1/2} , \quad (2.17)$$

where  $c_0 = \frac{An}{\rho_0}$  is the linear sound speed of the liquid. Equation 2.16 is essentially the same difference between pressure at the wall and pressure in the liquid that appears on the right side of Eq. 2.13.

The combination of the Kirkwood-Bethe hypothesis and modified Tait equation provides an acoustic propagation speed  $C+U$ , which increases with increasing pressure according to a material description of the liquid and accounts for convection of the wave by the movement of the liquid. Convection and material nonlinearity are the two factors considered in finite-amplitude acoustic theory.<sup>32,33</sup>

### 2.1.7 Summary of the Gilmore equation

Here is a brief summary of the Gilmore equation. The Gilmore equation models the radial response of a single spherical bubble to an acoustic pressure. Assumptions are repeated here:

1. a single bubble in an infinite medium
2. the bubble remains spherical at all times
3. conditions are spatially uniform inside the bubble
4. the initial radius of the bubble  $R_0$  is much less than the wavelength of the acoustic excitation
5. no body forces (i.e., gravity)
6. bulk viscous effects can be ignored
7. the bubble was initially at equilibrium
8. constant gas content in the bubble (i.e., no diffusion, mass transfer, or evaporation across the bubble wall)
9. the gas within the bubble behaves as an ideal gas
10. flow in the liquid around the bubble is isentropic.

Surface tension and viscosity appear at the bubble interface. Speed of acoustic propagation in the liquid is approximated by the Kirkwood-Bethe hypothesis and a modified Tait equation.

## 2.2 Numerical solution of the Gilmore equation

In this section, the algorithm to solve the Gilmore equation and the algorithm to utilize experimentally obtained pressure waveforms as input are explained.

### 2.2.1 Solution algorithm

Our numerical code substitutes bubble radius  $R$  and bubble wall velocity  $U$  at one instance of time into Eq. 2.14 to calculate  $R$  and  $U$  at the next instance of time. Initial conditions are given by  $R = R_0$  and  $U = U_0$ . Time  $t$  is the independent variable. Time is in discrete steps, which are determined by the algorithm to maintain a constant small numerical error. Intermediate dependent variables are pressure  $p_g$ , pressure  $p(R, t)$ , enthalpy  $H$ , and sound speed  $C$  where  $p(R, t)$ ,  $H$ , and  $C$  are in the liquid at the bubble wall. At each time step, the code solves sequentially auxilliary Eqs. 2.9, 2.8, 2.16, and 2.17 for intermediate variables  $p_g$ ,  $p(R, t)$ ,  $H$ , and  $C$ . Acoustic pressure  $p_a(t)$ , which is defined by the pressure pulse we choose, enters the problem in the calculation of  $H$  because the pressure in the liquid far from the bubble  $p_\infty$  is the sum of the hydrostatic and acoustic pressures. The code uses a fourth-order Runga-Kutta algorithm, Eq. 2.14, and  $R$ ,  $U$ ,  $H$ , and  $C$  at one time step to calculate  $U$  and  $R$  at the next time step. The final result is a string of times and a string of radii. A string of other values, such as gas pressure, can also be saved. The maximum pressure in the gas is used in this dissertation.

Church<sup>5</sup> wrote the first “Gilmore code” (numerical formulation of the Gilmore equation) for lithotripsy. Choi et al.<sup>18</sup> and Ding and Gracewski<sup>8</sup> also followed Church’s method and wrote codes for lithotripsy research. The code used in the investigation reported here was written by R. O. Cleveland (Applied Physics Laboratory, Seattle, Washington). Cleveland gave the author the job of testing and debugging the code. The constants used in our code are those used by Ding and Gracewski and are similar

to those of Church. The values are for water and an ideal gas at 30 °C. The constants are

$$\mu_0 = 0.0008019 \text{ Ns/m}^2,$$

$$\rho_0 = 995.646 \text{ kg/m}^3,$$

$$n = 7,$$

$$\sigma = 0.071035 \text{ N/m},$$

$$p_0 = 0.1 \text{ MPa},$$

$$A = 300.1 \text{ MPa},$$

$$\gamma = 1.4,$$

$$c_0 = 1509.7 \text{ m/s, and}$$

$$B = 300 \text{ MPa.}$$

The code was written in MatLab (The MathWorks Inc., Natick, Massachusetts). The longest cases took nearly 3 hours to run on a 70 MHz Apple Macintosh PowerPC 7100 with 24 MB ram.

### 2.2.2 Measured waveforms as inputs to the code

What is left to describe then are the descriptions of the acoustic pressure waveforms fed to the algorithm. The goal in writing the code was to make it so that pressure waveforms experimentally obtained with a hydrophone and digitized by an oscilloscope could be input into the Gilmore code. In this way, experimental and numerical results can be compared directly. The way the code was written to accept measured waveforms is discussed here. Numerical results with measured waveforms are presented in Chapter 4, where the measured waveforms are presented.

The hydrophone converts a pressure pulse to an electrical pulse. A digital oscilloscope records the electrical pulse as two strings of numbers. The first string is the time the signal came in and the second is the electrical potential, which when multiplied by the hydrophone calibration is a number representing the pressure. Each time has a corresponding pressure. But values by definition were sampled, and pressures were recorded only at certain times. Uniform sampling was used. When the waveform is plotted, the second string, pressure, is plotted versus the first, time.

A 10–20  $\mu$ s segment of a recorded wave was used (i.e., an appropriate section of the time string where the difference between the value of the first member of the string and the value of the last was 10–20  $\mu$ s and the corresponding section of the pressure string). The peak positive pressure was centered in the segment. We wanted the bubble to “see” no acoustic pressure before a pulse or after a pulse, so the ends of the waveforms were padded with 50 zeros. A Hanning window was tried for the purpose of making sure the ends of the pulse were at zero pressure, but, except for in a very few cases, the Hanning window weakened the negative sections of the wave unacceptably.

To obtain a two pulse sequence, two single pulse waveform segments were chosen. The pressure string of the pulse to be delayed was tacked on the pressure string of the first pulse so that the pressure string was twice as long. The desired delay between pulses was added to each value of the time string of the pulse to be delayed. The new time string of the delayed pulse was then tacked on the time string of the first pulse. When the elongated pressure string is plotted versus the elongated time string, a two pulse sequence is obtained.

When the delay between pulses was so short that the pulses overlapped, a different strategy was used. The index of the first time value greater than the delay time,  $i_d$ , was obtained from the time string of the pulse to be delayed. The index states how many values in the string are smaller than the delay time. The delay time was added to each of the last  $i_d$  values of the time string of the delayed pulse. The values were then tacked on the end of the time string of the first pulse to obtain the time string for the sequence. The first  $i_d$  values of the pressure strings of the first pulse were the first  $i_d$  values of the pressure string of the sequence. The last  $i_d$  values of the pressure string of the delayed pulse made up the last  $i_d$  values of the sequence pressure string. The first values of each of the remaining sections of the pressure strings were added, and the second values were added, and so on. The string of sums made up the middle of the pressure string of the sequence.

The problem in using a digital waveform instead of an analytical description of a wave is that values of the pressure may be needed where no sample was taken. The Runge-Kutta routine of the Gilmore code takes its own separate discretized time steps. The algorithm determines at what time steps the values of the waveform must

be known. When the sampled waveform did not have a datapoint that corresponded to the time used in the algorithm, the waveform and its numerically calculated time derivative had to be interpolated. The interpolation was done in MatLab using a linear spline algorithm.

### **2.3 Benchmarking our numerical code**

In this section, the solution algorithm is tested with analytical descriptions of lithotripter pressure waveforms, not experimentally obtained waveforms, and our code is benchmarked against other codes.

#### **2.3.1 Goal and method of benchmarking**

A Gilmore code that accepts measured waveforms is a powerful tool, but without comparison to other results, the code is untested. Here, benchmarking against other codes is reported. Test cases were run with two analytical descriptions of lithotripter waveforms and compared to results obtained by others with these waveforms. Measured waveforms were not used; instead our code was adjusted to run with analytical descriptions of the acoustic pressure. The code was also modified to calculate the sound radiated by the bubble and the temperature within the bubble. The modifications served two purposes. One, since both sound and temperature depend on the radius solved by the code and since Church<sup>5</sup> solved for sound and temperature, sound and temperature calculation provide another means of benchmarking. Two, calculations for a number of test cases revealed that temperature in the bubble and sound radiated outside the bubble were always proportional to the pressure in the bubble. Therefore, to compare one bubble response to another, only one measure need be presented. In this paper, pressure in the bubble is the measure.

#### **2.3.2 Benchmarking against Church<sup>5</sup>**

The first comparison is to the results obtained by Church.<sup>5</sup> His method of obtaining sound radiated and temperature are described. Then the acoustic pulse description he used is defined. Finally, our results that agree with his are presented.

In addition to the pressure within the bubble, the sound radiated outside the bubble is calculated according to the approximation described by Akulichev.<sup>7</sup> Hence, Church refers to the model as the Gilmore-Akulichev formulation of bubble dynamics. At a distance  $r > R$  measured from the center of the bubble, the sound pulse radiated,  $P_r$ , is

$$P_r = A \left[ \frac{2}{n+1} + \frac{n-1}{n+1} \left( 1 + \frac{n+1}{rc_0^2} G \right)^{1/2} \right]^{2n/(n-1)} - B , \quad (2.18)$$

where  $R$  is the radial coordinate of the bubble interface,  $H$  is the enthalpy of the liquid at the interface relative to the enthalpy far from the bubble,  $U$  is the radial velocity of the interface, and  $n$  is an empirical constant in the modified Tait equation, Eq. 2.15. An invariant of bubble motion  $G$  is defined at the bubble wall as  $R(H + U^2/2)$ .

The maximum temperature  $T$  in the bubble was estimated by Church<sup>5</sup> as

$$T = T_0 (R_{M0.2}/R_{\min})^{3(\gamma-1)} , \quad (2.19)$$

where  $T_0$  is the initial temperature of the liquid, and  $R_{M0.2}$  is the bubble radius at which collapse speeds equal 20% of the local sound speed. The choice of 20% is arbitrary. Church<sup>5</sup> chose a point very near the collapse. Since Eq. 2.19 describes adiabatic collapse (an outgrowth of our assumption of an ideal gas and isentropy), error in the adiabatic assumption is reduced by reducing the time over which the assumption is made.

### 2.3.3 Church's waveform as input to the code

Church's waveform was a mathematical model of a Dornier lithotripter shock wave given by

$$p(t) = 2P^+ K(1 - e^{-\beta t}) e^{-\alpha t} \cos(\omega t + \pi/3) . \quad (2.20)$$

The pressure waveform, shown in Fig. 1.1(a) and repeated in Fig. 2.1(b), was designed to model experimental results obtained with a PVdF membrane hydrophone by Coleman *et al.*<sup>34</sup>;  $P^-$  is the maximum negative pressure. The peak positive pressure at zero rise time is  $P^+$ , and  $K(1 - e^{-\beta t})$  with  $K = 1.03$  and  $\beta = 9.21 \times 10^7 \text{ s}^{-1}$  were added to produce a 50-ns rise time while preserving zero area under the curve. A 50-ns rise time corresponds to a 20 MHz response of the hydrophone. So at an equivalent

thickness of  $75 \mu\text{m}$ , even the shock front of the pulses was larger than the radius of the micron-size bubbles we considered. The decay constant,  $\alpha$ , is  $9.1 \times 10^5 \text{ s}^{-1}$ , and the frequency  $f = \omega/2\pi$  is  $83.3 \text{ kHz}$ .

Equation 2.20 was used to verify our code against Church's results. Figure 1.1(b), repeated in Fig. 2.1(b), shows the R-T curve generated for an ideal gas bubble in water using the Church pulse with  $P^+ = 1000 \text{ bar}$  ( $\sim 100 \text{ MPa}$ ),  $R_0 = 3 \mu\text{m}$ . The profile has a general shape from which some nomenclature is defined:  $(R/R_0)_{\min 1}$  is the initial collapse of the bubble by the positive portion of Fig. 2.1(a);  $(R/R_0)_{\min 2}$  is the primary, delayed, or inertial collapse of the bubble, and  $t_c$  is the bubble duration or time between the arrival of the acoustic pulse and the primary collapse. With other waveforms, a second growth and collapse cycle, which we labeled "rebound," or a third collapse, is possible. The maximum pressures  $P_{\max}$  and temperatures  $T_{\max}$  in the bubble occur when the bubble is the smallest; in Fig. 2.1(b),  $T_{\max} = 8.7 \times 10^6 \text{ K}$  at  $t_c = 260 \mu\text{s}$ . Both values match Church's results, although again, it is pointed out that the absolute values are an upper limit approximation of real values because of the assumptions in the Gilmore code. Moss *et al.*<sup>10</sup> have published more rigorous results for the case of sinusoidal excitation in which they considered shock wave formation in the gas within the bubble.

### 2.3.4 Benchmarking against Ding and Gracewski<sup>8</sup> and Ding and Gracewski pulses as inputs to the code

Our results were also compared to those of Ding and Gracewski,<sup>8</sup> who looked at among other things, a waveform consisting of a sequence to  $2 \mu\text{s}$  unipolar pulses. They chopped the negative tail off Fig. 2.1(a) to obtain a positive pulse and inverted the positive pulse to get a negative pulse. Figure 2.2 shows a sequence of Ding and Gracewski's pulses. Our code produced the same results they obtained when our code was run with their pulses.

Ding and Gracewski looked at the case of a positive pulse and a delayed negative pulse and the case of a negative pulse and a delayed positive pulse. They varied the delay between pulses and the size of the bubble. They did not consider two negative pressure pulses. In addition, since they were modeling a different source, their pulses

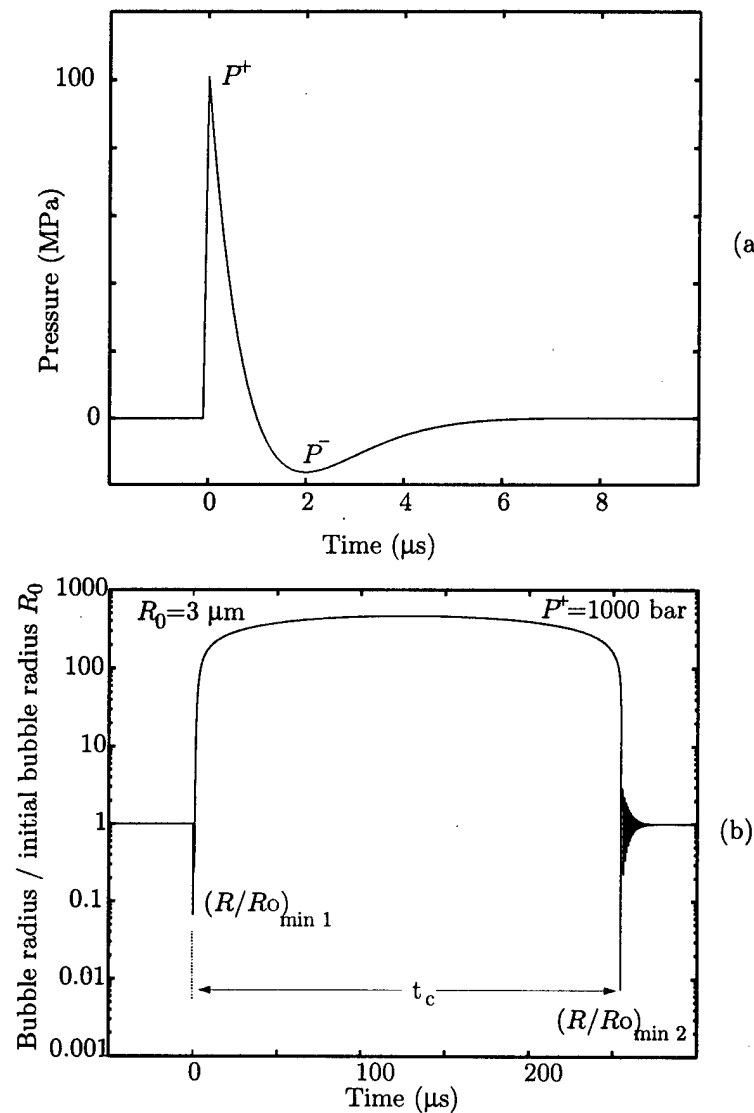


Figure 2.1: Recreations of Church's<sup>5</sup> (a) modeled lithotripter waveform and (b) predicted radial response of a bubble to the waveform in (a). Initial bubble radius  $R_0$  was  $3 \mu\text{m}$ , and peak pressure of the waveform in (a) was  $P^+ = 1000$  bar.

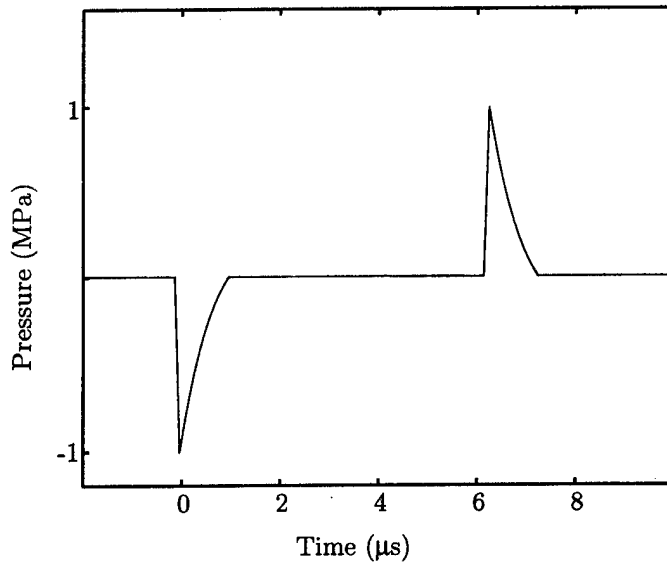


Figure 2.2: Sequence of pulses used by Ding and Gracewski.<sup>8</sup>

AS-97-4

were much weaker than the focal pulses in ESWL. They did not vary the amplitude or the shape of their pulses. The negative pulse is, by the way, very unrealistic. When a negative pressure pulse of finite-amplitude propagates, the most strongly negative portions fall to the back of the pulse and don't gather at the front as in the pulse in Fig. 2.2. But how important is amplitude, duration, or shape of the bubble? What effects can a second pulse have on the bubble? These topics are explored in the next section.

#### 2.4 Explorative Gilmore code predictions with idealized triangular pulses and sequences of two pulses

In this final section of the chapter, the response of a bubble to two pulses is explored. The waveforms fed to the code are triangle pulses, which are simple but unrealistic representations of the acoustic pressure pulses. The section is a step beyond benchmarking, because the results are new. But they are not results that are to be compared with the experiment. Such numerical results appear in Chapter 4. Instead, this section provides an acquaintance with the parameters that influence a bubble hit by a single

pulse or a sequence of two pulses and the interesting responses created with a two-pulse sequence.

The section has three parts. First the parameter space of a single bubble and a single unipolar pulse is explored. Second sequences of two unipolar sequences are investigated. Third, a step is taken toward more realistic waveforms – sequences of bipolar pulses are considered – in an effort to anticipate changes that result when experimentally obtained waveforms are used as input. The third section has the added effect of creating a useful view of a bipolar pulse as two parts, one negative and one positive.

#### 2.4.1 Single unipolar pulse – what are the important parameters in the model?

Numerical results with single triangular acoustic pulses are shown in Figs. 2.3 and 2.4. Acoustic pulses are plotted on the left (pressure versus time), and the acoustically driven bubble pulsations (radius versus time) are on the right. The pulse is applied to the static bubble at  $t = 0 \mu\text{s}$ . Graphs contain two plots, black and grey, for comparison. The acoustic pulse in black or grey strikes the bubble at  $t = 0 \mu\text{s}$  and creates the bubble response shown in the same color. Parameters investigated are pulse polarity, amplitude, duration, shape, and initial bubble size. The goal is to determine to which parameters the bubble is most sensitive and which parameters may be put aside to fine tune our general model to specific cases.

Figure 2.3(a) compares a positive and a negative-pressure pulse. Both have the same magnitude, 10 MPa, and duration, 1  $\mu\text{s}$ . Initial bubble radius  $R_0$  is 2  $\mu\text{m}$ . The positive compresses the bubble as it passes. Then, the bubble pulsates (rings) slightly for another couple microseconds after the positive pressure has passed. The positive-pressure response is negligible compared with the negative-pressure response. The bubble expands as the negative pulse passes and then continues to grow after the microsecond-duration acoustic pulse has long passed. The bubble then collapses after 37  $\mu\text{s}$  and rings. The minimum radius with the negative-pressure pulse,  $R_{\min} = 0.013 \mu\text{m}$ , is more than 50 times smaller than the  $R_{\min} = 0.69 \mu\text{m}$  produced with the positive pulse. The corresponding maximum pressure in the gas,  $6.90 \times 10^6 \text{ MPa}$ , is

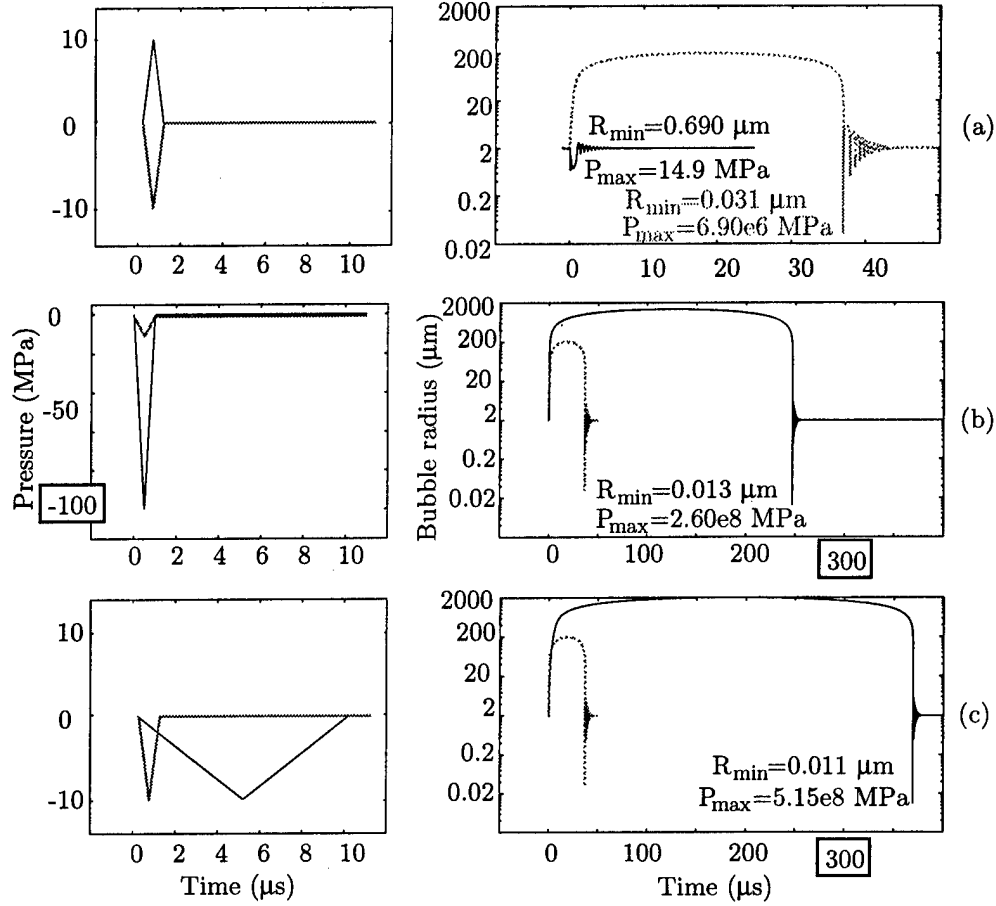


Figure 2.3: Comparison of driving acoustic pulses (left) and bubble radial pulsation versus time (right) calculated with the Gilmore formulation: (a) positive (black) and negative (grey) 10 MPa, 1  $\mu\text{s}$  duration pulses, (b) -100 MPa (black) and -10 MPa (grey) 1  $\mu\text{s}$  duration pulses, and (c) 10  $\mu\text{s}$  (black) and 1  $\mu\text{s}$  (grey) duration, -10 MPa pulses. Positive pulses have little effect on the static bubble. Duration and amplitude of the negative pulse have a very strong effect on the maximum pressure created within the bubble, with duration's effect being slightly stronger. ( $R_{\text{init}} = 2 \mu\text{m}$  in all cases.)

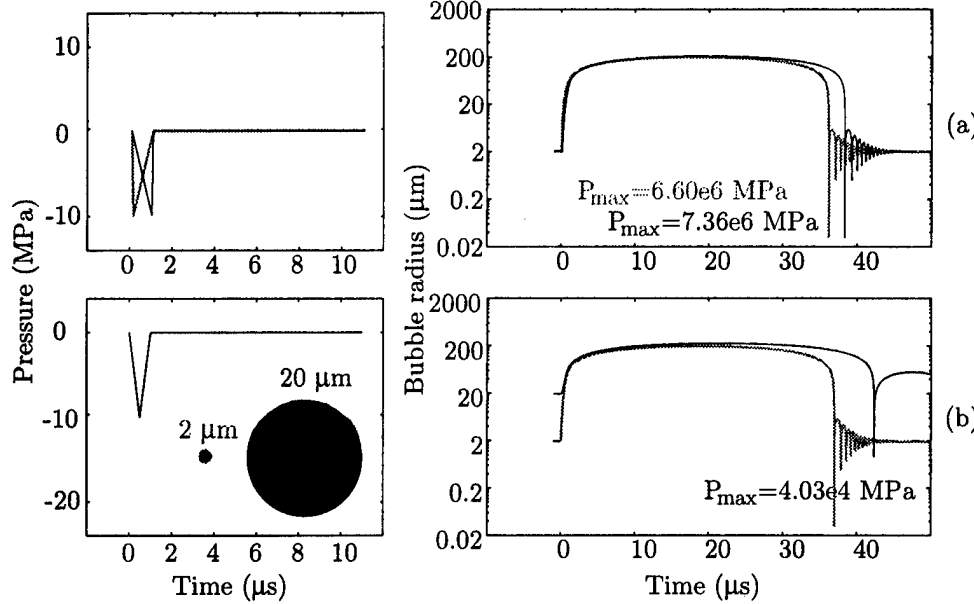


Figure 2.4: Comparison of driving acoustic pulses (left) and bubble radial pulsation versus time (right) calculated with the Gilmore formulation: (a) tenfold decrease (black) and increase (grey) in fall time of -10 MPa, 1  $\mu$ s duration acoustic pulse, (b) tenfold increase in bubble size, 20  $\mu$ m (black) and 2  $\mu$ m (grey). Pulse fall time has little effect on the bubble dynamics. Both large and small bubbles grow and collapse in nearly the same span of time, but the small bubble exhibits larger relative changes in size and higher internal collapse pressure.

AS-97-6

more than 40,000 times greater with the negative pressure. Consequently, only single negative pulses are investigated further: the bubble duration of 37  $\mu$ s and pressure  $P_{\max} = 6.90 \times 10^6$  MPa serve as points of comparison.

In Fig. 2.3(b) and (c), changes to the pulse's strength are considered. We define strength as the relative area under the pressure-time curve. In Fig. 2.3(b), the pulse is changed from -10 MPa to -100 MPa. The bubble grows an order of magnitude larger, lasts almost 7 times as long, and collapses with  $P_{\max} = 2.60 \times 10^8$  MPa, 37 times greater. Longer bubble duration correlates with higher collapse pressure. When the duration of the -10 MPa pulse is increased tenfold as in (c), bubble response is even more pronounced and  $P_{\max}$  doubles again. Note that tiny changes in  $R_{\min}$  between (b) and (c) correspond to big changes in  $P_{\max}$ . The bubble is more sensitive to changes in duration of the triangular pulse than to amplitude changes. However, bubble sensitivity

to amplitude and duration is of the same order. Variations in amplitude studied in Secs. 2.4.2 and 2.4.3 are meant to be equally representative of slightly smaller variations in duration.

Mass diffusion is neglected in our model. When the bubble grows, the pressure gradient and surface area at the bubble interface grow and draw gas from the surrounding liquid into the bubble (see Crum<sup>35</sup> for details). Church used a zeroth-order estimate of diffusion that was proposed by Eller and Flynn<sup>36</sup> and found that diffusion reduced collapse pressures. As stated before, our pressure estimates are upper limit estimates of the real pressure anyway. We model the case of no gas in the liquid surrounding the bubble. Church also found that even with an estimate of diffusion, longer bubble duration still meant higher collapse pressure. In other words, although more diffusion is expected to occur for longer bubble durations, the additional diffusion has a small effect.

The bubble is less sensitive to changes in pulse shape than pulse strength. One representative shape factor is fall time, which here is defined as the time to go from zero pressure to minimum acoustic pressure. A short fall time and the triangular pulse leans forward (to the left). Changes to fall time do not affect the pulse strength (i.e., the area under the pressure-time curve). Effects of a tenfold decrease and increase in fall time of the pulse are seen in Fig. 2.4(a). Bubble duration and maximum pressure decrease less than 5% for a shorter fall time and increase less than 5% for a longer fall time. Fall time changes and shape changes are minor compared with changes in pulse strength. Changes in pulse strength (e.g., increased amplitude or duration of the pulse) are shown above to cause an approximately 5000% increase in internal collapse pressure. Therefore, small changes in shape to make the triangle pulses more realistic waveforms have small effect and are not be considered further. Symmetric triangle pulses are used.

Bubble size within the range of interest<sup>5,8,18</sup> is also a small effect. Figure 2.4(b) compares the responses of a  $R_0 = 2\text{-}\mu\text{m}$  bubble and a  $20\text{-}\mu\text{m}$  bubble to a -10-MPa, 1- $\mu\text{s}$  duration pulse. The tenfold increase in initial bubble radius increases bubble duration less than 10%, increases rebound (continued pulsation after the first collapse), and softens the collapse. The response of the larger bubble has a similar form and duration

but produced lower pressures. Church<sup>5</sup> and Choi *et al.*<sup>18</sup> found that bubble duration became increasingly less dependent on initial bubble size as acoustic pressure goes up. Church and Flynn<sup>37</sup> used as a pressure waveform a low-amplitude, short sinusoidal burst and found a specific bubble radius that produced the largest response at the frequency of the excitation. This study or that by Church<sup>5</sup> used a broadband pulse as an excitation, and no “optimal” bubble radius was observed in either study. An initial radius of  $2 \mu\text{m}$ , which was also used by Ding and Gracewski,<sup>8</sup> is used throughout the rest of this paper.

#### 2.4.2 Exploration of a bubble response to a sequence of two unipolar pulses

Calculated bubble responses to a two-pulse sequence are presented here. Four possibilities exist: a positive-pressure pulse followed by a negative pressure pulse, a positive-pressure pulse followed by a positive pressure pulse, a negative-pressure pulse followed by a positive pressure pulse, and a negative-pressure pulse followed by a negative pressure pulse. In Sec. 2.4.1, it is demonstrated that a positive-pressure pulse incident on a static bubble produces a negligible radial response of the bubble. A minimal change can, therefore, be expected from the sequences where a positive-pressure pulse arrives first. In addition to the type of sequence, interpulse delay  $\tau$  and relative amplitude of the second pulse are considered.

Figure 2.5(a) shows a negative-pressure pulse (grey) and a sequence of a positive pulse and a  $1 \mu\text{s}$  delayed, negative pulse (black) and the bubble responses. The bubble responses are almost identical. The response created with the sequence of pulses has an initial constriction in the first microsecond. The constriction is the only contribution of the positive pulse. The negative pulse in the sequence acts as if it were alone. Changes in amplitude and duration of the positive pulse or in interpulse delay have little effect.

No plots are shown for a positive-positive sequence. As with the positive-negative, the bubble response to the first positive is so short that the second pulse effectively acts independently of the first. Two weak responses result.

When the negative pulse arrives first, interaction is much more interesting. The negative-pressure pulse sets the bubble expanding, and a delayed positive-pressure pulse tries to collapse the expanding bubble. Roughly, if the positive pulse has equal

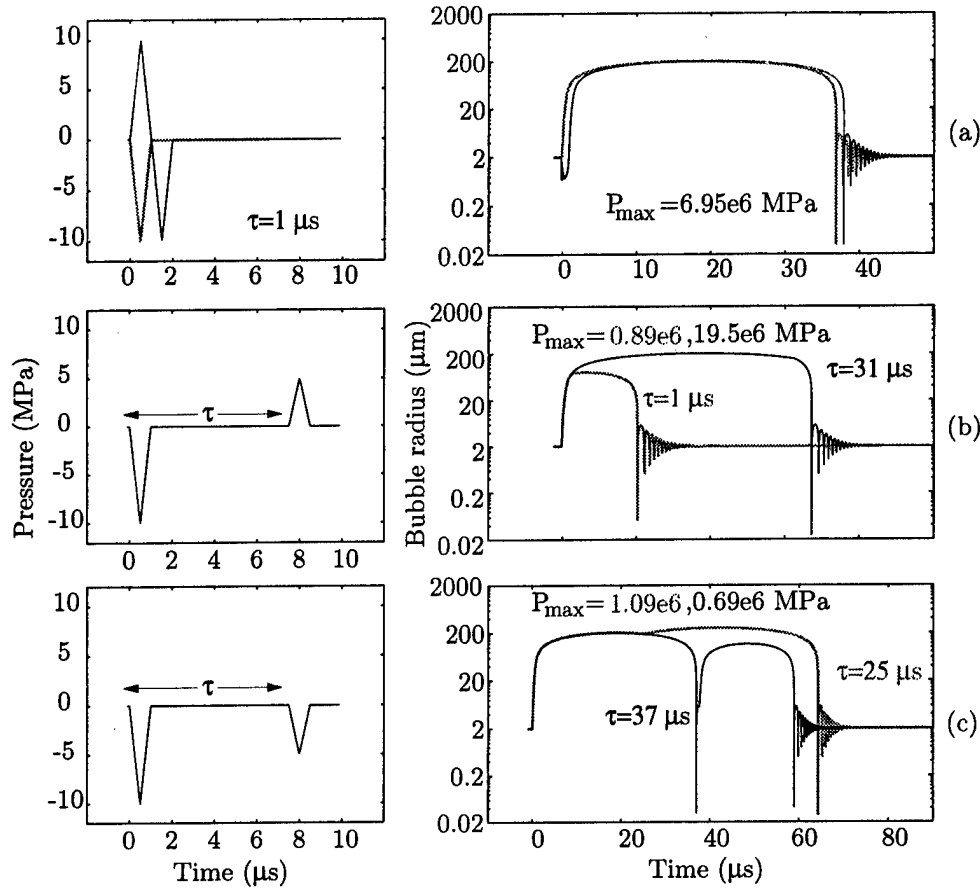


Figure 2.5: Two pulse results: (a) positive-then-negative-pressure pulse (black) has nearly identical bubble response to that with a single negative pulse (grey); (b) a sequence of a negative-pressure pulse and a time-delayed half-amplitude positive pressure pulse reduces (“stifles”) and increases (“kicks”) collapse pressure in the bubble, depending on interpulse delay  $\tau$ ; (c) a sequence of a negative pressure pulse and a time-delayed, half-amplitude negative-pressure pulse increases (“bounces”) and reduces (“catches”) collapse pressure in the bubble.

AS-97-7

or greater strength (area under the pressure-time curve) than the negative pulse has, the positive pulse crushes the bubble almost immediately and increases collapse pressure. The effect is strongest when the positive hits as the bubble is rapidly expanding or contracting. Ding and Gracewski<sup>8</sup> considered only the equal amplitude case and so calculated only increased collapse pressures. The other extreme is that the positive pulse is so weak that the bubble responds only to the negative pulse. Halfway between the extremes is a positive pulse with half the strength of the negative pulse. Figures 2.5(b) and 2.6(a) show results for a 1  $\mu$ s, -10 MPa pulse and a delayed 1  $\mu$ s, 5 MPa pulse. With small  $\tau$ , the positive pulse stifles the bubble's growth, and the bubble collapses sooner and less violently. The longer  $\tau$  and the positive-pressure pulse give the collapsing bubble an extra kick and increase the collapse pressure.

In Fig. 2.6(a),  $P_{\max}$  is plotted versus  $\tau$ . The auxiliary positive pulse decreases  $P_{\max}$  by up to a factor of 7 or increases  $P_{\max}$  nearly threefold depending on the delay. The positive pulse must be delayed no more than 37  $\mu$ s to affect  $P_{\max}$ . At 37  $\mu$ s, the bubble excited by the negative pulse naturally collapses and, in the code, returns to equilibrium. Physically, the bubble may break up after the violent collapse, but fragmentation of the bubble is not included in the model. The end effect of a delay longer than 37  $\mu$ s is that the second pulse arrives too late to influence the bubble response initiated by the first pulse.

The spatial length of the 1  $\mu$ s duration positive-pressure pulse was 1.5 mm when a sound speed of 1500 m/s is assumed. The length is a factor of eight times larger than the largest bubble radius. So the assumption that wavelength (pulse length) is greater than bubble diameter is not violated even when the the second pulse arrives when the bubble is largest. Were a real bubble to get larger than the pulse, asymmetric collapse and microjetting (water jets through the bubble) would result because acoustic pressure on the bubble is not uniform. Our model is restricted to cases for which the bubble is smaller than the pulse length because a spherical bubble is assumed.

For  $\tau$  less than the duration of the first acoustic pulse, the pulses superimpose. Detailing the superimposed waveforms is beyond the scope of this paper. Many superpositions, however, lend themselves quickly to the discussion, and a few points such as  $\tau = 0$  are mentioned. For example, at  $\tau = 0$  in Fig. 2.6(a),  $P_{\max}$  is low because

superposition of a 5 MPa and a -10 MPa pulse leaves only a -5 MPa driving pulse.

In a negative-negative pulse sequence (Fig. 2.5(c)), the bubble is expanded twice, as evidenced by the two-humped bubble profile. When  $\tau$  is short, the bubble responds to two closely spaced impetuses to expand. Larger growth results in stronger collapse. With longer  $\tau$ , the expansion impetus of the second pulse conflicts with the collapse phase of the first cycle. The expansion due to the second pulse softens the collapse and “catches” the bubble. Where a second positive pulse squeezes, a second negative pulse expands. Correspondingly, Fig. 2.6(b) is a mirror image of (a), as Fig. 2.6(b) is for a 1  $\mu$ s duration, -10 MPa pulse and a delayed 1  $\mu$ s duration, -5 MPa pulse. A weaker second pulse has less effect. With a stronger second pulse, two small changes occur. The expansion is larger, so enhancing is greater. The strong delayed pulse expands the bubble even after the bubble has started to collapse. The expansion of a collapsing bubble means 1) intensified collapse is observed over a longer range of  $\tau$ , and 2) “catching” turns to “bouncing.” The bubble rebounds and the second collapse is stronger, thus defeating the softening effect. In our  $P_{\max}$  versus  $\tau$  plots, the  $P_{\max}$  value recorded is the larger collapse of the two collapses when the bubble “bounced.” Our model is idealized, and we have assumed that the bubble stays spherical and whole. Physically, at the very collapse, the model may break down. The softened first collapse may be sufficient to break up the bubble and thus bounce, and higher collapse pressures do not occur.

#### 2.4.3 Exploration of a bubble response to a sequence of two bipolar pulses

The waves produced with the rigid and pressure release reflectors are most nearly bipolar, so at best experimentally we produce a sequence of two bipolar pulses. In the numerical results of this section, a sequence of two simple bipolar pulses is constructed from four triangle pulses and run through the Gilmore code. All four possible sequences are considered. Interpulse delay is a variable as is relative amplitude of the positive and negative portions. Both positive triangle pulses are identical, and both negative triangle pulses in each sequence are identical. Numerical results are interpreted as modifications of the two unipolar pulse results.

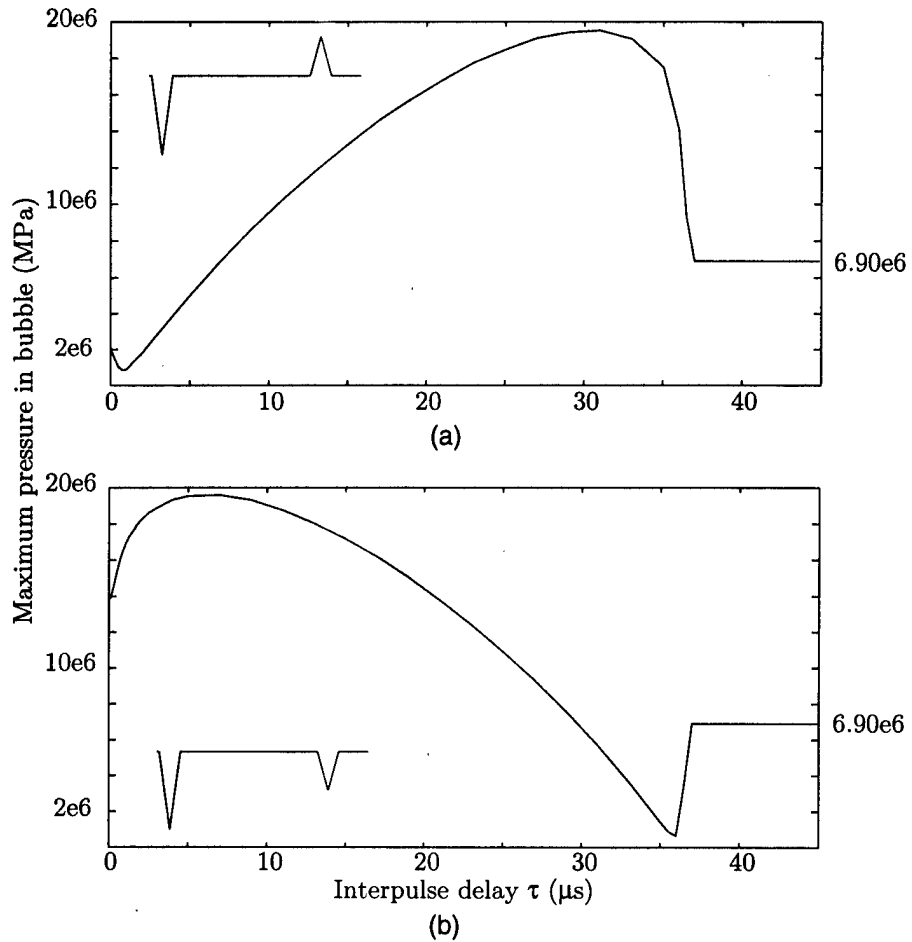


Figure 2.6: Peak pressure  $P_{\max}$  in the bubble versus interpulse delay  $\tau$  for (a) negative-pressure pulse then half-amplitude positive-pressure pulse and (b) negative-pressure pulse then half-amplitude negative-pressure pulse sequences. Interpulse delays that reduce or increase  $P_{\max}$  exist for both (a) and (b).

AS-97-8

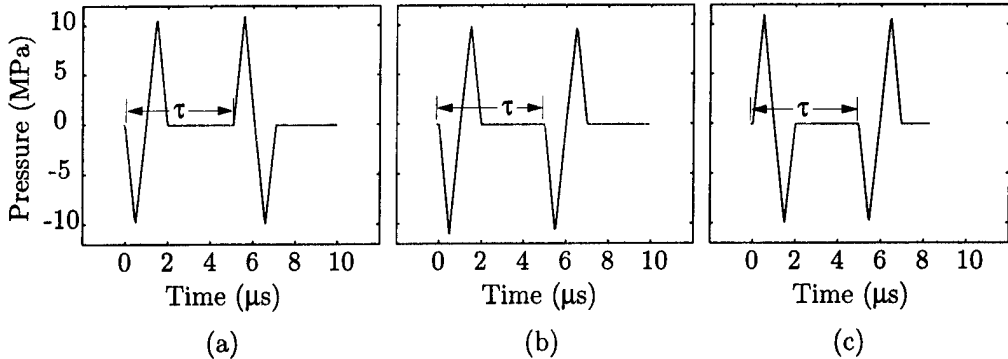


Figure 2.7: Four bipolar pulse sequences: (a) negative-positive then positive-negative ( $np - pn$ ), (b) negative-positive then negative-positive ( $np - np$ ), and (c) positive-negative then negative-positive ( $pn - np$ ).

AS-97-9

The two sequences where a negative-positive  $np$  bipolar pulse comes first are shown in Fig. 2.7(a) and (b). The  $np$  pulse crudely approximates a waveform measured at the focus of a pressure release reflector. As shown above, the  $np$  pulse has a shorter bubble duration than a pure negative. The shorter duration pulse means that there is less time for the second pulse to interact. A range of amplitudes were investigated for both sequences, and the second pulse always enhanced the bubble collapse.

The positive-negative then negative-positive ( $pn - np$ ) pulse sequence is shown in Fig. 2.7(c). The  $pn$  pulse crudely models the waveform measured at the focus of a rigid reflector. As shown above, the first positive pulse  $p_1$  can be neglected because a positive pulse produces negligible response in a static bubble. The sequence reduces to a negative pulse followed by a bipolar pulse. The bipolar pulse is found to act similarly to a triangle pulse with equivalent area under the pressure-time curve (e.g., a bipolar pulse with a strong positive phase acts like a positive pulse). Thus the bipolar pulse sequence can be viewed as either an  $n - p$  or  $n - n$  two-pulse sequence.

Figures 2.8(a) and (b) show pressure versus  $\tau$  plots for two  $pn - np$  bipolar pulse sequences. The plots are every similar to the plots in Figs. 2.6(b) and (a). To obtain Fig. 2.8(a), 5 MPa, -10 MPa bipolar pulses were used. The negative dominates, and the area of each bipolar pulse is  $\frac{1}{2} (5 \text{ MPa} \times 1 \mu\text{s}) + \frac{1}{2} (-10 \text{ MPa} \times 1 \mu\text{s})$ , which equals

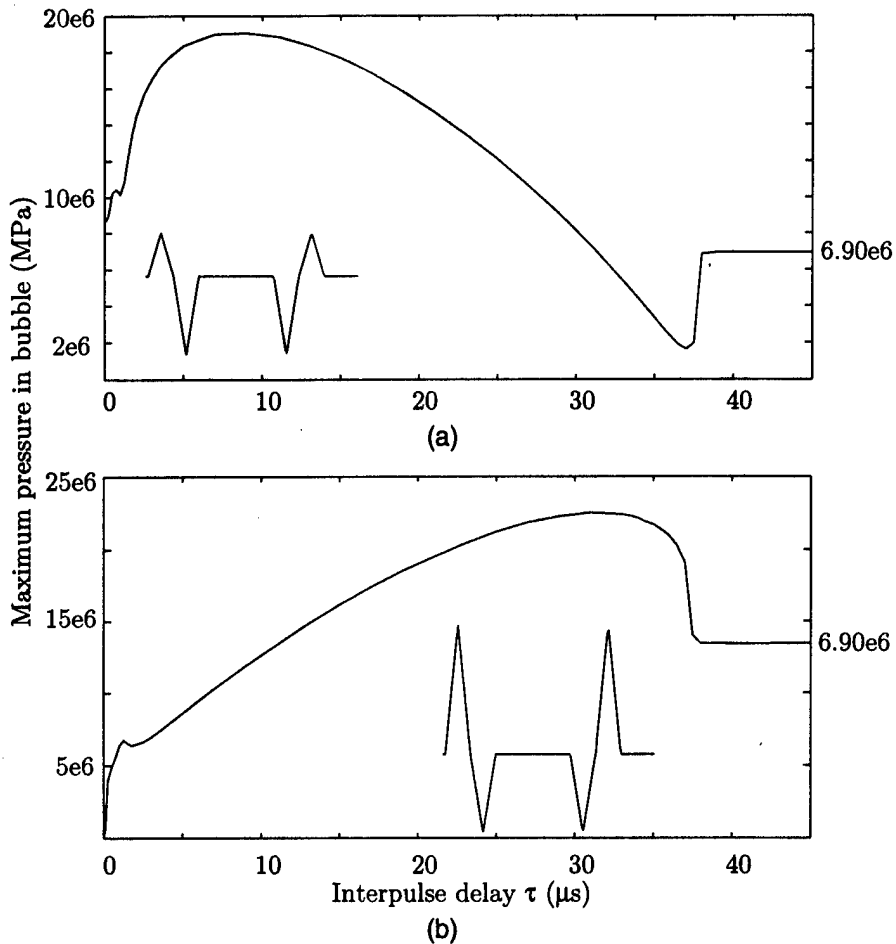


Figure 2.8: The positive-negative then negative-positive ( $pn - np$ ) pressure pulse sequence has either (a) the negative pressure dominate (half-amplitude positive), which looks like Fig. 2.6(b), or (b) the positive pressure dominate (150%-amplitude positive), which has a result nearly identical to Fig. 2.6(a).

AS-97-10

$\frac{1}{2}(-5 \text{ MPa} \times 1 \mu\text{s})$ . The  $-5 \text{ MPa}$  triangular pulse used to produce Fig. 2.6(b) has the same area. Correspondingly, the figures are very similar. They differ at  $\tau = 0$ . In Fig. 2.8,  $P_{\max}(\tau = 0) = 0$  because the acoustic signals cancel and no driving force exists. In Fig. 2.6(b), pulses do not completely cancel at  $\tau = 0$ . Figure 2.8(b) is for 15 MPa,  $-10 \text{ MPa}$  pulses (area = 5 MPa) and similarly agrees with Fig. 2.6(a).

The fourth sequence is two positive-negative pulses ( $pn - pn$ ) and is shown in Fig. 2.9. As can be seen, the first positive pressure produces a slight initial constriction. Then the bubble grows in response to the negative pressure. The second positive crushes the bubble, and the second negative again grows the bubble. The two humped

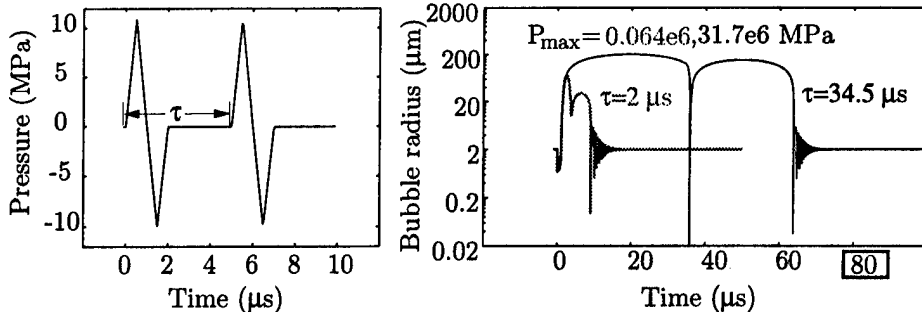


Figure 2.9: The positive-negative then positive-negative ( $pn - pn$ ) “stifles” the bubble growth and collapse with short delays  $\tau$  between the bipolar pulses and “kicks” the collapse when the second pulse arrives as the bubble, responding to the first pulse, collapses.

**AS-97-11**

radius-time curves are shown for 11 MPa, -10 MPa pulses. Neglecting the first positive pressure, the ratio of the area under the positive portion of the pressure-time curve to the negative portion was approximately 1/2. The same ratio exists for the sequence in Fig. 2.6 where stifling and kicking are observed.

In Fig. 2.10,  $P_{\max}$  is plotted against  $\tau$ . The middle (b) corresponds to the conditions of Fig. 2.9. When  $\tau$  is short, the bubbles are stifled. When  $\tau$  is long, collapse is intensified. When the rate of growth or collapse is high, the bubble is particularly sensitive to the second pulse.  $P_{\max}$  is increased fivefold and decreases nearly tenfold.

Figure 2.10(a) shows results for positive phase equal to 5 MPa, half the area of the negative phase. The curve looks very much like Fig. 2.6(b), except at the ends. Differences at small  $\tau$  are due to acoustic superposition. At large  $\tau$  (around  $\tau = 36 \mu\text{s}$ ), the positive part of the bipolar can kick the collapsing bubble. The bubble is collapsing very quickly at  $36 \mu\text{s}$ , making it very sensitive to kicking. Therefore, although the positive-pressure pulse is weak, it is effective at collapsing the bubble late in the collapse cycle. The bubble collapses before the negative pulse arrives to turn the collapse around. A purely negative pulse cannot demonstrate the kicking effect.

When the positive pulse is much stronger, 20 MPa in Fig. 2.10(c), no stifling

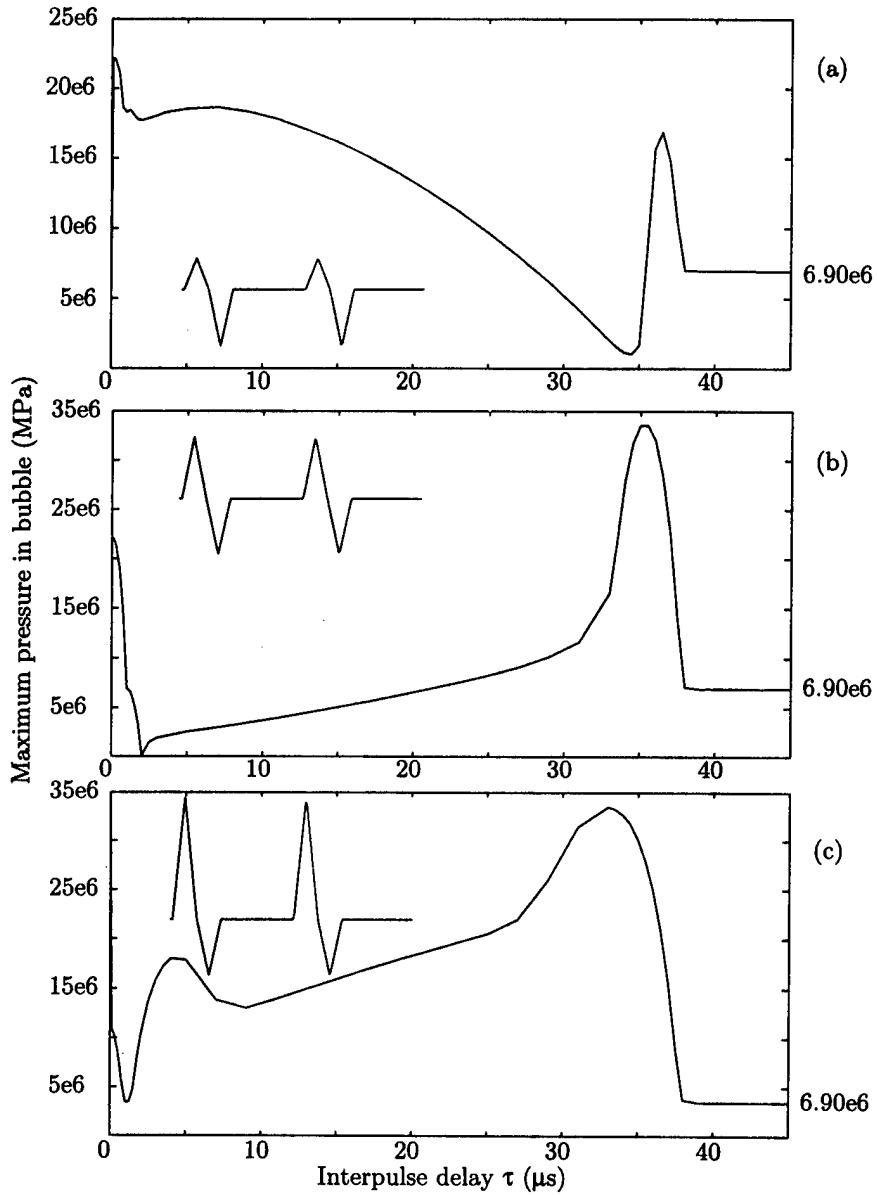


Figure 2.10: Effect of pulse strength in the positive-negative then positive-negative ( $pn - pn$ ) pressure pulse sequence: (a) half-amplitude positive pulse and full-amplitude negative pulse "catches" the collapsing bubble. A slightly longer delay and the positive pulse is able to "kick" the collapse; (b) nearly equal amplitude positive and negative phases yield large regions of interpulse delay time for "stifling" and "kicking"; (c) a double strength positive and the collapse is always "kicked."

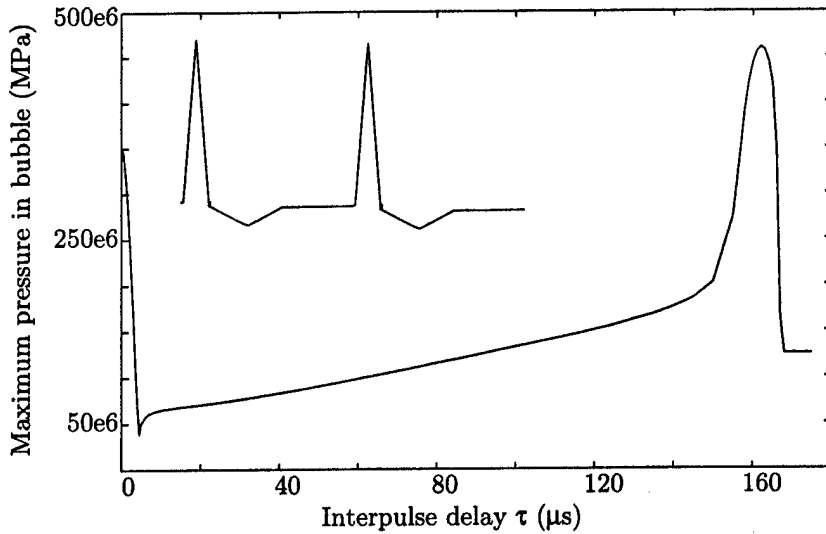


Figure 2.11: A four-pulse sequence roughly mimicking a lithotripter pulse: both a stifling region and a kicking region are present.

AS-97-13

or catching occurs. The collapse pressure is always increased. Collapse pressure is shown above to always increase when the delayed pulse is a single strong positive pulse. The times of rapid change in radius are again the most sensitive to the second pulse. Although the waveform in Fig. 2.10(c) looks more like a lithotripter pulse, the area in Fig. 2.10(b) is much closer to that of a lithotripter pulse, and Fig. 2.10(b) is, therefore, a better representation for lithotripsy. For Fig. 2.10(c) to be more accurate, the duration of the negative phase has to be increased, which results in a plot almost identical to Fig. 2.10(b). Figure 2.11 is for 50 MPa, -10 MPa pulses where the negative has been lengthened to 4.5  $\mu$ s. The plot has the same shape as Fig. 2.10(b). Values of  $\tau$  are larger because the stronger negative phase produced a longer bubble duration.  $P_{\max}$  is also larger because of the stronger pulses.

The plot indicates that in our experiments kicking and stifling might be observed. A short delay between the experimental pulses and cavitation is expected to be tempered. A long delay and the cavitation is intensified. Comparison of numerical results with measured waveforms and experimental measurement of cavitation intensity are presented in Chapter 4.

## 2.5 Summary

In this chapter, our numerical model was described, and the use of a two-pulse sequence to control of maximum pressure in a cavitating bubble numerically explored. The Gilmore equation is solved. Bubble radius as a function of time and maximum pressure in the bubble are calculated. Input to the the code is an acoustic pulse or sequence of pulses. The change in pressure caused by the pulse(s) drives the bubble motion. In this chapter, idealized pulses are used. In Chapter 4, pressure pulses measured with a hydrophone are used. In Chapter 2, the code is verified against other codes. The response of a bubble to a two-pulse sequence is explored. The indication is that tempered and intensified cavitation may be observed in our experiments with ellipsoidal reflectors.

## Chapter 3

### Experimental setup

In this section, experimental procedure and equipment are described. The heart of the system is a spark within an ellipsoidal reflector: together the spark and reflector, both underwater, produce a strong, focused acoustic field. Figure 3.1 shows the focusing of the spark-generated shock wave by an ellipsoidal reflector. The acoustic field in turn produces a cavitation field at the focus. Both the acoustic and cavitation fields were measured. The experimental configuration, spark generators, reflectors, and measurement techniques are described.

#### 3.1 General setup

Here, the large support structure of the experiments is discussed. Measurements were made in water. Tank and water treatment are discussed. Built around the tank were a positioning system to locate measurement equipment in the tank and spark-generating equipment to provide the spark sound source within the tank.

Most measurements presented here were made with the experimental lithotripter at Applied Physics Laboratory (APL) in Seattle, Washington. Preliminary and some presented data were measured at Applied Research Laboratories (ARL) in Austin, Texas. One of two identical spark sources built in Austin was added to the Seattle experimental lithotripter as a modification. Supporting measurements were made with a clinical Dornier HM3 lithotripter at Methodist Hospital in Indianapolis, Indiana. Measurements with the Dornier lithotripter were made in conjunction with Indiana University Medical School (IUPUI) in Indianapolis, Indiana.

Here, some confusion over the term lithotripter may arise. In Chapters 1 and 2, “lithotripter” is used to describe the device producing the focused pulse, because in its barest form a lithotripter is a device to produce focused sound. In our experiments and in the Dornier HM3, the device includes a spark-generating system, electrodes, and an ellipsoidal reflector. In this chapter, these three elements, the basic elements

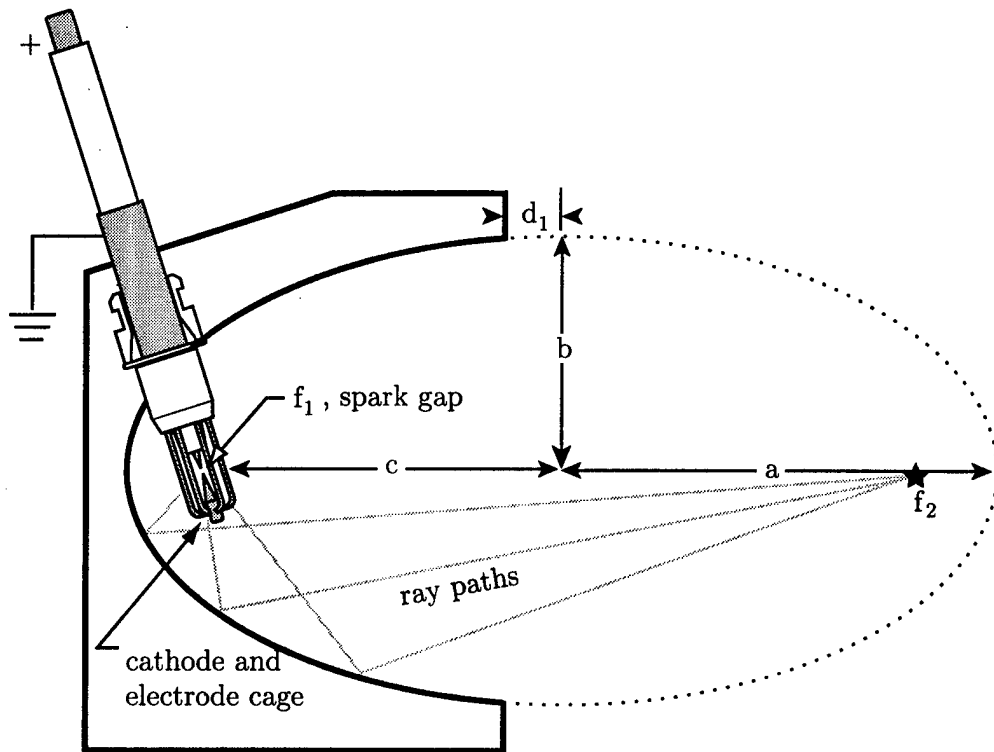


Figure 3.1: Schematic and nomenclature of electrode and ellipsoidal reflector.

AS-97-14

needed, are referred to as a sound source. The term lithotripter is broadened to include the positioning system, water bath, water-conditioning systems, and alignment system, added to make the sound source a usable experimental or clinical tool. The definition is broadened to fit what is commonly meant in referring to the Dornier HM3 lithotripter and what is locally meant at APL by the term experimental lithotripter.

The Seattle experimental lithotripter, shown in Fig. 3.2, is described. The water system, positioning gantry, reflector, and spark generator that make up the experimental lithotripter were constructed though not entirely assembled at California Institute of Technology (Caltech), Pasadena, California, as part of an NIH PPG grant. As part of the grant, Caltech provided an experimental lithotripter to IUPUI, as well. R. O. Cleveland with help from G. Keilman, both at APL, assembled and made both systems function.

### **3.1.1 Tank and water**

Experiments were conducted in a  $57.8 \times 95.3$  cm acrylic tank. The tank bottom has a  $14^\circ$  slant. The maximum height of the tank is 59.1 cm; the minimum is 35.6 cm. The water level for the experiments was 20 cm from the tank top.

A thorough degassing system is part of the experimental lithotripter. A 70-gallon stainless steel tank stored the water. Water conductivity was  $1500 \mu\text{S}/\text{cm}$  and was tested with a Model EP water conductivity meter (Myron L Company, Carlesbad, California). A pump was used to fill the tank or recirculate the water for filtering or degassing. A Cole-Parmer (Cole-Parmer Instrument Co., Chicago, Illinois)  $100\text{-}\mu\text{m}$  pore filter was used. Degassing was accomplished in a large glass T-joint (9 cm ID) located above the aluminum tank. A vacuum pump drew a vacuum in the T-joint. Recirculated water sprayed into the T-joint through a plate with  $200\text{-}\mu\text{m}$  holes. The vacuum drew gas from the water, and the large surface-area-to-volume ratio of the fine spray particles accelerated the process. Gas content was checked with a Model 51B oxygen meter (Yellow Springs Instrument Co., Inc., Yellow Springs, Ohio) and was maintained below a reading of 4 parts per million of oxygen.

With the help of J. Swalwell (APL), a smaller acrylic tank, also with a bottom sloped at  $14^\circ$ , was built to hold the membrane hydrophone. The small tank ( $25.4 \times 38.1$

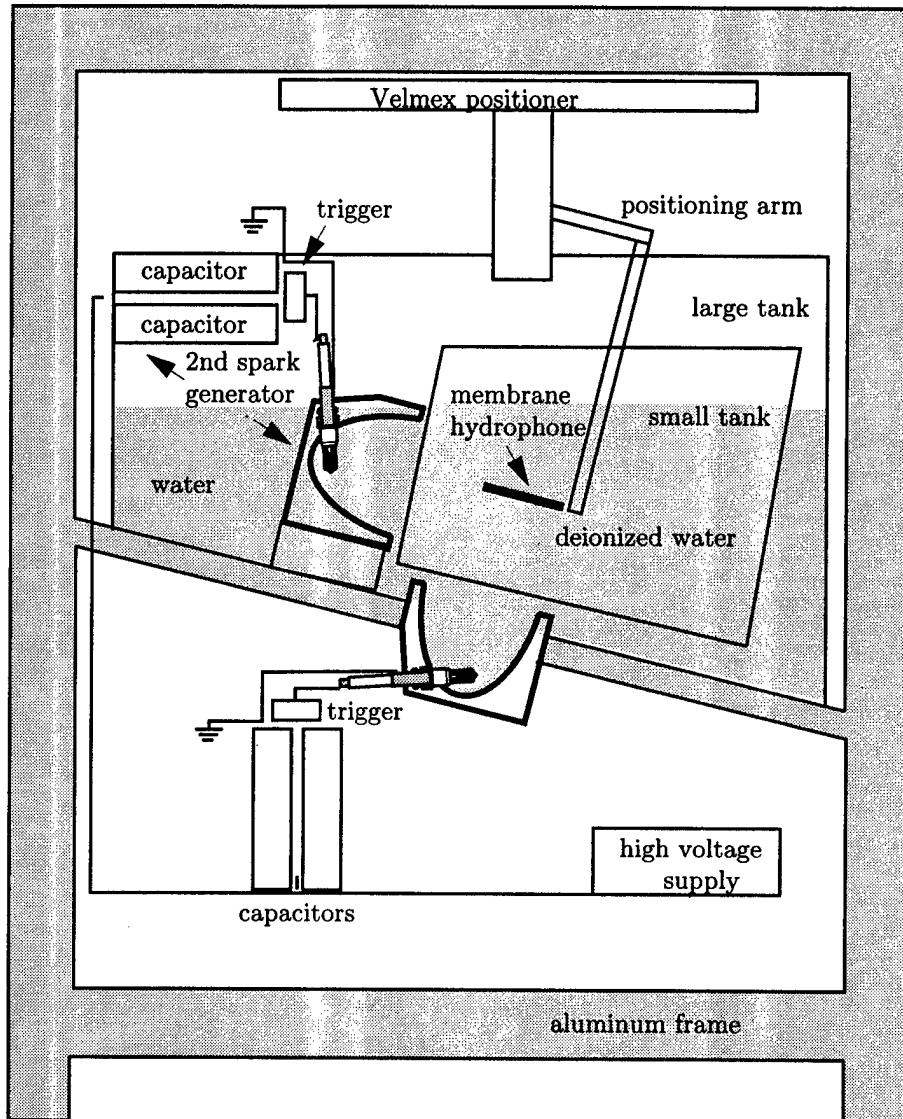


Figure 3.2: Schematic of the experimental lithotripter and the added second spark generator and reflector. It was necessary to use the membrane hydrophone in deionized water. The small tank contained the deionized water. Walls of the small tank contained large acoustically transparent windows made of polyethylene membrane.

AS-97-15

cm, 23.5 cm minimum height, 33.7 cm maximum height) was positioned within the large tank and filled with deionized water (conductivity less than 5  $\mu\text{S}/\text{cm}$ ). The membrane hydrophone needs water in this conductivity range.<sup>38</sup> Filling the big tank with deionized water is not practical, and in addition, sparks are more repeatable and louder in conductive water.<sup>39</sup> A thin membrane of polyethylene was stretched across 20  $\times$  20 cm windows cut in the acrylic. The polyethylene separates the two water baths but permits sound to enter the small tank with no measurable attenuation.

The small tank is degassed with a multiple pinhole degassing system.<sup>40</sup> Water is recirculated through a Cole-Parmer pump. The inlet to the pump is a grid of tiny holes. The outlet is flexible tube directed so the open end faces up. The method and mechanism are described by Kaiser *et al.*<sup>40</sup> In summary, the turbulence created by the pinholes rips the gas from the water and creates a two-phase flow of gas and water. At the outlet the gas floats to the water surface.

### 3.1.2 Positioning system

Velmax (Bloomfield, NY) micro-stepping motors and slides positioned above the tank locate measurement devices within the tank. The motor resolution is 200 steps per millimeter. The limit switches we found to be sensitive to the electrical noise of the sparks and in future experiments will be better protected or disconnected entirely. Three axes are controlled with a hand held controller or via RS-232 bus from the computer. To move at the 14° angle, parallel or perpendicular to the tank bottom, it is necessary to move two axes.

### 3.1.3 Spark sources

Two spark sources were used in a number of experiments. In Austin, two identical spark generators were used. In Seattle, one of the Austin generators was used; the other was the generator in the experimental lithotripter. The generators were nearly identical and differed only in the triggering circuitry. Both were designed to mimic the Dornier HM3 lithotripter and to utilize the Dornier HM3 electrodes.

The spark-generating equipment of the experimental lithotripter is located under the tank and enclosed in a grounded metal box. No increase in electrical noise was mea-

sured without the box, although adding a ground strip to Cleveland's circuit reduced electrical noise by orders of magnitude. The spark generator is described by Howard and Sturtevant.<sup>41</sup> An isolation transformer was designed and included in the package from Caltech, but we decided to omit it and ground the capacitors to earthground.

The system with the grounding is no different from that described by Coleman<sup>11</sup> or Bailey.<sup>42</sup> Maxwell low inductance capacitors ( $0.1 \mu\text{F}$ ) are connected through a switch to a Dornier clinical electrode. Coleman *et al.*<sup>11</sup> pointed out that low inductance (i.e., a short lead) is best and that sequential shots erode the electrodes. Erosion makes the spark louder. Coleman found a 1% increase in acoustic pressure every three shots in the first 150 shots on a new electrode but a more gradual 0.01% increase every three shots between 150 and 750 shots. Electrodes with between 150 and 2200 shots were used in our experiments.

The switch in the experimental lithotripter is an EG&G trigger and spark gap cannister filled with pressurized nitrogen. The switch on the Austin generator is an autocoil and an open-air spark gap (see Bailey<sup>42</sup>). Both triggers have a high-potential end connected to the capacitors, a low-potential end connected to the electrode, and a third, or trigger, electrode between them. A low-current, high-potential signal fires the trigger electrode, which initiates the breakdown between the main electrodes.

When the triggered gap breaks down, the electrodes underwater arc. The discharge heats the water suddenly and creates a spherically diverging shock wave.<sup>43,2</sup> The points of the electrode are centered at the near focus  $f_1$  of an ellipsoidal reflector, as shown in Fig. 3.1. The spark arcs between two points. The lower point is connected by a metal cage. The rest of the electrode is coaxial.

Some of the spherical acoustic wave created by the discharge radiates directly out of the reflector; the rest reflects off the ellipsoid and is focused at the second focus  $f_2$ . At  $f_2$ , the focused wave is much larger than the direct wave. Ray paths illustrate the reflection and focusing of the sound in Fig. 3.1.

### 3.1.4 Ellipsoidal reflectors

The various ellipsoidal reflectors used in experiments are described here. The principal difference is the acoustic impedance of the reflector. Rigid and pressure-release

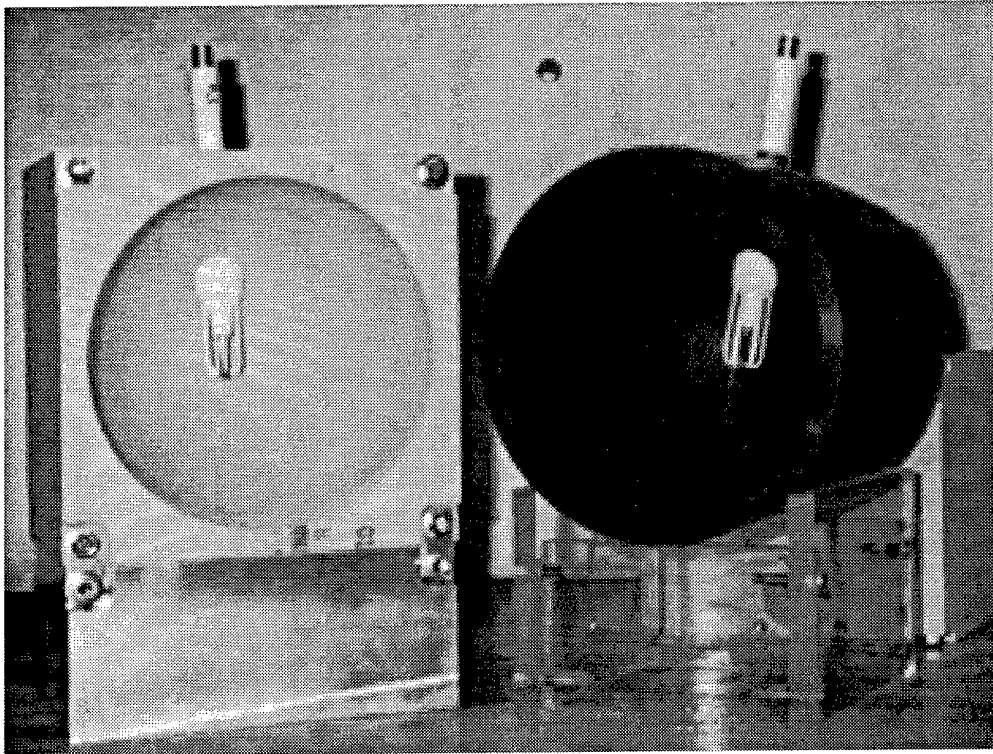


Figure 3.3: Photograph of a rigid reflector and a pressure-release reflector.

AS-97-16

reflectors are compared. Figure 3.3 shows a photograph of a rigid reflector and a pressure-release reflector in a nearly confocal arrangement.

Table 3.1 lists and describes the reflectors. The first column is the letter assigned each reflector. Reflector *Q*, for reference, is a Dornier HM3 reflector. Reflectors *R* and *C* are shown in Fig. 3.3. The second column is reflector material, either brass or polyurethane foam, and the third is the pressure reflection coefficient *R* based on use in water. Brass is nearly acoustically rigid in water, and polyurethane foam is nearly pressure release. Values for material properties of brass were obtained from the book by Kinsler and Frey,<sup>44</sup> and for polyurethane foam, from the manufacturer, General Plastics, Tacoma, Washington.<sup>45</sup> The foam has fine, closed pores and comes in lightweight bricks or sheets. It has a solid form that holds its shape as it is milled. The foam reflectors were machined on a Bostomatic CNC milling machine in the Mechanical

letter	material	R	a (cm)	b (cm)	E (%)	$\tau$ ( $\mu$ s)
$Q, Q_I$	brass	0.94	13.8	7.75	90.7	—
$R$	brass	0.94	13.8	7.75	100	—
$S$	brass	0.94	13.8	7.75	90.7	—
$A, C$	polyurethane foam	-0.88	13.8	7.75	100	—
$D$	polyurethane foam	-0.88	13.208	6.638	90.2	8
$E$	polyurethane foam	-0.94	13.355	6.927	90.3	6
$F$	polyurethane foam	-0.97	13.5	7.202	90.4	4

Table 3.1: Description of reflectors used in this study.

Engineering Department's student machine shop at The University of Texas at Austin. Aberrations in the surface are less than  $2.5 \mu\text{m}$ , or 1/3000th the length of the acoustic pulse and 1/200th the size of the active spot of our hydrophone.

Columns  $a$ ,  $b$ , and  $E$  describe the dimensions of the ellipsoidal reflectors (see Fig. 3.1). Foci of the ellipsoid are separated by the distance  $2c$ ;  $a$  and  $b$  are the major and minor half axes, respectively; and  $d_1$  is the distance between  $a$  and the reflector depth. The percentage  $E = (a - d_1)/a$  is used to define how closely a reflector resembles a half ellipse. All reflectors with  $E \neq 100$ , except  $S$ , have small cuts in the aperture edge. The cuts accommodate balloons, which house the fluoroscopy imaging system of the Dornier lithotripter.

Three polyurethane shells or masks, reflectors  $D$ ,  $E$ , and  $F$ , were made. Each consists of two equal but separate halves. The outside of each insert has the ellipse dimensions  $a = 13.8$  and  $b = 7.75 \text{ cm}$  and, therefore, fits snuggly into the brass bowl. The insides have smaller ellipse dimensions, but all share the same foci with the brass reflector (i.e.,  $c = b/a$  was constant). Figure 3.4 illustrates how the inserts are used to create a pressure-release reflector. Duct tape (not shown) forms a  $<1 \text{ cm}$  ridge or awning over the mask that keeps it in place.

Half-polyurethane-half-brass reflectors are made by inserting one half of either reflector  $D$ ,  $E$ , or  $F$  in a brass reflector. Figure 3.5 shows the configuration. Paths 1 and 2 are sample ray paths from the spark source. A pulse on Path 1 reflects from the polyurethane and arrives first because the path length ( $2a_{\text{mask}}$ ) is shorter. A pulse

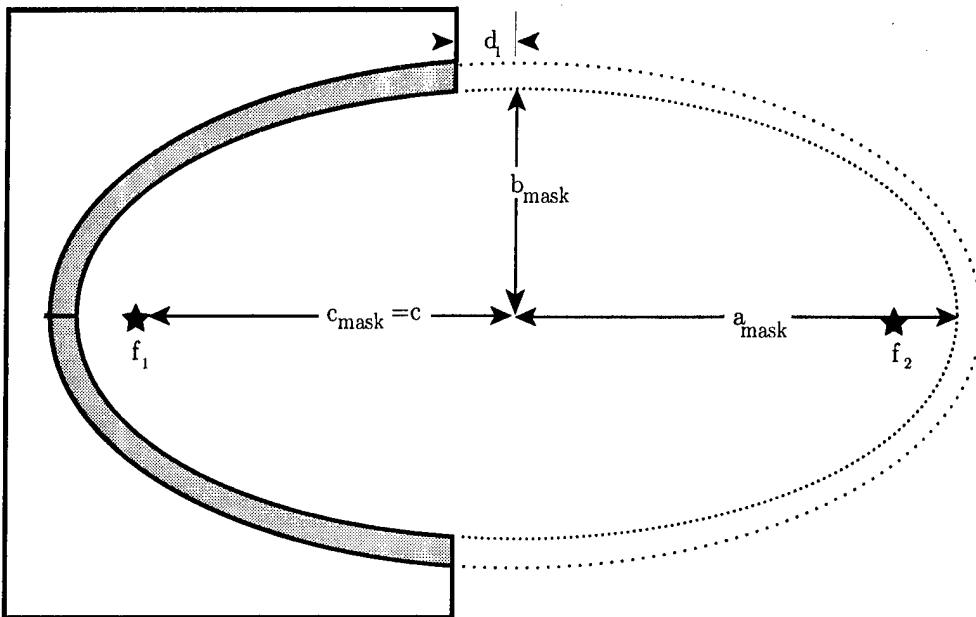


Figure 3.4: Both halves of the pressure-release insert placed within rigid reflector.

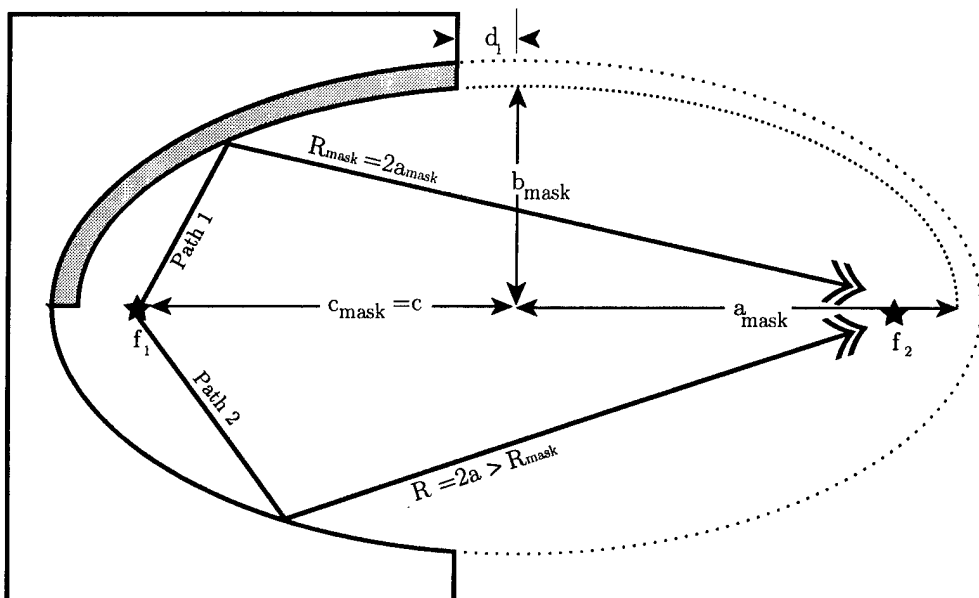


Figure 3.5: One half of the pressure-release insert placed within rigid reflector.

on Path 2 reflects from the rigid and arrives second. The delay times, calculated with sound speed  $c_0 = 1500$  m/s, are included in the last column in Table 3.1.

In the experimental lithotripter, the aperture of brass reflector  $S$  fills a hole in the bottom of the water tank so that the axis of the reflector is  $14^\circ$  from the vertical. The electrode enters from the horizontal snuggly through a hole (1.57 cm dia.) in the reflector. Water fills the tank and the bowl and surrounds the electrode points.

Three normal axes  $x$ ,  $y$ , and  $z$  are assigned with an origin at  $f_2$ . Axis  $z$  is along the major axis of the reflector. Positive  $z$  is away from the bowl. Axes  $x$  and  $y$  are transverse to the axis. Consider the aperture of the reflector to be a clock face. The electrodes enter from 12 o'clock. Axis  $x$  runs from 12 to 6 across the clock face. Axis  $y$  runs from 3 to 9. Axis  $y$  is an axis of symmetry; axis  $x$  is not because of the presence of the electrodes.

### 3.2 Modified or alternative configurations

In this section, modifications to the experimental lithotripter are described. The differences between the Seattle experimental lithotripter and the Austin configuration are addressed. The Indianapolis clinical lithotripter is also described.

#### 3.2.1 Seattle dual spark systems

A second spark system (one of the two built in Austin) was added to the the experimental lithotripter. The two systems were run individually and in tandem. Only the high voltage supply was shared, but high voltage diodes prevented back current through the high voltage supply to the other system. Two parallel capacitors (0.06  $\mu$ F, 90 nH each) and other electronics were placed on a shelf above the tank. Brass reflector  $R$  or polyurethane reflector reflector  $C$  was placed on a 7.6 cm platform on the tank bottom. The axis of reflector  $R$  or reflector  $C$  was perpendicular to the axis of reflector  $S$ . But the experimental lithotripter and the second system were confocal, meaning that  $f_2$  was the same point for both systems.

The experimental lithotripter trigger was fired with a  $\pm 5$  V transistor-transistor logic (TTL) output from an Apple Macintosh PowerPC 7100/80. The TTL signal was split off and also used to trigger a pulse generator, which fired the trigger of the second

spark system. A delay could be added in the pulse generator to fire the added system second. Delays on the order of 100  $\mu$ s were repeatable to within 10%. The system was temperamental when both spark generators were triggered simultaneously: delays between the spark discharges of up to 30  $\mu$ s were measured. Nevertheless, simultaneous discharge occurred half the time.

Photo diodes were used to detect the time of discharge of the underwater sparks. A diode was pointed at each spark. The more directive diode detected only the spark it faced. The other picked up a strong signal from the spark it faced and a weak signal from the other spark. The time delay between sparks was obtained either of two ways: comparison of arrival times of the strong signals on each channel or comparison of strong and weak on one channel.

The experimental lithotripter had an inherent delay between the trigger signal and the underwater spark discharge. The delay was 1 ms, which potentially meant we could trigger the added spark first by up to 1 ms. But when the added spark discharged, the experimental lithotripter fired 20 to 50  $\mu$ s later, regardless of the triggering. It seemed the electrical noise from the added spark could trigger the experimental lithotripter. Therefore, the experimental lithotripter was always triggered first.

### 3.2.2 Austin experimental configuration

The Austin configuration differed in that two spark generators of the same type were used, and deionized, partially degassed water filled a 104  $\times$  58  $\times$  46 cm polycarbonate tank having a horizontal bottom. The reflectors were positioned horizontally with the electronics above, as shown in Fig. 3.6. The angle between two confocal reflectors was 100°, not 90°. Sparks were weaker than in the experimental lithotripter because each system now had one capacitor and higher inductance, and sparks are less efficient in deionized water.<sup>39</sup> The deionizing system was described by Ten Cate.<sup>46</sup> Our partial degassing technique, described in IEEE standards,<sup>47</sup> was to let the water sit in the tank for 2 days. No meter was available to test the gas content of the water.

An automated positioning table straddled the tank and positioned the hydrophone in the tank. Uncertainty in the position was less than 1 mm. More on the positioner was written by Bailey.<sup>42</sup> Operation of the positioner was the same as that in Seattle.

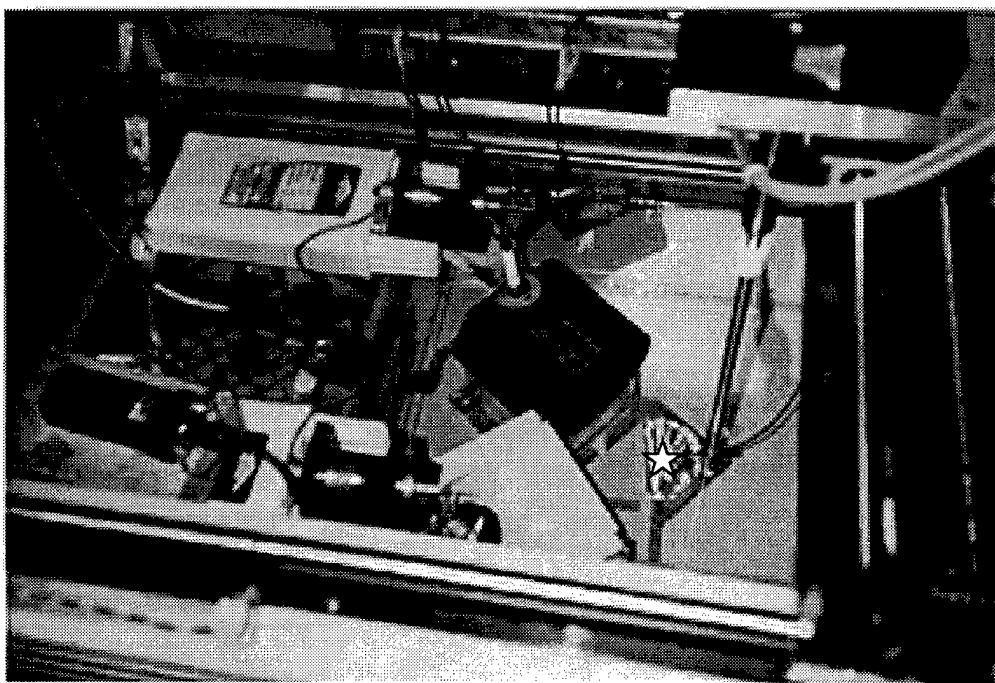


Figure 3.6: Bird's eye view of the Austin confocal arrangement of a rigid and a pressure-release reflector. Electronics are in the tank but above the water level. The capacitors are white. The brass bullet shapes on the black holders are the open-air triggers. Aluminum foil is positioned at  $f_2$ , which is indicated with a white star.

AS-97-19

### 3.2.3 Indianapolis clinical lithotripter

The Dornier HM3 lithotripter in Indianapolis includes not only a spark source and reflector but a positioning system and water tank. A photo of the system is shown in Fig. 3.7. In the center is the stainless steel water tank. The spark and reflecting bowl are in the bottom of the tank, facing up. The axis of the reflector is 14° from vertical.

Raised above the bath is the positioning gantry, which is used clinically to support and position the patient in the water bath. For our experiments, a hydrophone was held to the gantry on the end of a long positioning arm. The large white barrels on the sides of the tank swing so that they face down into the tank. They are the receiving side of two fluoroscopy imaging systems. Clinically the fluoroscopy is used to image kidney stones; we used it to locate the hydrophone. The images appeared on two TV monitors along with a graphic of the location of  $f_2$ . The positioning system was then moved as the operator watched the hydrophone image line up with  $f_2$  on the screen. Positioning, fluoroscopy, waterfill, and triggering controls are on the instrument rack in the back of the photograph.

The spark-generating system is located under the tank. The energy is stored in a 80 nF capacitor at 12-30 kV. The energy is released to the spark gap through a pressurized nitrogen trigger. The nitrogen supply for the triggers as well as the deionizing and degassing systems for the water are in an adjacent room.

## 3.3 Measurement configuration

Three types of measurements were made: direct pressure measurement of the acoustic fields of the rigid and pressure-release reflectors, passive cavitation detection with a focused hydrophone, and active cavitation detection with aluminum foil.

### 3.3.1 Direct pressure measurement

The acoustic fields were measured with a Sonic Industries (SI) Reference Shock Wave hydrophone (Sonic Industries, Hatboro, Pennsylvania). The SI hydrophone consists of an unshielded membrane of polyvinylidene difluoride (PVdF) in a plastic cassette. The cassettes are detachable from the submersible preamplifier and are replaceable.

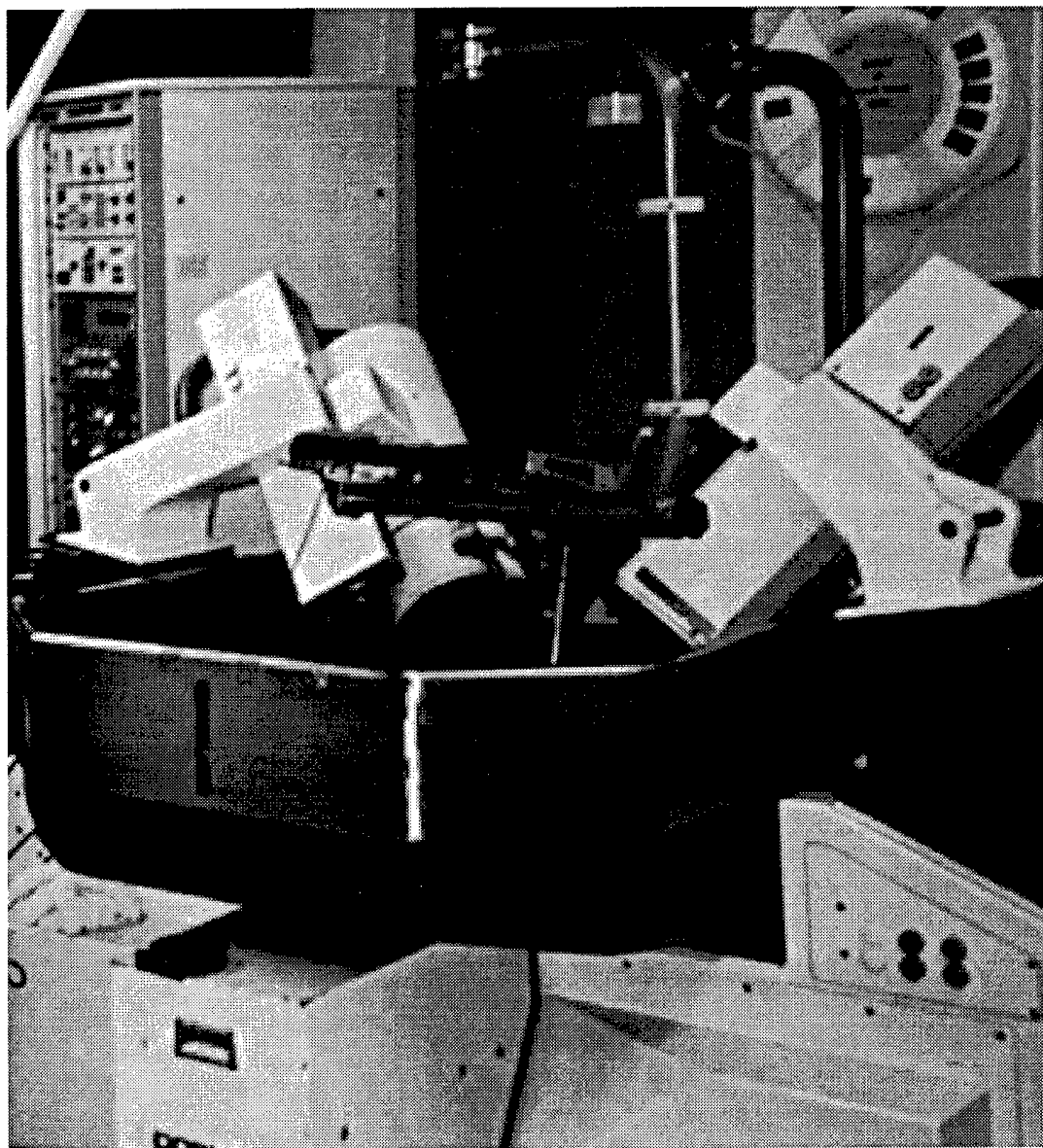


Figure 3.7: Dornier HM3 lithotripter (used for research) at Methodist Hospital, Indianapolis, Indiana.

AS-97-20

Diameter of the active spot is less than 0.5 mm. According to manufacturer's specifications,<sup>38</sup> frequency response is flat ( $\pm 2$  dB) to 50 MHz and response is linear to 100 MPa. Calibrations are traceable to the National Physical Laboratory in Teddington, U.K.

Figure 3.8 shows the cassette dimensions. The membrane window is  $5.7 \times 5.7$  cm square. The relatively small size makes reflections or membrane waves excited at the edge of the window a concern. Membrane waves on membrane hydrophones were discussed by Campbell *et al.*<sup>43</sup> and are addressed further in Chapter 4. The black cross hairs on the membrane in the figure represent the electrodes to the active element. The electrodes and element are not electrically shielded from the water. Because of lack of shielding, the water in which the hydrophone is placed has to have a conductivity of less than  $5 \mu\text{S}/\text{cm}$  for reliable measurement.<sup>38</sup> The bare metal electrodes also present a possible cavitation site, which Staudenraus and Eisenmenger<sup>48</sup> suspect shortens the duration of negative pressure phase of a lithotripter pulse.

Although measurements were made with a number of other hydrophones, only three types are mentioned. In one and two, membranes were purchased from K-Tech and Sonic Industries, affixed to a plastic ring, and insulated with a thin layer of silicone. These hydrophones were designed and constructed by R. O. Cleveland (APL). They were used *in vivo* under Cleveland's direction. The third is an NTR piezoceramic needlepoint hydrophone. It consists of a 1.5 mm diameter piezoceramic (PZT) disk at the end of a 5 cm post. The frequency response is peaked at 1 MHz, and the large amplitude negative pressure response is suspect. The NTR needle hydrophone was used in measurements in Austin, where the Sonic Industries membrane hydrophone was not available. The waveforms measured with the needle and membrane hydrophones are directly compared in Chapter 4.

Hydrophone signals were recorded on a Sony Tektronix RTD digitizer and passed to computer via GPIB. Interfacing was done via LabVIEW (National Instruments, Austin) software and boards. Sampling rates were 100-250 MHz. Postprocessing of waveforms was done with MatLab (The Mathworks, Inc., Natick, Massachusetts). Text figures were finished with Adobe Illustrator (Adobe Systems Inc., Mountain View, California).

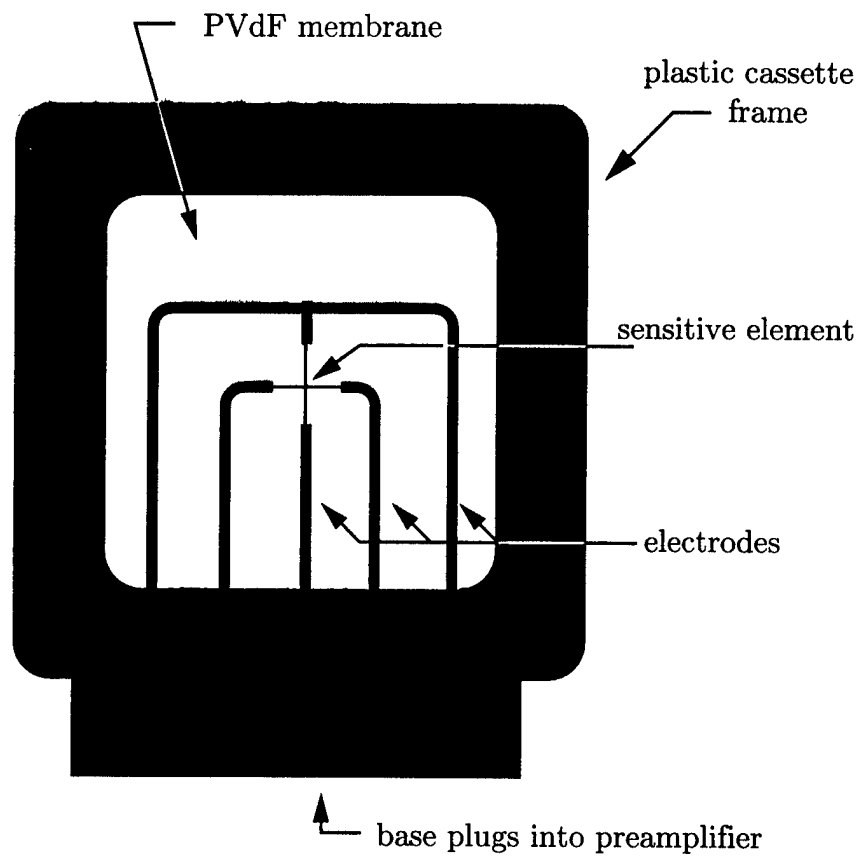


Figure 3.8: Schematic of Sonic Industries reference shock wave hydrophone (actual size). The thickness of the frame is 6 mm, and of the PVdF membrane is 25  $\mu\text{m}$ .

AS-97-21

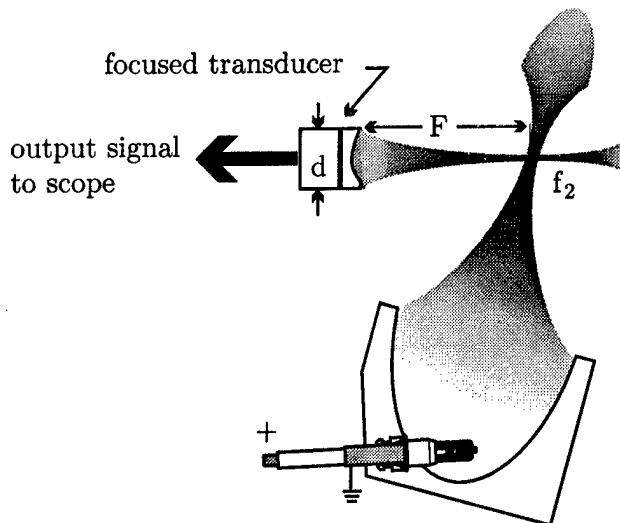


Figure 3.9: Confocal arrangement of lithotripter and passive cavitation detector (PCD).  
AS-97-22

### 3.3.2 PCD

A focused transducer, the passive cavitation detector (PCD), was used to listen for the shock waves created by bubble collapse at the focus of the lithotripter. Figure 3.9 shows our passive cavitation detection scheme. The lithotripter beam and the sensitivity beam of the transducer cross perpendicularly.

#### How the PCD worked

The PCD measures a strong signal when the lithotripter pulse arrives at the focus of the transducer. Here ambient bubbles are squeezed. The squeezed bubbles radiate a measurable shock wave. Then the bubbles grow in response to the negative tail of the lithotripter pulse. Inertial forces eventually collapse the bubbles to a very small radius. The collapse radiates a strong pressure wave also detected by the PCD.

The amplitude of the signal contains information about the strength of collapse. Averaging many signals is, however, necessary because number and location of the bubbles reacting is random. In addition, because the PCD is narrowband, high amplitudes

associated with high frequencies are lost.

A simpler measure of collapse strength is the time of silence between the initial collapse and a final collapse. As seen in Chapter 2, bubble duration and collapse pressure are directly related: long duration correlates with greater collapse pressures. Passive cavitation detection in general is discussed by Roy.<sup>49</sup> The specific use in measuring a lithotripter field is discussed by Church<sup>5</sup> and Coleman *et al.*<sup>14,15</sup>

The PCD signal was passed through a 300 kHz high pass filter to remove strong ringing of the ceramic's radial mode when the lithotripter was fired. All calibrations were also done with the filter. The signal was recorded on the Sony Tektronix digitizer. Cavitation measurements were sampled at 5 MHz.

The cavitation field of the lithotripter was assessed by varying the location of the PCD focus. A map was obtained by scanning the PCD focus along and across the lithotripter beam. Alignment was made with a pointed cap that fits over the PCD. The end of the point indicates the focus of the PCD. The accuracy of the cap was verified with a hydrophone that was run as a source. The hydrophone was moved until the largest response was found in the PCD signal. The cap was placed on the PCD, and the point on the cap was at the same place as the hydrophone. Reciprocally the hydrophone was run as a source and the PCD as a receiver. Results were identical.

### **How the PCD was made**

The heart of the PCD is a concave, piezoceramic disk with a 10 cm radius of curvature and 10 cm diameter aperture. The disk is C5400 (PZT) and was manufactured by Channel Industries (Santa Barbara, California). We measured the resonance frequency to be 1.08 MHz.

The housing was designed by O. Sapozhnikov (Moscow University, Moscow, Russia) and constructed at the machine shop at APL. All but the face is shielded by a metal housing. Because electrical contacts were made with conductive rubber, the disk can easily be replaced by other disks of different curvature. No backing material was used in the housing behind the ceramic.

### How the PCD was calibrated

The transducer is nonintrusive; without backing, it is sensitive but narrowband. The -6dB focal region was measured to be 2 cm axial and 2 mm transverse. Pressure focal gain is 56. Characterization of the PCD was directed and completed by O. Sapozhnikov.

Region measurement was made by recording the peak signal (average of 100 recordings) from a Dapco PVdF needle hydrophone driven as a source. The 0.5 mm source was our best approximation of a point source. The source was hit by a  $0.5 \mu\text{s}$  electrical pulse in an effort to produce a short acoustic burst, simulating a bubble collapse. Two acoustic cycles at 1 MHz, the source resonance, were obtained, which was not a single spike. However, the signal was nevertheless short. Because the PCD is also narrowband, calibration was not much different from calibration with long tone bursts. With the tone burst, side lobes and nulls could be seen. When hit by the short acoustic burst, the PCD rings for many cycles. The  $1/e$  amplitude decay time is  $10 \mu\text{s}$ . The corresponding  $Q$  of 10 is typical for piezoceramics.

Pressure calibration of the source was also made by direct comparison to a Marconi bilaminar membrane hydrophone (Chelmsford, Essex, England). Calibration enabled Sapozhnikov<sup>16</sup> to estimate the peak pressure of the collapsing bubble. His result of 114 bar compares well to Church's theoretical collapse pressure of 100-300 bar<sup>5</sup> and Vogel and Lauterborn's experimental result of 70 bar.<sup>50</sup> The calibration of the hydrophone used by Coleman *et al.*<sup>14</sup> was not stated. But the signal-to-noise level was poorer than ours.

Data acquisition and postprocessing of the PCD signals was the same as with the hydrophones.

#### 3.3.3 Aluminum foil detectors

Cavitation was also detected by pitting of aluminum foil. Pitting of aluminum foil is a well documented,<sup>12,13</sup> highly sensitive method of detection: one lithotripter pulse created visible pitting. In this investigation and unless otherwise stated, only one pulse or one sequence of two pulses was used per foil, and the foils were positioned along the acoustic beam, not perpendicular to it.

### Preparation and alignment of the foils

Foil was glued to semicircular frames. The edge of the foil nearest the source was left free to minimize disturbance of the sound field. The frame/foil packet fit into a V-shaped holder for exposure in the water tank. The configuration is shown in Fig. 3.10.

Effort was made to keep the aluminum foil taut and wrinkle free. Foil was stretched as a drum skin over a barrel, and semicircular frames were glued to the stretched foil. Kraft standard foodservice aluminum foil (Kraft Foodservices Inc., Dist., Glenview, Illinois) was used. The foil was 0.0007 inch (18  $\mu\text{m}$ ) thick. The frames were 0.165 cm thick, had 3.8 cm ID and 4.6 OD, and were, in fact, 220° arcs (slightly larger than a semicircle). Holes (0.24 cm dia.) were drilled 10° back of the ends of the frame. Duct tape was used to hold the foil to an aluminum barrel. Metalset A4 epoxy resin cement (Smooth-On, Inc., Gillette, New Jersey) was painted on the frame in a thin layer, and the frame then placed on the foil drum. One pound of weight was then placed on the frame. The weight put tension on the foil. After 3 hours, a circle around the frame's outer diameter was traced. The free end was cut straight between the open ends of the frame. A guillotine paper cutter was used for a straight edge.

In Austin, the NTR needle hydrophone was placed 2 mm above the foil at a downward angle of 45°. The hydrophone was positioned 2 mm above  $f_2$ . Pit patterns were unaffected by the presence of the hydrophone. The hydrophone gave a measure of the timing of the pulses.

In the experiment, the packets were held in a V-shaped fixture made of aluminum. Each arm of the V-shape was 1 cm wide and 10 cm long. A stainless steel spring was attached 9 cm down each arm. At the apex were two 0.25 inch holes 0.75 inch apart. The holes were used for attachment to the positioner and held in place a lip into which the foil packet fit. The lip was simply two aluminum layers that sat on the V. The layers each had two 0.25 inch holes 0.75 inch apart positioned so that the top layer overhung by 0.3 inch. A foil packet slid under the groove. The springs fit into holes at the ends of the packet and held the foil free end taut.

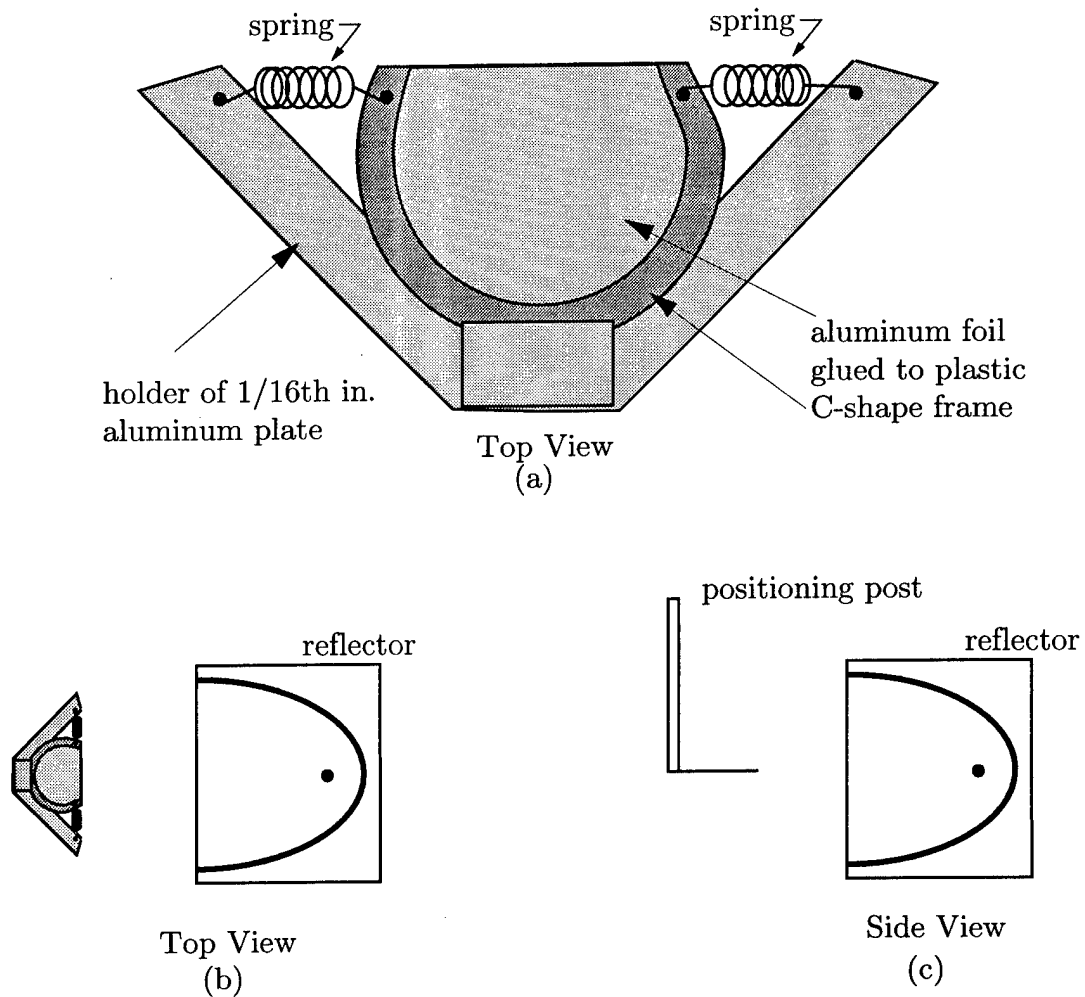


Figure 3.10: Sketch of (a) aluminum foil on plastic frame on V-shaped holder, (b) top view of foil and holder positioned at  $f_2$  of the reflector, and (c) side view of foil and holder positioned at  $f_2$  of the reflector.

AS-97-23

### Measurement of foil pits

Pits were readily seen by eye. Ofoto software was used to scan foils on a flat bed scanner. The scanned images appear in this paper.

The scans were also opened in NIH-Image (free software from the National Institutes of Health), where statistical measures of the pits were made. Scans were a collection of pixels. Each pixel was one of 256 of shades of grey. Black was 0, and white was 255. Shade was determined by the light reflection in the scanner. Flat foil appeared very nearly all one shade. Pits reflected the scanner light differently and, therefore, appeared light or dark. More shade appeared with more pitting. A histogram was made of how many pixels are in each of the 256 greyscale bins. The standard deviation of the histogram, we argue, gave an indication of the amount of pitting; the number of white pixels represents the number of deep pits. The technique was a modification of a technique described by Lifshitz *et al.*<sup>13</sup> They used more severely pitted foils and counted the number of pixels that appeared in the extremes 0 and 255.

Direct measurement of pit depth and extent was made on an Alpha Step 500 surface profiler (Tencor Instruments, Mountain View, California). Effort was made to make our own profilometer with the positioning system, but positioner resolution was not sufficient.

The Microelectronics and Engineering Lab, University of Texas at Austin, permitted us use in the clean room environment of the Tencor Instruments profilometer. The foils were taped to an aluminum plate, and the foil and plate were dipped in methanol. The methanol cleaned the foil and, as it evaporated, made the foil cling to the plate, which minimized the gross wrinkle on the foil not associated with the cavitation. The plate and foil were then placed in the profilometer.

The profilometer scans the foil in steps using a stylus which touches the foil. The stylus descends, senses contact, records the height, ascended, makes a horizontal step, and repeats the process. The stylus touches the foil but no discernible impression is left. Repeated scans were identical. The vertical resolution of the instrument is 25 Å, and the horizontal steps of 4  $\mu\text{m}$  were taken. Centimeter-long linear scans were made across sections of the foil, and a magnifying video camera displayed the area being scanned.

## Chapter 4

### Results

Results are presented in six sections. Results in earlier sections are used in later ones. For example, experimentally determined waveforms presented in Sec. 4.1 are used as input to obtain the numerical code results presented in Secs. 4.2-4.5. Consequently, numerical and experimental results are presented side by side.

In Sec. 4.1, measured pressure waveforms produced by rigid and pressure-release reflectors are presented and discussed. Waveforms were recorded with a membrane hydrophone at a number of on-axis and off-axis locations. Comparison is made with other experimental and theoretical works. A correction to deficiencies of the hydrophone is proposed. The section establishes the driving force on the bubbles.

In Sec. 4.2, output of the Gilmore code with experimentally recorded acoustic waveforms as input is compared to cavitation measurement with the passive cavitation detector (PCD). As the electrical potential of the spark generator was increased, acoustic pressure amplitude increased, and bubbles were driven into a longer growth and collapse cycle. The numerical results show that stronger acoustic pulses produced longer bubble cycles and higher collapse pressures. The section establishes a baseline agreement between our numerical code and experimental techniques.

In Sec. 4.3, cavitation fields produced by rigid and pressure-release reflectors (used separately) are numerically and experimentally described and compared. Reduced aluminum foil pitting when the pressure-release reflector was used is interpreted as support for the numerical prediction of "stifled" bubble collapse. The section establishes the extent and duration of bubble activity with single reflectors and gives the first glimpse at manipulation of cavitation intensity.

In Sec. 4.4, quantified assessment of cavitation intensity as measured by surface pitting is presented for single reflectors and pairs of confocal reflectors. A profilometer was used to determine that deeper pits resulted in foils placed under conditions that led to computational prediction of higher collapse pressure. The results in this section

demonstrate that cavitation can be intensified or mitigated by addition of a second pulse or alteration of a single pulse.

In Sec. 4.5, PCD data were used to further describe the bubble dynamics of two-pulse cavitation and the extent of the region over which pitting is produced. The PCD measured signal where collapse was predicted and none where collapse was not predicted. The section contains three independent descriptions – one numerical and two experimental – of intensified and mitigated cavitation.

Sections 4.6 and 4.7 include initial results directed toward applications. In Sec. 4.6 an arrangement of reflectors to reduce foil pitting to a localized region is described. The lithotripsy application is isolation of cavitation to near the stone to (1) accelerate comminution, and (2) minimize cavitation damage to tissue. In Sec. 4.7 modification of a clinical lithotripter is discussed. Huge measured negative pressures and preliminary *in vivo* studies are reported. The sections touch on work in progress and applications of the dissertation.

## 4.1 Acoustic fields of rigid and pressure-release reflectors

Determining the acoustic driving force is the first step to understand acoustic cavitation. Acoustic waveforms were recorded along and across the reflector axis with a Sonic Industries (SI) PVDF membrane hydrophone. Of the hydrophones available, the SI hydrophone had the flattest frequency response and was the least intrusive. Both a rigid and a pressure-release reflector were studied.

Theoretical prediction of waveforms is not presented in this dissertation. No claim is made to being able to explain thoroughly the waveforms produced with the pressure-release reflector, but effort is made to grasp what is physically happening.

### 4.1.1 Acoustic waveforms of rigid and pressure-release reflectors

The pressure fields of the rigid reflector  $S$  and pressure-release reflector  $C$  were mapped with the SI hydrophone. Each electrical discharge produces a direct wave from the spark, followed by the focused reflected wave. At the second focus  $f_2$ , the direct wave is a  $\sim 1$  MPa, nearly unipolar pulse. The pressure peak of the focused wave is greater

than 30 MPa, the trough is deeper than -5 MPa. Because the direct wave is so much weaker, only the focused signals are reported and discussed here.

Our experimental results are compared to known results in the cases where known results exist. The focused wave produced by the rigid reflector has been well defined experimentally by Coleman and Saunders.<sup>4</sup> Waveforms in general agreement with the experimental results were obtained by Coleman *et al.*,<sup>63</sup> who used a numerical code based on the Burgers equation. The experiments that most closely resemble ours with the pressure-release reflector were completed by Müller,<sup>3</sup> and the only theoretical work, of which we know, is a newly initiated, unpublished investigation by Cleveland and Averkiou,<sup>53</sup> who use a numerical model<sup>54,55</sup> based on the Khokhlov-Zabolotskaya-Kuznetsov (KZK) equation.<sup>56</sup> For the rigid reflector, our measured waveforms are in agreement with previously determined results.

For the pressure-release reflector, waveforms are so new that no published results exist for comparison. Our original expectation was an inverted form of the rigid-reflector waveform, because the pulse reflected from a pressure release surface is the inverse of the pulse reflected off a rigid surface. However, the simple original idea neglects focusing and finite-amplitude effects which appear to play a significant role. Because finite-amplitude effects, which are important in the experiment, are neglected in Hamilton's<sup>51</sup> model, Hamilton's solution to reflection from an ellipsoidal mirror is not used for comparison. An unpublished result calculated by Cleveland and Averkiou<sup>53</sup> does compare well to our waveforms; see Fig. 4.1. The waveform in Fig. 4.1 was calculated using linear ray theory within the ellipsoid and a KZK code<sup>55</sup> for propagation beyond the reflector aperture. The pulse in Fig. 4.1 was calculated for the axial position 11 mm beyond the focus and has a negative pressure phase followed by a sharp positive spike. The shape agrees with what we measured but not with what we originally expected. Cleveland has recently modified the calculation and included nonlinear effects along the ray paths within the bowl. Cleveland's new results are not yet available. However, our experimental results and Müller's experimental results do not agree, largely we suspect, because the experiments differ significantly.

The common aspects of the waveforms produced by the rigid and pressure-release reflectors are now discussed. Figures 4.2 and 4.3 show a representative waveform

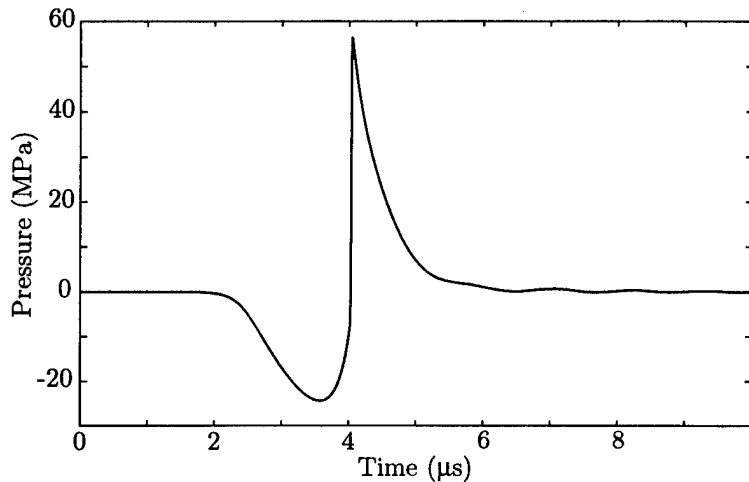


Figure 4.1: Acoustic waveform produced by a pressure-release reflector and calculated numerically by Cleveland and Averkiou.<sup>53</sup>

AS-97-24

at three off-axis positions,  $y = 5, 10$ , and  $15$  mm, and ten axial positions,  $-50 \text{ mm} \leq z \leq 40 \text{ mm}$  in steps of  $10$  mm, where the origin  $y, z = 0, 0$  is at  $f_2$ . Figure 4.3 also contains waveforms for  $(y, z)$  coordinates  $(5, -10)$  and  $(10, -10)$ . Figure 4.2 contains the rigid-reflector data; Fig. 4.3 contains the pressure-release-reflector data. The ellipse is actual size, and the reflector aperture is shown. All pressure plots are on the same scale and were plotted versus time. The length of the pulses drawn on the page is twice the actual length of the acoustic pulses. An arbitrary retarded time is used; the picture sequences do not accurately show changes in pulse arrival. The inaccuracy was caused by spark jitter, which caused changes in arrival time of 1 to  $2 \mu\text{s}$  between sequential firings at one location.

Each waveform in both Figs. 4.2 and 4.3 shows a high-frequency, low-amplitude, microsecond-duration, electrical noise burst. The spark generator created the electrical noise, which was picked up by the hydrophone and oscilloscope through the air or water and on ground lines. The noise was reduced by improving the shielding and grounding. The figures show the reduced noise.

Rigid-reflector waveforms (see Fig. 4.2) have a strong positive phase followed by

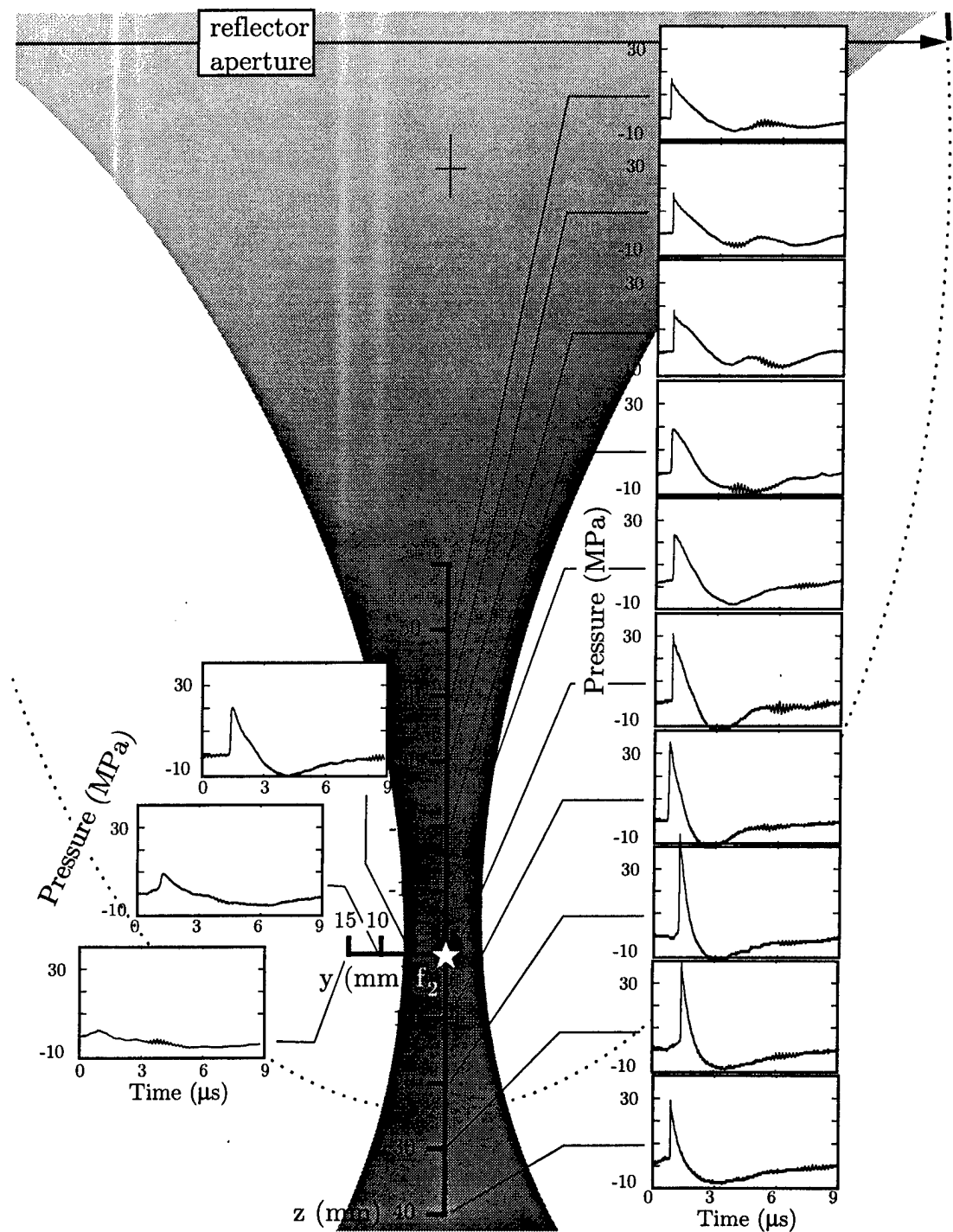


Figure 4.2: Acoustic field of rigid-reflector  $S$  (actual size) measured with SI membrane hydrophone.

AS-97-25

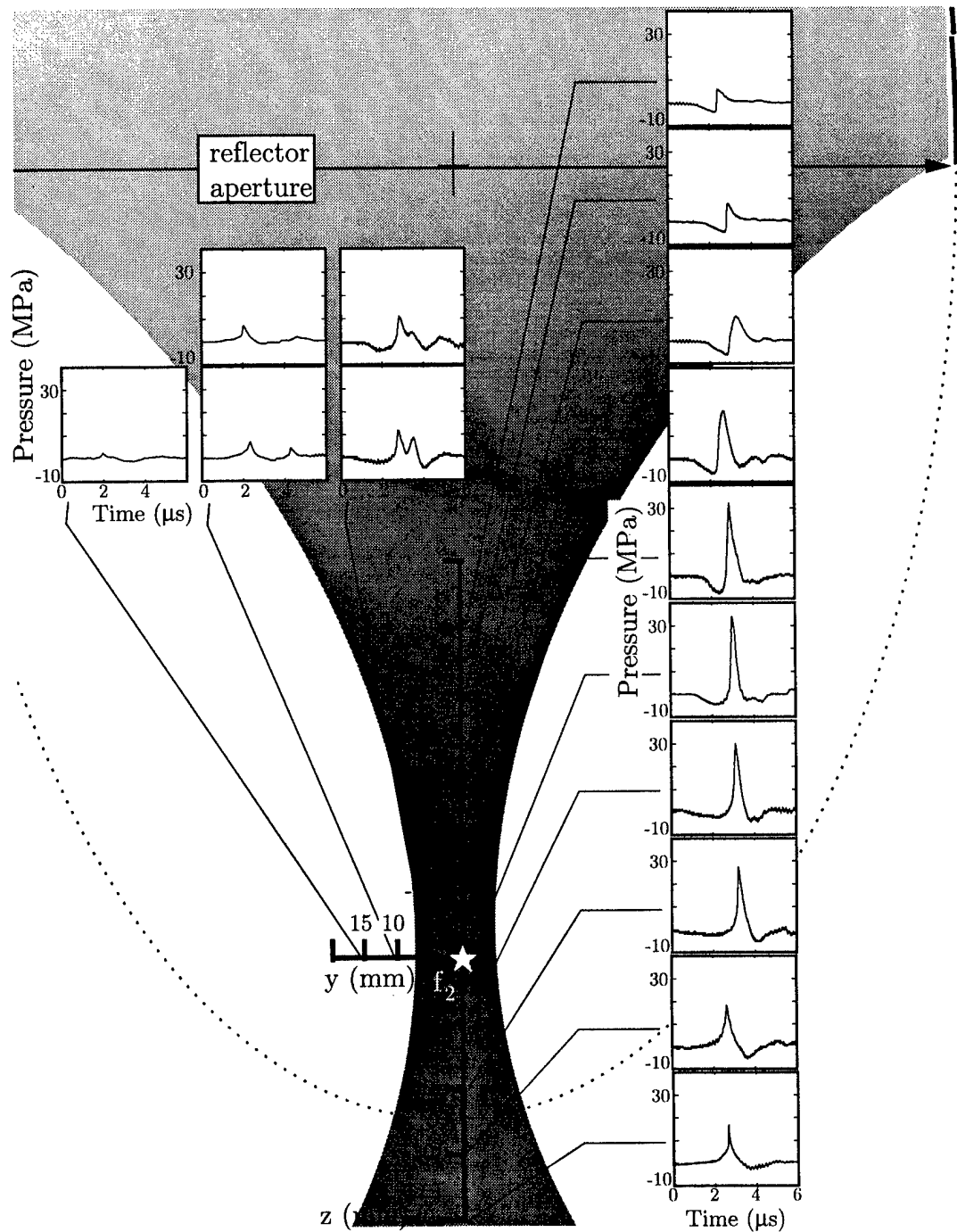


Figure 4.3: Acoustic field of pressure-release reflector C (actual size) measured with SI membrane hydrophone.

AS-97-26

a weaker, longer duration negative phase. The basic positive-negative shape does not change greatly with change in axial position. The duration of the positive phase of the pulse decreases as  $z$  increases. The results are in good agreement with waveforms measured by Coleman *et al.*<sup>34</sup> and predicted by Hamilton.<sup>51</sup> In fact, the edge wave (diffraction from the aperture of the reflector) can be seen appearing ahead of the positive pulse in postfocal waveforms, as measured by Wright and Blackstock<sup>52</sup> and predicted by Hamilton.<sup>51</sup>

The waveforms are weak off axis. Weak off-axis signals are indicative of the reflector's sharp focus. By definition of an ellipse, the total distance from  $f_1$  to any point on the ellipsoidal reflector to  $f_2$  is uniform regardless of the point chosen. Therefore, a reflected wave from point  $A$  on the reflector arrives at  $f_2$  at the same time as the reflected wave from point  $B$ , and waves  $A$  and  $B$  sum coherently. Off axis the coherence is lost, and the waveforms are weaker. The length of the pulse determines how narrow the focus is, as two reflected signals cannot sum if the second arrives after the first has passed. Our pulse length is  $\sim 6$  mm, and at  $y = 5$  mm the measured pulse has two-thirds the amplitude of the axial pulse. The beam is less acutely focused along the axis where axial symmetry is maintained.

Pressure-release-reflector waveforms (see Fig. 4.3) also have a strong positive phase and a weaker, longer negative phase. Peak pressure amplitudes are on the same order as peak pressure amplitudes produced by the rigid reflector. Off-axis waves again deteriorate as expected for a focused wave, although the waveform seems to break into two weak coherent sections rather than the single, reduced-amplitude pulse seen off the axis of the rigid reflector. On axis close to the pressure-release reflector, the negative phase in the waveform is before the positive spike. Away from the reflector, the spike comes first, and the waveforms look like rigid-reflector signals. Near  $f_2$ , the positive falls with a negative phase on either side. We doubt that a simple explanation of the change in waveform exists, and as these are new measurements, no explanations have been previously offered. However, two factors exist: finite-amplitude effects and focusing. One effect is that perhaps the spike is overtaking the trough. Such an explanation is applicable for the case of plane waves, but our situation is complicated by the focusing. The first effect is not sufficient. Focusing causes phase shifts in the

spectral components of the waveform. Since all the frequencies in a finite-amplitude wave do not necessarily shift equally,<sup>57</sup> the waveform may change shape as the wave passes through the focus.

The waveform from the pressure-release reflector is by no means simply an inverted form of the rigid-reflector waveform (see Figs. 4.4 and 4.5 for easy comparison). Although the reflected pulses at the rigid reflector and the pressure-release reflector may be inverses of one another, finite-amplitude effects and focusing make the pulse at the focus of the pressure-release reflector differ from the inverse of the pulse at the focus of the rigid reflector. Our waveforms are in good agreement with numerical calculations by Cleveland and Averkiou.<sup>53</sup>

Some insight into the waveform shape might be gleaned from a discussion of a uniform piston. If the aperture of either ellipsoidal reflector were a uniform piston, the explanation would be as follows. The pressure waveform in the farfield of the piston has the shape of the derivative of the pressure waveform at the piston face.<sup>58-60</sup> The change in shape is caused by the edge wave. Let the positive idealized pulse in Fig. 2.2 represent the spark-generated pulse. The pulse reflected at the rigid reflector has the same shape. When the reflected pulse reaches the aperture, the aperture may be treated as a piston, and the positive pulse as the wave produced at the piston face. The derivative of the positive pulse is a short strong positive spike followed by a weaker longer negative tail. A positive spike and a negative tail is exactly what is produced by the rigid reflector.

The approach works with the pressure-release reflector also when finite-amplitude effects are included to explain why the positive phase is stronger. Initially on reflection from the pressure-release surface, the pulse looks like the negative pulse in Fig. 2.2, but as the pulse propagates to the aperture, the peak of negative pressure trough falls to the back of the waveform. So on our aperture/piston, the negative pulse has arguably a slow fall to the peak of the negative phase and then an abrupt rise. The derivative of such a pressure waveform is a long small negative phase and a short strong positive spike. Finite-amplitude effects have been used earlier in this section to explain how the positive phase propagates faster than the negative phase.

Finite-amplitude propagation would also mean that the pulse at the rigid-reflector

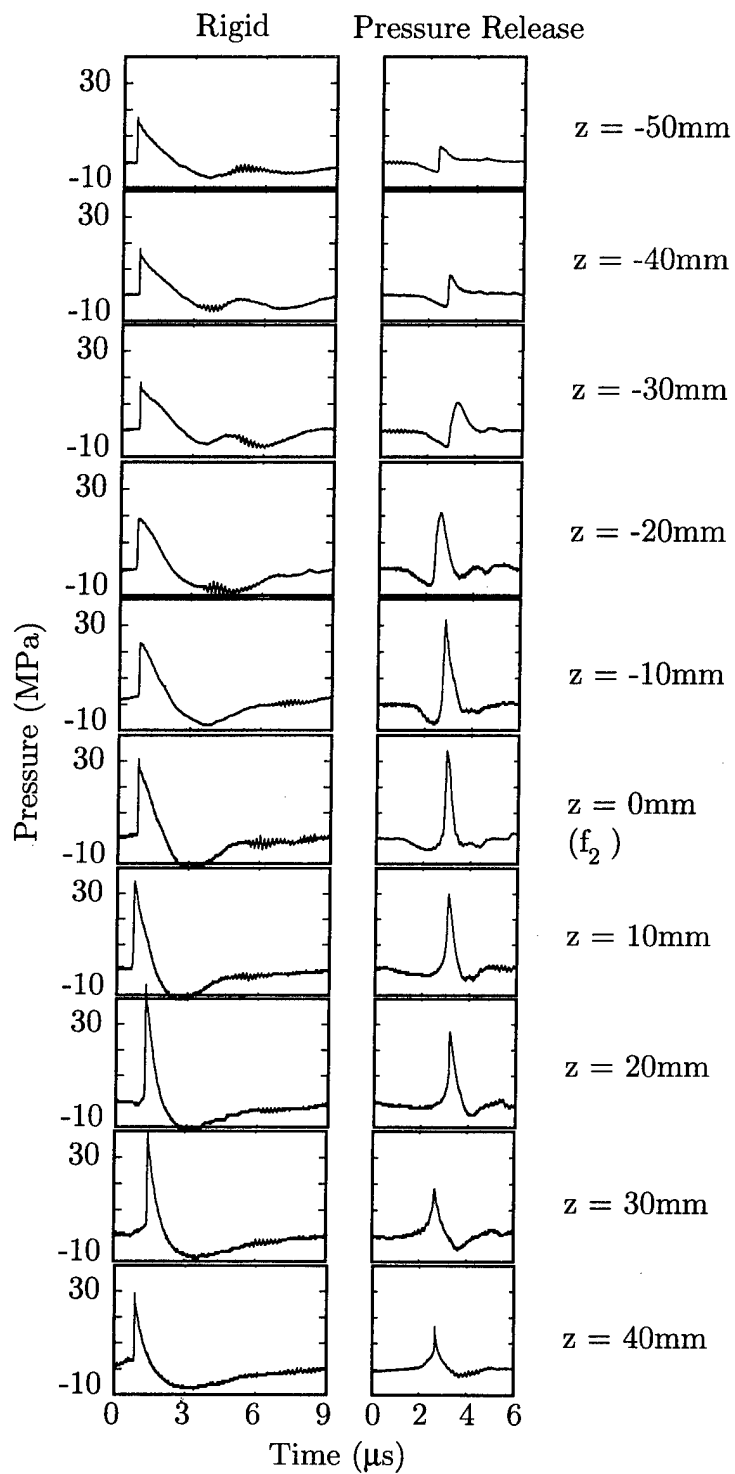


Figure 4.4: Side-by-side comparison of axial pressure mappings produced by a rigid reflector and a pressure-release reflector.

AS-97-27

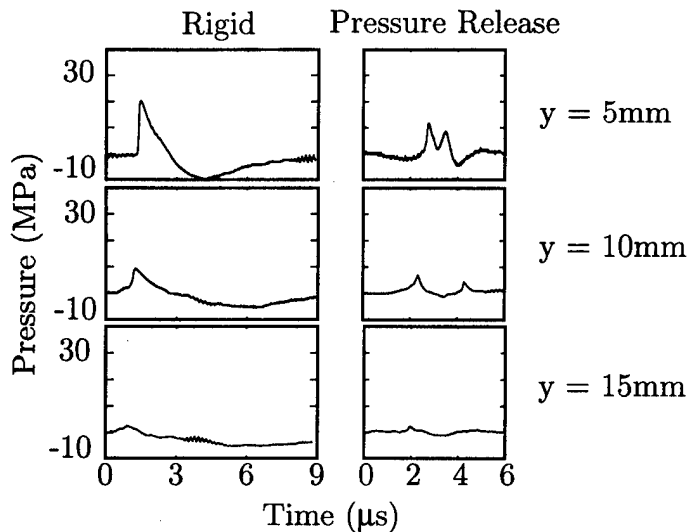


Figure 4.5: Side-by-side comparison of transverse pressure mappings produced by a rigid reflector and a pressure-release reflector.

AS-97-28

aperture would be longer than that at the pressure-release reflector aperture. The pulse reflected from the rigid reflector lengthens the whole time it propagates. The reflection from the pressure-release reflector lengthens only after the shock has moved to the back of the pulse. The explanation may account for the longer duration of the focused wave measured for the rigid reflector.

However, modeling the aperture as a uniform piston is extremely naive. At the very simplest, the aperture is a focused piston. The edge wave of a focused piston is much weaker than the focused direct wave at the focus and subsequently cannot affect the same phase changes observed in the uniform piston wave. Modeling the aperture as even a focused piston neglects the “wake” calculated by Hamilton<sup>51</sup> and Naze Tjøtta and Tjøtta.<sup>61</sup> The wake is the integrated effect of reflection from the whole curved surface of the ellipsoid. The wake is difficult to identify in our measured waveforms. Finally, the pressure amplitude in the aperture is shaded. Shading results because the attenuation of the pulse is different as it spherically diverges toward the reflector compared with its converging after being reflected and because the path of each part of the reflector is not uniform.

Hamilton,<sup>51</sup> who used a model other than a piston model and assumed small signal

theory applied, predicted that the pressure pulse at the focus of an ellipsoidal reflector is the derivative of the pressure pulse reflected at the wall of the ellipsoid. The result perhaps shows that we are not too far off in discussing our results relative to the derivative of the reflected pulses. However, because nonlinear effects play a significant role in our experiments, Hamilton's small signal model was not used to obtain quantitative results for comparison in this dissertation.

Müller's measurements<sup>3</sup> offer the closest experimental results to which to compare the waveforms for the pressure-release reflector. Müller placed a PVdF needle hydrophone at  $f_1$  and a spark at  $f_2$  of a shallow polyurethane reflector. He obtained a -9 MPa pulse that was less than 1  $\mu$ s in duration. The positive portion was even shorter and was difficult to discern, although Schlieren photographs taken concurrent to the hydrophone measurements indicate a strong positive peak. With the hydrophone at  $f_1$  of a shallow rigid reflector, he measured a nearly unipolar 50 MPa pulse that was 400 ns in duration. Neither waveform is in good agreement with what we measured. Müller did make measurements with a rigid reflector and a spark at  $f_1$ , which are in good agreement with our rigid-reflector waveforms.

Two reasons for the poor agreement are proposed. Both relate to the edge wave, which contributes to the bipolarity of the pulse. One reason is that for Müller's hydrophone to record the edge wave, the edge wave had to be deflected at a steeper angle than that of the edge wave in our experiment. Edge waves deflected at sharp angles are weak. The second reason is that hydrophone sensitivity is a function of the angle of incidence of the wave. The edge wave in Müller's experiment is again at a steep angle. Although we do not know the directivity of his hydrophone, a diminished sensitivity could account for the near unipolarity of his waveforms and disagreement with our waveforms. The directivity of our hydrophone is included in Appendix A.

Müller compared, at the focus, the peak pressure amplitudes of the focused and direct pulses. He found amplifications in the rigid reflector of 54 and in the pressure-release reflector of -7. We obtained approximately 42 and -7. Our amplification factors and Müller's amplification factors are in good agreement. Müller proposed that the negative pulse has less amplification because the pulse loses strength because it excites cavitation bubbles in the water.

#### 4.1.2 Uncertainty in recorded waveforms

Any measurement device has its own transfer function that affects the measurement. Campbell *et al.*<sup>43</sup> and Staudenraus and Eisenmenger<sup>48</sup> compared lithotripter waveforms recorded with different hydrophones. Waveforms considered had a positive pulse followed by a negative tail. In general, agreement was attained on the positive pulse but not with the negative phase. Three reasons for difficulty with the negative phase are as follows: (1) Because the hydrophone has no time to recover from the positive pulse before sensing the negative phase, transient hydrophone responses, such as ringing caused by the positive spike, have not died away. (2) The backing on some hydrophones inhibits their ability to expand under tensile stress. (3) Cavitation may have occurred at the hydrophone. Motivating the desire for an improved record of the negative pressure phase is the phase's disproportionately influential role in cavitation. The negative pressure amplitudes in this paper are in excellent agreement with the strongest negative pressures measured with lithotripters. Christopher<sup>62</sup> proposed that the negative phase of the rigid-reflector wave was limited by the tensile strength of water.

Sources of error inherent in measuring lithotripter pulses with PVdF membrane hydrophones are shortening of the negative phase<sup>48</sup> and membrane waves.<sup>43</sup> The errors stem from the high pressures of the lithotripter: the lithotripter *is* designed to break materials (kidney stones) placed at its focus.

Staudenraus and Eisenmenger found at  $f_2$  of a Siemens Lithostar lithotripter that a fiber optic hydrophone measured a negative tail 267% longer than that measured with a PVdF membrane. They proposed that under strong negative pressure, the water tore away from the metalized sensitive element of the membrane hydrophone and thus cut short the negative tail on the measured waveform. The water-glass adhesion is much stronger (in fact stronger than water-water adhesion), so the fiber optic hydrophone measured the full tail length. Waveforms measured by Jöchle *et al.*,<sup>68</sup> who used a fiber optic hydrophone, corroborate Staudenraus and Eisenmenger's results. Based on Staudenraus and Eisenmenger's work, we propose and demonstrate a correction factor, whereby we lengthen the negative tail of membrane-measured waves by 267%. The original and adjusted waves are shown in Fig. 4.6. The adjusted

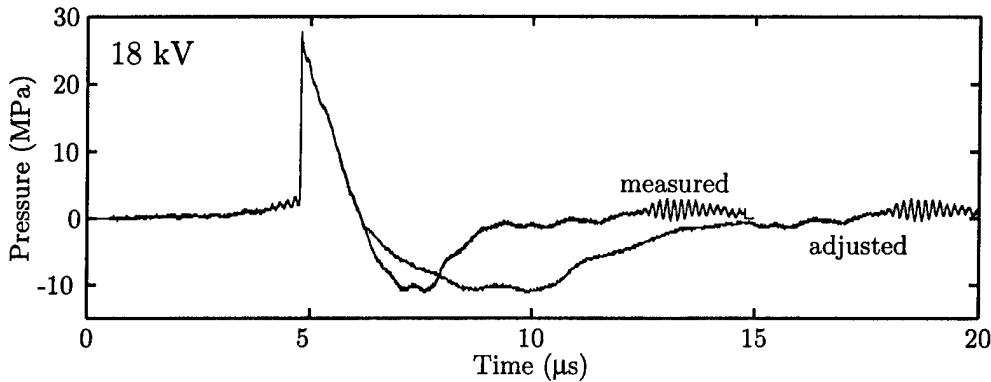


Figure 4.6: Rigid-reflector waveform measured with SI membrane and waveform, negative phase lengthened to correct for shortening by membrane hydrophone, as measured by Staudenraus and Eisenmenger.<sup>48</sup>

AS-97-29

waveform was used in numerical calculations presented in Secs. 4.2 and 4.3. The adjusted waveforms are also in better agreement with waveforms calculated by Coleman *et al.*<sup>63</sup> who based their model on the Burgers equation. Because Coleman *et al.*, Staudenraus and Eisenmenger, and Jöchle *et al.* do not have data for a pressure-release ellipsoidal reflector, no adjustment of our pressure-release-reflector waveforms was attempted.

The correction to the duration of the negative phase of the pulse is new. However Church,<sup>5</sup> in his original paper describing the Gilmore code, finds that an input based on a pulse measured with a PVdF membrane hydrophone produces calculated bubble growth-and-collapse cycles that are less than half as long as cycles that have been measured. Church's correction was in the amplitude of the pulse. However, the pulse that he created to produce cycle durations comparable to measured cycle durations had a peak negative pressure of -33 MPa. A -33 MPa phase is at least double the negative pressure measured in a conventional lithotripter with either a PVdF membrane or a fiber optic hydrophone. Therefore, we think our correction to the waveform is favorable.

The negative tail may also be corrupted by a membrane wave excited by the acoustic pulse.<sup>43</sup> The active spot in the center of the membrane measures the acoustic wave and then the membrane wave. Near  $f_2$  the strongest acoustic waves are focused at

the hydrophone active spot, and membrane waves are excited at the center, radiate outward, and are not noticeable on the signal. Off  $f_2$ , the strong waves hit elsewhere on the membrane and excite a membrane wave, which interferes with the tail of the acoustic signal. The interference is especially obvious prefocal where converging acoustic waves created converging membranes waves. Complicating matters further is the wake predicted by Hamilton.<sup>51</sup> The wake is the wave that results from the amplitude shading along the reflector face and adds fine structure to the waveform. Although our prefocal waveforms look very much like prefocal waveforms predicted by Hamilton,<sup>51</sup> it is difficult to discern in the slowly oscillating tail what is reflector edge wave, what is membrane wave, and what is wake. See the  $z = -50$ , -40, and -30 mm waveforms in Fig. 4.2.

More obvious and distorting artifact is seen with the NTR needle hydrophone, which rounds the waveform and rings because of nonflat frequency response. The NTR hydrophone underestimates the peak pressures (especially the negative) because of directivity and material constraints (i.e., the ceramic simply cannot expand sufficiently to represent the huge negative pressure phase of the lithotripter pulse). Figure 4.7 shows a comparison of the waveforms of the pressure-release reflector measured with the membrane and with the NTR piezoceramic needle. The frequency response of the NTR is peaked near 1 MHz, and 1 MHz ringing can be seen following the signals. The poor high frequency response of the hydrophone results in the rounding of the waveforms and poor estimation of the pulse rise time.<sup>42</sup> The difference is more obvious with the rigid reflector where the pulses contained a strong shock. The most notable difference in Fig. 4.7 is the much smaller negative phases in the NTR waveforms. We speculate that the piezoceramic needle is not as pliable as PVdF and does not stretch sufficiently to measure the large negative pressures. The quick decay in wave amplitude on either side of  $f_2$  may result from higher hydrophone directivity due to the larger (1.5 mm) sensitive element of the piezoceramic needle.

Since the wavefronts are focused and not planar, hydrophone directivity can play a role. Directivity played a larger role in the *in vivo* measurements where we could not see how the hydrophone was aligned. For the *in vivo* technique, see Cleveland.<sup>64</sup> For a measurements of the membrane directivity, see Appendix A.

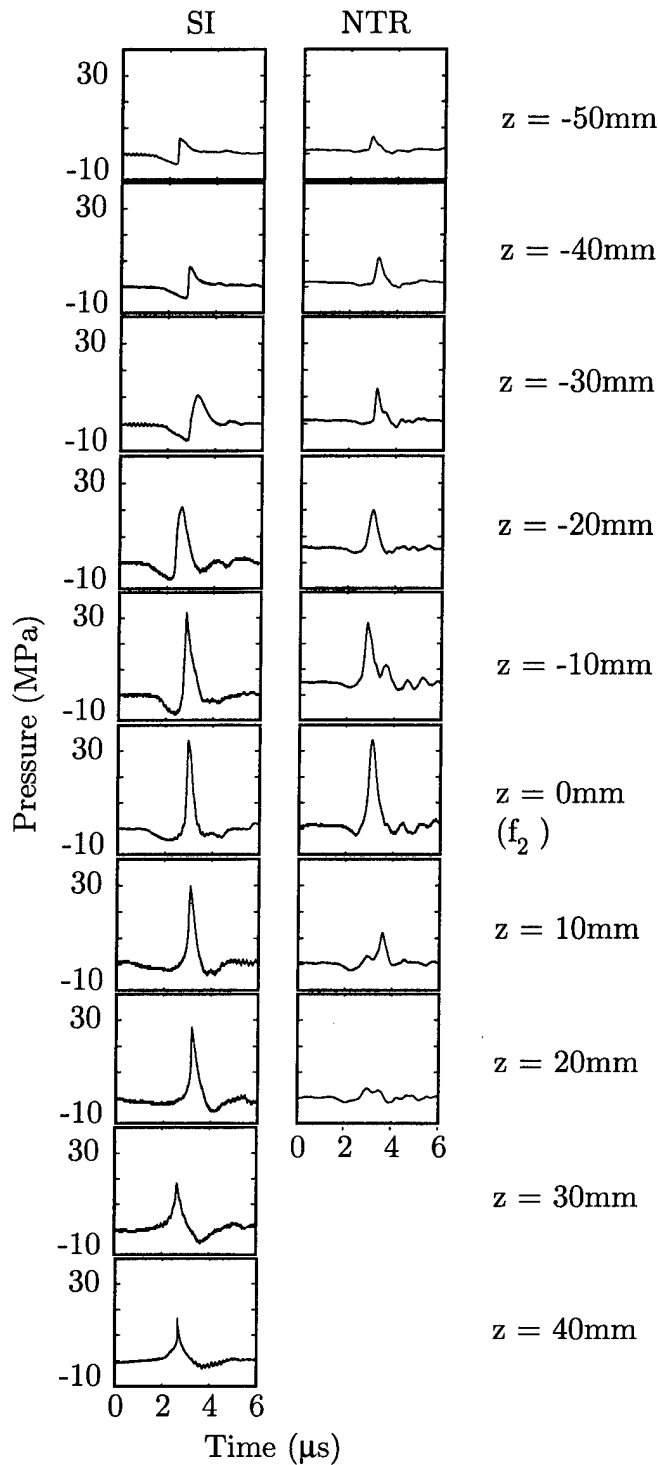


Figure 4.7: Side-by-side comparison of pressure-release reflector axial pressure mappings with SI membrane and NTR needle. The needle records weaker negative pressures.

#### 4.1.3 Peak pressure mappings – rigid and pressure-release reflectors

Spatial maps of peak positive and negative pressure for the pressure-release and rigid reflectors are plotted in this section. The “hot spots” are long and thin. Since the acoustics drive the cavitation, peak pressure (especially peak negative pressure) maps offer an indication of the cavitation field. But caution is urged since 1) as discussed above, considerable uncertainty exists in the negative pressure measurements, 2) pressure maps are an average of many shots and therefore are broadened by shot-to-shot variation in the location of  $f_2$ , and 3) the waveform – including the duration of the negative phase and timing of the positive spike – determines the cavitation behavior. Finally, the inception of cavitation is not discussed, but pressure maps may have more or less relevance with many bubbles, such as after several sparks, as opposed to when only a few bubble seeds exist.

In Fig. 4.8, peak negative and positive pressures are plotted versus hydrophone position for reflectors *S* and *C*. Data for the pressure-release reflector are in black, and data for the rigid reflector are in grey. Figure 4.9 includes the same data normalized to the highest value along each line. Each line connects the average of the peak pressures of ten waveforms measured at each position. Cross-hatched lines mark the standard deviation. Standard deviation is highest at the focus where it is 20%. The high standard deviation is a result of spark jitter (the shot-to-shot variation in the exact location of the spark at  $f_1$  and spark strength). Spark jitter moves the “hot spot” around on the order of millimeters and allows the hydrophone to catch the peak amplitude only some of the time.

The focal region for both reflectors is long along the axis and narrow across the axis at  $f_2$ . Thorough measurements were not made of the width off  $f_2$ , but Coleman *et al.*<sup>4</sup> found that a rigid reflector had a cigar-shaped focal region 12 cm long by 2 cm wide. The region was termed the -6 dB region because outside the cigar, peak pressure amplitudes were less than half the maximum amplitude. With our rigid reflector (see Fig. 4.8), the -6 dB length to within error was also 12 cm (the whole length tested), and the width was 1.5-2 cm. With the pressure-release reflector, the region was shorter and narrower. The region was  $7 \times \sim 1$  cm. For each reflector, the -6 dB region for peak negative pressure was broader and at least as long as that for peak positive

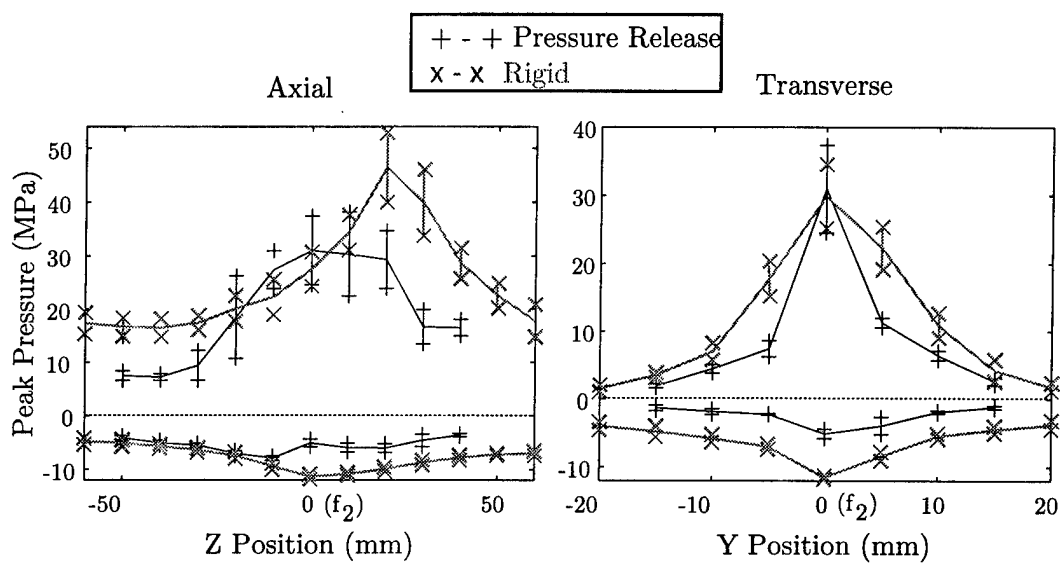


Figure 4.8: Axial and transverse peak pressure mappings for rigid (grey) and pressure-release (black) reflectors. Each point is the mean of ten sparks. Standard deviation lines are shown and capped with x's (rigid) or +'s (pressure release). The -6 dB region is long and narrow for both.

AS-97-31

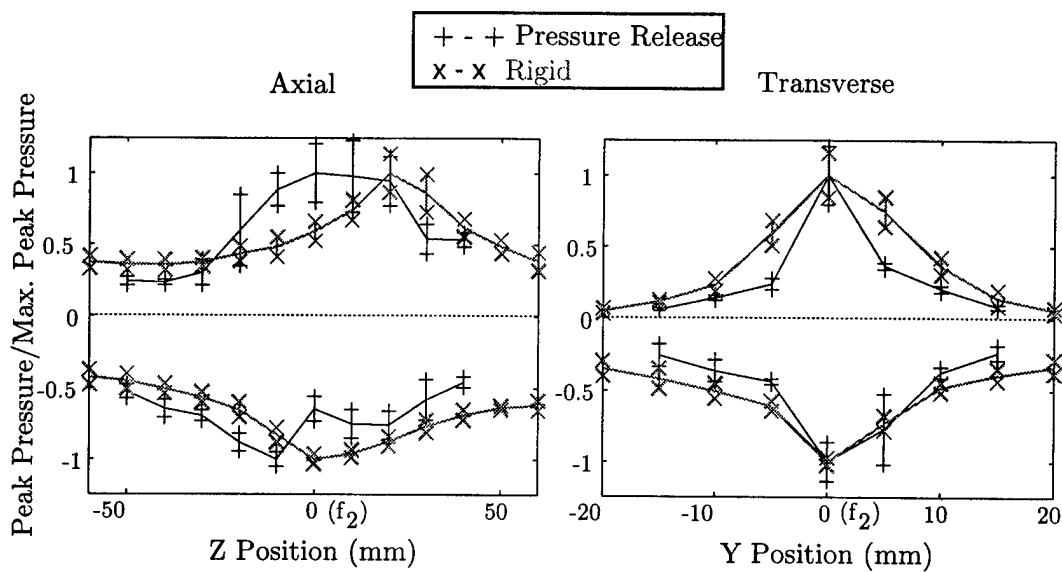


Figure 4.9: Axial and transverse peak pressure mappings normalized to the peak peak pressure along each curve. Each point is the mean of ten sparks. Standard deviation lines are shown and capped with x's (rigid) or +'s (pressure release). The -6 dB region for the pressure-release reflector (black) is nearly half as long and wide as that of the rigid reflector (grey).

AS-97-32

pressure. In fact, the amplitude of negative pressure decayed very slowly off axis for the rigid reflector. The larger region was due in part to hydrophone artifact (described previously) and in part to maximum peak negative values that are lower than the maximum peak amplitudes of the positive pressure. The off-axis peak amplitudes of positive and negative pressure were very comparable. However, the -6 dB point was calculated relative to the on-axis peak, and the on-axis peak negative was smaller than the on-axis peak positive. Hence, the -6 dB region for the negative is broader. Peak negative pressure is limited by the tensile strength of the water, whereas peak positive pressure is not. The broader -6 dB region of the negative pressure is in agreement with numerical calculations by Cleveland and Averkiou.<sup>53</sup>

The location of the maximum (peak peak) values varies between reflectors. For the rigid reflector, the largest negative pressure is at  $f_2$  and the largest positive pressure is at  $z = +20$  mm. For the pressure-release reflector, peak peak negative pressure is at  $z = -20$  mm and peak peak positive pressure is in the broad region between  $z = -10$  and  $z = +40$  mm. The finding that the negative pressure phase focused ahead of the positive pressure phase corroborates numerical predictions by Averkiou *et al.*<sup>65</sup>

Both the narrower focus of the pressure-release reflector and the earlier focusing by the negative phase are, we propose, demonstrations of self-refraction. Self-refraction is the bending of rays caused by the contribution of the sound field itself to the propagation speed. For example, a localized negative pressure region on the acoustic wavefront bends the wavefront toward the region (i.e., focuses the wavefront). Bending occurs because the sound speed is lower in the negative pressure region and sound rays bend toward slower sound speed. Bending produces a concave or converging wavefront. A strong positive region on the wavefront pushes rays away, and the front curves the other way (i.e., defocuses the wavefront). Bending makes a convex or diverging wavefront. See the thesis by Gelin<sup>66</sup> for a more detailed discussion of self-refraction. As for application to lithotripsy, the focused waves are inherently strongest on the axis. Therefore, rays are either bent toward the axis or away from the axis, and the focus either tightened or broadened. The strong negative-pressure phase at the head of the waveform produced by the pressure-release reflector creates, by self-refraction, a tight focus. Because the positive spike must overcome defocusing by self-refraction, its focus

is delayed.

One final observation of Fig. 4.9 is that the peak amplitude of the negative pressure has a dip at  $f_2$  with the pressure release. The  $f_2$  waveform in Fig. 4.3 appears useful in the explanation. If the positive pressure phases and negative pressure phases can be thought of as two separate pulses, then at  $f_2$ , they destructively interfere as the positive pulse appears exactly in the middle of the negative pulse.

## 4.2 Acoustic pressure amplitude and cavitation – rigid reflector

In this section, numerical prediction and experimental measurement of cavitation are compared. The acoustic pressure amplitude (measured as in Sec. 4.1) was varied, and the cavitation collapse was detected with the passive cavitation detector (PCD) and aluminum foil. Pressure amplitude was altered by adjusting the the electrical potential placed on the lithotripter capacitors. Charging potential ranged from 15 to 24 kV, and the sequence of measurements is referred to as kV tests. The PCD measurements were made with and without aluminum foil in the lithotripter field to assess the intrusiveness of the foil measurements. Only the rigid reflector is considered.

### 4.2.1 Acoustic amplitude and charging potential

The pressure waveforms for four charging potentials are shown in Fig. 4.10. Mean and standard deviation of the peak amplitudes of the negative and positive pressure phases are plotted versus charging potential in Fig. 4.11. The pressure amplitude increases nearly linearly with potential. The pulse duration increases by 20%. At the risk of too-much hand-waving nonlinear acoustics, it is pointed out that higher amplitude shocked pulses lengthen more as they propagate. The speed of the front shock is faster than the rest of the pulse and is proportional to the shock amplitude. A stronger shock moves ahead faster and stretches the pulse more than a weaker shock does.

### 4.2.2 Computed bubble response and charging potential

A stronger acoustic driving force means theoretically a longer bubble cycle and stronger collapse. The radius versus time (R-T) curves calculated with the Gilmore code are plotted in Fig. 4.12. The initial bubble radius was 2  $\mu\text{m}$ . The Fig. 4.10 waveforms,

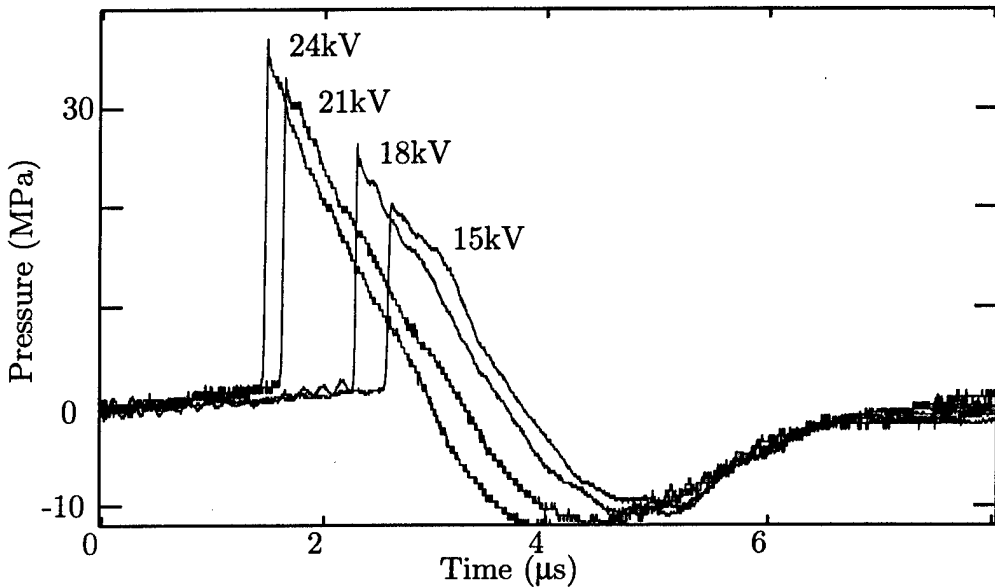


Figure 4.10: Pressure waveforms for four lithotripter-charging potentials.

AS-97-33

adjusted according to Staudenraus and Eisenmenger's results,<sup>48</sup> were used as inputs. The bubble durations and maximum pressure within the bubble increased nearly linearly with charging potential. At the initial collapse and then at the second collapse, a strong spherically diverging pressure spike is radiated from the bubble in the model.

#### 4.2.3 Measured bubble response and charging potential

The single growth and collapse cycle shown in the numerical predictions was measured with the PCD. The PCD detects the pressure spikes emitted in the initial and final collapses. Figure 4.13 shows the PCD results of the kV test. The PCD is discussed in Chapter 3. The PCD measured two strong signals with a varying delay between them. The first signal occurred when the focused lithotripter wave arrived at  $f_2$  and initially squashed existing bubbles. Then a period of silence occurred. During the silence, the bubbles at  $f_2$  grew in response to the lithotripter pulse's negative tail. The second signal resulted when the bubbles collapsed at  $f_2$ . No account for translation of the bubbles is made. The measured bubble durations increase with charging potential.

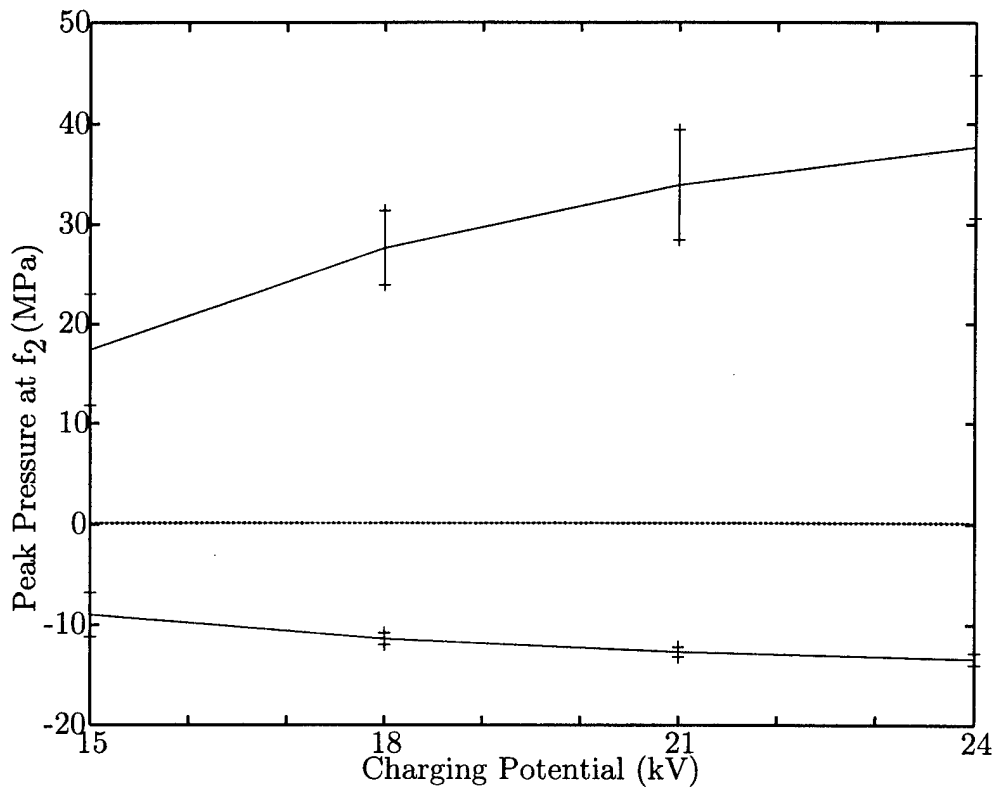


Figure 4.11: Peak positive and negative pressures for four lithotripter-charging potentials.

AS-97-34

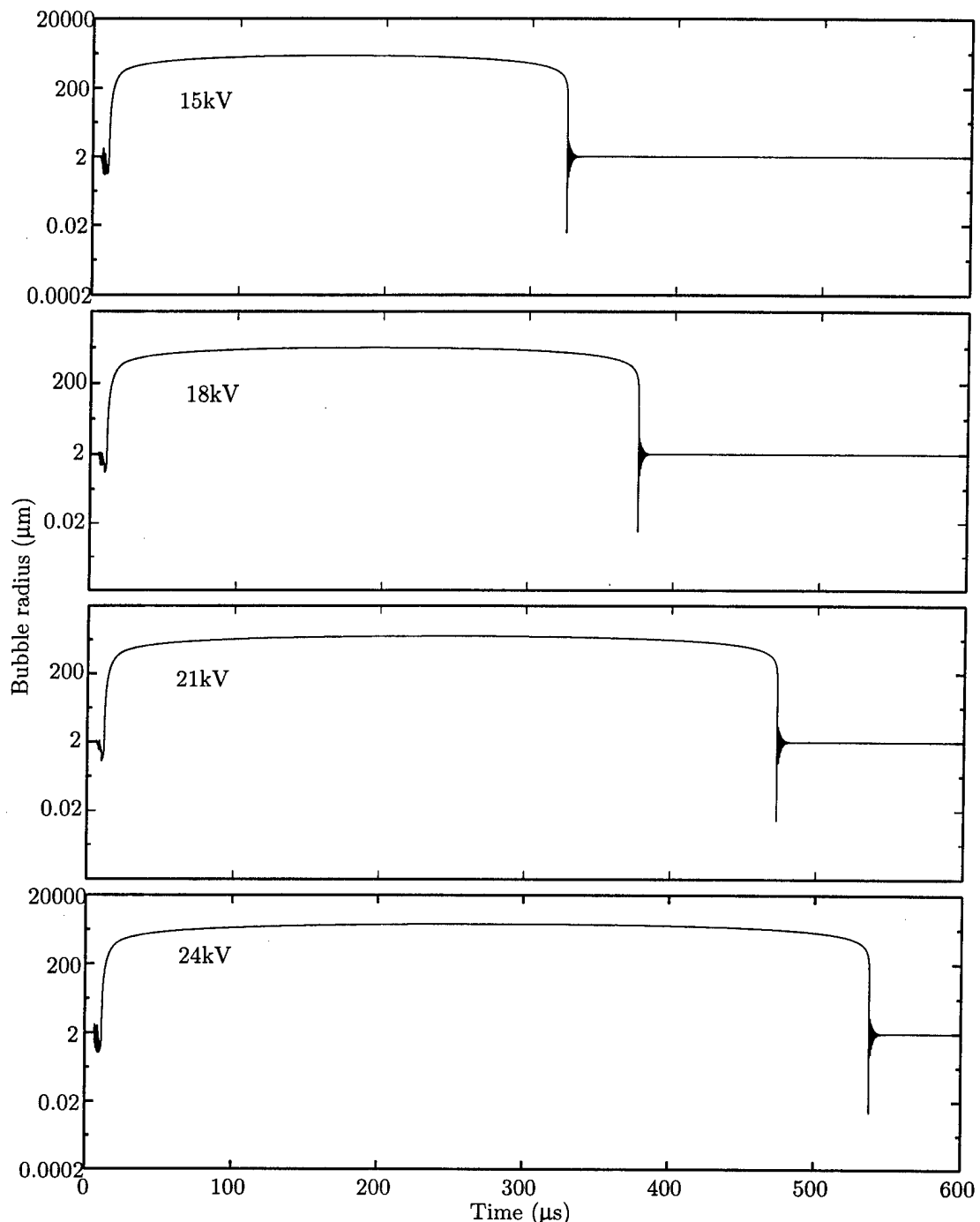


Figure 4.12: R-T curves calculated with Gilmore code for waveforms at four charging potentials.

AS-97-35

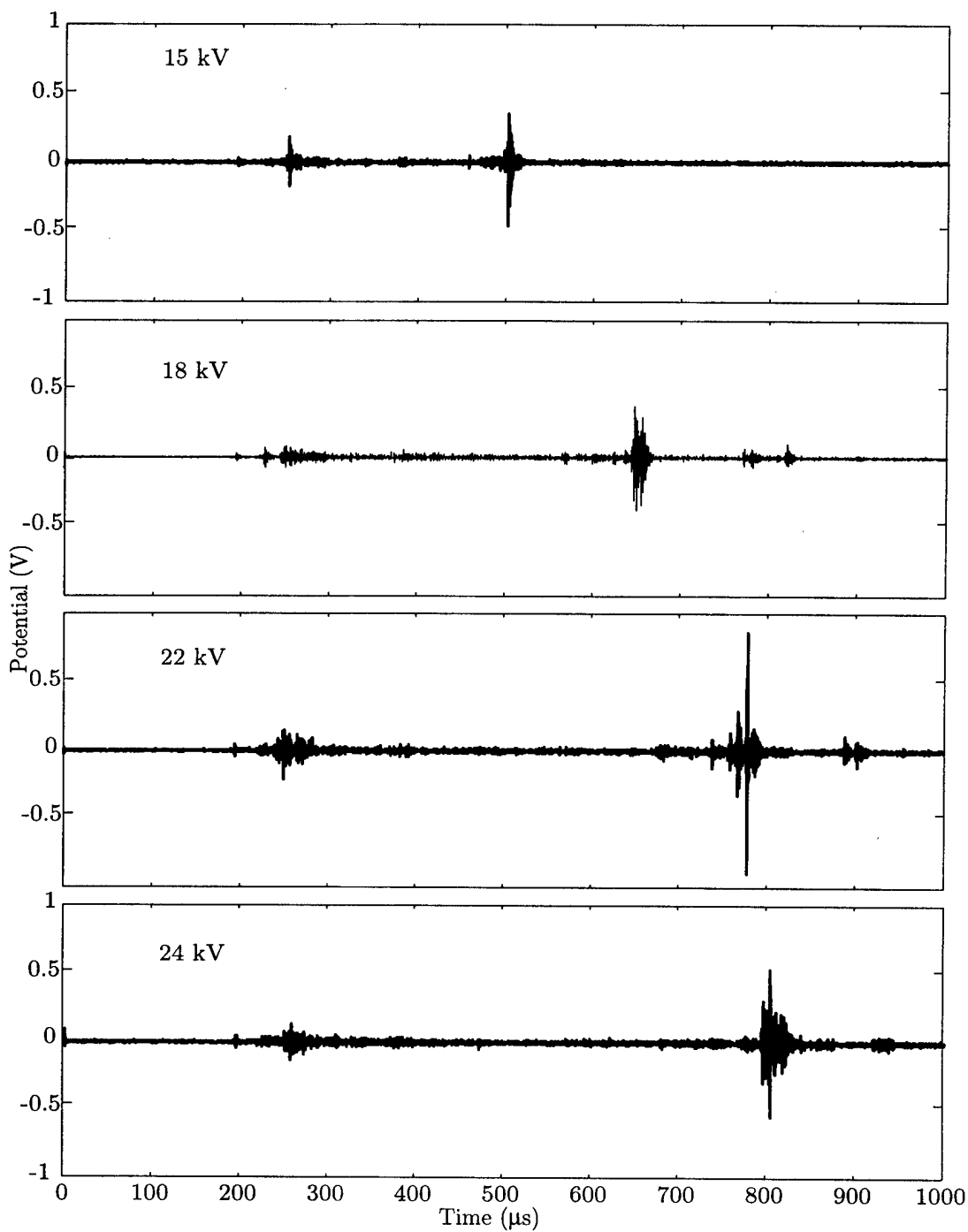


Figure 4.13: Signals measured with the passive cavitation detector (PCD) for four lithotripter-charging potentials.

AS-97-36

#### 4.2.4 Comparison of theory and experiment

Experimental results with the PCD are in excellent agreement with the bubble durations numerically predicted using waveforms corrected on the basis of Staudenraus and Eisenmenger's experimental results.<sup>48</sup> Figure 4.14(a) shows the calculated and measured durations versus charging potential. A line connects the numerically calculated values. Ten measurements at each potential were averaged, and the mean values plotted as circles. Cross-hatched lines demark standard deviation. The dominant error was variation in the pressure amplitude, which has two nearly equal components, spark amplitude and spark location. The PCD measurement was less sensitive than the hydrophone measurement to variation in the location of the spark (and therefore the hot spot) because the sensitive area of the PCD is much larger. The deviation in the PCD is therefore due to spark amplitude and correspondingly is smaller, 10% or about half that of the hydrophone at  $f_2$ . The deviation becomes slightly greater at lower potential because the electric fields driving the discharge are weaker. The standard deviation (not plotted) in the Gilmore code is 20%, created by the 20% standard deviation in the pressure waveforms of Fig. 4.10. Measured and calculated durations agree to within error.

The peak pressure in the bubble was calculated with the Gilmore code and is plotted in Figure 4.14(b). Peak internal pressure occurs at the final collapse (not the initial squeeze) of the bubble. Pressure inside the bubble directly correlates to the amplitude of the pressure pulse radiated into the liquid surrounding the bubble. The calculated internal pressures increased with charging potential. Acoustic driving force, bubble duration, and internal collapse pressure increased with potential (available energy) on the capacitors. The amplitude of the second (collapse) signal also increased with potential.

#### 4.2.5 Simultaneous measurement with the PCD and foil

The PCD and aluminum foil were used simultaneously to detect cavitation as a check on how the presence of the foil altered the bubble field. Aluminum foil was placed at  $f_2$  along the axis of the reflector as described in Chapter 3. Bubble collapse near the foil pits the foil. Whether adding the foil also added bubbles already clinging to

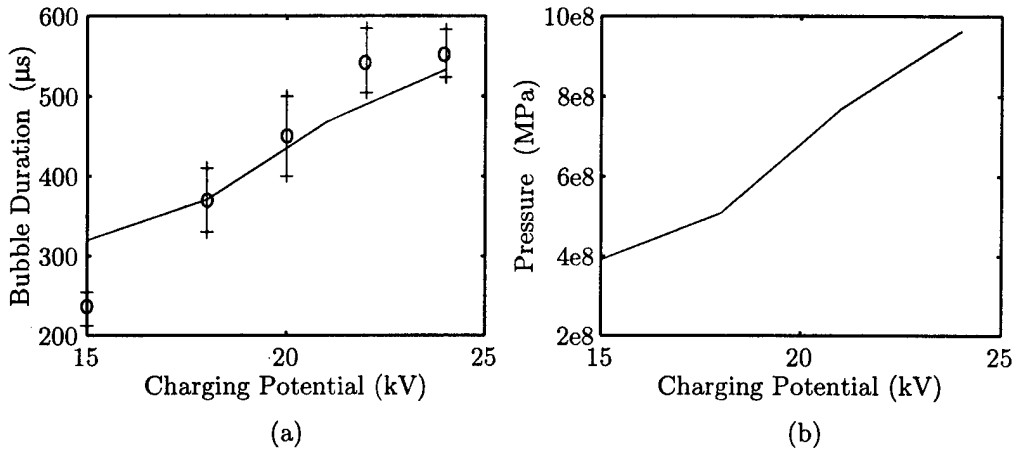


Figure 4.14: Bubble duration (a) calculated with Gilmore code and measured with PCD and bubble internal collapse pressure (b) calculated with Gilmore code.

AS-97-37

the foil was not known. The bubble dynamics are expected to be the same regardless of how the bubbles got there, but to answer whether the cavitation measured with the foil overestimated the amount of cavitation in the free field, the PCD was used to listen to cavitation with and without the foil present. Representative signals and the 10 shot mean and standard deviation of the amplitude and time of silence are plotted in Fig. 4.15. Differences in amplitude are not statistically significant, and bubble durations are nearly identical. The presence of the foil does not appear to alter the cavitation field.

#### 4.2.6 More interpretation of the PCD signal

The PCD signal is discussed in more detail here. Refer to Figs. 4.13 and 4.15. Additional signals, time delays, waveforms, and amplitude information are addressed.

Why does the first big signal appear at  $250\ \mu\text{s}$ ? The PCD trace began when the spark was fired. The travel time of the focused wave to  $f_2$  is  $180\ \mu\text{s}$  (assuming  $c_0 = 1500\ \text{m/s}$ ). The acoustic pulse radiated at  $f_2$  (i.e., emitted from bubble collapse), then took  $70\ \mu\text{s}$  to reach the PCD. Hence in the PCD measurements at the focus, the first big signal occurs at  $180+70=250\ \mu\text{s}$ . In the numerically generated R-T curves, the initial collapse occurs at  $5\ \mu\text{s}$ , as  $175\ \mu\text{s}$  of the propagation are neglected.

What are the smaller signals at  $220$  and  $195\ \mu\text{s}$ ? The smaller signals at  $195$  and

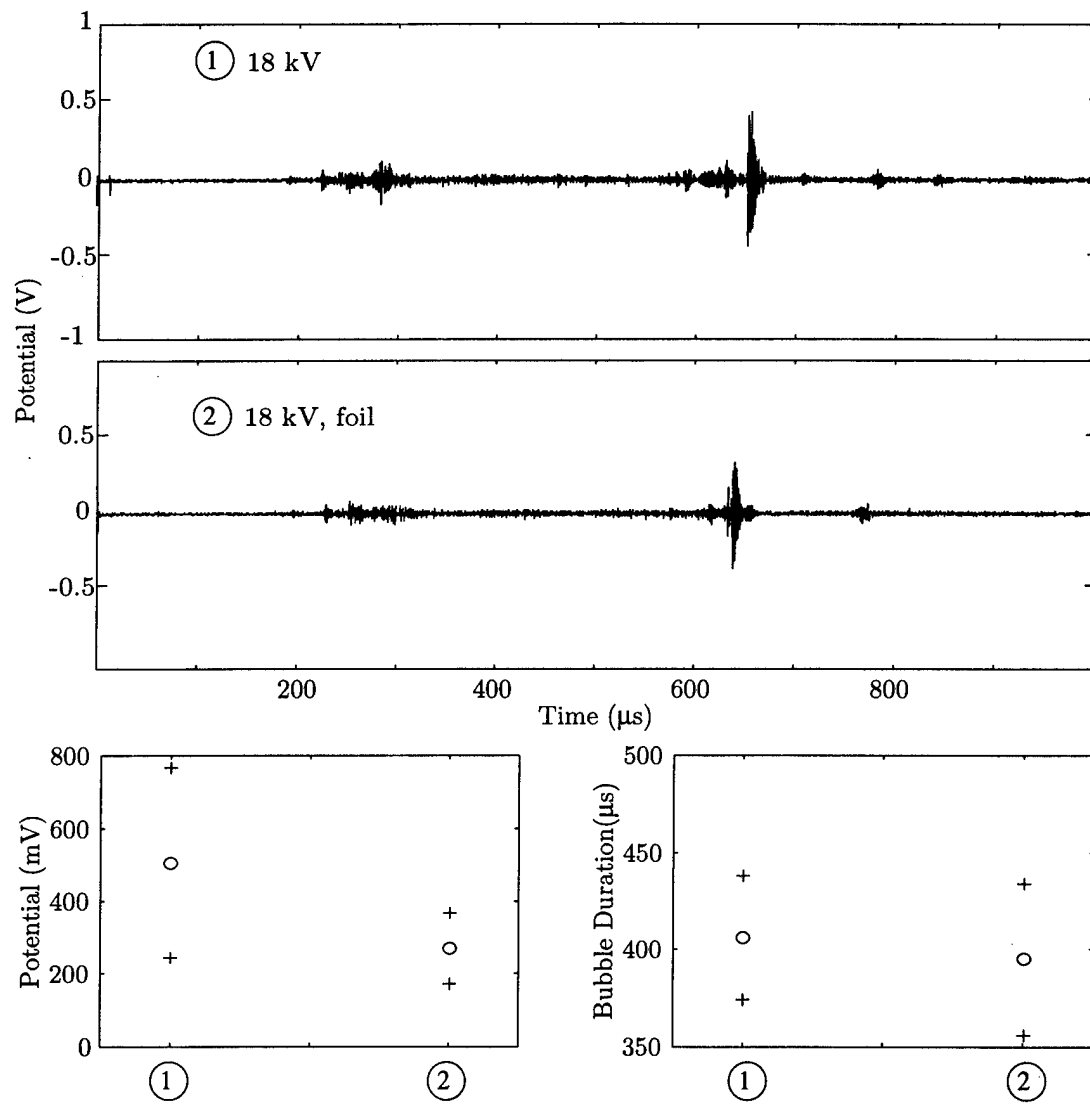


Figure 4.15: PCD signal and statistics with and without aluminum foil at  $f_2$ .

AS-97-38

220 are the result of the direct wave. The direct wave arrived at  $f_2$  after 150  $\mu$ s, 30  $\mu$ s ahead of the focused pulse. The direct wave was weak but nevertheless squeezed the bubbles. Radiation from the bubbles again traveled the 70  $\mu$ s to the PCD. The total delay was 220  $\mu$ s. Signal at 195 corresponds to the direct wave itself striking the PCD at a point where the contact was at nearly normal incidence. Signal did not appear at 130  $\mu$ s when the direct wave hit the near edge of the PCD. Lack of signal may be because of the shallow angle of incidence. The directivity of the PCD was not measured. The reader is also reminded that a high pass filter at 300 kHz cut-on was used to remove the large 15 kHz signal created by excitation of the piezoceramic's first radial mode.

How about the small signal at 380  $\mu$ s? After each signal originating at  $f_2$ , a weaker signal delayed by 130  $\mu$ s was measured; the one at 380  $\mu$ s is the most obvious. The 130- $\mu$ s delayed signals were not cavitation measures but were instead reflected pulses. Signal reflected from the bowl and traveled back to  $f_2$  where the signal bounced off (or was reradiated by) bubbles back to the PCD. The path is 20 cm, which at  $c_0 = 1500$  m/s is 130  $\mu$ s. The reflection from the PCD and ringing in the signal might be improved by replacing the air behind the piezoceramic bowl with a damping material: the trade-off is sensitivity.

Why do the signals look like noise instead of clean waveforms? The waveforms recorded by the PCD do not look like pressure spikes. The waveforms are all 30  $\mu$ s or more of oscillations, ringing. What is actually measured is the impulse response of the transducer not an accurate picture of the waveform. In response to our experimental approximation of an impulse, the PCD output has the shape of 1 MHz oscillations that fall to the 1/e amplitude in 10  $\mu$ s. Off axis, the decay is even slower. The signal at 190  $\mu$ s produced by the direct wave incident on the PCD is very similar in origin and appearance to the impulse response.

The signals originating at bubble collapse are further complicated by the collapse of a number of scattered bubbles. Longer signals are a smear of several collapses. In our work, two signals less than 30  $\mu$ s apart cannot be resolved. Therefore, the number of collapses cannot be counted nor the true waveform amplitude determined. In theory the impulse function can be deconvolved to obtain the true information, but

description of the collapse spikes is beyond the scope of this paper.

Can anything be learned from the amplitude of signals in the figures? The amplitude of the signal is an estimation of the true amplitude, and the PCD was calibrated to our experimental impulse. The final collapse signal is larger than the initial collapse as predicted. And the direct-wave-induced initial collapse is weaker than that by the focused pulse as expected. In addition, pressure amplitudes, calculated with a calibration determined by Sapozhnikov,<sup>16</sup> show good agreement with bubble collapse pressures calculated by Church<sup>5</sup> and measured by Vogel and Lauterborn.<sup>50</sup> Nevertheless caution is urged in the use of amplitude information. One, the ringing in the PCD can cause overestimation of the true amplitude. The overestimate was essentially included in our calibration, but the overestimate is waveform specific. Therefore, the applicability of the calibration to bubble collapses depends on how closely our impulse approximated the collapse signature. Two, we sampled at 5 MHz, which means peaks in one 1-MHz cycle were likely missed. Three, the location of the bubble in the focal region and scattering off other bubbles was not addressed, but bubbles must be present upon which to act. The initial collapse varies in Fig. 4.13 largely because the number of ambient bubbles, upon which the pulse acts, varies. Sequences of shots were fired five seconds (many bubble cycles) apart, but as a general trend, the initial collapse got louder. Subsequent shots seemed to act on bubbles created by previous shots. The creation and growth of bubbles are not addressed here but are factors in the amplitude measured.

### 4.3 Cavitation fields of rigid and pressure-release reflectors

In this section, mappings of the cavitation fields of the rigid and pressure-release reflectors are presented and compared. Pitting on a sheet of aluminum foil served as one map. Bubble collapse was detected, and another map made by moving the focus of the PCD around the lithotripter focal region. High speed video images are also presented. The size of the cavitation field is measured with the PCD, video, and foil and compared to the size of our acoustic field and to the size of cavitation fields measured by others. The foil, and to a limited extent the PCD, are used to measure cavitation intensity, and results are compared to numerical calculations.

#### 4.3.1 Measured cavitation field of a rigid reflector

The cavitation field of the rigid reflector is a long thin stripe. Bubble durations are the longest and the collapse the strongest along the axis where the acoustic driving force is strongest. Collapse off axis occurs but is often too weak to measure with our methods of detection.

Several measurements of the narrowness of the rigid-reflector cavitation field are shown in Fig. 4.16. The dimensions are full scale. An image of aluminum foil stretched over a thin C-shaped frame is located at  $f_2$  in the figure. Pitting can be seen in a streak along the reflector axis through the length of the foil. The width of the streak is 1-2 mm. One shot was recorded.

Superimposed below the foil in Fig. 4.16 is a frame of a high speed video and a 3 times enlargement of the image. The frame is upside down for easier visual comparison to the foil:  $f_2$  is at the very top and sound is coming from the bottom. The camera recorded bubbles growing and collapsing in a streak in front of  $f_2$ . Shown is a frame 667  $\mu$ s after spark discharge. The bubbles are near final collapse. The width of the streak is 1-2 mm.

Above the foil in Fig. 4.16 is the PCD amplitude plotted versus transverse position. The focus of the PCD was moved across  $f_2$  in steps of 2.5 mm. Signals similar to those in Fig. 4.13 were recorded at each location. The time of silence was  $355 \pm 45 \mu$ s for all positions, but the amplitude of the second signal quickly decayed off axis. The amplitude of the second signal is plotted here. Each position has the average of 10 shots. Error bars are shown and arise from spark jitter, randomness in the distribution of bubbles, and sampling rate. Error in the signal amplitude is discussed in more detail in Sec. 4.2.6. The -6 dB width is 5 mm, which is broader than with the other measures.

The PCD data are an average of many shots. Each shot may have a 1-2 mm stripe. However, because of spark jitter, the stripes do not lie right on top of one another. Their lateral locations vary by  $\pm 1.5$  mm. The average is, therefore, a broader stripe.

In addition to averaging, the transfer function of the PCD acts to broaden the measured cavitation field. The top plot in Fig. 4.16 is the transfer function of the PCD. The width of the function 2 mm is the narrowest beam resolvable with the PCD. The PCD data in (b) with or even without consideration of the broadening due

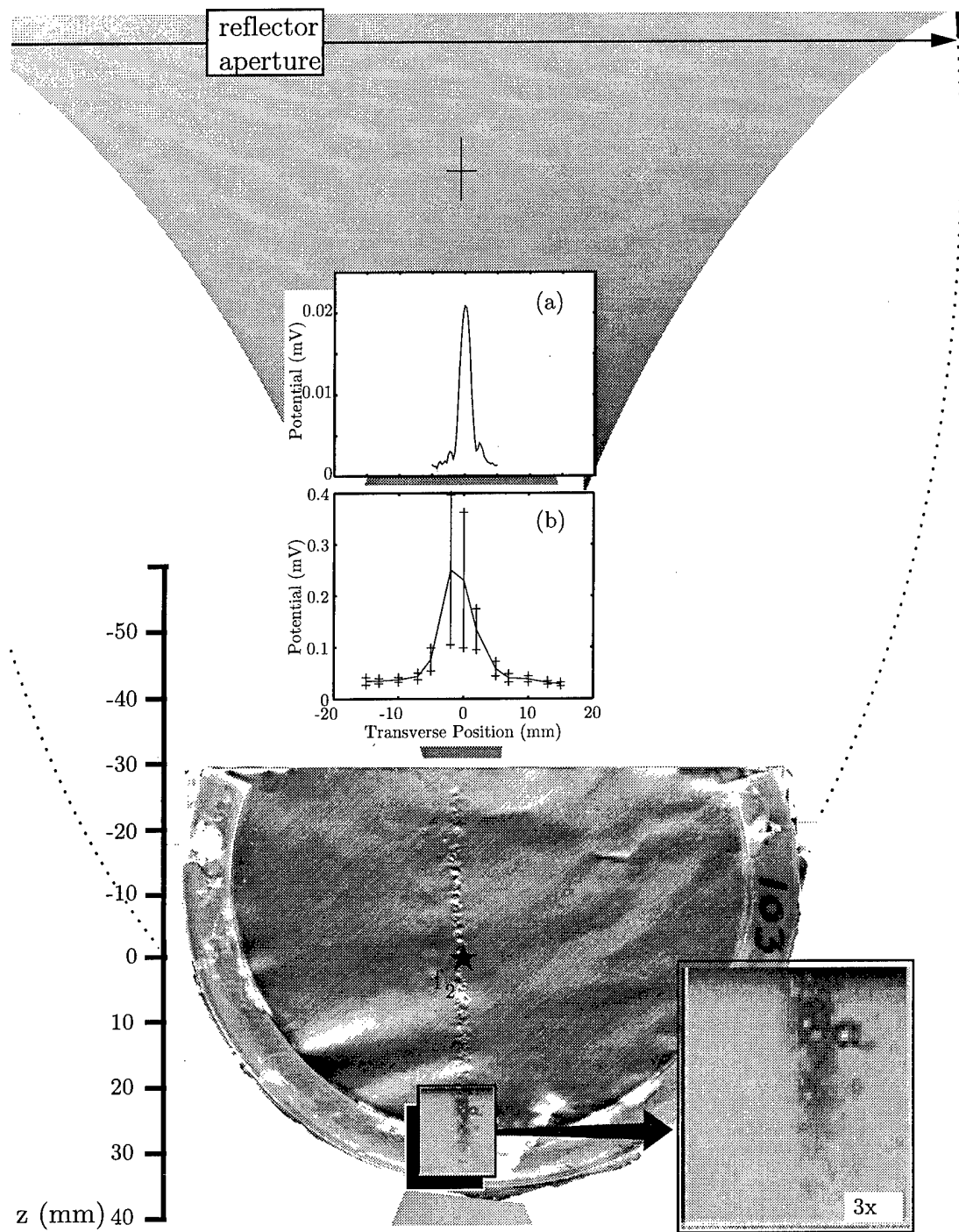


Figure 4.16: Transverse cavitation field of rigid reflector measured with PCD, aluminum foil, and high speed video camera. Dimensions are actual size. The top plot is the transfer function of the PCD. Video images were borrowed from Church et al.<sup>67</sup>

to averaging are close to the transfer function (a). The thinnest beam measurable with the PCD is 2 mm, and with averaging 5 mm was measured. With these considerations, the PCD plot is in good agreement with the foil and video results.

The rigid-reflector cavitation field that we have detected was 1-2 mm narrow but 80-90 mm long as seen in Fig. 4.17. In the middle, PCD time of silence versus axial position is plotted. The longest durations are at  $f_2$  where the hydrophone measured the largest negative pressures. On top, five PCD measurements at  $f_2$  are plotted. The collapse signal and time of silence are very pronounced. The deviation between shots is also noticeable.

Three foils, one shot each, were used to map the axial field. A foil was placed in front of  $f_2$ , a spark fired, and the foil removed. Then a foil was placed so that  $f_2$  was in the middle of the foil, pitting from one shot recorded, and the foil removed. The third foil was placed behind  $f_2$ , and the procedure repeated. Shown in Fig. 4.17 are the three foils on top of one another and in their axial positions. No pitting was recorded from  $z=-60$  to  $-40$  mm. The pit steak begins about 40 mm in front of  $f_2$ . The streak is very narrow and well defined until about 30 mm postfocal where pitting becomes weaker and the steak diverges. After  $z=+50$  mm, no pitting is observed.

#### 4.3.2 Interpretation of the cavitation field of a rigid reflector

Why do Figs. 4.2 and 4.16 make it appear that the cavitation field is much narrower than the acoustic field? For one, it has already been pointed out that the waveform, not just peak negative pressure, drives the bubbles and that both waveform and peak negative pressure measurements off axis encompass distortions created by the hydrophone. In addition, it has been noted that the acoustic measurements are averages and that, because the hot spot varies from shot to shot, plots made by averaging over many shots are broader than direct measurement of field width made for any single shot. Nevertheless, here it is argued that the cavitation field is as broad as the acoustic field, but the detection schemes are too insensitive to pick up weaker off-axis collapses.

A path of bubbles nearly as broad as the -6 dB width of acoustic field is seen in the second in a sequence of four high speed video frames (see Fig. 4.18). Church *et al.*<sup>67</sup> filmed the video. Cavitation was at the focus of a Dornier HM3 clinical lithotripter.

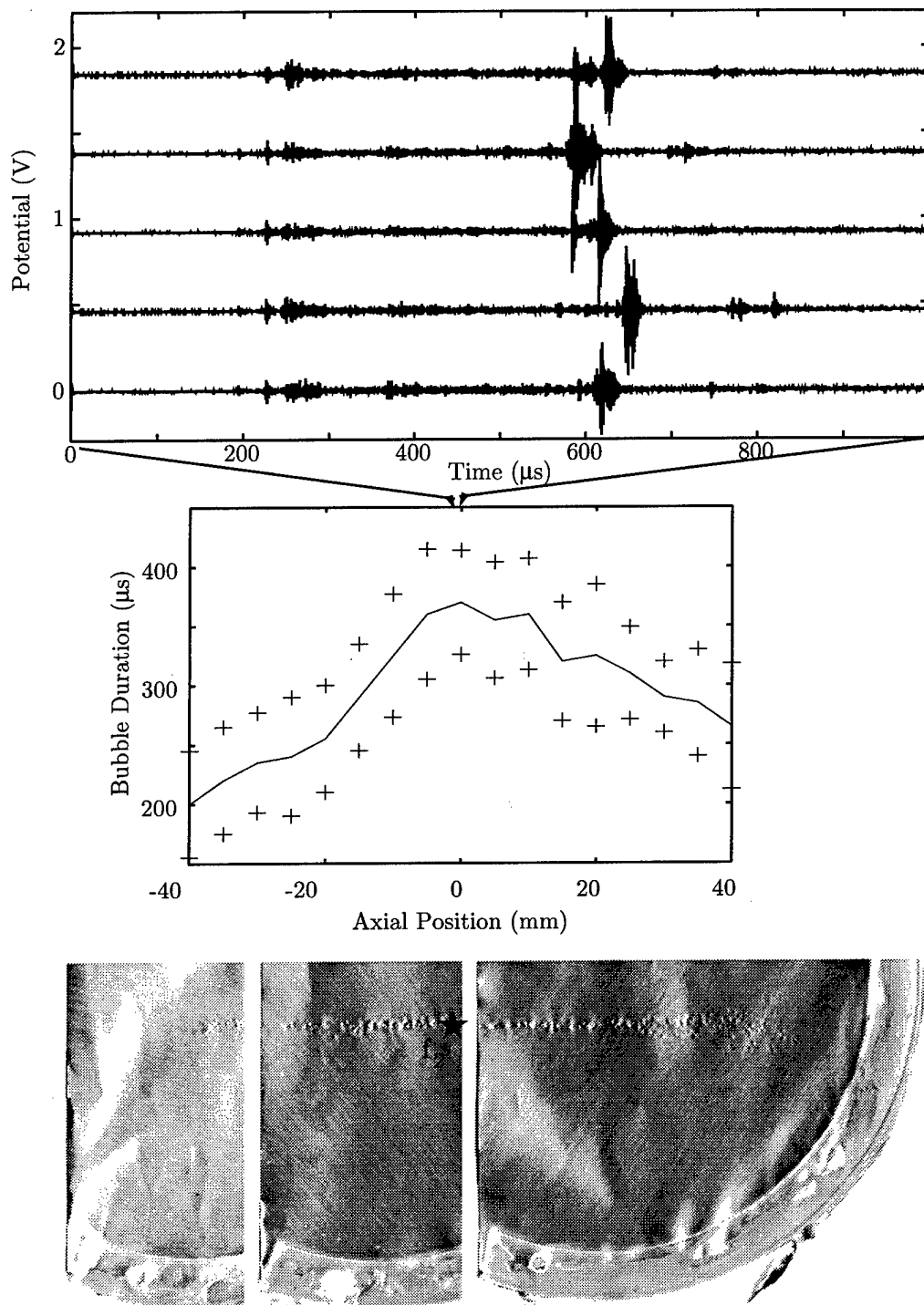


Figure 4.17: Axial cavitation field of rigid reflector measured with PCD and aluminum foil. Dimensions are actual size.

AS-97-40

The charging potential was 18 kV. The camera was focused such that  $f_2$  was at the base of each frame. In the reference of Fig. 4.18, the lithotripter bowl was off the top of the page. The sequence caught a 1-ms time history of the bubble cloud. The spark discharge occurred at  $t=0$ , and light reflecting off tiny bubbles or plaster particles (from model stones) floating in the water can be seen in Fig. 4.18(a). The focused acoustic wave took 180  $\mu$ s to reach  $f_2$  and arrived between Fig. 4.18(a) and Fig. 4.18(b). At  $t=333 \mu$ s, the streak of bubbles was nearly 1 cm wide, and bubbles were growing. Individual bubbles were on the order of 0.5 mm in diameter. The bubbles at the center of the cloud were driven hardest by the strongest acoustic wave, the wave on axis. The bubbles off axis collapsed between Fig. 4.18(b) and Fig. 4.18(c). In Fig. 4.18(c), which is the frame taken 667  $\mu$ s after the spark discharge (and nearly 400  $\mu$ s after the acoustic pulse reached  $f_2$ ), a thin axial stripe of bubbles remains. Individual bubbles are smaller, which indicates they were collapsing. At 1 ms, the bubbles had collapsed. A small cloud of debris flecked from the plaster stone at the base of the images can be seen. In the actual video, distinction in appearance between the debris and the bubbles is clearer. The cycle on axis was about 400  $\mu$ s. The duration is in excellent agreement with the PCD measurements and Gilmore code predictions for the experimental lithotripter. Off-axis bubbles were excited more weakly than on-axis bubbles and collapsed sooner.

Our data agree with other profiles of bubble duration. Jöchle *et al.*<sup>68</sup> presented a time sequence of stroboscopic photographs similar to the video sequence in Fig. 4.18. Bubbles and cloud width grew large and then shrunk down to a line on axis. They also observed that bubbles lost their spherical shape and formed microjets in the final stages of collapse. Coleman *et al.*<sup>15</sup> using passive cavitation detection, found that the off-axis bubbles collapsed earlier than did on-axis bubbles.

The foil is a nonlinear or threshold measure; only the strong collapses on the axis damaged our foils. However, Coleman *et al.*<sup>12</sup> measured a broader swath of pits on foil. The main difference was the number of shots fired per foil. Coleman *et al.* fired on the order of 100 shots; we fired one. Fig. 4.19 shows a thin stripe after one shot and a broader stripe after ten shots fired at 1 Hz. Spark jitter, responsible for variation in the location of the focal hot spot, plays a major role in broadening the

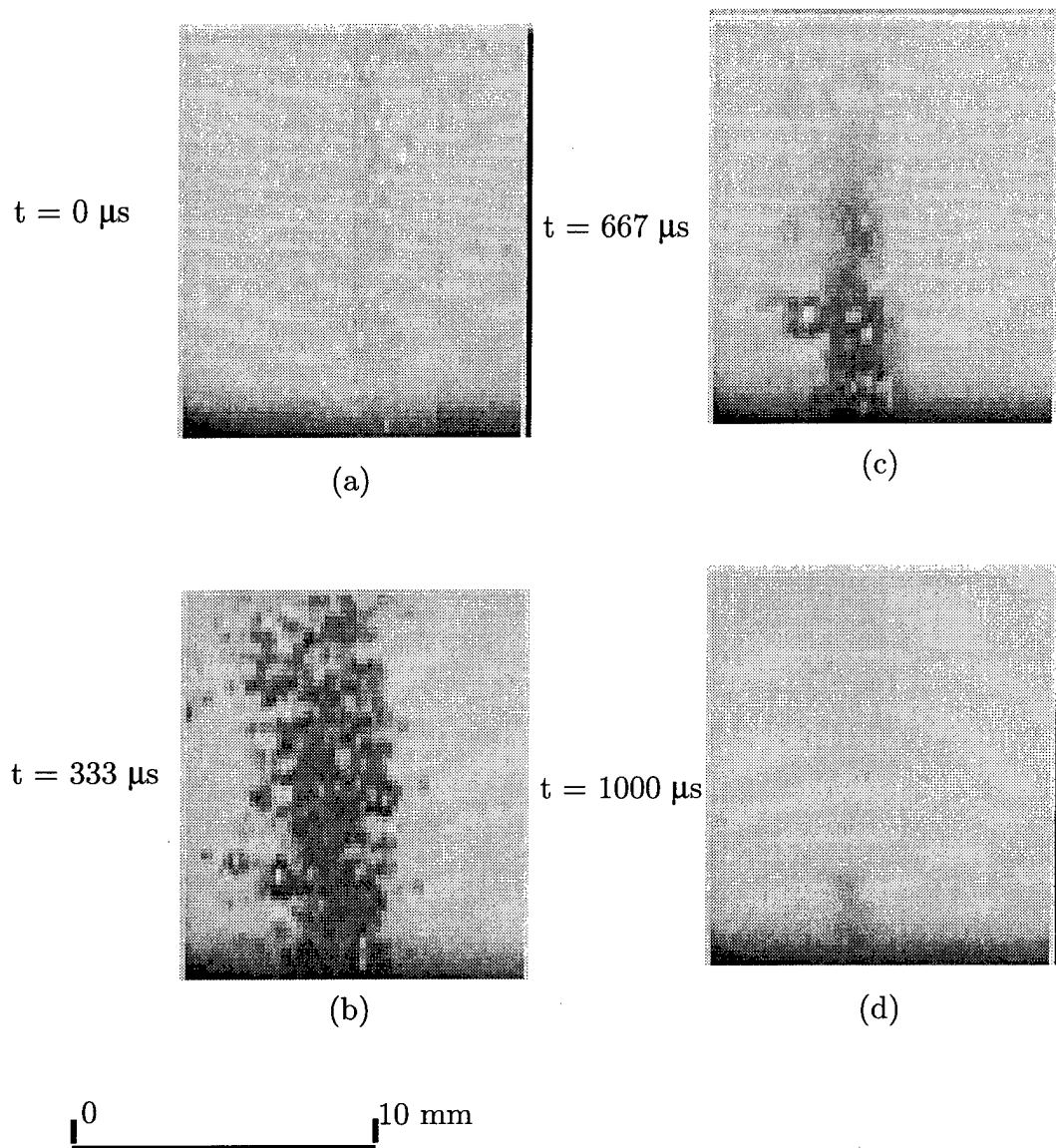


Figure 4.18: A sequence of four video frames taken at 3000 frames/second: (a) lithotripter spark discharge occurs, and a few ambient bubbles or dirt reflect the flash, (b) broad streak of broad bubbles  $150 \mu\text{s}$  after the arrival of the acoustic pulse, (c) off-axis bubbles have collapsed; thin stripe on axis still collapsing, and (d) no bubbles appear after collapse. Video images were borrowed from Church *et al.*<sup>67</sup>

path. In addition, previous shots create bubbles that are acted on by the next shot. The second difference between Coleman *et al.*'s data and ours is that Coleman *et al.* placed their foil perpendicular to the field; we placed the foil along the field. With the perpendicular arrangement, bubbles convected by radiation pressure collect on the foil, and in both the Dornier HM3 and experimental lithotripter reflectors, the perpendicular foils collected bubbles rising because of buoyancy.

#### 4.3.3 Measured cavitation field of a pressure-release reflector

The cavitation field of the pressure-release reflector was mapped and is, here, compared to the cavitation field of a rigid reflector. Differences in the extent of the cavitation are less dramatic than differences in the intensity of the cavitation. Measured and computed relative intensities are in agreement.

The cavitation fields of the pressure-release and rigid reflectors differ more than the acoustic waveforms. Figure 4.20(a) shows a waveform measured at the focus of the pressure-release reflector. The waveform has a positive phase comparable to that produced by the rigid reflector, but a substantial negative phase precedes before the positive spike. The numerically predicted R-T curve of a bubble subjected to the waveform is show in (b). Arrows indicate the change in time scales between plots. The bubble duration was only 5  $\mu$ s. The positive spike crushes the growing bubble almost immediately. The collapse pressure is an order of magnitude smaller than predicted for a bubble subjected to the rigid-reflector waveform. The negative phase that follows the positive spike creates a bounce in the model bubble, and a second growth and collapse occurs. However, internal pressure in second collapse is another order of magnitude smaller. The pressure-release-reflector waveform inherently stifles cavitation.

Data measured with the PCD support the predicted lifetime of the bubble. PCD recordings are shown in Fig. 4.20(c): ten shots are shown to demonstrate the repeatability. As indicated by the arrows, the entire predicted bubble response in Fig. 4.20(b) fits within the length of the noise signal in (c). Unlike the rigid-reflector case, no signal was measured (or predicted) after hundreds of microseconds.

There is no indication in the PCD measurements of the third collapse shown in Fig. 4.20(b). Three possible explanations are proposed. One, the third collapse was

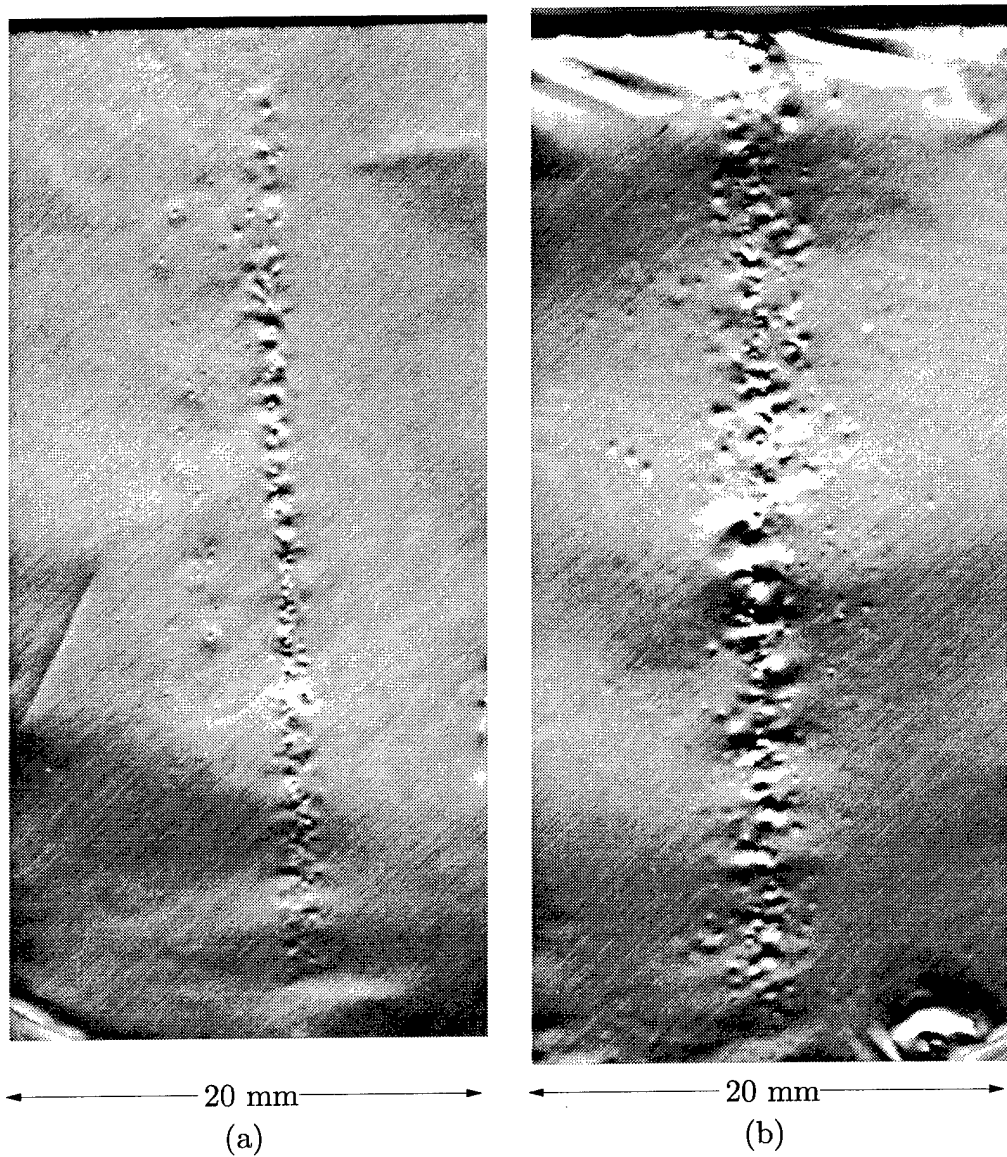


Figure 4.19: A comparison of foil pitting after (a) one spark and (b) ten sparks in a rigid reflector. Note the broadening of the pit path, which results from creating bubbles with successive shots and variation in position of the focus between successive sparks (magnified 2.5 times).

AS-97-42

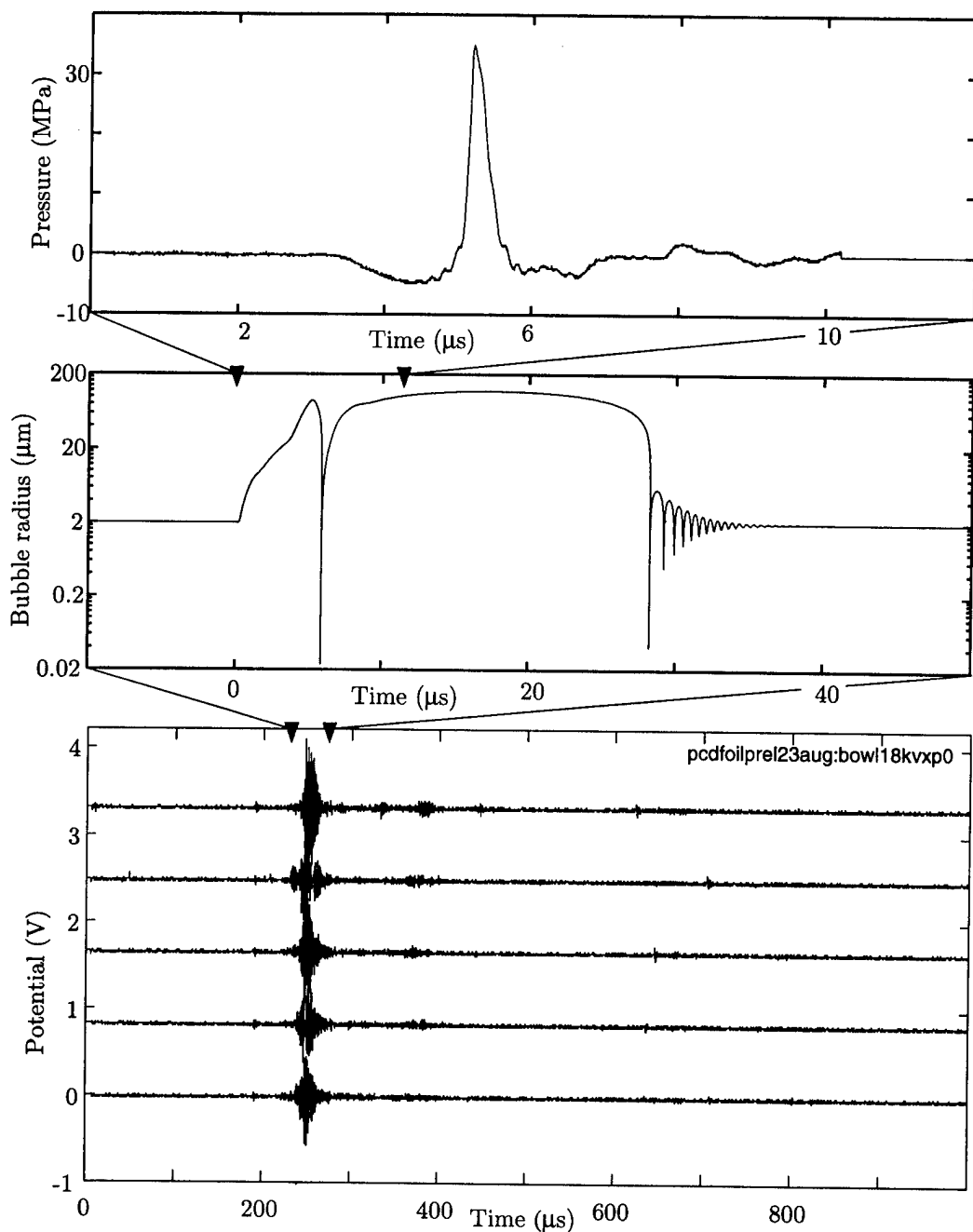


Figure 4.20: From top to bottom: waveform measured at  $f_2$  of a pressure-release reflector, bubble R-T curve predicted with Gilmore code, and shock waves radiated by bubble collapse and recorded by the PCD, which was focused at  $f_2$ . Arrows show the relative time scales of each plot. Note no collapse, delayed by hundreds of microseconds, is either measured or predicted with the pressure-release reflector.

AS-97-43

predicted to be weaker and might not have been detected. Two, perhaps we cannot resolve the third collapse in the ringing response of the PCD to the second collapse. With a deconvolution routine or a damped hydrophone, the ringing could be removed, and the resolution made. Three, the prediction of a bounce, or second growth cycle, may be erroneous because it is assumed in the model that the bubble stays spherical and intact at all times. Jöchle *et al.*,<sup>68</sup> who used a rigid reflector, showed with photographs that the bubbles remain spherical through much of the cycle. However the bubbles become asymmetric and form microjets in the final stage of collapse. Bubbles even break up into smaller bubbles. Our model therefore differs significantly from the experimental situation after the first collapse cycle. Other experimental evidence later in this chapter also suggests that bounce does not occur.

The measured and computed bubble duration produced by the pressure-release reflector is shorter than that produced by the rigid reflector, and as shown next, the measured and predicted collapse intensity is less. Parallelism between duration and intensity is again observed; although caution is warranted in using duration as a measure of collapse pressure with the pressure-release reflector. Collapse pressure, induced by the waveform in Fig. 4.20(a), can increase without increased bubble duration. Simply increasing the positive portion collapses the bubble at least as quickly but more violently.

Pitting on aluminum foil, however, remains a measure of collapse intensity. Figure 4.21 compares pitting by ten sparks in a rigid reflector to ten sparks in a pressure-release reflector. A single spark in a pressure-release reflector is too weak to be seen on the foil or recorded from the foil with the digital scanner. The foil placed in front of the pressure-release reflector has smaller, shallower pits. Smaller pits correspond to numerically calculated, smaller collapse pressures.

An extended map of the cavitation field of the pressure-release reflector is presented in Fig. 4.22. Foil images are magnified two times. The reflector focus  $f_2$  is at  $z=0$  on the scale in the figure. The left foil was placed prefocal, treated with ten shots, and removed. Then the right foil was centered at  $f_2$  and treated with ten shots. Image (b) is placed slightly to the side to show most of (a). The field is hourglass shaped. The pit path is several centimeters wide prefocally. The path shrinks to a couple millimeters at

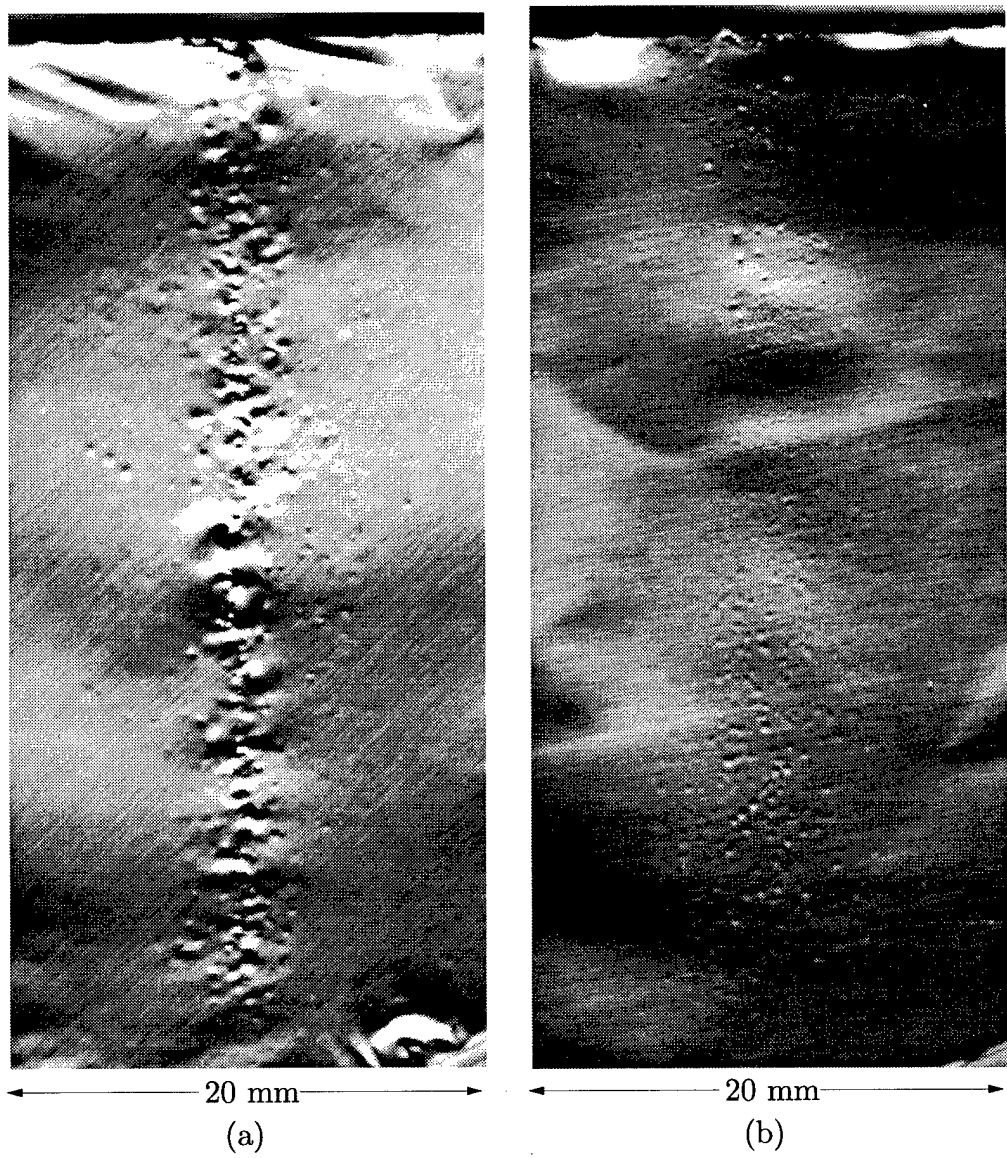


Figure 4.21: Comparison of pitting by ten sparks in a (a) rigid reflector and (b) pressure-release reflector (magnified 2.5 times).

AS-97-44

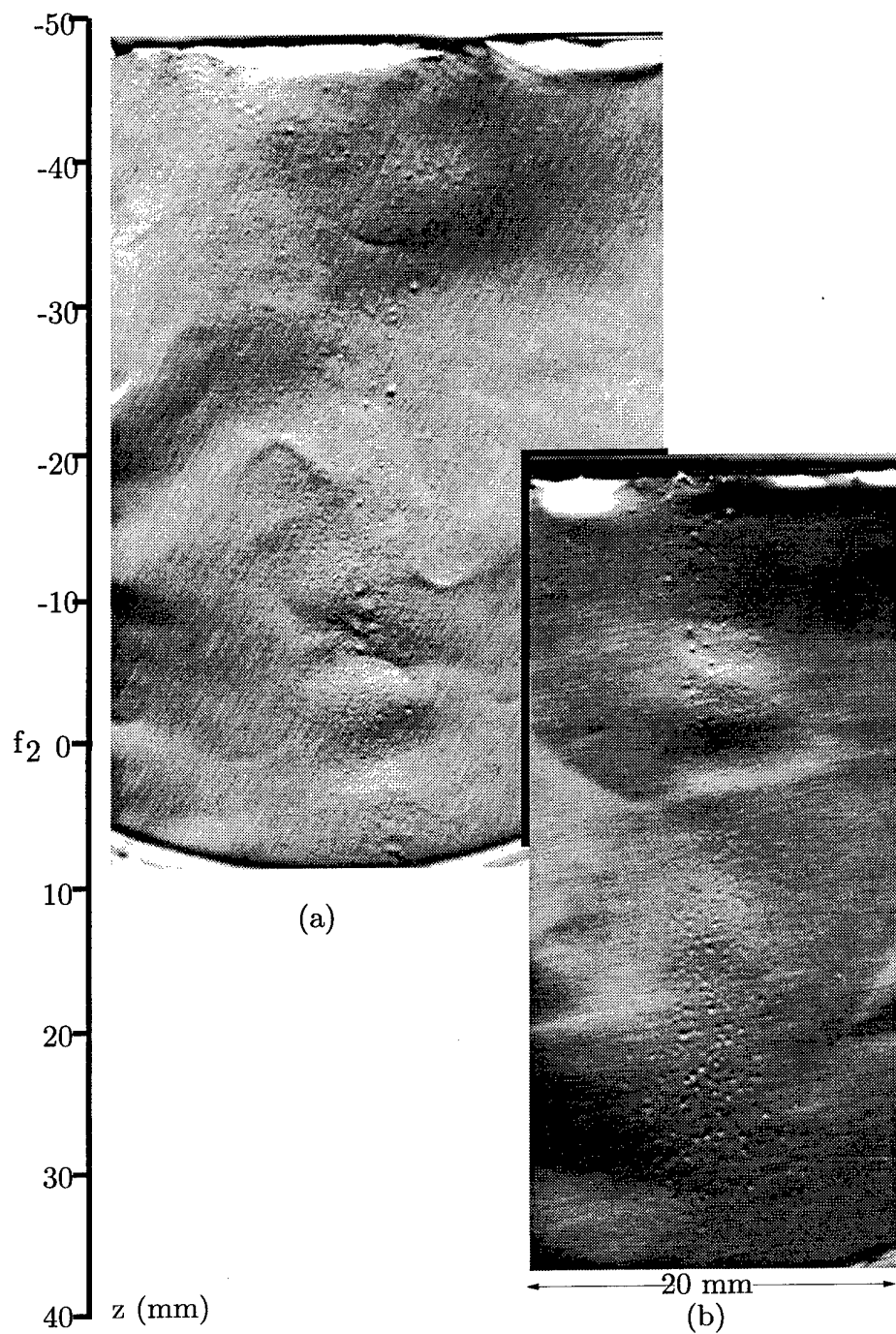


Figure 4.22: Map of pitting by ten sparks produced by a pressure-release reflector (magnified 2 times). Pit path is hourglass shaped.

AS-97-45

the focus and widens again postfocally. The path is much broader than the thin stripe of the rigid reflector, although the path and the stripe have nearly the same length.

The size and density of the pits change along the axis of the pressure-release reflector but not noticeably along the axis of the rigid reflector. Prefocally, small pits are sparse. Tiny pits in a small dense cluster occur at  $f_2$ . Postfocally, the pits are larger and sparse. The acoustic waveforms along the axis of the pressure-release reflector also changed, whereas the waveform of the rigid reflector are more constant (see Sec. 4.1). The waveforms of the two reflectors are most similar postfocally where the positive phase precedes the negative phase for both reflectors. Postfocally, the pits also share the closest resemblance and have large size and rounded shape.

Using Schlieren photography, Müller<sup>3</sup> observed cavitation collapse as a collection of spherically diverging shock waves 5-10  $\mu\text{s}$  after the shock wave from a pressure-release reflector. His interpretation was that the pressure-release reflector produced more cavitation, since the collection of spherically diverging shock waves was not measured behind the shock wave from a rigid reflector. Müller's observation is a measurement of the quick collapse of cavitation bubbles with the pressure-release reflector. The observation supports predictions and measurements presented here. We propose that Schlieren photographs taken hundreds of microseconds after the passage of the reflection from a rigid ellipsoid would have shown cavitation collapse as a collection of spherically diverging shock waves.

A sequence of Schlieren photographs, we propose, could, therefore, be used as a cavitation detection method. Time of collapse and location and number of collapses could be measured. Relative or even absolute collapse pressures could theoretically be determined. Schlieren photography, however, is beyond the scope of this paper.

#### 4.4 Quantification of surface pitting by single reflectors and dual reflector confocal arrangements

In this section, quantified measures of cavitation-induced pits are presented for single reflectors and for two reflectors that focus at the same point. Data were taken in Austin with the experimental configuration described in Chapter 3 and shown in Fig. 4.23. The angle formed by the axes of the two reflectors is 110°. Angles 90° and 180° (i.e.,

the reflectors face each other) are considered later in this chapter. Regardless of the angle, we refer to the arrangement where the reflectors focus at the same spot as confocal reflectors.

First, single spark results are presented, then dual spark results. Each foil shows only a single shot or a single sequence of two shots. It is shown that pit depth can be increased or decreased by swapping a single rigid reflector for a single pressure-release reflector or by applying an appropriately timed sequence of pulses produced by a confocal reflector pair. In addition, good correlation is found between statistical measures of the digitally imaged foil and actual pit size measured with a profilometer.

#### 4.4.1 Pit depth with pressure-release and rigid reflectors

In this section, the size of aluminum foil pits produced by either a single rigid reflector or a single pressure-release reflector is presented. The results for the pressure-release reflector are presented first. Then the results for the rigid reflector are presented.

##### Pit depth with a pressure-release reflector

Figure 4.24 contains a quantified comparison of (A) unpitted foil to (B) pits produced with a pressure-release reflector. Foil image, profilometer measurement, and greyscale histogram of the image are shown for both pitted an unpitted regions.

The foil pitted with the pressure-release reflector is shown at three times magnification in Fig. 4.24. The pits are so shallow and small that the digital scanner picked up only a section of the pit path extending down from the arrow at the top of the foil. The big arrow above the foil image marks the reflector axis and the direction of wave propagation.

The profilometer results are on the lower left of Fig. 4.24. The lower line is a 1-cm long recording across an unpitted section (A) of the foil. The stripe is a baseline value. Some small gradual variations in height exist. The upper line, offset arbitrarily by 40  $\mu\text{m}$  to separate it from the unpitted data, is a profilometer pass across the center pitted region (B) of the foil. The pits were 5  $\mu\text{m}$  in depth and 0.2 mm in diameter. Pits are densely packed, and the region is broad. The pits are near the threshold of

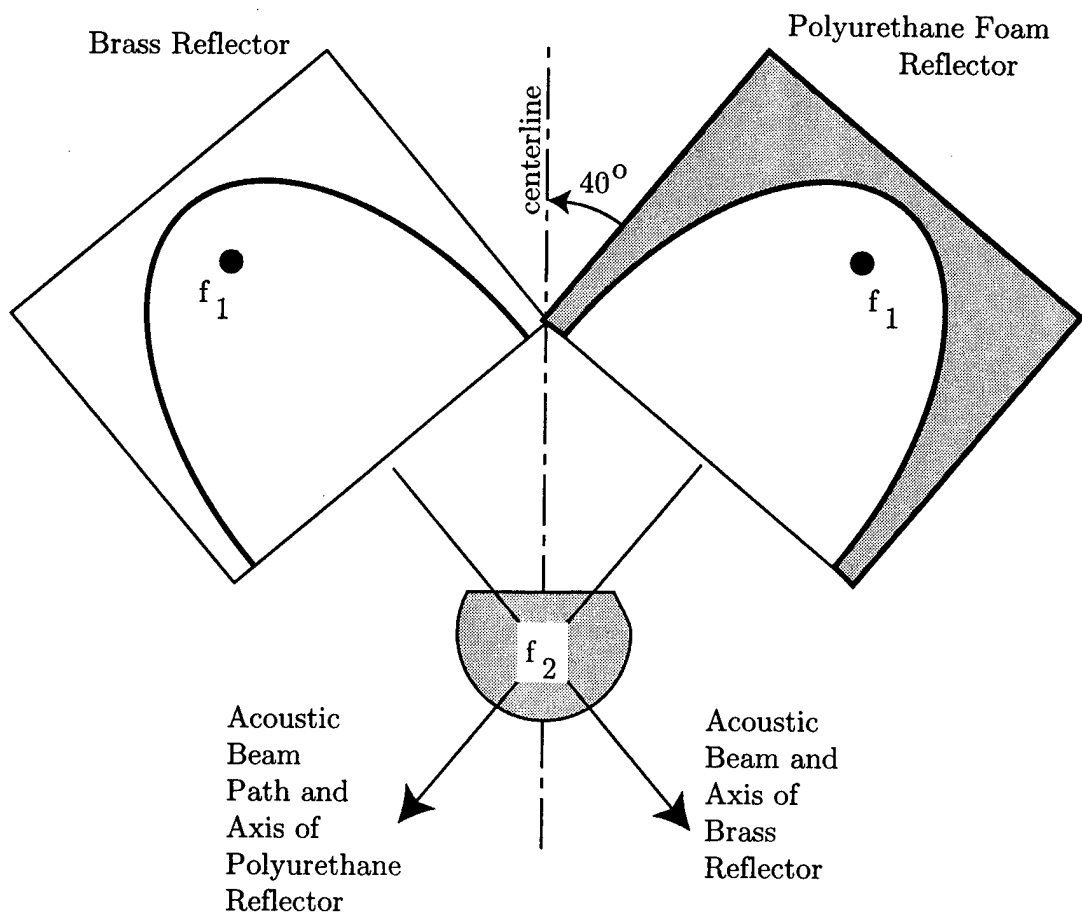


Figure 4.23: Worm's eye view of the Austin two spark configuration. Both reflectors were angled so they shared the same  $f_2$ . Each foil was placed at  $f_2$  along the axes of the reflectors. Pressure release on the right in some experiments was replaced with a rigid reflector.

AS-97-46

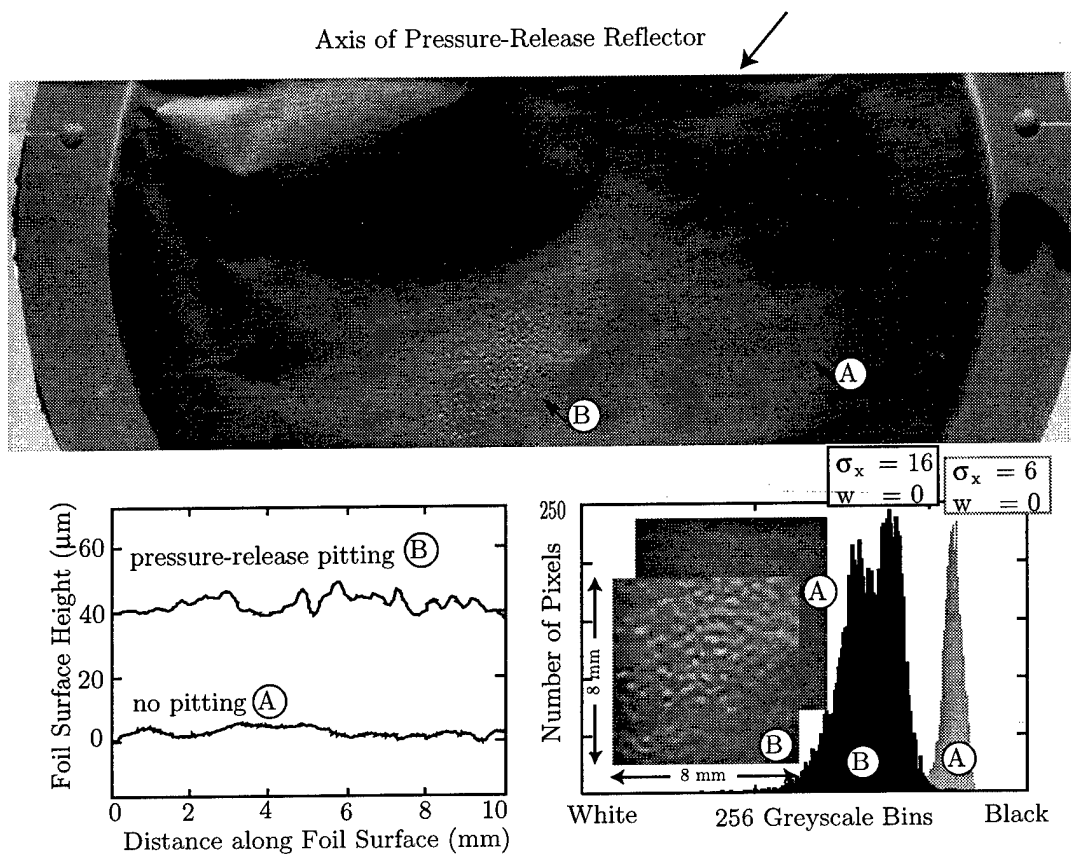


Figure 4.24: Foil pitted with pressure-release reflector, profilometer comparison of pitted and unpitted section of foil, and histogram pixel color distribution as indirect measure of pitting.

AS-97-47

what we can see, what the profilometer can detect, and what the digital scanner can image.

In the lower right of Fig. 4.24 are enlargements of images of 8 mm square sections of foil. The profilometer data shown were taken through the center of each square. The pitted section overlaps the unpitted section to save space. The pitted section can be distinguished with the eye from the unpitted section.

Statistical measures of the digitized images of the square sections also appear in the lower right of Fig. 4.24. Plotted are two separate but overlapping histograms, one corresponding to each of the overlapping imaged sections of foil. Each pixel (300 per inch) in the imaged section is a single shade of grey out of 256 shades, for which zero is white and 255 is black. The histogram contains the tally of how many pixels of each shade appear. We hypothesized that for a very flat surface, the scanner light is reflected evenly and that all the pixels have nearly the same color. The standard deviation  $\sigma_x$  of the histogram is a measure of the uniformity of the color distribution and thus, Lifshitz *et al.*<sup>13</sup> proposed, an indirect measure of the pitting. The white pixels we speculate are places where the foil was very close to the scanner and produced the strongest reflection. Number of white pixels  $w$  might therefore be an indirect measure of deep pits. Lifshitz *et al.*<sup>13</sup> proposed the application of the statistical measurement. However, results presented here are the first test of the accuracy of the measures.

The grey histogram of the flat section of foil has  $\sigma_x = 6$  and  $w = 0$ . It has a tight distribution as hypothesized. The black histogram is for the pitted section and has a broader distribution  $\sigma_x = 16$  but no pits that appear as white pixels. Fairly tight distribution and no white pixels by our argument (and Lifshitz *et al.*'s<sup>13</sup>) indicate shallow pits. Shallow pits are the result measured with the profilometer and apparent to the eye.

### Pit depth with a rigid reflector

Here, size of pits produced with the rigid reflector are presented and compared to the size of pits produced with the pressure-release reflector. The rigid reflector produced deeper, larger pits. Profilometer and statistical measures are presented for the pits produced with the rigid reflector.

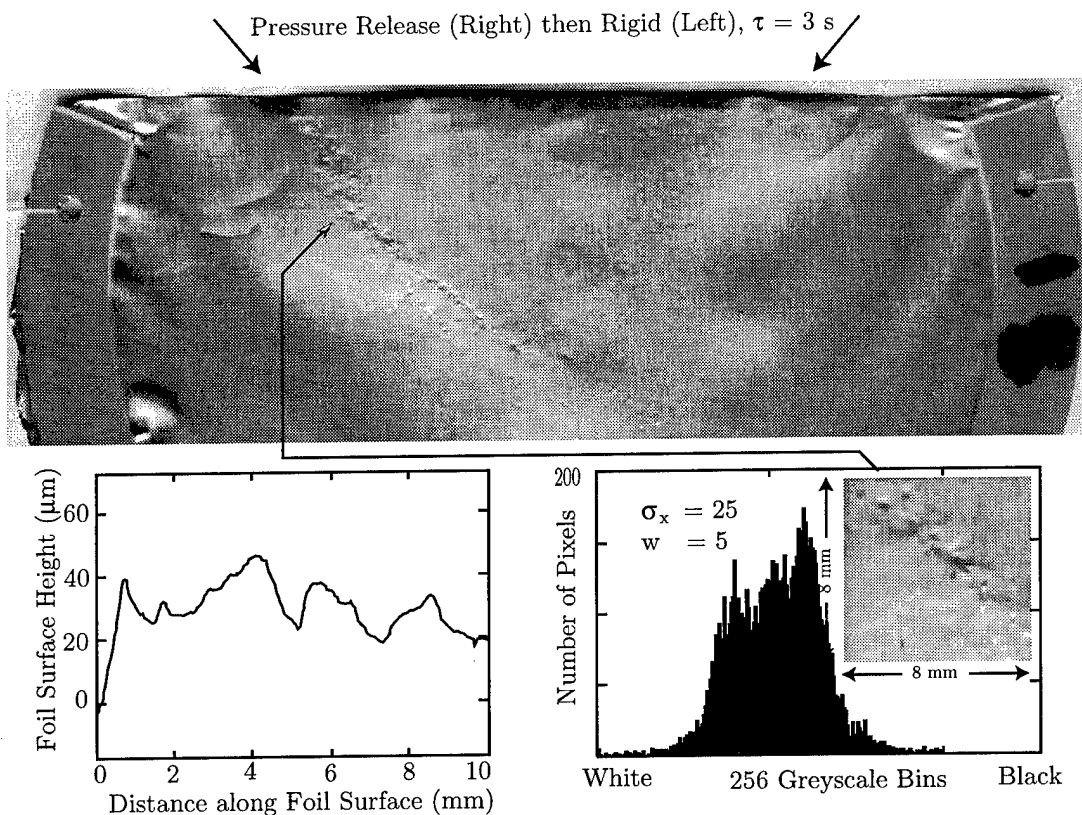


Figure 4.25: Foil pitted with rigid reflector. Profilometer measurement shows deeper larger pits with the rigid reflector than with the pressure-release reflector (see previous figure), and histogram has a higher standard deviation. **AS-97-48**

The long thin pit path is prominent along the rigid-reflector axis from top left to bottom middle of the foil in Fig. 4.25. A small arrow indicates the region where profilometer and statistical measures were made. The profilometer plot on the lower left shows that pits were  $15\text{--}20 \mu\text{m}$  deep and  $2 \text{ mm}$  wide. The depth was three to four times deeper, and the diameter was an order of magnitude larger than corresponding dimensions of pits produced by the pressure-release reflector.

The greyscale histogram in the lower right corner of Fig. 4.25 shows a higher standard deviation,  $\sigma_x = 25$ , and five white pixels. The trends in the histogram, higher  $\sigma_x$  and more white pixels, track the increased pit size measured with the profilometer and distinguished with the eye.

The foil in Fig. 4.25 actually shows two pit stripes, one on the rigid-reflector axis and the other on the pressure-release reflector axis. The prominence of the path produced by the rigid reflector and the near imperceptibility of the path produced by the pressure-release reflector underscores the difference in pit depth. In addition, the foil shows two overlapping but noninteracting pit paths. The spark in the pressure-release reflector was fired, bubbles grew, collapsed, and pitted the foil along the axis of the pressure-release reflector. Then 3 s later, which corresponds to 100,000 bubble cycles (i.e., a long time later in this reference frame), the spark in the rigid reflector was fired. Bubbles grew, collapsed, and pitted the foil along the rigid-reflector axis. No bubbles were kicked or stifled. The foil provides a reference for the foils in the next section, which contains results in which bubbles were kicked and stifled.

#### **4.4.2 Confocal pair consisting of a pressure-release reflector and a rigid reflector**

In this section, numerical and experimental results of the confocal arrangement of a pressure-release reflector and a rigid reflector are presented. The spark in the pressure-release reflector and the spark in the rigid reflector were fired with a variable delay between them. The results are similar to, but less spectacular than, the results of two rigid reflectors presented in the next section. The lack of spectacle stems from the shorter bubble period of the pressure-release reflector. The short period is responsible for the weaker pitting by the pressure release and simply gives the experimenter a narrower window in which to apply the second pulse.

It should be stated that the original idea was to create a strong negative pressure and more cavitation with the pressure-release reflector and then add the auxiliary positive pulse of the rigid reflector. However, the positive tail was discovered in the pressure-release-reflector waveform. The tail meant the pressure-release reflector by itself could be used as in the previous section to demonstrate stifling. In this section, the pressure-release reflector was used in conjunction with a rigid reflector to demonstrate kicking as well as stifling.

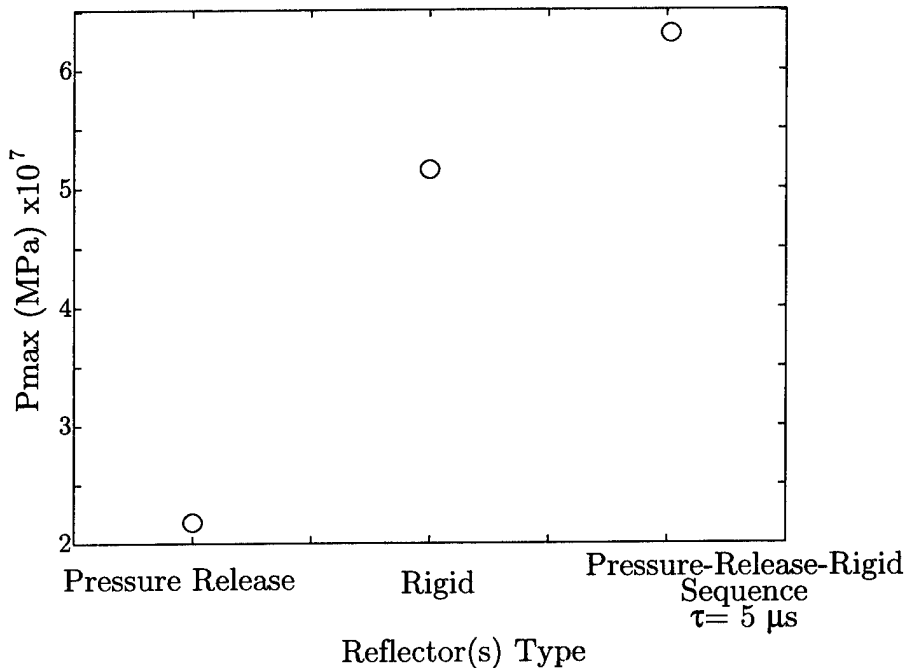


Figure 4.26: Comparison of numerically calculated maximum pressure within the bubble. The pressure-release reflector produced a lower pressure than did the rigid reflector. However, a confocal pair of a rigid reflector and a pressure-release reflector in which the pulse from the rigid reflector was delayed by  $5 \mu\text{s}$  yielded the highest pressure. The result illustrates kicking because the delayed pulse increased the collapse pressure.

AS-97-49

### Numerical results

Numerical prediction of the maximum pressure within the bubble is presented here for three cases: 1) a spark in a pressure-release reflector, 2) a spark in a rigid reflector, and 3) a spark in a pressure-release reflector and a spark delayed by  $\sim 5 \mu\text{s}$  in a rigid reflector that is confocal to the pressure-release reflector. Figure 4.26 shows the result. The two pulse sequence produced higher pressures than either reflector used singly.

The Gilmore code was run with waveforms measured at  $f_2$  of the pressure-release and rigid reflectors. The numerically calculated maximum pressure in the bubble

is  $5.12 \times 10^7$  MPa for the rigid reflector and  $2.14 \times 10^7$  MPa for the pressure-release reflector. Larger pressures were obtained with waveforms measured beyond the focus of the rigid reflector. The correction based on the Staudenraus and Eisenmenger's work<sup>48</sup> was not used because they did not measure a pressure release wave. The waveforms we measured are compared straight up. The factor of  $\sim 2.5$  difference in internal gas pressure is in good agreement with the factor of three- to four-times difference in measured pit depth.

The two-pulse sequence was constructed by adding the digitized waveform created by the pressure-release reflector to the digitized waveform measured with the rigid reflector. The delay was obtained by adding the appropriate number of zeros on the front of the rigid-reflector waveform. At 5  $\mu$ s delay, the highest internal pressure was calculated. The delay corresponded to an arrival of the second pulse as the bubble was collapsing. Prediction of a higher pressure  $6.41 \times 10^7$  MPa, which is three times higher than the internal pressure created with the pressure-release reflector alone, is an example of kicking.

As shown in Fig. 4.20, the predicted bubble period for a bubble excited with the pressure-release reflector is 5  $\mu$ s. The Austin waves are about three-fifths the strength, but the predicted bubble duration with the pressure-release reflector is the same, because still the positive tail forces the bubble to collapse. The bubble duration with the rigid reflector is, however, one-third that in Sec. 4.2, in part because of the weaker wave and in part because the correction based on the Staudenraus and Eisenmenger's results<sup>48</sup> was not implemented. Collapse pressures are also lower.

The radius-time (R-T) curve for the sequence does not differ significantly from that of the pressure-release-reflector waveform alone. The rebound cycle is longer. The change in minimum radius between the R-T curve for the sequence and the R-T curve for the single pulse produced by the pressure-release reflector is imperceptibly smaller on the plots, so the sequence curve is not included. Pressure in the gas, which is presented in Fig. 4.26 and increases threefold with the addition of the second pulse, is more interesting and relevant than the radius.

Radius-time curves for both the sequence and the pressure-release reflector show a second growth and collapse cycle—a rebound. Evidence that the spherical bubble

model breaks down at the collapse has been presented, and the unlikelihood that the bubble survives to rebounded stated (see Sec. 4.3). Plotted in Fig. 4.26 is the pressure maximum for the first cycle.

With a delay of  $-2 \mu\text{s}$ , meaning the rigid reflector was fired first, the lowest maximum pressure of the first cycle is calculated. The value is  $0.11 \times 10^7 \text{ MPa}$  which is more than an order of magnitude smaller than with the pressure-release reflector alone. Reduced pressure is due to stifling. Delays from  $2 \mu\text{s}$  to less than  $-2 \mu\text{s}$  produced stifling.

### Experimental measurement of intensified cavitation

In this section, profilometer and statistical measures of surface pitting are presented for a pulse sequence designed to intensify cavitation. The spark in the pressure-release reflector was fired first, and the spark in the rigid reflector was fired approximately  $5 \mu\text{s}$  later. Results are compared to pitting by each reflector used singly and to a sequence with a longer delay between sparks.

Figure 4.25 shows a foil in which the pulse produced by the rigid reflector followed well after the pulse produced by the pressure-release reflector. No interaction occurred. The two stripes crossed and overlapped.

Figures 4.27-4.29 show foils in which the wave from the rigid reflector arrived as the bubble excited by the pressure-release reflector collapsed. Interpulse delay was measured with the NTR needle hydrophone 2 mm above  $f_2$  where  $f_2$  was on the foil. The foils show an interaction region in the center of the foil around  $f_2$ .

In Fig. 4.27, the pulses arrived at  $f_2$ ,  $5 \mu\text{s}$  apart. The additional pitting caused by kicking the bubble excited by the pressure-release reflector occurred at  $f_2$  and along the centerline between the reflector axes.

In Fig. 4.28, the delay between pulses was  $8 \mu\text{s}$  at the centerline, but because of the geometry, the delay was  $5 \mu\text{s}$ , 3 mm to the left of the centerline. To the left, the pulse produced by the pressure-release reflector has traveled farther than the pulse produced by the rigid reflector. Therefore, the head start of the pulse produced by pressure-release reflector is diminished, in this case from  $8 \mu\text{s}$  to  $5 \mu\text{s}$ . It was 3 mm to the left of  $f_2$  that the intensified pitting occurred. Pits are larger than observed

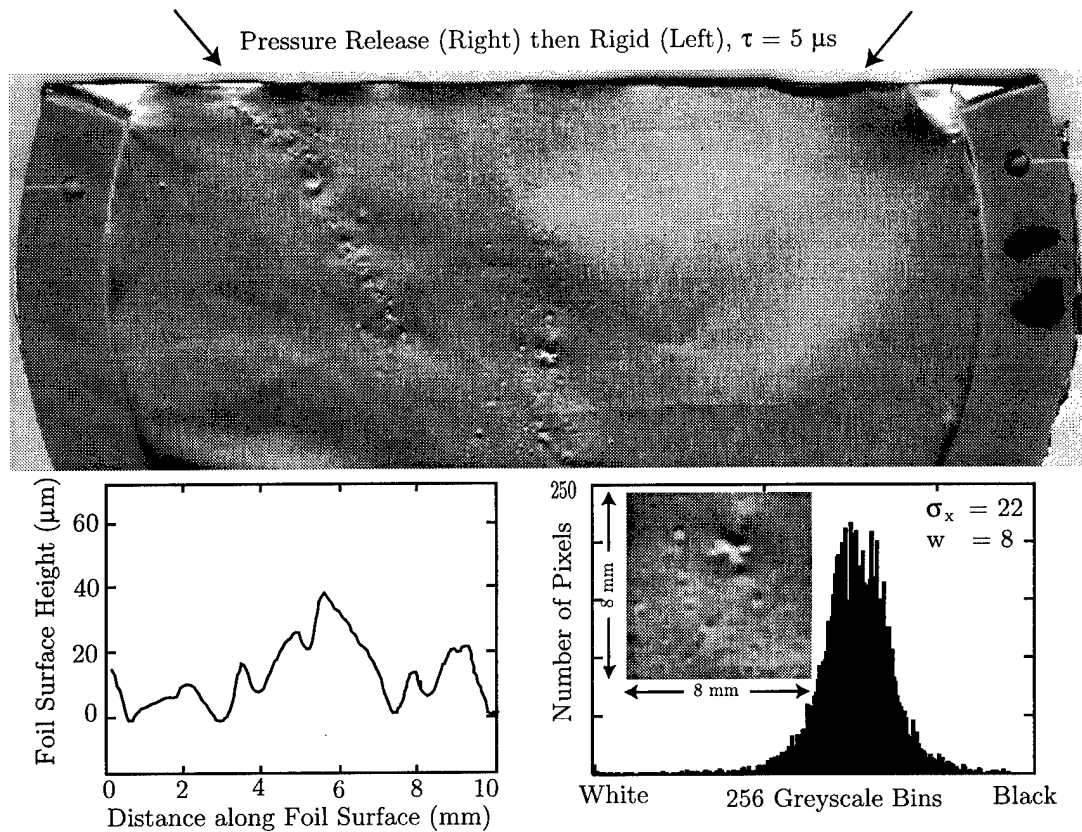


Figure 4.27: Pitting produced by a spark in pressure-release reflector and a spark delayed by  $5 \mu s$  in the rigid reflector. Pitting is seen in the center of the foil at  $f_2$  and along the centerline between the reflectors. The pits are deep and large. **AS-97-50**

with either the rigid reflector or pressure-release reflector alone. Standard deviation and number of white pixels also increased.

In Fig. 4.30, lines of constant interpulse delay are superimposed on the foil to help visualization of the spatial map of interpulse delays. Interpulse delay is defined here as the time between the arrival of the pulse produced by the pressure-release reflector and the arrival of the pulse produced by the rigid reflector. A negative delay corresponds to the wave from the rigid reflector arriving first. Although a single pair of sparks is fired with just one delay, each foil maps a range of interpulse delays. Pulses arrive at the centerline with an interpulse delay equal to the delay between the sparks. Interspark delay in Fig. 4.30 was  $5 \mu s$ . To the right the interpulse delay is greater

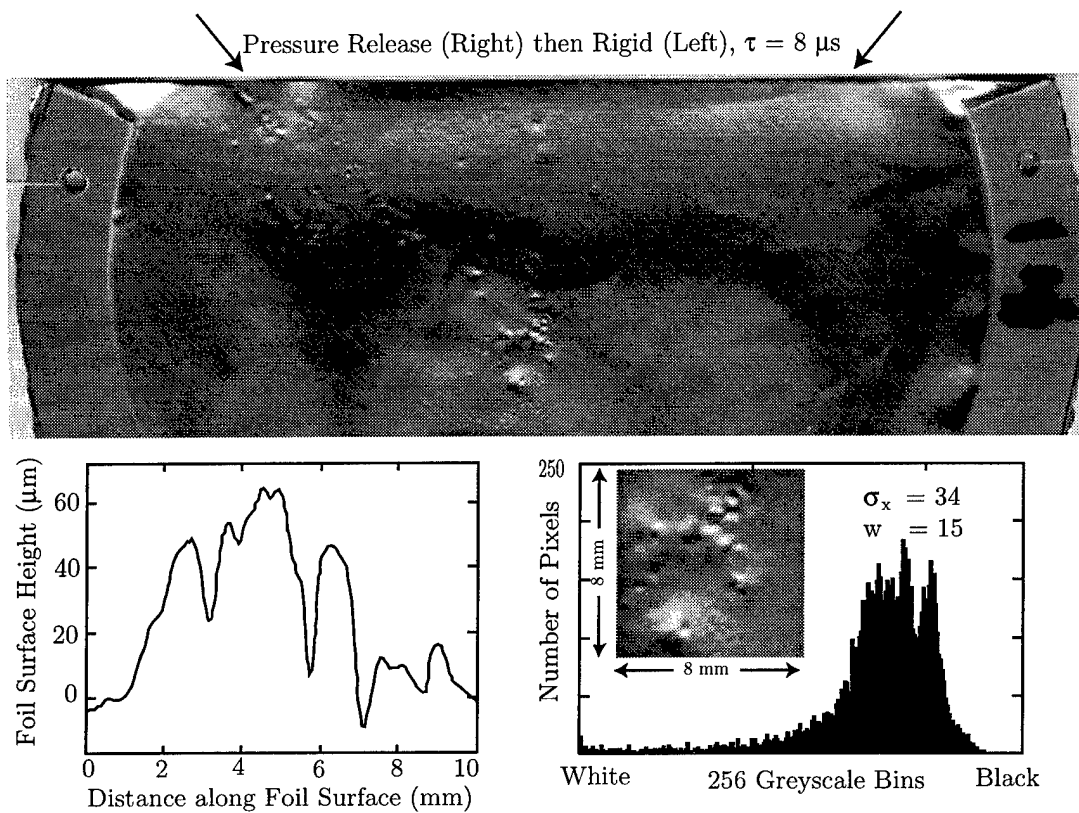


Figure 4.28: Pitting produced by spark in pressure-release reflector and a spark delayed by  $8 \mu\text{s}$  in the rigid reflector. Pitting is seen in the center of the foil at  $f_2$  and along the centerline between the reflectors. Results are similar to those of Fig. 4.27, but the pitting has moved up and to the left. Foils in both figures show additional deep pitting created by the pressure-release-then-rigid-reflector sequence.

AS-97-51

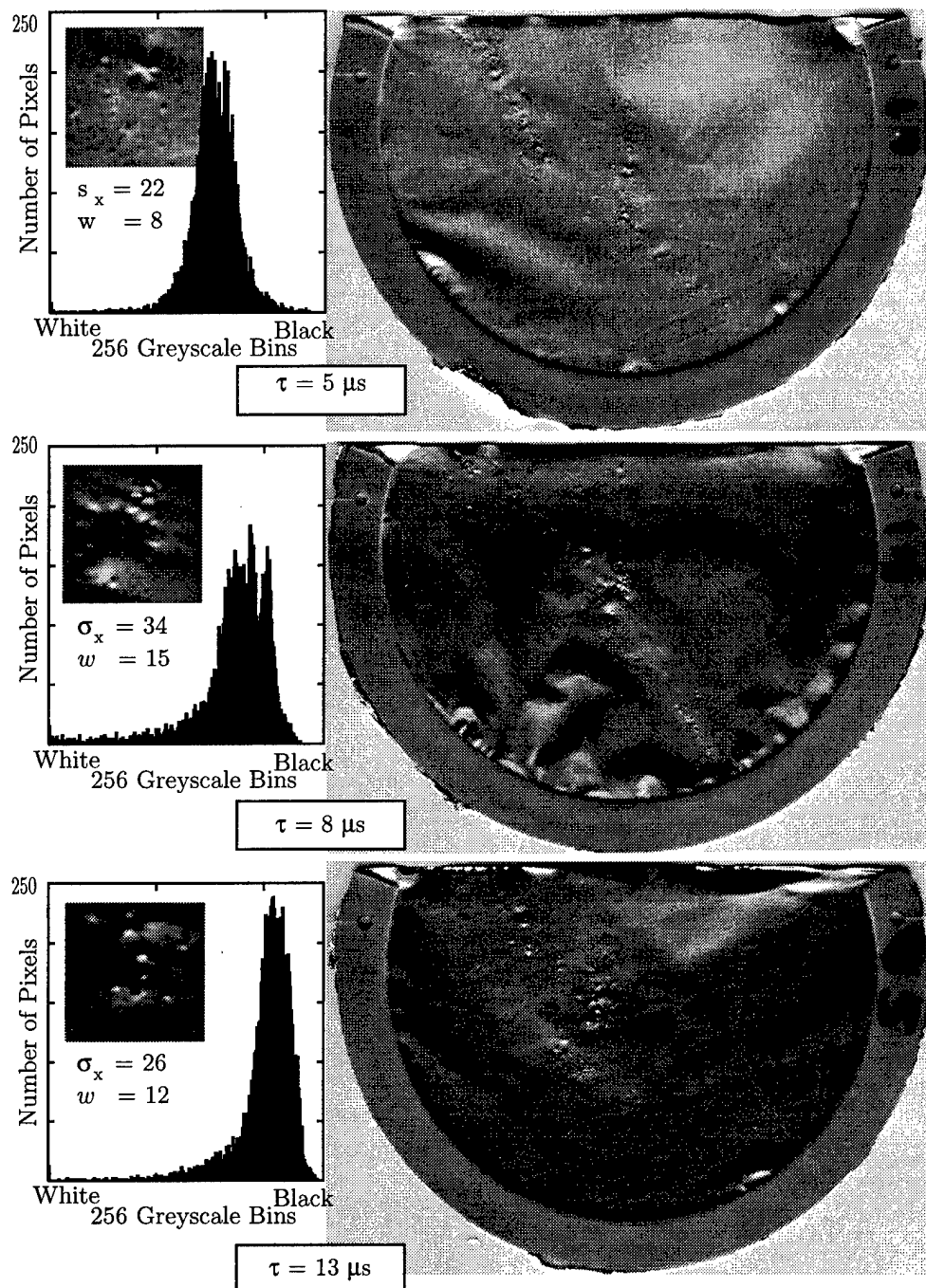


Figure 4.29: Kicking with the pressure-release-rigid reflector sequence. Three foils in which the pressure-release reflector was fired first. Intensified pitting is noted in the center ( $f_2$ ) of the foil.

AS-97-52

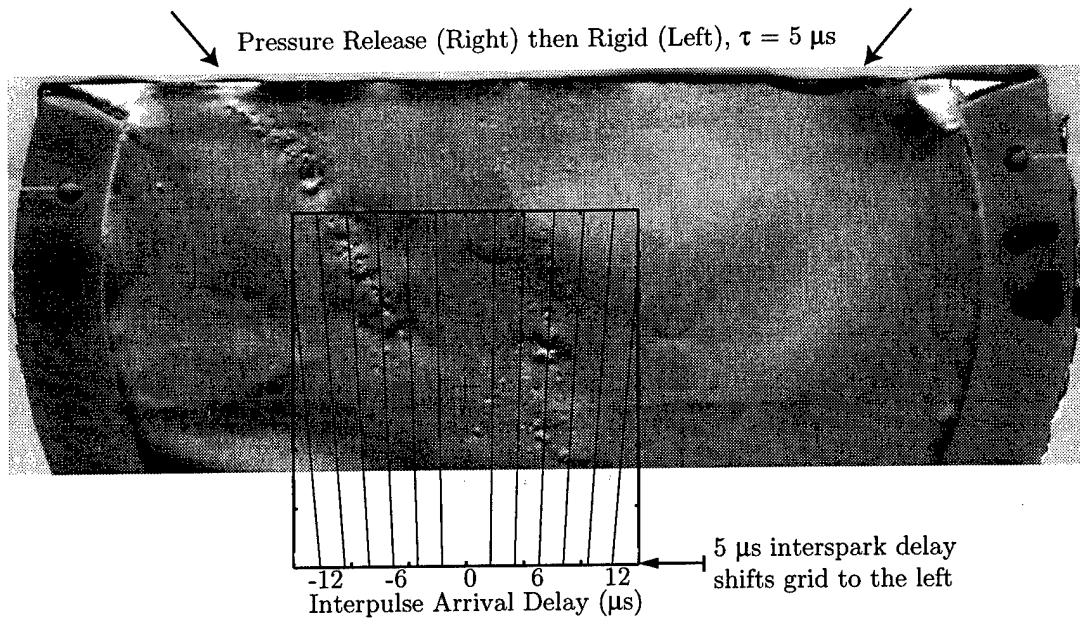


Figure 4.30: Lines of constant interpulse delay superimposed on foil. Intensified pitting occurred at an interpulse delay of  $5 \mu s$ . Reduced pitting occurred around  $\tau = 0$ , where the pulses canceled each other and stifled bubble growth. **AS-97-53**

than the interspark delay. To the left it is less. The region in which the pulses arrive simultaneously (in fact the whole grid) moves to the left as the interspark delay is increased. With increasing delay between pressure release and rigid reflectors, the intensified spot continues to move up and to the left (see Fig. 4.29). The position always corresponded to region where the delay between pulses is  $5 \mu s$ .

Although pulses were added at an appropriate delay to kick the rebound predicted in Fig. 4.20, intensified pitting was not observed. The kick was not predicted to be as intense and simply may not have been intense enough to pit the foil. Or the bubble may have broken up after the first collapse and not rebounded. Further work is needed to decipher which, but the test may provide a means of testing whether bubbles stay intact through a collapse.

In Fig. 4.31, pit depth and pit diameter are compared for a pressure-release reflector, a rigid reflector, and a confocal reflector pair with a  $< 8 \mu s$  delay between sparks. Measurements were made by profilometer in the foil area around  $f_2$ . Circles are the mean, and lines indicate the standard deviation for a number of foils and a number

of profilometer scan paths on each foil. Pits with the sequence are 3-6 times deeper and 10-30 times larger than the pits with the pressure-release reflector alone. Cavitation was intensified. Numerical results in Fig. 4.26 show a three times increase in  $P_{max}$ . The agreement with pit depth is excellent. The order of increasing pit depth in Fig. 4.31 is pits produced by the pressure-release reflector, by the rigid reflector, and by the sequence and is the same as the order of increasing calculated internal pressure in Fig. 4.26. Pit depth and internal pressure represent cavitation intensity, and the most intense cavitation is produced by the sequence.

### Experimental measurement of tempered cavitation

In this section, profilometer and statistical measurements of surface pitting are presented for a pulse sequence designed to mitigate cavitation. A  $-2 \mu\text{s}$  delay between pulses was investigated (i.e., the acoustic pulse from the rigid reflector arrived first and the acoustic pulse from the pressure-release reflector arrived  $2 \mu\text{s}$  later.). A  $-2 \mu\text{s}$  interpulse delay was found numerically to yield the lowest collapse pressures. Other interpulse delays that numerically produced stifling were also investigated.

Figs 4.27 and 4.28 show a small region of reduced pitting (evidence of stifling) just to the left of the intensified pitting. As seen in Fig. 4.30, the stifled region is centered where the pulses arrived  $-2 \mu\text{s}$  apart. Numerical calculations of pressure in the bubble also found a maximum stifling at  $-2 \mu\text{s}$ .

In Fig. 4.32, the interspark delay, and therefore the interpulse delay at  $f_2$ , was  $-2 \mu\text{s}$ . A region around  $f_2$  is devoid of pits. The profilometer measured small ( $\pm 4 \mu\text{m}$ ), gradual changes in foil height but no discernible pits. Standard deviation (17) and number of white pixels (0) are low.

Figure 4.33 shows images of three foils in which the rigid reflector was fired first and the pressure-release reflector fired after a short delay. Each image shows a region around  $f_2$  without pits. The stark contrast between kicking (see Fig. 4.29) and stifling (see Fig. 4.33) is obvious.

As indicated in Fig. 4.33, an interpulse delay of  $-40 \mu\text{s}$  yielded reduced pitting. Numerical results showed a reduced collapse pressure with a  $-40 \mu\text{s}$  delay. The reason a  $-40 \mu\text{s}$  delay is effective and a  $+40 \mu\text{s}$  is not is that the bubble cycle produced by

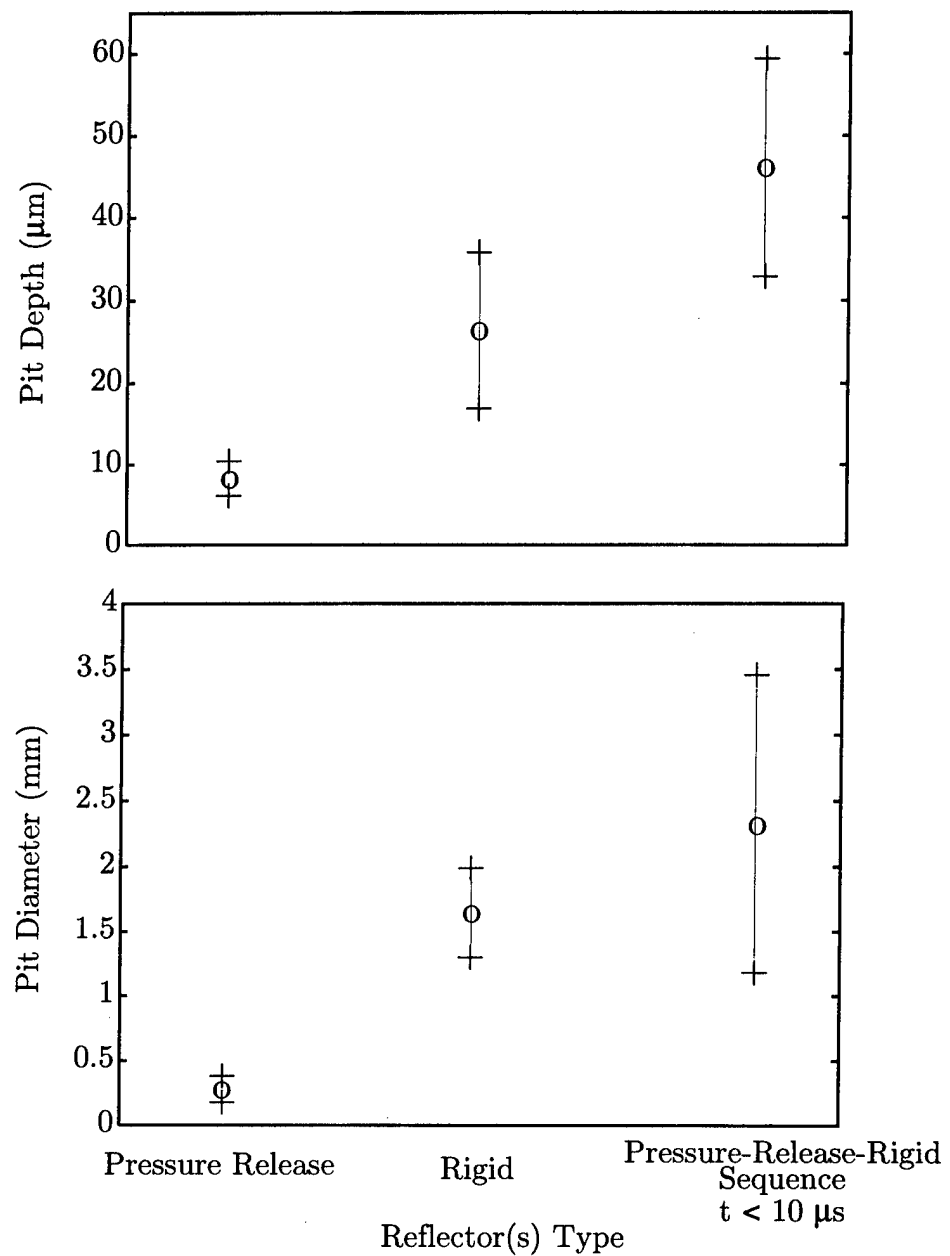


Figure 4.31: Pit depth (a) and diameter (b) are plotted for the pressure-release reflector alone, rigid reflector alone, and both reflectors fired in sequence with the rigid reflector delayed no more than  $8 \mu s$ . The sequence produced the deepest pits.

AS-97-54

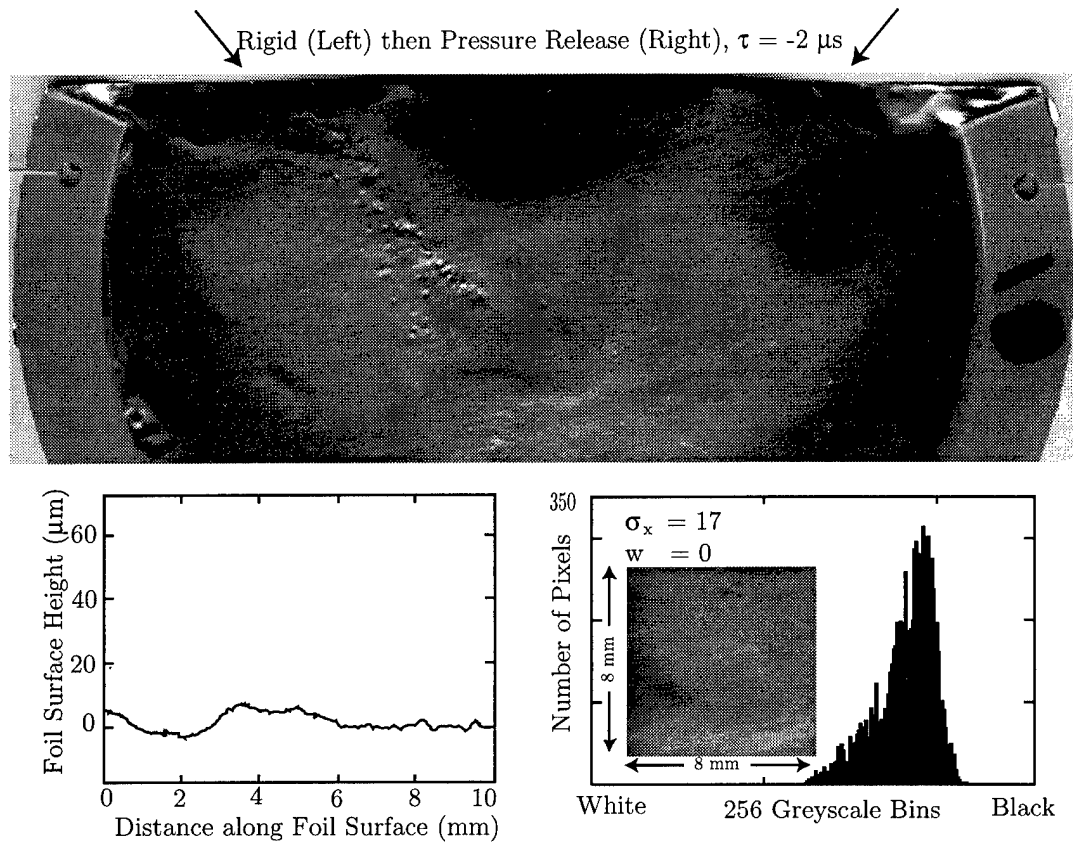


Figure 4.32: Pitting produced by spark in rigid reflector and a spark delayed by  $2 \mu\text{s}$  in the pressure-release reflector. No pitting along the centerline is observed. Pitting is reduced in the focal region.

AS-97-55

the rigid reflector is much longer than  $40 \mu\text{s}$  ( $250 \pm 30 \mu\text{s}$ ), and the cycle produced by the pressure-release reflector is much shorter than  $40 \mu\text{s}$  ( $5 \mu\text{s}$ ). Therefore,  $-40 \mu\text{s}$  still stifles the growth of the bubble excited by the rigid reflector, but a  $40 \mu\text{s}$  delay means the second pulse falls after the bubble excited by the pressure-release reflector has collapsed.

Pit depth and calculated maximum pressure within the bubble demonstrate a direct correspondence. High pressures correlate with deep pits. Sufficiently low pressures correspond to no pits. The pits produced with the pressure-release reflector are the smallest pits measured. The corresponding calculated collapse pressure is  $2.14 \times 10^7 \text{ MPa}$ . The pressure provides a relative threshold for pitting.

The threshold pressure is an upper limit estimate of the pressure required to pit the foil. First, some dissipation mechanisms are neglected in our numerical model; the calculated pressure is an upper limit estimate of the true pressure within the bubble. Second, pressure pulse radiated by the bubble into the liquid is a better estimate of the force required to pit the foil than is the pressure within the bubble. In the numerical model, the pressure within the bubble is higher than the amplitude of the radiated pressure pulse. However, the two show a direct relation: both increased or both decreased. The difficulty with working with the radiated pressure pulse is that the pulse amplitude depends on distance from the bubble. Our estimate of the force required to pit the foil was not refined because we lacked a good estimate of the distance between the foil and the bubble.

In the numerical prediction of the pressure-release-rigid reflector sequence, the bubble rebounds and has a second cycle. The collapse pressure of the second cycle, contrary to that of the first cycle, was high regardless of the delay. Our measurements, which showed a dependence on interpulse delay, suggest our model is accurate to the end of the first cycle only. The bubble does not rebound as predicted. The breakdown likely results because the bubble does not stay spherical or necessarily intact after the collapse.

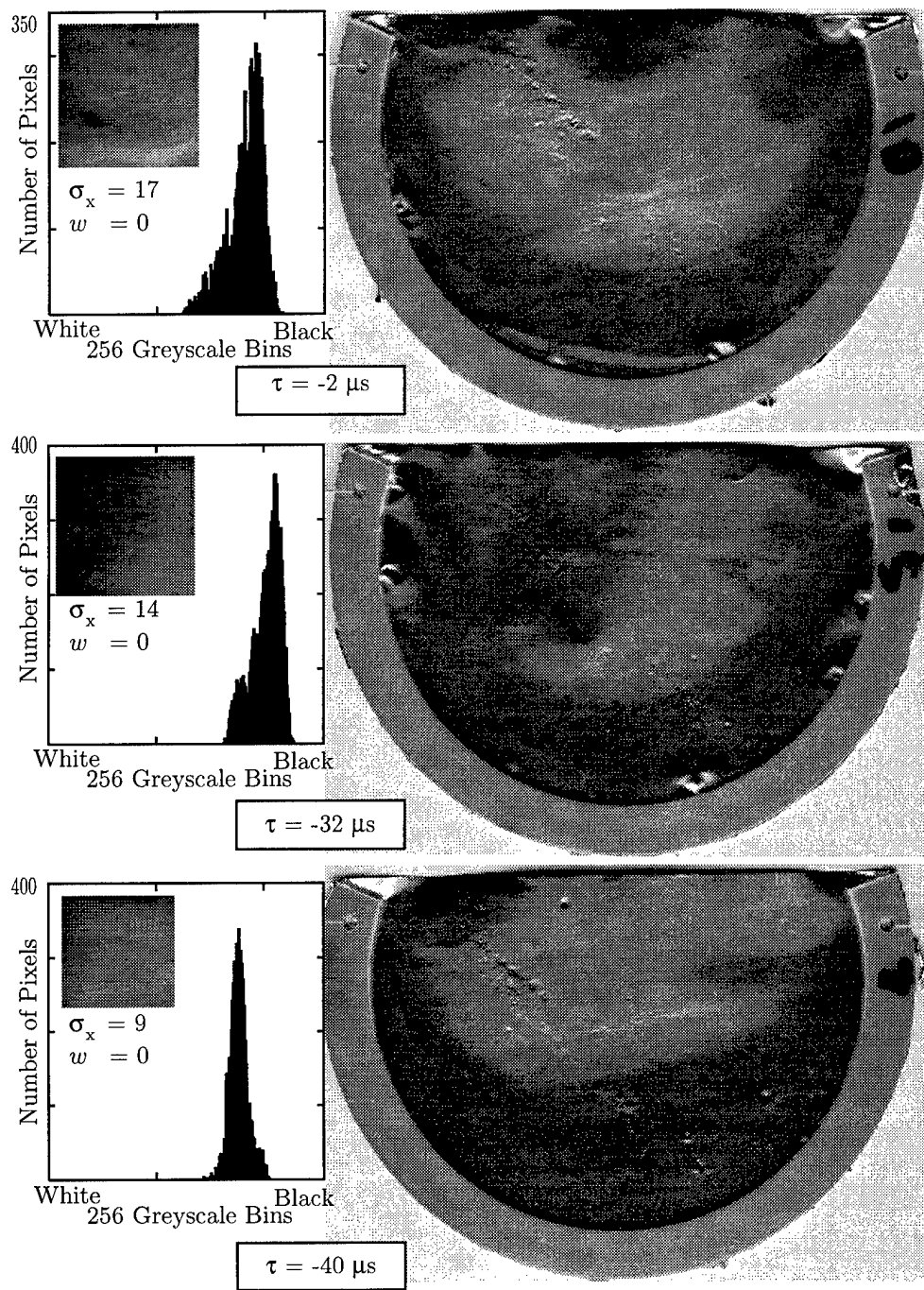


Figure 4.33: Stifling with the rigid-pressure-release reflector sequence. Three foils in which the rigid reflector was fired first. Tempered pitting is noted in the center ( $f_2$ ) of the foil.

#### 4.4.3 Cavitation by a sequence of two pulses produced by a confocal pair of rigid reflectors

In this section, numerical and experimental expressions of collapse intensity are discussed for two confocal rigid reflectors fired in sequence. Collapse pressure numerically calculated as a function of interpulse delay is presented first. Pit depth in aluminum foil experimentally determined as a function of interpulse delay is discussed second. Third, collapse pressure (theory) and pit depth (experiment) are compared. Lastly, the specific case of two simultaneous pulses is addressed.

##### Collapse intensity versus interpulse delay—theory

This section contains computed results for maximum pressure within the model spherical bubble. Maximum internal pressure is used to represent cavitation intensity as described in Chapter 2. A digitized acoustic waveform measured at  $f_2$  of a rigid reflector was used to drive the Gilmore code. The digitized waveform was not adjusted to make it possible to compare results in this section and those in Sec. 4.4.2. The peak positive pressure of the acoustic waveform was 28 MPa, which was comparable to the peak positive pressure of the Austin configuration. As stated previously, the Austin waves were approximately three-fifths the amplitude of the Seattle waveforms. The weaker waves resulted because half the capacitance was used, leads were longer (therefore inductance was higher), and deionized water was used throughout the tank.

A second pulse was added after a variable delay, and the maximum pressure within the bubble was calculated. Waveshape of the second pulse was identical to the first pulse, but the peak amplitude was 35 MPa. A larger second pulse corresponded to the measurement configuration of results in Sec. 4.5 and made comparison to that section easy. Physically, a small pulse then a larger pulse corresponds to the acoustic pressure seen by a bubble just off axis of one reflector and on axis of the other.

The time scales were scaled to simplify comparison between experiments and interpretation of off-axis results. Scales were normalized to the duration of the growth and collapse cycle produced by the first pulse alone. The true bubble cycle duration for the experiments in this section was  $250 \pm 30 \mu\text{s}$ .

Figure 4.34(a) contains a calculated R-T curve for the bubble response to the single pulse. Collapse occurs at the normalized time  $t_n = 1$ . An arrow indicates time placement of a second pulse. Sequences were considered where the second pulse arrived as the bubble grew ( $t_n < 0.5$ ), as the bubble collapsed ( $0.5 < t_n < 1$ ), and after the bubble collapsed ( $t_n > 1$ ).

Figure 4.34(b) is a plot of the collapse pressure  $P_{\max}$  inside the bubble versus the normalized interpulse delay  $\tau_n$ . The maximum pressure calculated for one pulse was  $5.12 \times 10^7$  MPa. The maximum pressure of the gas in the bubble occurred at the second collapse  $R_{\min 2}$ . For  $\tau_n > 1$ ,  $P_{\max}$  for the first cycle is also  $5.12 \times 10^7$  MPa because the second pulse arrives after the collapse. For  $0.3 < \tau_n < 1$ , the maximum pressure was higher; the bubble was kicked. For  $\tau_n < 0.3$ , the pressure was lower; the bubble was stifled. For  $\tau_n = 0$ , the acoustic pulses arrived simultaneously and were added. The bubble was driven twice as hard, so the collapse pressure is higher. Radius-time curves for the data are shown in Sec. 4.5.

For an off-axis bubble, the curves in Fig. 4.34 are the same. The absolute times and pressures are less. Kicking and stifling occur, but on a different time scale. A late pulse that kicks the on-axis bubble might fall after the collapse of an off-axis bubble. Or a pulse that stifles the on-axis bubble might fall insufficiently late to kick the off-axis bubble.

### **Collapse intensity versus interpulse delay – measurement**

In this section, pit depth in foil versus delay between the sparks in two confocal rigid reflectors is presented. The confocal arrangement is shown in Fig. 4.35. Reflector  $R$  was on the right and fired first, and reflector  $Q$  was on the left. Since the single bubble duration at  $f_2$  was  $250 \pm 30 \mu\text{s}$ , a range of interpulse delays between 0 and  $300 \mu\text{s}$  was investigated. Results are presented in order of decreasing interpulse delay. Pit depth is used to represent cavitation intensity.

A  $300\text{-}\mu\text{s}$  delay is sufficiently large ( $\tau_n > 1$ ) that the two pulses acted independently. The bubbles from the first pulse collapsed and pitted the foil before the second pulse arrived. Independence is evidenced by the overlap of two equally thin pit stripes in Fig. 4.36. No intensified regions were observed.

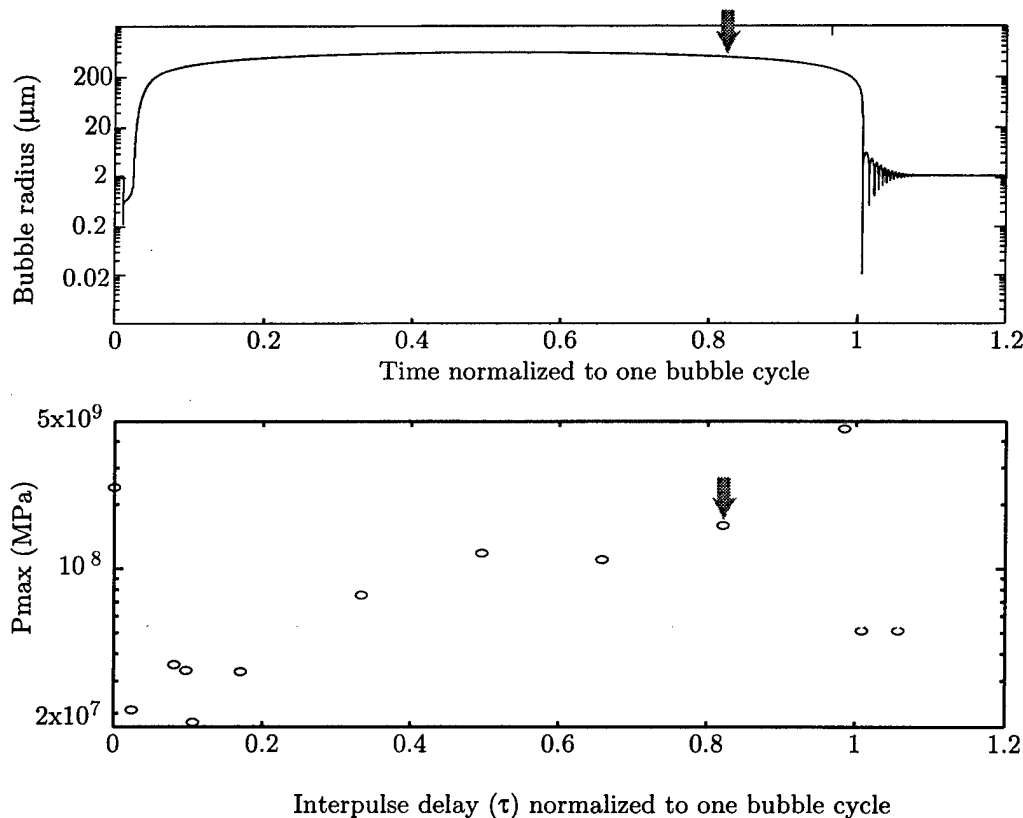


Figure 4.34: Calculated radius-time curve for one pulse (a) and the bubble's maximum internal pressure for a sequence of two pulses plotted versus interpulse delay (b). Times are normalized to bubble cycle for the one pulse. The arrow in (a) indicates a delayed arrival of a second pulse and in (b) the corresponding pressure increase for the kicked bubble. The grey line in (b) indicates the collapse pressure with a single pulse.

AS-97-57

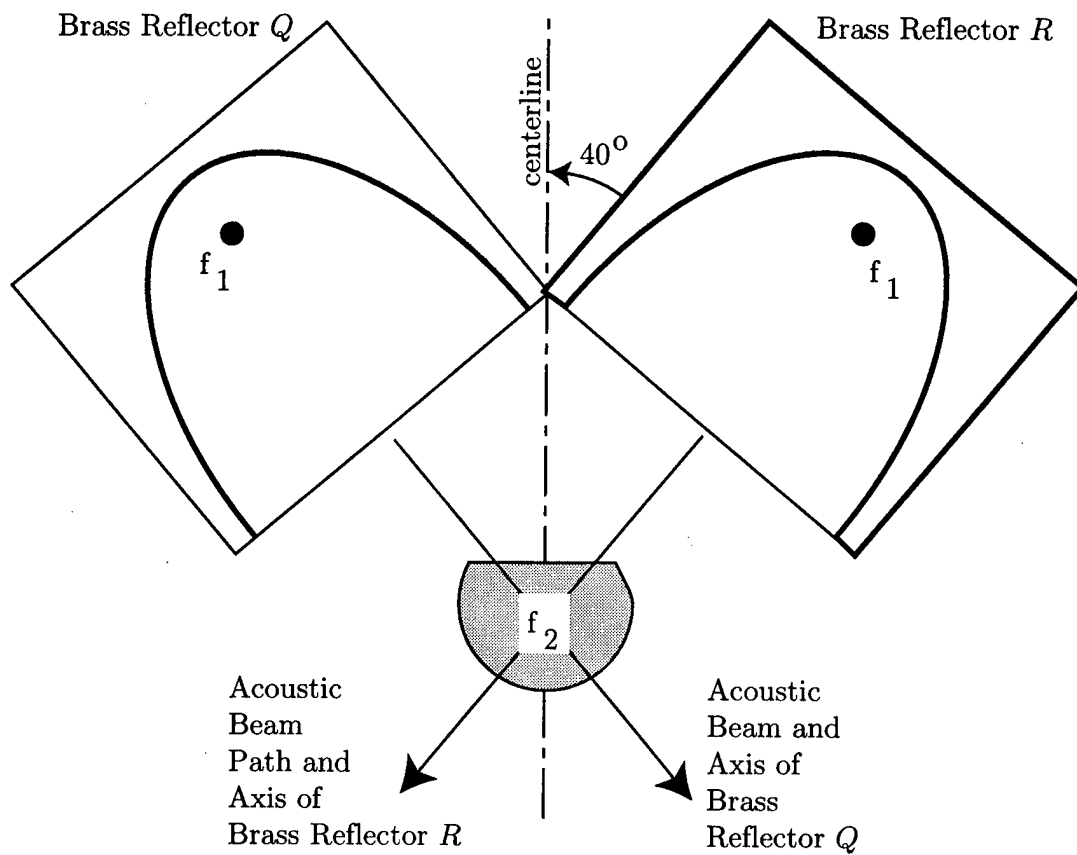


Figure 4.35: Worm's eye view of the Austin confocal rigid reflectors. Both reflectors were angled so they shared the same  $f_2$ . Each foil was placed at  $f_2$  along the axes of the reflectors.

AS-97-58

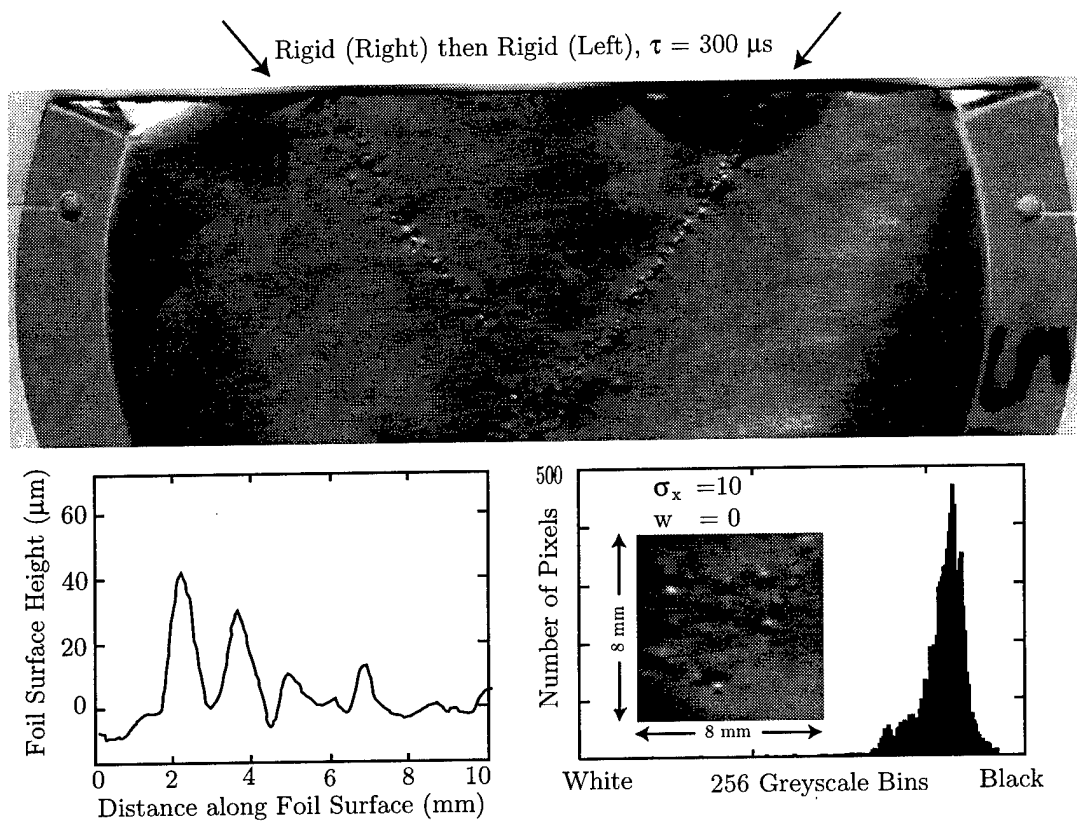


Figure 4.36: Pitting produced by a spark in the right rigid reflector and a spark delayed by  $300 \mu\text{s}$  in the left rigid reflector. Two thin crossed rigid-reflector pit paths are seen. No area of intensified or mitigated pitting appeared.

AS-97-59

A second pulse delayed 190  $\mu\text{s}$  arrived during the collapse of the bubbles excited by the first ( $0.5 < \tau_n < 1$ ). Pit depth measured by profilometer and indirectly measured by the number of white pixels are higher for the 190- $\mu\text{s}$  delay in Fig. 4.37 than for the 300- $\mu\text{s}$  case in Fig. 4.36. The bubbles were kicked, and the cavitation intensified. As for the picture of the foil in Fig. 4.37, the right spark arced first. The path of the right reflector is not only deeper but broader. The depth resulted from kicking the bubbles. The breadth resulted from kicking the bubbles off to the side of the axis of reflector  $R$ .

Off-axis bubbles were excited by the lithotripter but were more weakly excited because the sound waves were weaker off axis. The durations were shorter, and the collapse, therefore, less violent with just the single reflector. The weak collapses did not pit the foil when just a single reflector was used. But with the kick of a second pulse, the off-axis bubbles collapsed violently enough to pit the foil. The pit path was thereby broadened. Broadening resulted when the second pulse fell late enough in the bubble period to intensify the collapse but not after the bubble had already collapsed. The farther off axis the bubble was, the earlier the time window, in which the bubble could be kicked, occurred.

With a delay of 92  $\mu\text{s}$  (see Fig. 4.38), the path was further broadened, but although intensified, the pitting was not intensified as much in the 190- $\mu\text{s}$  case. On axis, the second pulse fell with  $0.3 < \tau_n < 0.5$ . Broadening occurred because bubbles further off axis were kicked. For the far off-axis bubbles, interpulse delay that was normalized to the off-axis bubble cycle was greater;  $0.5 < \tau_n < 1$ . In the previous foil, the pulse delayed 190  $\mu\text{s}$  came too late to kick any bubbles that collapsed in less than 190  $\mu\text{s}$ . The path was therefore only 25 mm broad. The 92  $\mu\text{s}$  delayed pulse kicked bubbles far off axis ( $> 12$  mm) that were excited only strongly enough to last for 92-190  $\mu\text{s}$ . By kicking these bubbles, the calculated maximum internal pressure can be increased fivefold, and the energy concentration sufficiently increased to pit the foil.

The pits are not as deep because kicking is less effective early in the bubble duration than late in the duration. So, the bubbles on axis, which were excited most strongly by the first pulse, were not kicked as strongly with the 92- $\mu\text{s}$  delay as with the 190- $\mu\text{s}$  delay.

An even shorter interpulse delay, 46  $\mu\text{s}$  ( $\tau_n < 0.3$  on axis), yielded a wide path but

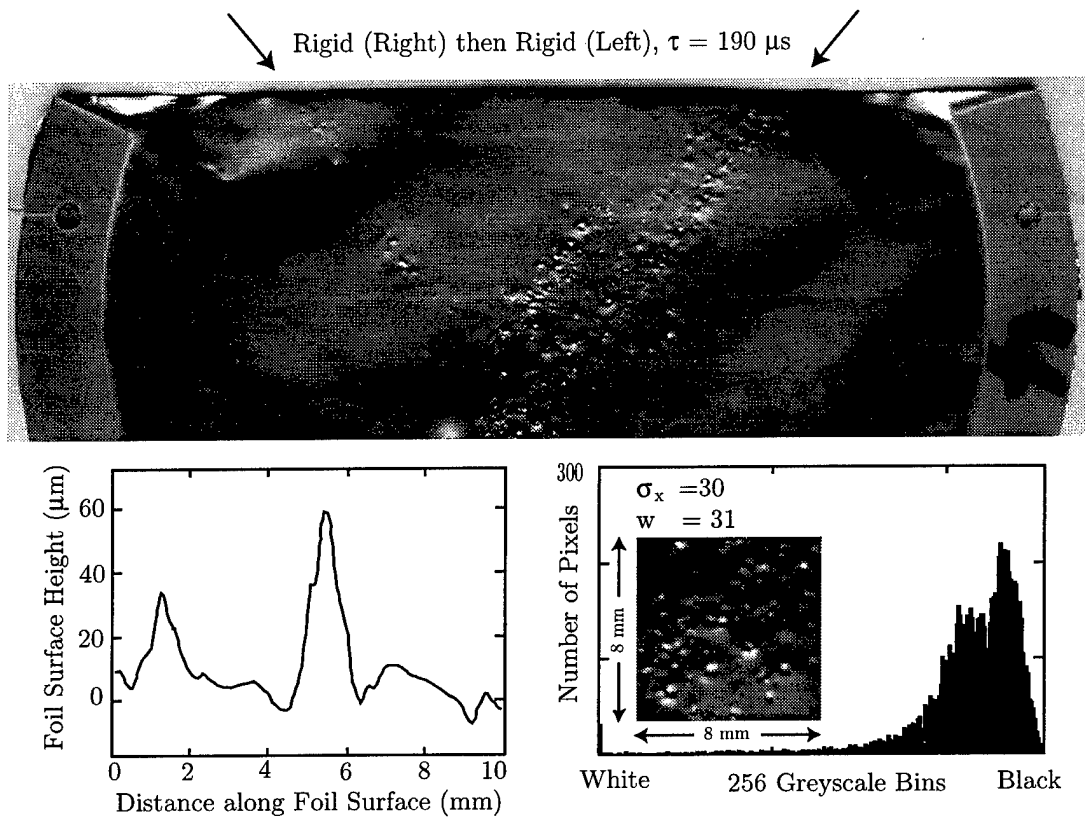


Figure 4.37: Pitting produced by a spark in the right rigid reflector and a spark delayed by  $190 \mu\text{s}$  in the left rigid reflector. The first path was broadened when the second pulse kicked the off-axis bubbles. Pit depth also increased because of the kick.

AS-97-60

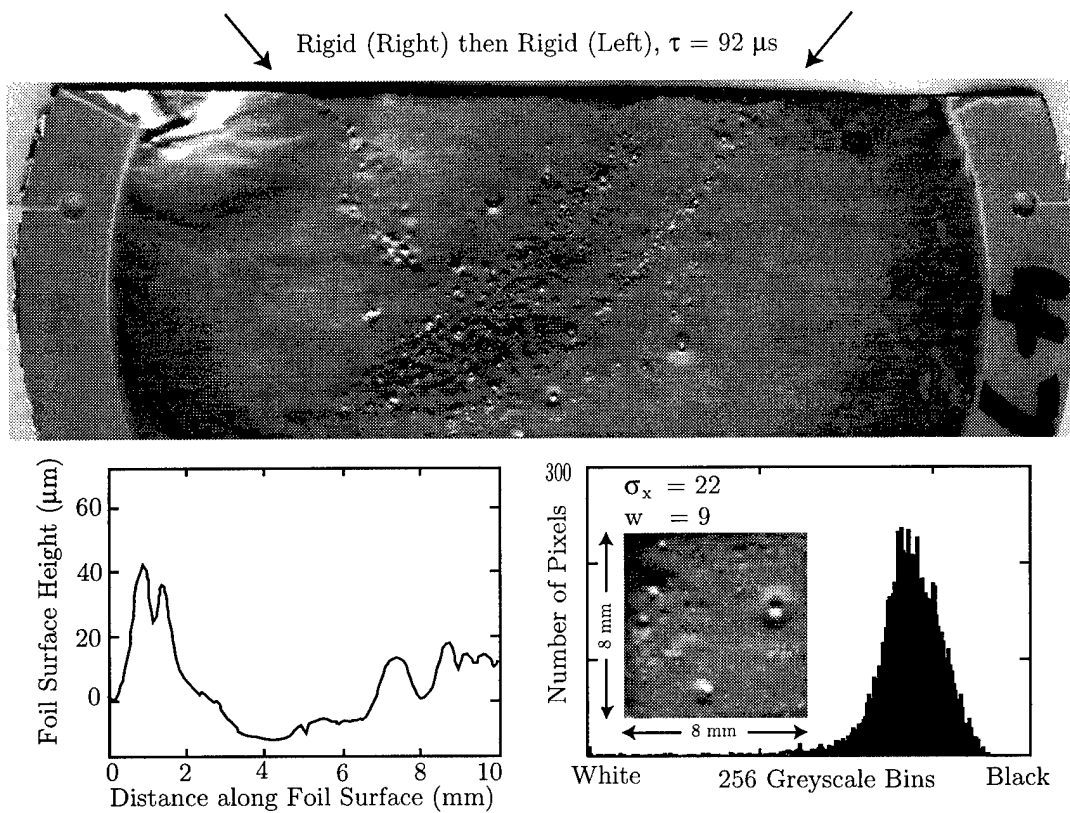


Figure 4.38: Pitting produced by a spark in the right rigid reflector and a spark delayed by  $92 \mu\text{s}$  in the left rigid reflector. The first path was broadened when the second pulse kicked the off-axis bubbles. However, on axis the bubbles were kicked only weakly because the second pulse was early in the bubble period. Pits were not as deep as with the  $190\text{-}\mu\text{s}$  delay.

AS-97-61

shallow pits. In this case the off-axis bubbles still received a kick, whereas the on-axis bubbles were stifled. Overall the pits are less deep than without the second pulse. The change with interpulse delay in pit depth and path width can be seen in the six-foil sequence shown in Figs. 4.39 and 4.40.

The foils in Fig. 4.40 and the profilometer data in Fig. 4.38 show fine structure similar to fine structure attributed to microjetting by Coleman *et al.*<sup>12</sup> Coleman *et al.* described a jet as shown in Fig. 4.41 (borrowed from Crum<sup>69</sup>) pitting the foil. The collapse of the toroidal bubble left by the jet collapsed in a ring around the pit. The result was a local mountain (within the collapse ring of the toroidal bubble) that contained a crater in its peak from the jet. Such a surface profile is seen in the profilometer reading of Fig. 4.38. Mountains with even deeper craters were measured on other sections of the foil.

### **Collapse intensity—measurement and theory**

Pit size and path width were measured directly off the foil. Indirect, statistical measurements were made off the digital scans. Here, the data are discussed and compared to numerical results presented in Sec. 4.4.3. Comparison is on the basis of collapse intensity versus time delay of the second pulse.

The four plots in Fig. 4.42 show measured cavitation intensity. The right most point in each plot corresponds to the case in which the second pulse arrived after the bubble collapsed. The point is therefore, the reference point to which to compare the other data because the point reflects no measurement of stifling or kicking. Time windows of stifling are relatively low points on the plots, and time windows of kicking are relatively high points. Both kicking and stifling were measured. The time windows are also, at least for the first three plots in Fig. 4.42, in good agreement with the plot in Fig. 4.34.

Figure 4.42(a) contains a plot of pit depth versus the time delay between the pulses used to pit the foil. The mean of several separate passes with the profilometer on separate foils all with the same time delay appears as a circle. The standard error appears as cross-hatched lines. The error in  $\tau$  is  $\pm 1 \mu\text{s}$  for (a) through (d) in Fig. 4.42. Plot (a) has the same shape as the plot of numerical calculations of maximum internal

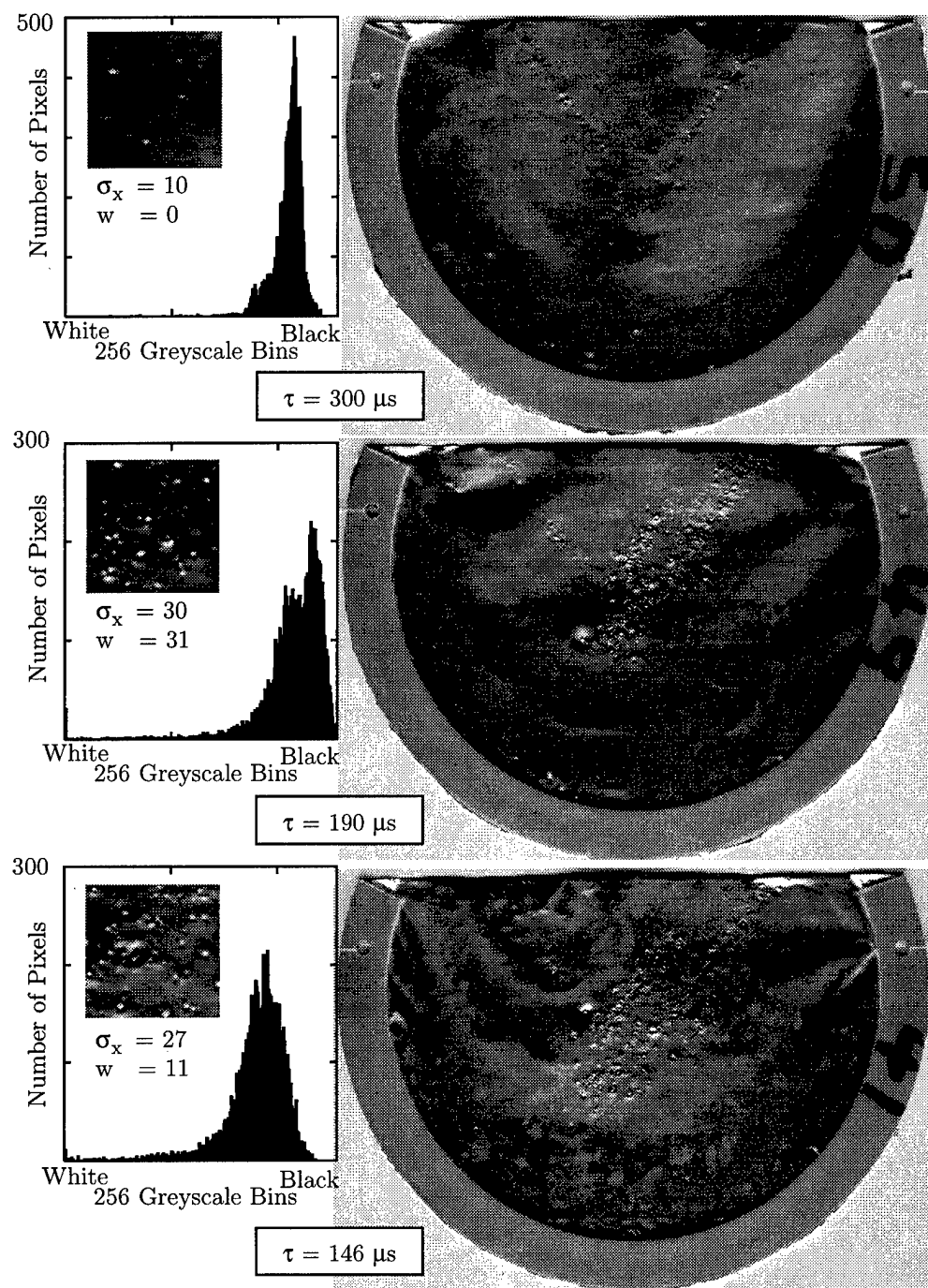


Figure 4.39: Foils subjected to a two-pulse sequence produced by a confocal pair of rigid reflectors. The right path is wider for decreasing time delay of the pulse from the left reflector. Histograms indicate increasing number and depth of pits.

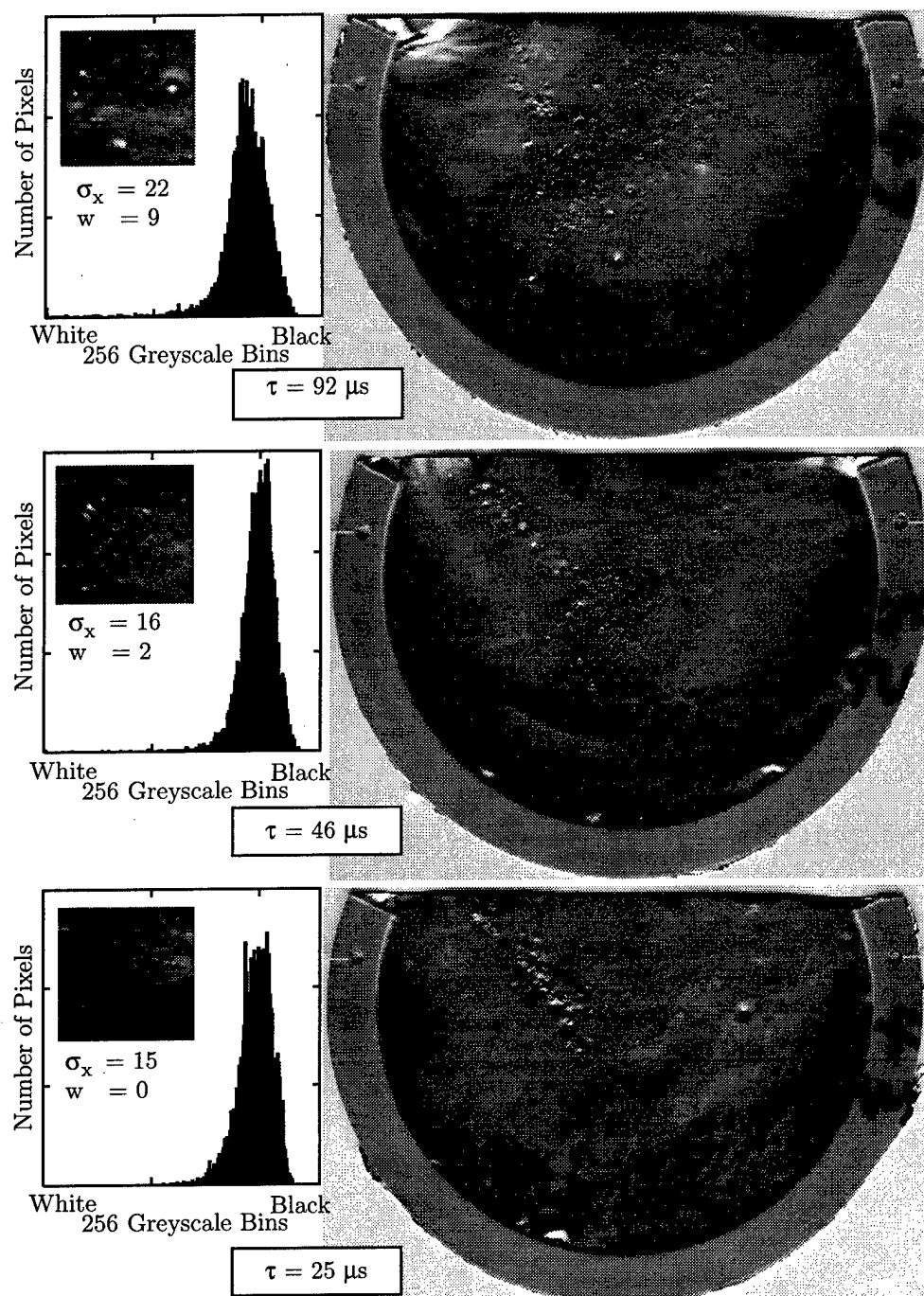


Figure 4.40: Foils subjected to a two-pulse sequence produced by a confocal pair of rigid reflectors. The right path is narrower and the pits shallower for decreasing time delay of the pulse from the left reflector. Histograms indicate decreasing number and depth of pits.

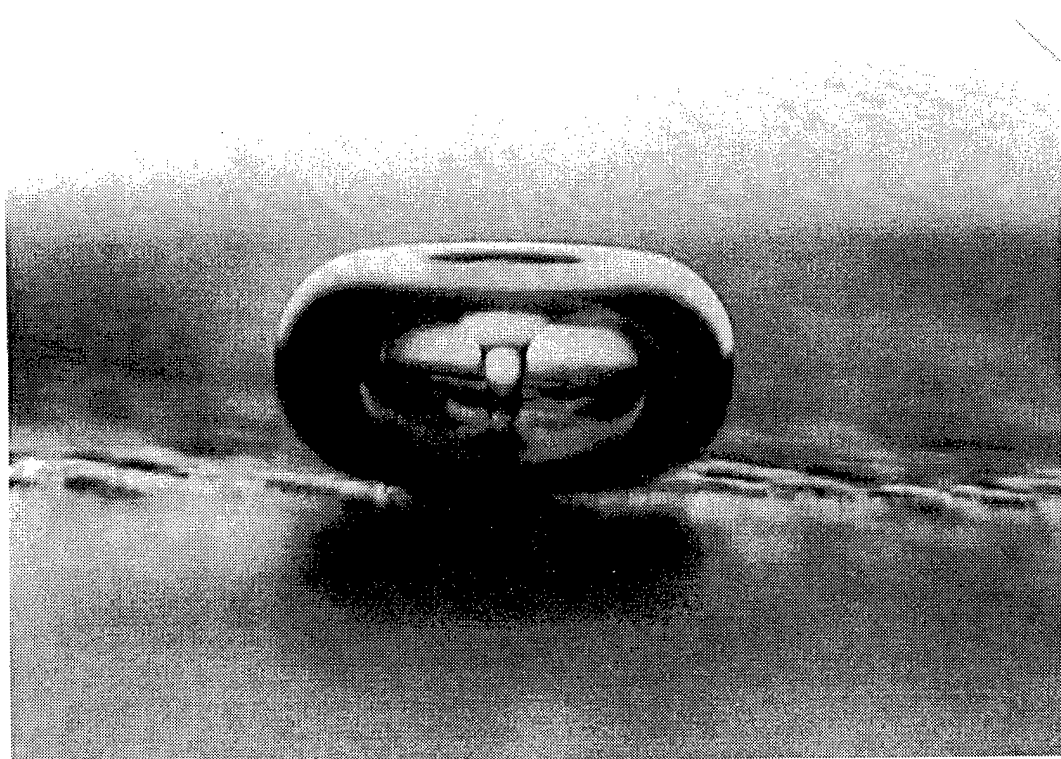


Figure 4.41: Photograph borrowed from Crum<sup>69</sup> of a microjet of water through a cavitating bubble. Bubble diameter is about 2 mm.

AS-97-64

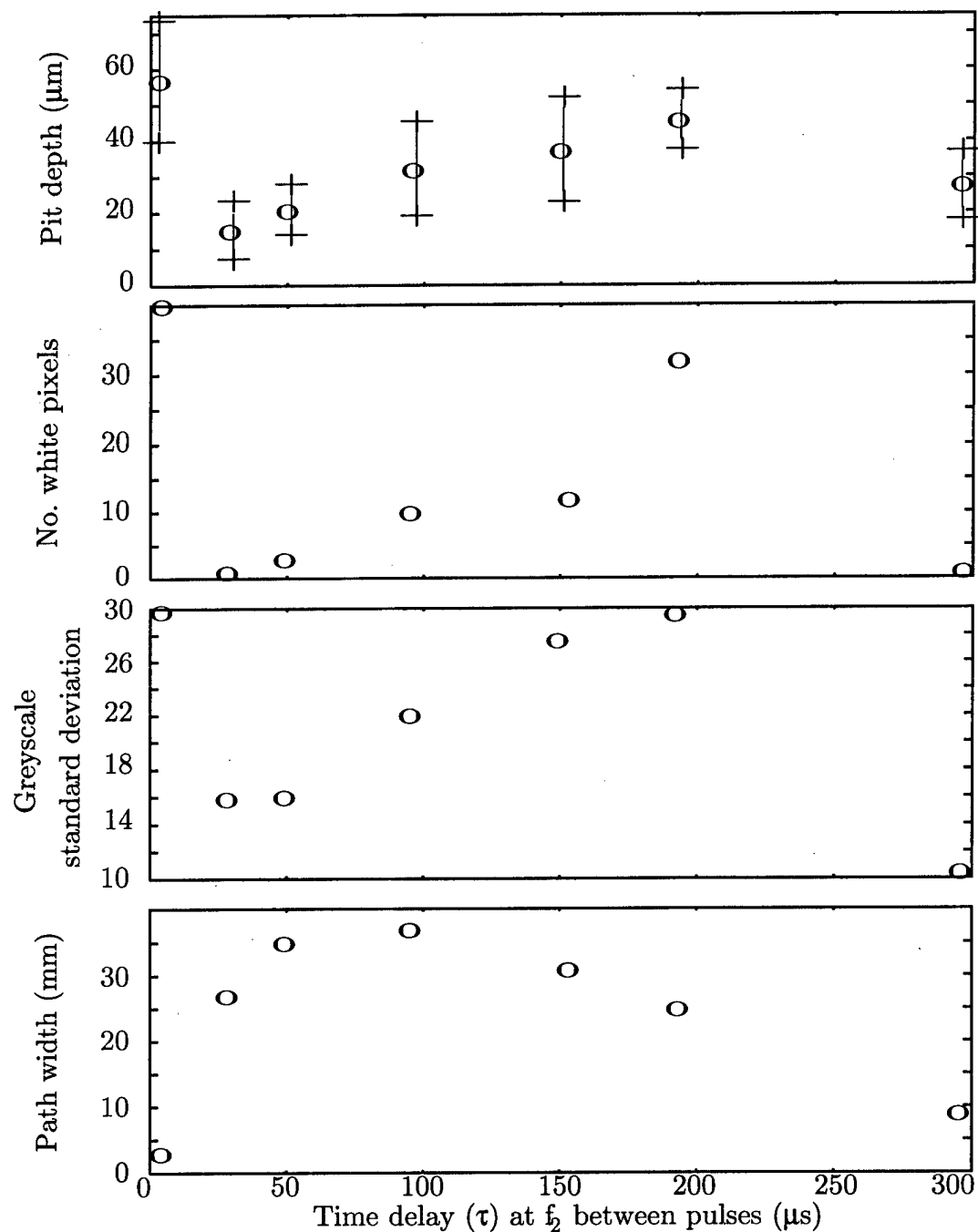


Figure 4.42: Measured (a) pit depth, (b) number of white pixels in foil image, (c) standard deviation of histogram of foil image, and (d) pit path width versus delay between pulses produced by two confocal rigid reflectors.

AS-97-65

pressure in Fig. 4.34. The cycle duration  $\tau_n = 1$  in Fig. 4.34 corresponds to  $250 \pm 30 \mu\text{s}$  in Fig. 4.42. At  $\tau_n > 1$ , the baseline is established, which corresponds to no interaction with the second pulse. At  $0.3 < \tau_n < 1$ , deeper pitting (intensified cavitation) was observed. At  $\tau_n < 0.3$ , shallower pitting (tempered cavitation) was observed. It is noted that the pit depth and predicted collapse pressures for  $\tau = 25 \mu\text{s}$  or equivalently  $\tau_n = 0.1$  are nearly equal to those of the pressure-release reflector. Pressures were above the pitting threshold. Lower pressures, pressures below the threshold, were seen with shorter delays. The values at  $\tau = 0$  are discussed the next section, Sec. 4.4.3.

The statistical measures in Fig. 4.42(b) and (c) are in good agreement with the direct measurement in Fig. 4.42(a) and numerical predictions in Fig. 4.34. Number of white pixels is plotted versus  $\tau$  in Fig. 4.42(b) and standard deviation plotted in Fig. 4.42(c). In both Fig. 4.42(b) and Fig. 4.42(c) as in Fig. 4.42(a), a local minimum occurred at  $25 \mu\text{s}$ , and a local peak at  $190 \mu\text{s}$ . Again, the values at  $\tau = 0$  are left for Sec. 4.4.3. The agreement may be used to defend the credibility of the statistical measures.

The path width plotted versus interpulse delay  $\tau$  in Fig. 4.42(d) did not follow the same trend as the other plots in the figure. The path of pits in the foil was narrowest when the pulses arrived simultaneously or when the second arrived after the bubble collapse caused by the first. The path was widest at  $92 \mu\text{s}$ . So the peak in Fig. 4.42(d) is not at  $190 \mu\text{s}$  as it is in Fig. 4.42(a)-(c).

Path width is a measure of collapse intensity inherently dependent on a bubble cloud that encompasses on- and off-axis regions. Only one bubble is considered in our model. Better agreement between the model and path width might be attained by averaging the collapse pressures predicted in a number of runs of the model. Each run would correspond to different off-axis locations for the bubble. Path width is discussed further in Sec. 4.4.3.

### Special case of simultaneous sparks

When the sparks were fired simultaneously, pronounced effects were seen. The effects are, however, in agreement with both the simple physical descriptions of kicking and stifling and the specific numerical calculations presented in Fig. 4.34.

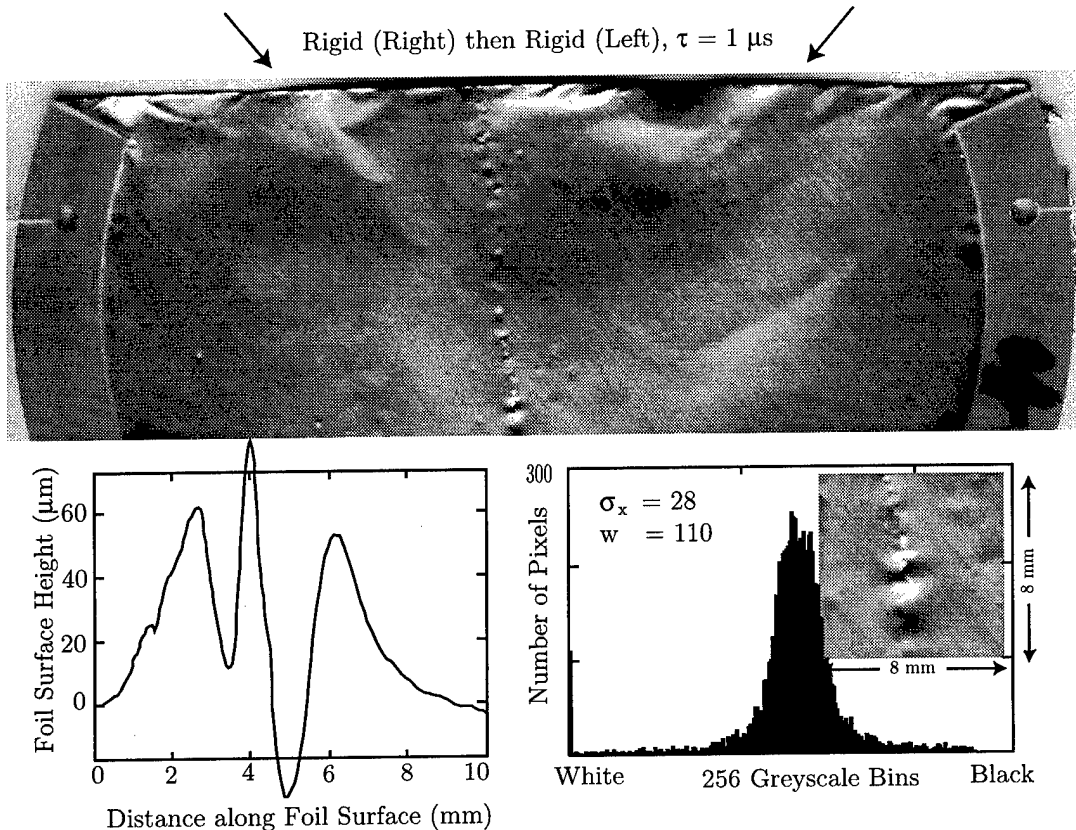


Figure 4.43: Pitting produced by a spark in the right rigid reflector and a spark delayed by  $0 \mu\text{s}$  in the left rigid reflector. A streak of deep pits is apparent along the centerline between the beams. No pitting occurred along the axis of either reflector.

AS-97-66

Figure 4.43 shows pitting by two simultaneous sparks in a pair of confocal rigid reflectors. Figure 4.44 shows the same foil as Fig. 4.43 and another foil. Intense pitting can be seen along the centerline. The profilometer shows a  $120 \mu\text{m}$  range of surface height, which is bigger than that measured for any other interpulse delay. Standard deviation of the histogram is 28. Number of white pixels is 110. The values are huge. Their relative measure is shown in Fig. 4.42. No pits are seen along the axes of the reflectors in Figs. 4.43 and 4.44. A line of pits was created on the centerline, and the pits normally seen on the axis of the reflector do not appear at all.

Along the centerline the acoustic pulses arrived simultaneously. Superposition of the two pulses produced the same waveform as one pulse but double the amplitude.

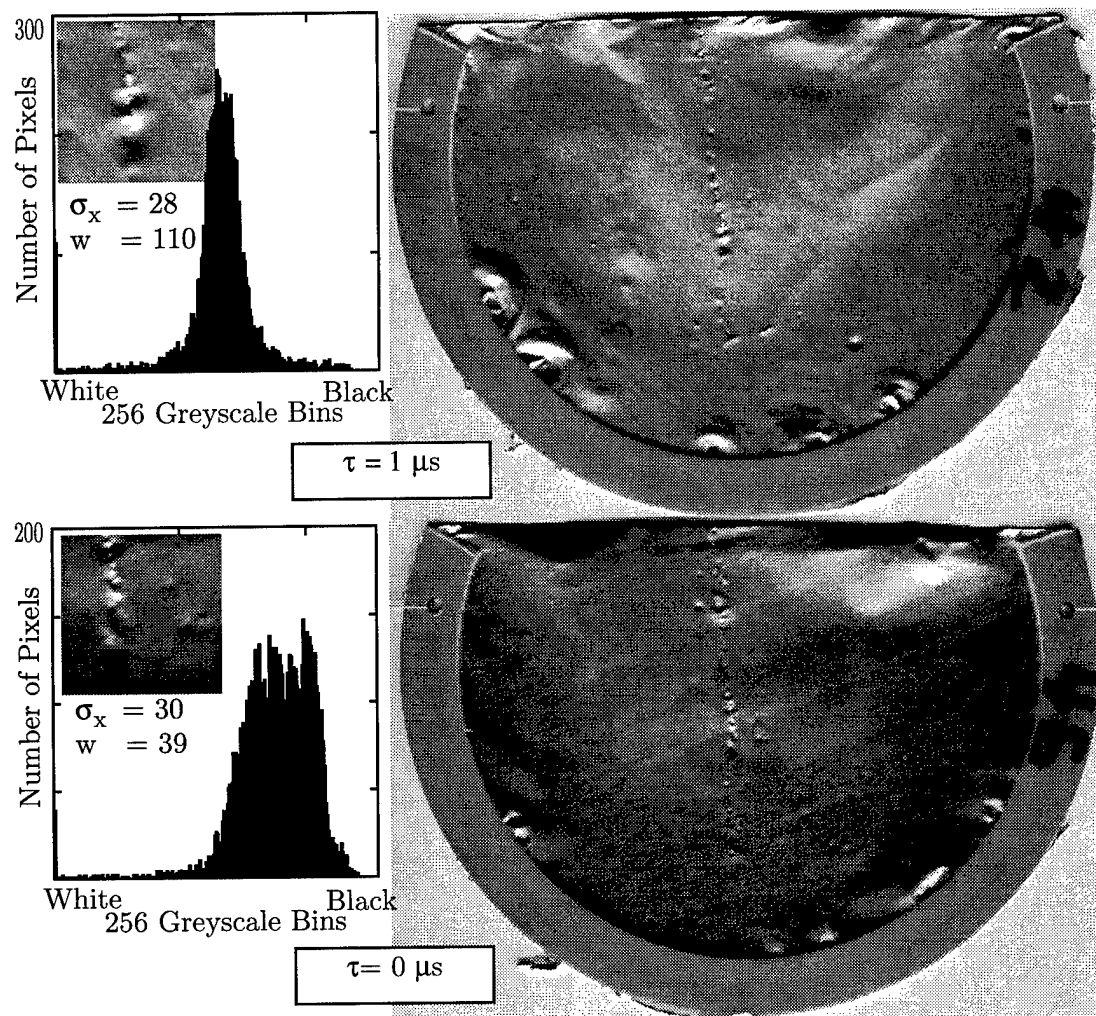


Figure 4.44: Foils subjected to two pulses produced by a pair of rigid reflectors. Pulses arrived simultaneously. The crossing beam paths do not appear at all. A long, deep narrow path of pits appears on the centerline. Many white pixels in the histograms indicate deep pits.

AS-97-67

Bubbles were, therefore, driven by a strong acoustic pressure along the centerline. Bubbles were driven especially strongly near  $f_2$ , which was on the axes of both reflectors. The bubble grew longer and collapsed more intensely. The result was deep pits in the foil.

To either side of the centerline the acoustic pulses had a tiny delay between them. Bubbles excited by the first pulse were quickly stifled by the second pulse. The result was to push the collapse pressure below the pitting threshold of the foil. No pitting was, therefore, measured on the axes because bubbles were stifled.

#### 4.5 Simultaneous PCD and foil measurement

In this section, PCD measurements and numerically calculated R-T curves are presented for two confocal rigid reflectors and varying interpulse delay. The PCD data supports the description of cavitation intensity and extent, which was provided by pits on aluminum foil. In addition, the PCD measurements give a time history of the cavitation, which supports our model of the bubble dynamics responsible for surface pitting.

Measurements in Sec. 4.4.3 were made in Austin; results presented in this section were measured in Seattle. Figure 4.35 illustrates the configuration. However, in Seattle, the reflectors were  $90^\circ$ , not  $80^\circ$ , apart, water was more thoroughly degassed, and the spark was louder. The measured duration of a single bubble cycle created by one acoustic pulse was  $500 \pm 150 \mu\text{s}$ . Time  $t = 500 \mu\text{s}$  corresponds to time  $t_n = 1$  in the normalized numerical plots. In results in Sec. 4.5.1, interpulse delays  $\tau$  from  $800 \mu\text{s}$  to  $100 \mu\text{s}$  (normalized delays  $\tau_n$  from eight-fifths to one-fifth) in steps of  $100 \mu\text{s}$  (one-fifth) were investigated. In results in Sec. 4.5.2, measurements were made at two different locations and one interpulse delay  $\tau = 0$ .

##### 4.5.1 Bubble dynamics versus interpulse delay–part I

Foil pitting, PCD measurement, and numerical prediction are presented side by side for seven separate time delays (no foil appears in the eighth). PCD recording and foil pitting were recorded simultaneously. A number of measurements were made at each interpulse delay.

### Second pulse arrives after collapse of the bubble

With delays 800-600  $\mu\text{s}$ , the second pulse arrived after the collapse caused by the first pulse. Numerical predictions of two separate collapse cycles agree with PCD measurement of two collapse cycles and foil measurement of two equal pit stripes. Data are presented and complications due to alignment and focusing are discussed in this section.

Figure 4.45(a) shows a PCD recording produced by two sparks 800  $\mu\text{s}$  apart. At  $t=0$ , the spark was triggered. At 250  $\mu\text{s}$ , the initial collapse of the bubbles at  $f_2$  was detected. The delay (shown in grey) corresponds to the acoustic travel time to  $f_2$  and then to the PCD. After  $450 \pm 100\mu\text{s}$  (at  $\sim 600 \mu\text{s}$  in this case), the collapse was detected. At 800  $\mu\text{s}$ , the second spark fired. The electrical noise was detected by the PCD. The noise has the appearance of one spike followed quickly by another with a long decaying tail. The electrical noise began when the switching spark triggered. A variable delay of  $\sim 20 \mu\text{s}$  was inherent before the underwater spark arced and sound was produced. Exact timing between the sparks was recorded by two directive photodiodes, which detected the light given off by the underwater discharges. Again 250  $\mu\text{s}$  (shown in grey) after the underwater spark, the initial collapse of the bubble at  $f_2$  was detected. After  $550 \pm 100\mu\text{s}$  (at  $\sim 1600\mu\text{s}$  in this case), the final collapse was detected.

The PCD measurement shows two independent bubble cycles: the first completed before the second started. Quoted duration of the cycles is the mean of many shots. The deviation in the mean was due to spark jitter. Slightly greater spark jitter was observed in the two-spark arrangement because, we suspect, the electric field of one system interfered with the other. The difference in duration between the first and second cycle was indication of slight misalignment of the PCD. Misalignment was verified by comparison of PCD focus (as indicated by a pointed cap that fit over the PCD) to the pit paths on each foil. The accuracy of the cap was previously verified. The PCD focus was  $1.5 \pm 0.5 \text{ mm}$  off the axis of the first reflector in the direction away from the second reflector and on the axis of the second reflector.

The first collapse cycle  $t_{c1}$  was shorter than the second cycle  $t_{c2}$  because the off-axis acoustic wave produced by the lithotripter was weaker than the on-axis pulse.

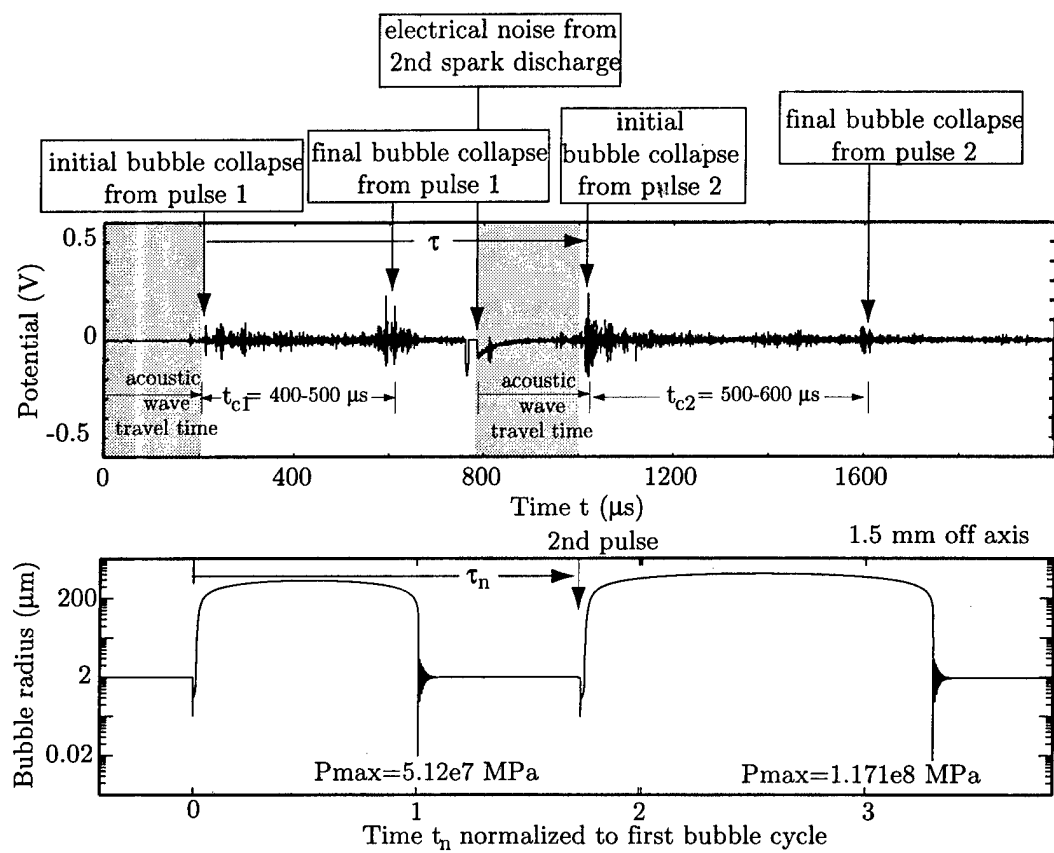


Figure 4.45: PCD detection (a) of two separate bubble cycles with 800- $\mu$ s delay between sparks in rigid reflectors. The first cycle is  $450 \pm 100 \mu$ s. Numerical prediction (b) for second pulse delayed by 8/5ths of the initial bubble cycle.

AS-97-68

The second pulse was strong because the PCD beam was recording on the lithotripter axis and was slightly postfocal where the lithotripter wave was strongest. Figure 4.46 shows the location of the PCD focus relative to the pit path from one shot of the first reflector. The PCD -6 dB beam width was less than 2 mm. PCD location was checked against each foil measurement, as spark jitter could have moved the pit path up to  $\pm 1.5$  mm.

PCD misalignment was addressed in our model by adjusting the relative amplitudes of the two pulses in the sequence. The first pulse amplitude was 28 MPa, and the second was 35 MPa. The first pulse was a representative waveform with the average peak pressure amplitude at 1.5 mm off axis. The second pulse was a representative waveform with the average peak pressure amplitude at  $f_2$ . Figure 4.47 shows the waveforms at an interpulse delay of 10  $\mu$ s. The first pulse amplitude also coincided with the on-axis amplitudes measured in Austin with the NTR hydrophone. These two waveforms in this order were, therefore, used throughout the numerical work in Secs. 4.4 and 4.5.

Figure 4.45(b) shows the numerically calculated R-T curve. Time zero corresponded to when the first pulse struck the bubble. Negative times were an offset incorporated to represent the acoustic travel time. The bubble grew and collapsed in normalized time  $t_n = 1$ . At  $t_n = 8/5$  (800  $\mu$ s/500  $\mu$ s), the second pulse struck the bubble. The bubble grew and collapsed. The second cycle was longer because the second pulse was stronger. The two collapse cycles were independent of one another.

Numerical and measured results both show two collapse cycles resolved in time. Measured signals correspond to collapses of the bubble. Agreement in the time histories is excellent.

In a region off the axis of either reflector, both acoustic pulses were weaker and both cycles shorter. The shorter cycles were also resolved as the delay between pulses changed relatively little with location on the foil. Unless the collapse in one cycle was intense enough to pit the foil, no pitting resulted at the off-axis location. The second pulse arrived too late to intensify the first collapse and pit the foil.

Figure 4.48 shows a foil pitted by, a PCD measurement of, and a calculated R-T curve for two pulses 700  $\mu$ s apart. The foil shows two thin stripes with no indication

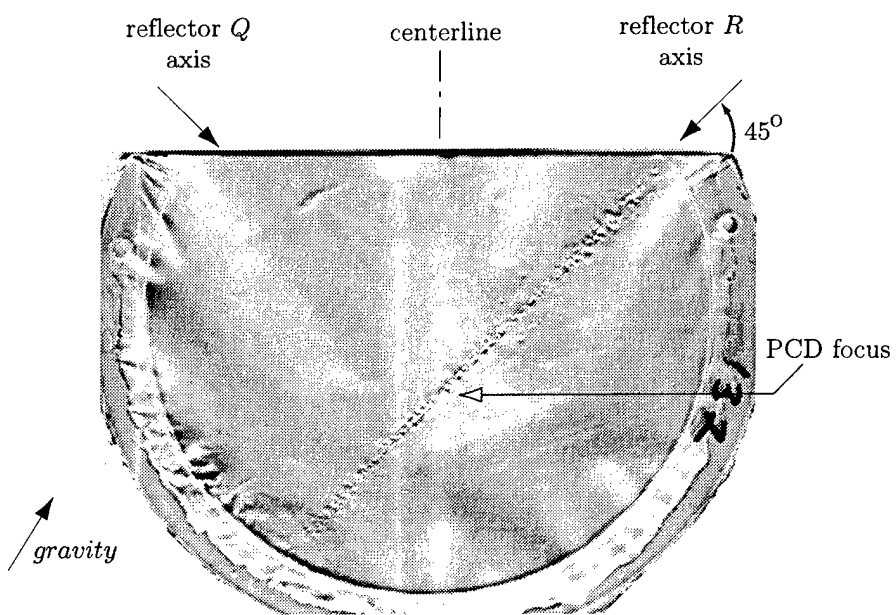


Figure 4.46: Foils pitted by a single shot with a single rigid reflector. The location of the PCD focus is indicated and was 1.5 mm off the axis. The measured collapse cycle is  $450 \pm 100 \mu\text{s}$ . The PCD was on the axis of the other reflector, and the other collapse cycle was  $550 \pm 100 \mu\text{s}$ .

AS-97-69

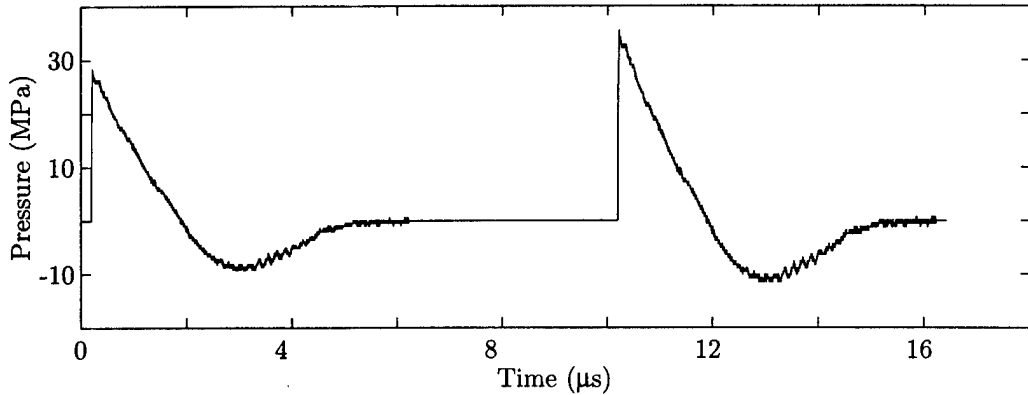


Figure 4.47: Pulse sequence used in numerical calculations. Peak pressure amplitude of the first pulse is 28 MPa, and peak pressure amplitude of the second pulse is 35 MPa. In this example, interpulse delay  $\tau$  is 10  $\mu$ s.

AS-97-70

of kicking or stifling. In the PCD measurement, the collapse of the first bubble was lost in the electrical noise of the second spark. The second collapse cycle was on the short side perhaps because of misalignment due to spark jitter. Numerical results show two resolved bubble cycles. All three results are in agreement; no stifling or kicking occurred.

Figure 4.48(a) shows an additional pit path parallel to the second pit path. The other figures in this section show the second path to varying extents, and Figs. 4.19 and 4.25 show hints of a second path. The additional paths (there is often one on the other side of the axis as well), we believe, are the measurement of cavitation caused by the reflector edge wave. Figure 4.49 shows an example.

The edge wave is a negative pulse converging from the aperture edge. The edge wave is strongest on the axis where the distance from all points on the aperture edge is the same, and, therefore, all scattered signals arrive simultaneously. Simultaneous arrival makes a coherent edge wave. But a coherent edge wave is highly dependent on the alignment, and because of spark jitter, neither the edge wave nor the additional cavitation was often measured. Bailey<sup>42</sup> has demonstrated ways of removing an edge wave. Kargl<sup>70</sup> has also proposed ideas.

The foil in Fig. 4.48 lacks the symmetry of edge wave cavitation on the other side

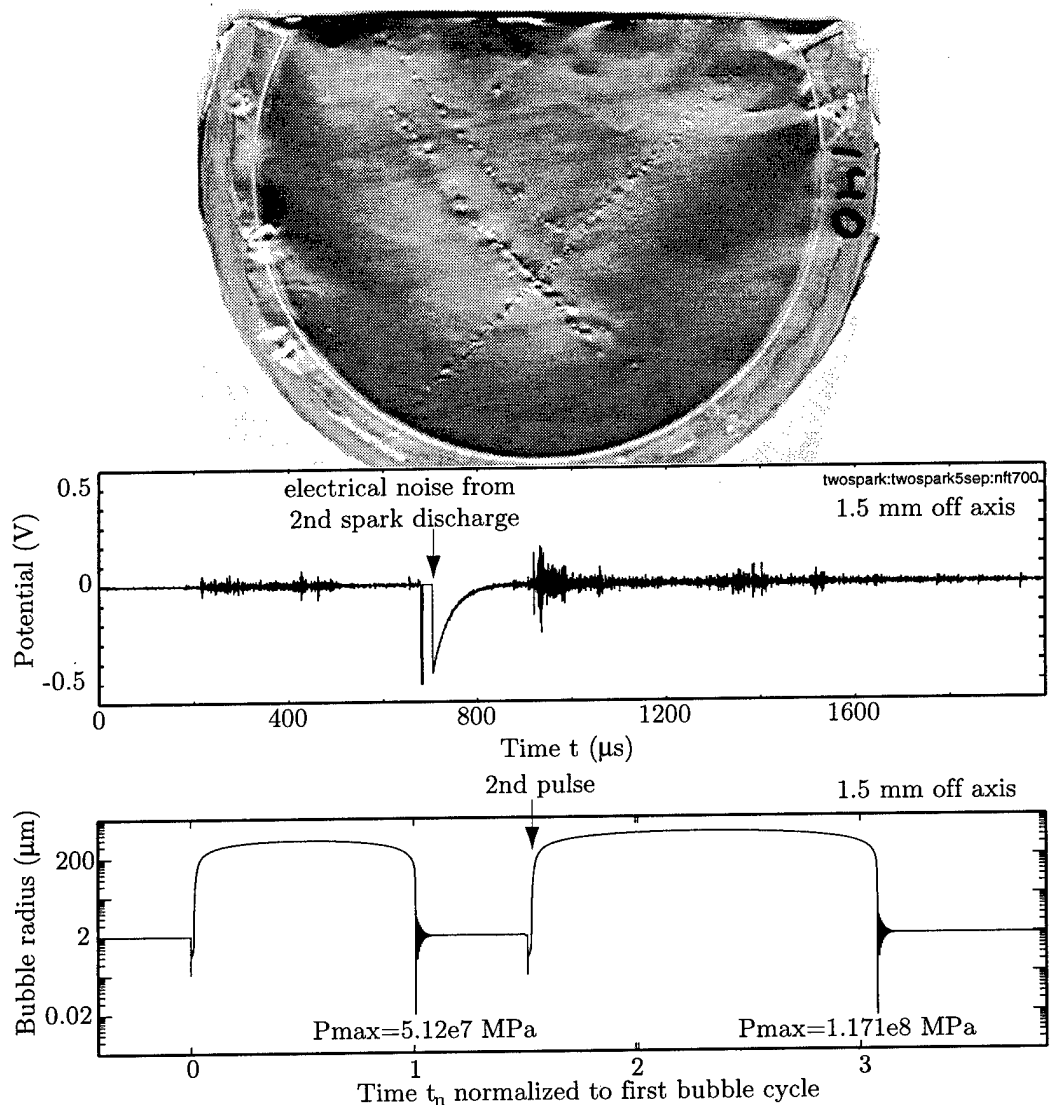


Figure 4.48: Foil (a) and PCD (b) measurement with 700- $\mu$ s delay between sparks in rigid reflectors and the corresponding numerical prediction (c). Two cycles are resolved. The collapse of the first was lost in the electrical noise of the second spark in the PCD data.

AS-97-71

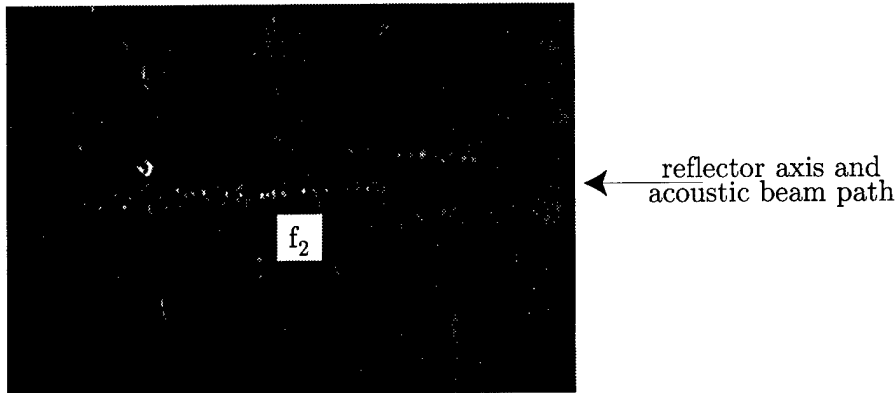


Figure 4.49: Narrow pit path and two edge wave pit paths.

AS-97-72

because the electrode disrupted the symmetry of the reflector bowl. As the foil is shown, the electrode would be lying left to right on the page. So the side, where the electrode blocked part of the reflector edge, did not create a pit path.

Figure 4.50 is of a 600- $\mu$ s delay. Results are the same as results with a 700- $\mu$ s delay. Neither pit path was broadened by interaction of the second pulse with the collapse cycle of the bubble excited by the first pulse. Calculated bubble cycles are resolved, and the PCD measurement shows two separate and independent collapse cycles. The first collapse can be seen in the electrical noise of the second spark.

### Kicking

With delays of 500-200  $\mu$ s, numerical predictions of a shortened first collapse cycle, no second cycle, and intensified collapse agree with PCD measurement of a single shortened collapse cycle and foil measurement of deeper pits and a broader pit path. Data are presented. The complication created by reflection of the second pulse from the bubble cloud produced by the first pulse is addressed.

A 500- $\mu$ s delay intensified pitting as seen Fig. 4.51. Compared to the results of a single shot shown in Fig. 4.46, the first foil path (top right to bottom left) in Fig. 4.51 is slightly broader and the pits are deeper. Broadening is most obvious from 1 cm prefocal to 2 cm postfocal on the first axis, which is where acoustic pressures are highest. The second path and flanking edge wave path are barely visible. We speculate that the

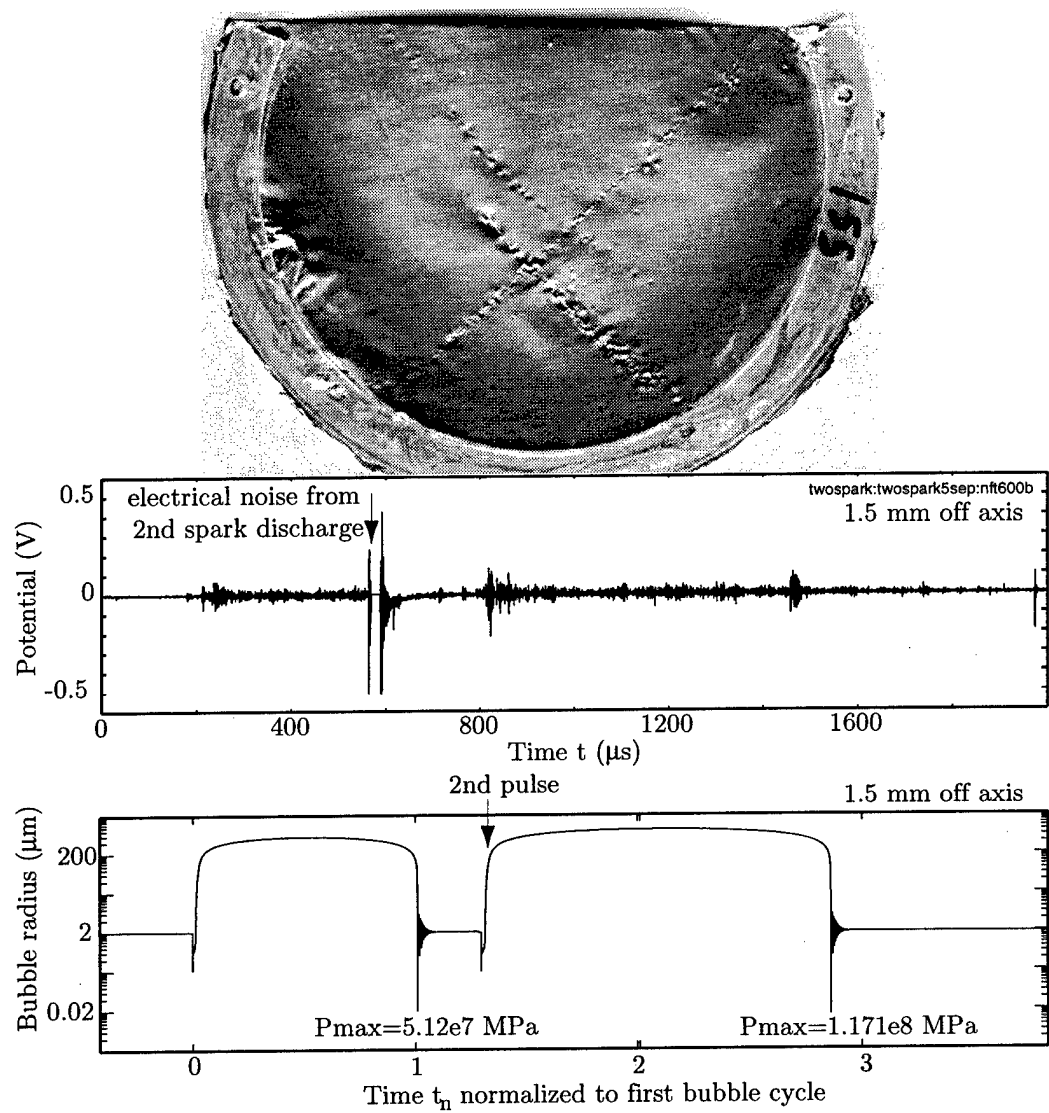


Figure 4.50: Foil (a) and PCD (b) measurement with 600- $\mu$ s delay between sparks and the corresponding numerical calculation (c). Two cycles are resolved. The collapse of the first is detectable in the electrical noise of the second spark in the PCD data.

AS-97-73

pressure pulse radiated by the intensified collapse along the first axis stifled the bubbles along the second axis.

In Fig. 4.51(b), the PCD detected the initial collapse of the first cycle; then a large signal as final collapse of the first cycle and arrival of the second pulse coincided. No second cycle was detected.

In Fig. 4.51(c), the first cycle was calculated. The second pulse arrived as the bubble collapsed. The bubble was kicked:  $P_{\max}$  of the first cycle was tripled. No second cycle resulted. Agreement between PCD measurement and numerical prediction is excellent.

The measurements and calculations are for a bubble slightly off the first axis. Bubbles were kicked, and therefore a slight broadening of the pit path was observed. A bubble much further off axis responded in two resolved cycles as the first cycle was shorter than on axis. Hence, no change off axis was observed.

In Fig. 4.52, the delay was 400  $\mu\text{s}$ . The pit path was roughly twice as broad with deep pits. The PCD measured the first initial collapse and a strong signal 400  $\mu\text{s}$  later when the second pulse arrived. Two signals can be distinguished at 650  $\mu\text{s}$  and 700  $\mu\text{s}$ , one when the second acoustic pulse hit and a second shortly after when the bubble was forced to collapse. The signal when the second pulse hit may in part be due to scattering off the bubbles and in part from microjets created immediately in some bubbles. Scattering and jetting were larger factors because the bubbles are large (approaching the length of the acoustic pulse) at this stage of the cycle. See Delius<sup>71</sup> for a study of a lithotripter pulse incident on a large bubble. No second cycle was detected.

The numerical results in Fig. 4.52 show excellent agreement with the measurements. The arrival of the second pulse hastened the collapse of the bubble and shortened the first collapse cycle. Collapse pressure was doubled.

The first pit path with 300- $\mu\text{s}$  delay was significantly broader (see Fig. 4.53) than the paths produced with longer delays between pulses. The second pulse kicked on- and off-axis bubbles. The second path and edge wave path are visible.

Additional pitting between the second path and the edge wave path (not seen in Fig. 4.48), we propose, was due to reflection from the first bubble cloud. When the

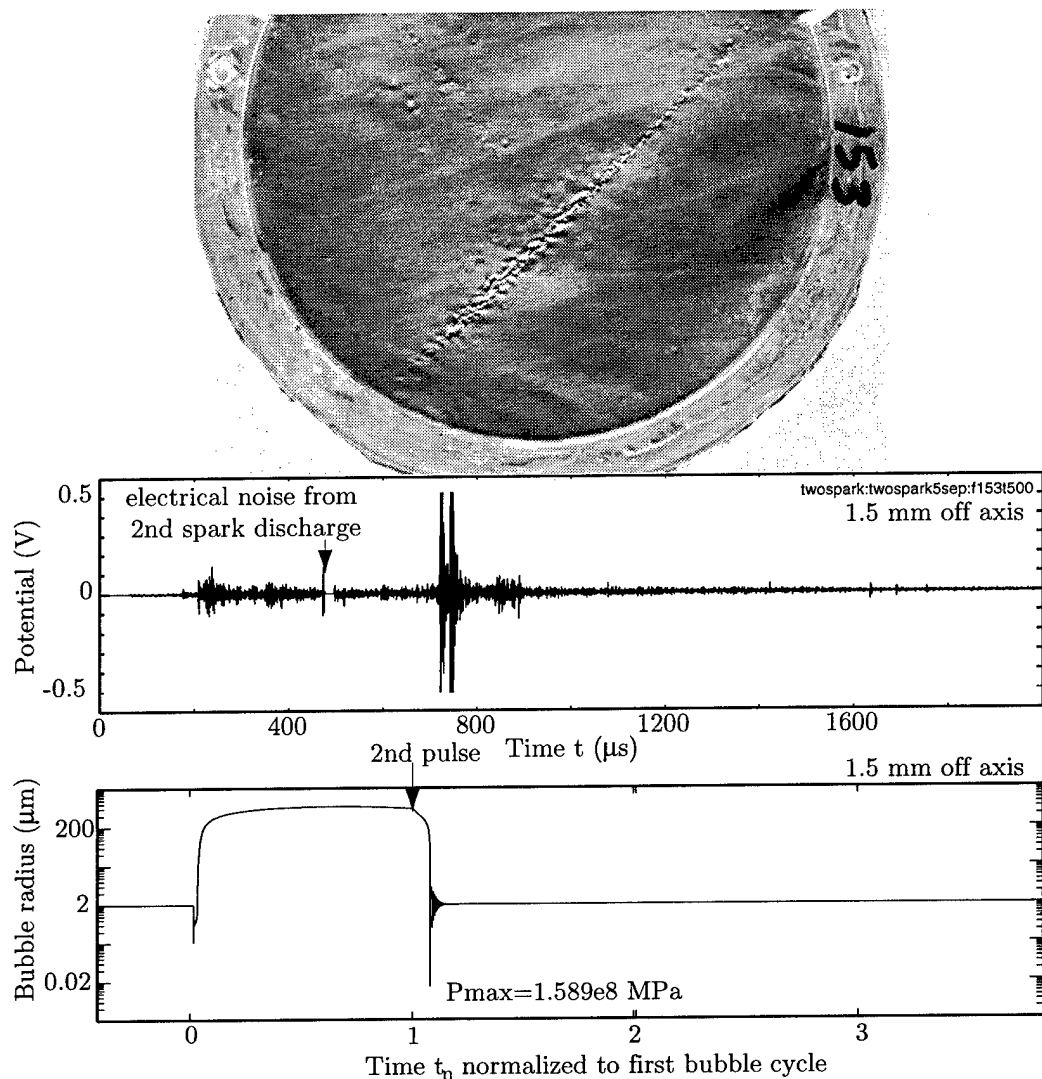


Figure 4.51: Foil (a) and PCD (b) measurement with  $500\text{-}\mu\text{s}$  delay between sparks and the corresponding numerical prediction (c). The second pulse kicked the collapse in the first bubble cycle. No second cycle was measured or calculated.

AS-97-74

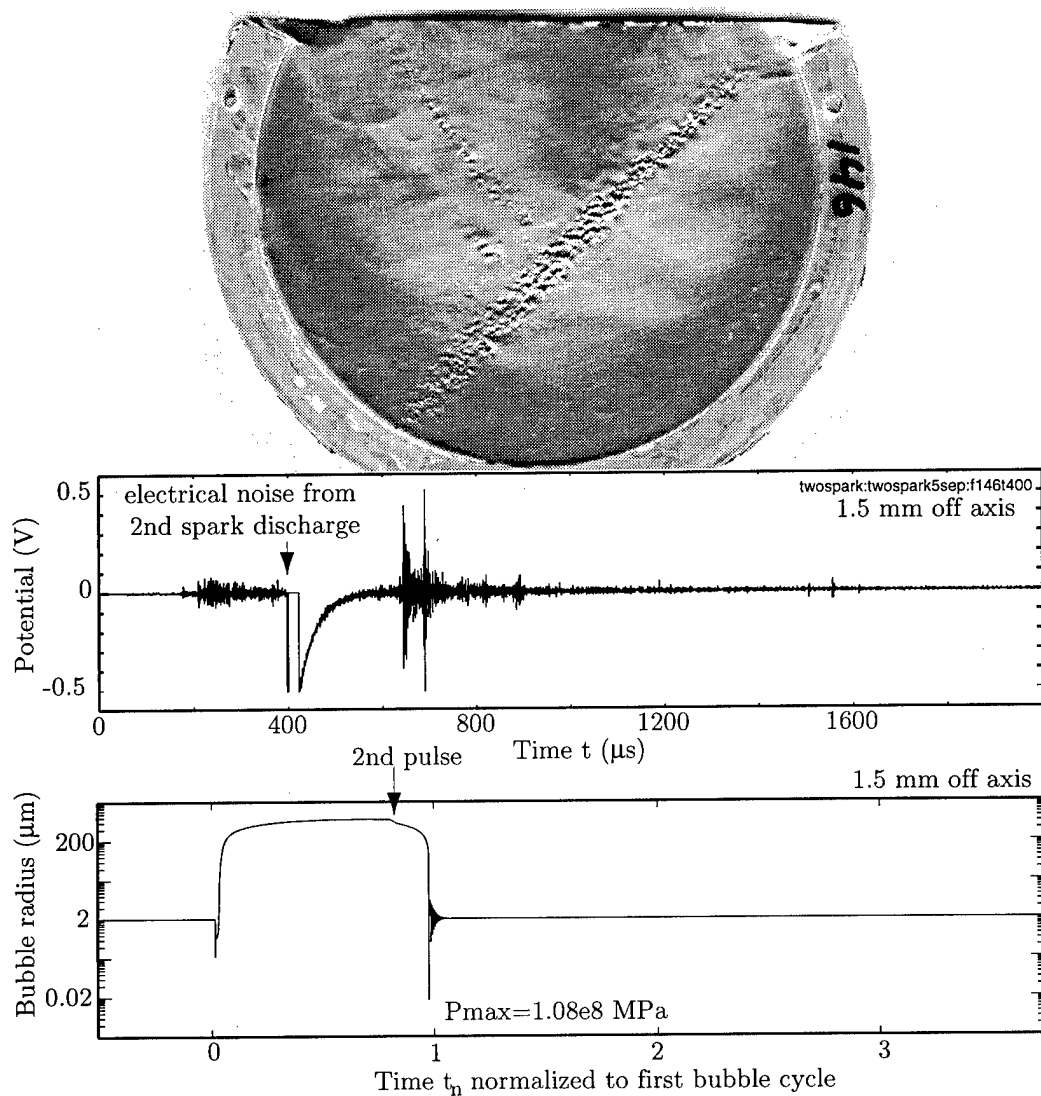


Figure 4.52: Foil (a) and PCD (b) measurement with 400- $\mu$ s delay between sparks and the corresponding numerical prediction (c). The second pulse kicked the collapse in the first bubble cycle. No second cycle was measured or calculated.

AS-97-75

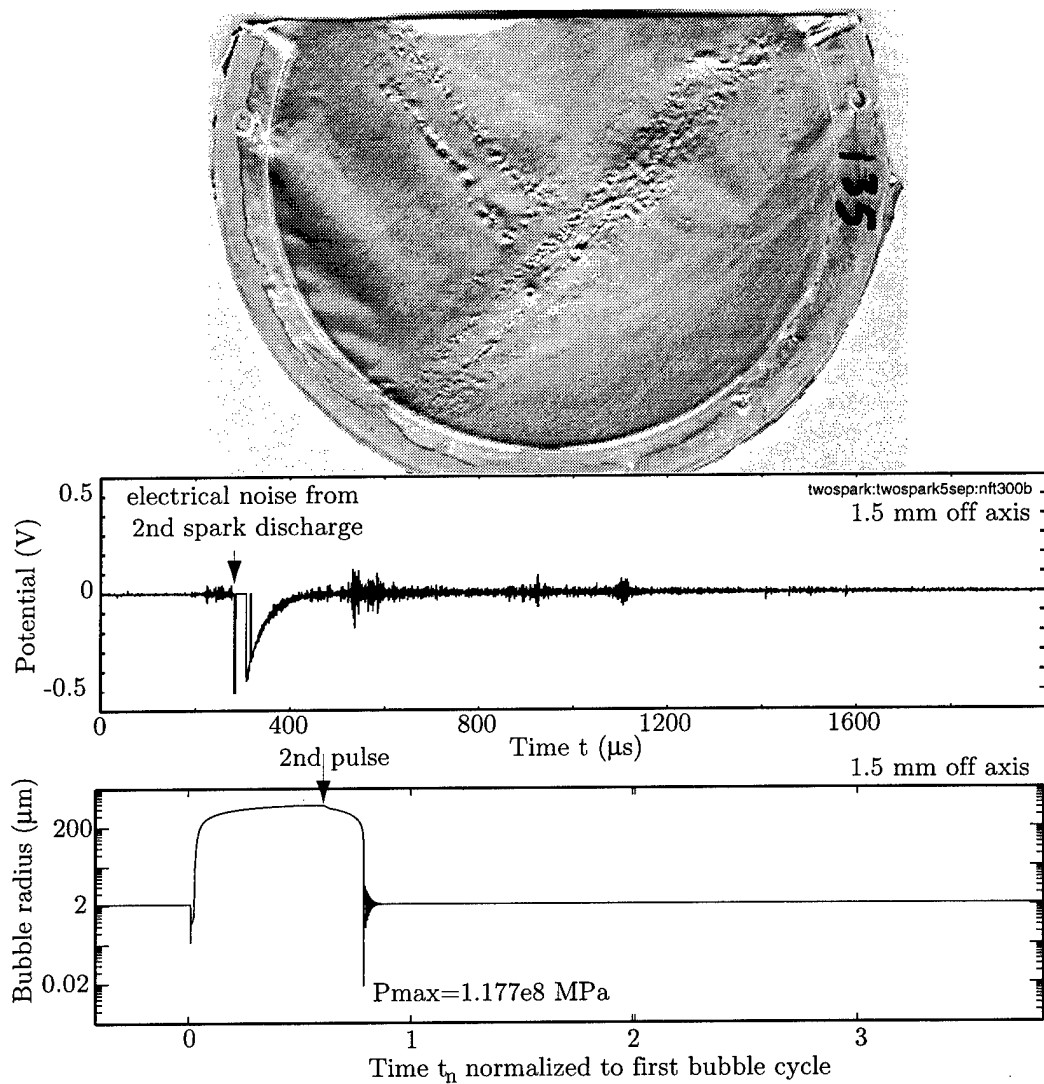


Figure 4.53: Foil (a) and PCD (b) measurement with 300- $\mu$ s delay between sparks and the corresponding numerical prediction (c). The second pulse kicked the collapse in the first bubble cycle. No second cycle was measured or calculated.

AS-97-76

second pulse arrived, the cloud of bubbles from the first pulse was large, and strong reflection was possible. A bubble cloud is pressure release, so the reflected pulse was inverted and contained strong negative pressures. The strong negative phases could have added to cavitation activity on the axis of the second reflector.

Not all rays were reflected; many rays seem to have penetrated the cloud, as evidenced by the broadening of the first pit path on either side of the axis. However, the transmitted pulse on the other side of the cloud was weak, as evidenced by the lack of continued pitting along the second axis beyond  $f_2$ .

A shortened first collapse cycle was measured with the PCD. Some signal is visible at 900  $\mu\text{s}$  and 1100  $\mu\text{s}$ , which may indicate that a few bubbles in the huge cloud were excited by the second pulse. The excited bubbles may have seen a strong negative pressure pulse which would make the bubbles grow. Such a pulse could be the lithotripter pulses reflected or diffracted from bubbles in the cloud.

The banding within the first pit path is interesting. Banding, or stripes, within the path are most obvious postfocally. An explanation may be found in the numerically calculated  $P_{\max}$  versus  $\tau_n$  curve in Fig. 4.34. The curve has a sharp peak when the normalized interpulse delay  $\tau_n$  is near 1. In this brief time window, the positive portion of the second pulse kicks the collapsing bubble most intensely. Collapse happens before the bubble sees the negative portion of the wave, which would act to soften or "catch" the collapse. Therefore, a band may have resulted because an off-axis bubble caught just at the end of its cycle collapsed much more violently than its neighbors to the outside with slightly shorter cycles or to the inside with slightly longer cycles. The shorter cycles collapse without the kick of the second pulse. The longer cycles see a catching by the negative pressure phase of the second pulse, which counteracts the kicking by the positive pressure phase.

Some of the effect of catching can be seen in the numerical results of Figs. 4.52 and 4.53. The collapse pressure in Fig. 4.53 is actually slightly higher than in Fig. 4.52. Nevertheless, the principle result that the second pulse hastened the collapse of bubbles and produced no second growth cycle was observed in the results presented in both Figs. 4.52 and 4.53.

In Fig. 4.54, an interpulse delay of 200  $\mu\text{s}$  produced a broad first pit path. The

second pulse arrived early and kicked off-axis bubbles before they collapsed. The intensified off-axis collapses pitted the foil. The path was therefore wider. Large pits appear along the axis of the second reflector. The large size may indicate a powerful spark in reflector two. Large pits may also be the result of reflection of the second pulse from the bubble cloud on the axis of the first reflector. The reflection from the pressure release surface may have accelerated the growth not the collapse of bubbles on the axis of the second reflector. The bubbles grew larger, collapsed harder, and produced larger pits. The second pit path stops at the first path, indicating weak transmission through the bubble cloud.

The PCD data show a large collapse signal, perhaps from so many bubbles collapsing. On the other hand, perhaps the second spark was very powerful, as evidenced by the large pits on the axis of the second reflector. A single collapse cycle is very obvious. A second strong collapse cycle was not measured, although a weak signal appeared at 800  $\mu$ s. The weak signal, we speculate, was the measurement of the collapse of an isolated bubble within the cloud not collapsed by the second pulse but excited by a reflected pulse.

Again numerically, one shortened cycle was predicted. The collapse pressure was increased 150%.

### **Stifling**

With an interpulse delay of 100  $\mu$ s, on-axis and near-axis bubbles were stifled by the second pulse.

In Fig. 4.55, the pit path is broad, but pits appear very shallow. The foil was wrinkled in post-experiment handling, so little can be said about the pit path on the axis of the second reflector.

The PCD results and numerical data show one collapse. The collapse was stifled. The calculated maximum pressure in the bubble was reduced by a third. The pressure was only 1.5 times the pressure of a bubble excited by a pressure-release reflector. The pits appear only slightly bigger than with the pressure-release reflector. A lower pressure is in agreement with shallower pits.

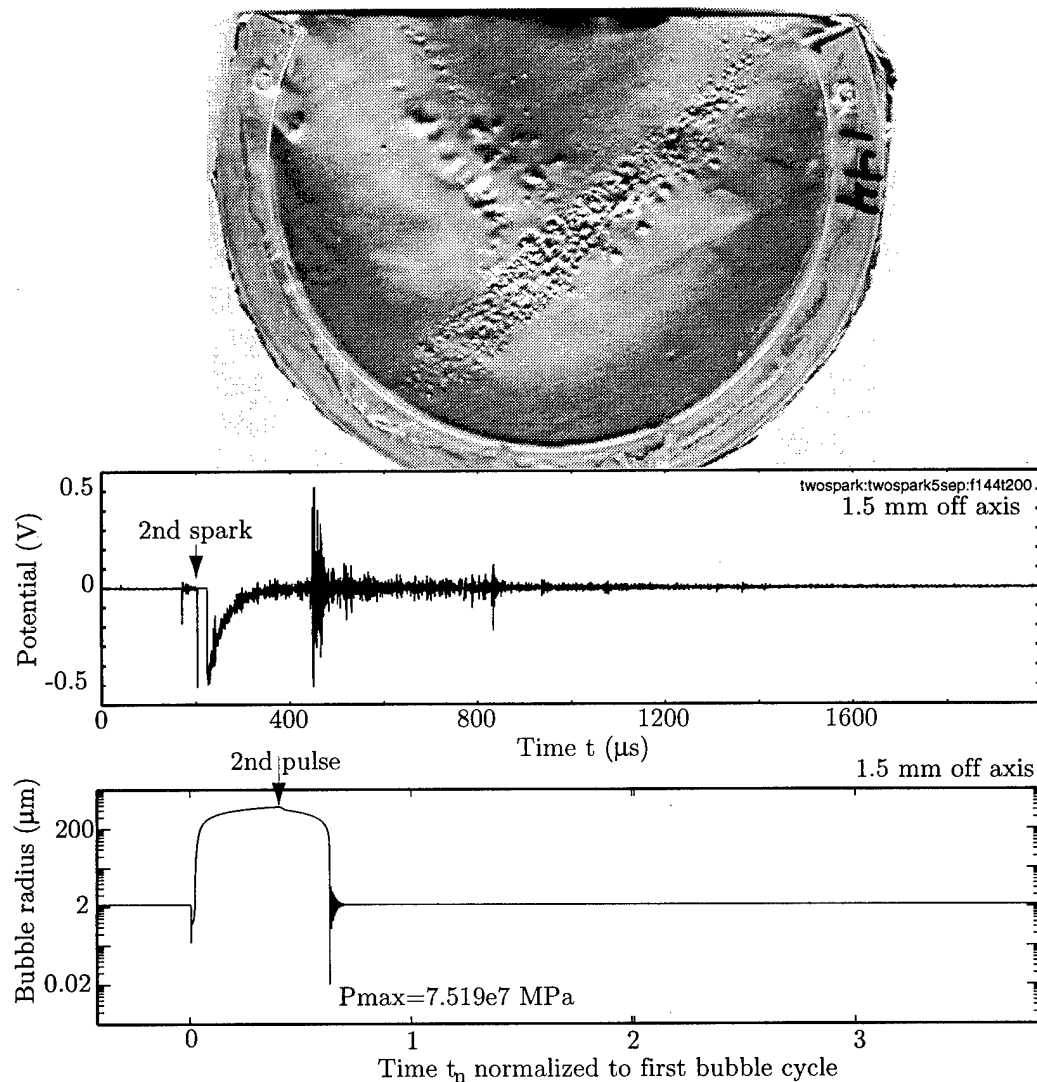


Figure 4.54: Foil (a) and PCD (b) measurement with 200- $\mu$ s delay between sparks and the corresponding numerical prediction (c). The second pulse forced the early collapse in first bubble cycle, but intensification is negligible. No second cycle was measured or calculated.

AS-97-77

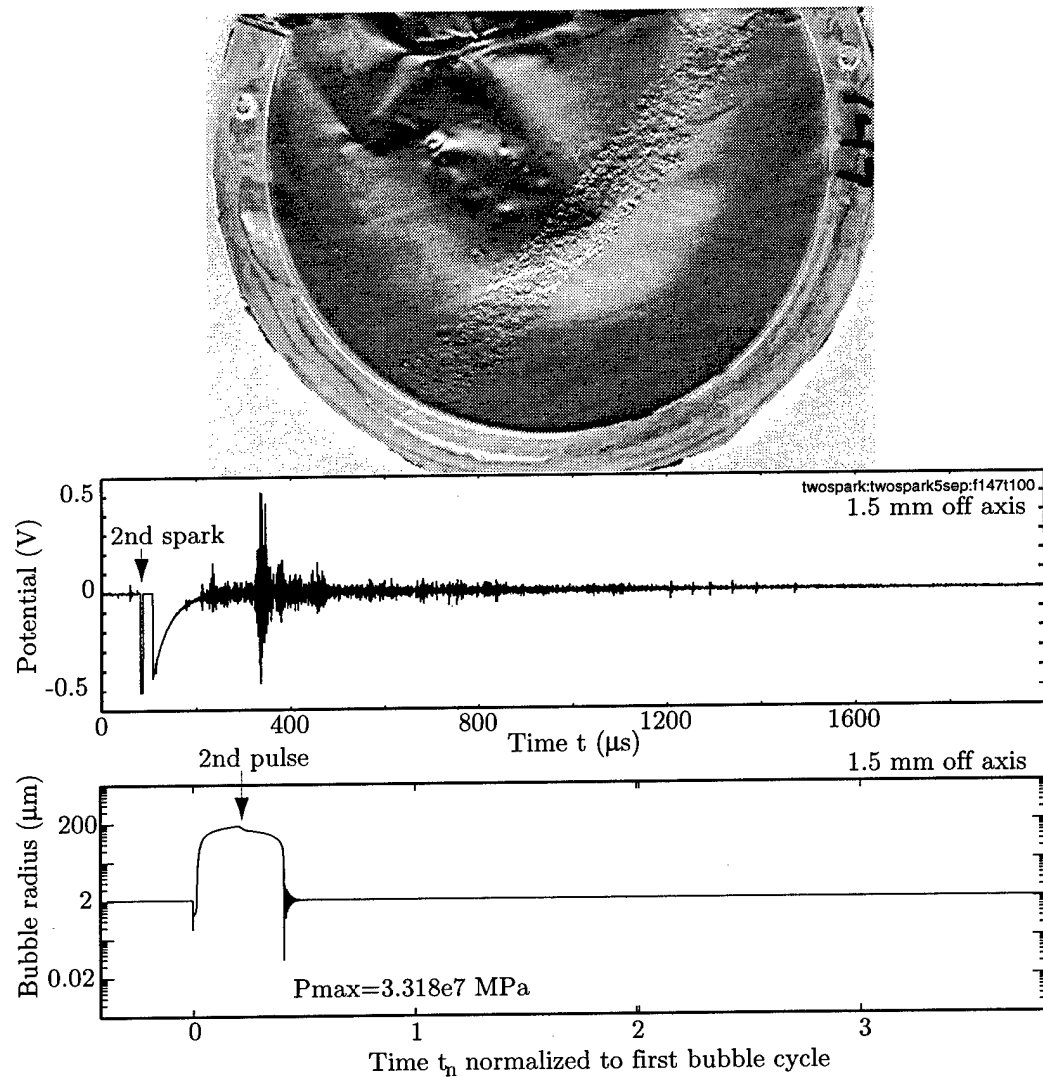


Figure 4.55: Foil (a) and PCD (b) measurement with  $100\text{-}\mu\text{s}$  delay between sparks and the corresponding numerical prediction (c). The second pulse stifled the collapse in first bubble cycle. No second cycle was measured or calculated.

AS-97-78

Although measurement and theory show near-axis bubbles were stifled, off-axis, bubbles were sufficiently kicked to pit the foil. Thus, the path was broad.

#### 4.5.2 Bubble dynamics versus interpulse delay–part II

In this section, measurements were made of one interpulse delay,  $\tau = 0$ , but at two different PCD locations. When the sparks were fired simultaneously, the most dramatic intensification and mitigation of cavitation was observed (see Figs. 4.43 and 4.44). Deep pitting was observed on the centerline. The appearance of pits on the centerline we attributed to pressure doubling (i.e., superposition of the two pulses). The disappearance of the pit paths of the axes of the reflectors, we have explained as stifling. Measurements and calculations are now presented for a centerline location and an axial location.

The two foils presented measured deep pitting on the centerline and cancellation of pitting along the axes. However, both foils contain a pit path that resulted from an extra spark in the right reflector. The extra spark was 3-5 s after the simultaneous pair of discharges. The experimenters watching the foils saw the centerline stripe appear. Then as one experimenter tried to discharge the system, the other saw the extra spark create a pit stripe along the reflector axis. The foils are, therefore, not as distinctly marked as those in Figs. 4.43 and 4.44, but the extra streak was helpful in verifying the alignment of the PCD focus on the axis of the right reflector. PCD recording was completed before the extra spark discharge took place.

In the numerical model, the same two pulses seen in Fig. 4.47 were used, although in the experiments the location of the PCD changed. Therefore, direct comparison to the results in Secs. 4.4 and 4.5 may be made. A predicted drop or rise in  $P_{\max}$  was not due to choice of a different waveform but instead was the result of stifling or kicking. The applicability of the model waveforms to the situation measured is addressed.

#### Passive cavitation detection where pits appeared

In the results in this section, the PCD was focused on the centerline 6 mm in front of  $f_2$ . The location was sufficiently far off axis that no collapse signal or pitting was measured at the location when either spark was fired singly. Acoustic peak pressure

amplitude for each reflector was 24 MPa, 2/3 of the axial peak amplitude. With pressure doubling caused by simultaneous spark discharge, the peak pressure amplitude at the location was 4/3 the axial peak amplitude. Our model slightly overestimated the peak pressure amplitude because we used a pulse with 80% amplitude and a pulse with 100% amplitude. Because the -6-dB region of negative pressure phase is broader than the positive-pressure region, pressure doubling of the negative phases yielded more than 1.5 times the peak amplitude of the negative phase of the axial waveform. In the model, the peak amplitude of the negative phase was 1.8 times the axial negative peak. Our overestimate of the negative phase is less than our overestimate of the positive phase. Because the period when the strong negative phase exists is brief (i.e., the time when the pulses overlap), the tensile strength would arguably play a minor role in reducing the large negative pressure.

Simultaneous firing yielded the huge pits on the centerline of the foil pictured in Fig. 4.56. The corrupting streak from the extra spark is also seen. The PCD recorded an 800  $\mu$ s collapse cycle, nearly twice as long as with one pulse on axis. Similarly, in the numerical calculation, the bubble duration was nearly doubled. The pressure of collapse was quadrupled and correlates with the huge pits recorded on the foil. The slight overestimation in duration of the numerically predicted cycle is due to the use of slightly large pulses in the model. Pressure doubling on the centerline yielded a nearly doubled collapse cycle, which produced an intensified collapse.

The measurements and calculations support our use of pressure doubling to explain appearance of pits along the centerline.

#### **Passive cavitation detection where pits disappeared**

Figure 4.57 presents data taken where the PCD was 8 mm postfocal on the axis of the right reflector. Pitting was not measured at the location when two sparks were fired simultaneously but was measured when sparks were fired singly or with a delay between them. Pitting that appears in Fig. 4.57 was the result of the extra inadvertent spark in the right reflector.

At the location, the PCD measured two signals separated by  $550 \pm 100 \mu$ s when just the right reflector was fired but only a single signal when both sparks were triggered

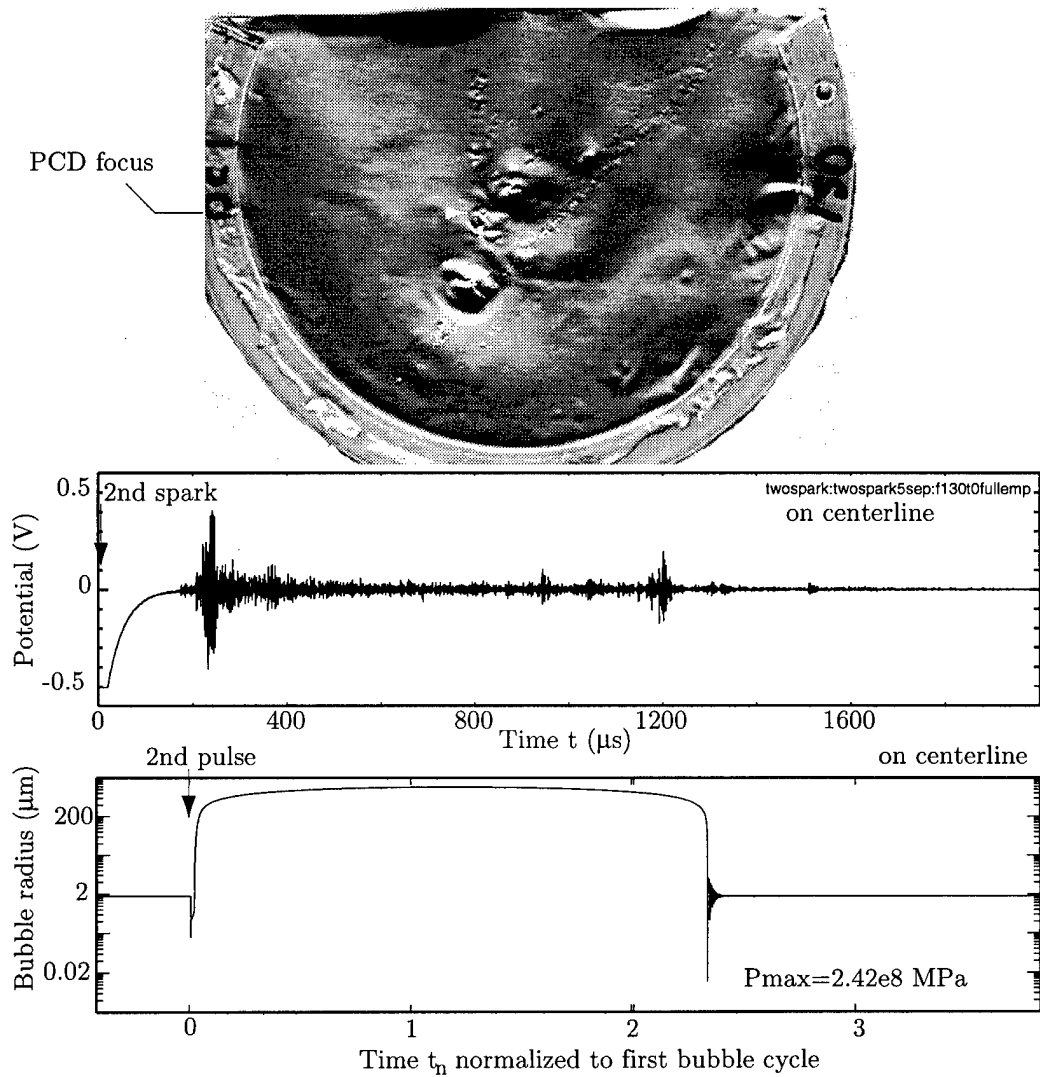


Figure 4.56: Foil detection (a), PCD measurement (b), and numerical calculation (c) of simultaneous pulses. PCD was located on the centerline just in front of  $f_2$ . Huge pitting, one long bubble cycle, and big collapse pressures are in agreement. Foil data were corrupted by a delayed additional spark in the first reflector, which made the streak along axis 1 where the simultaneous pulses had not produced pits.

AS-97-79

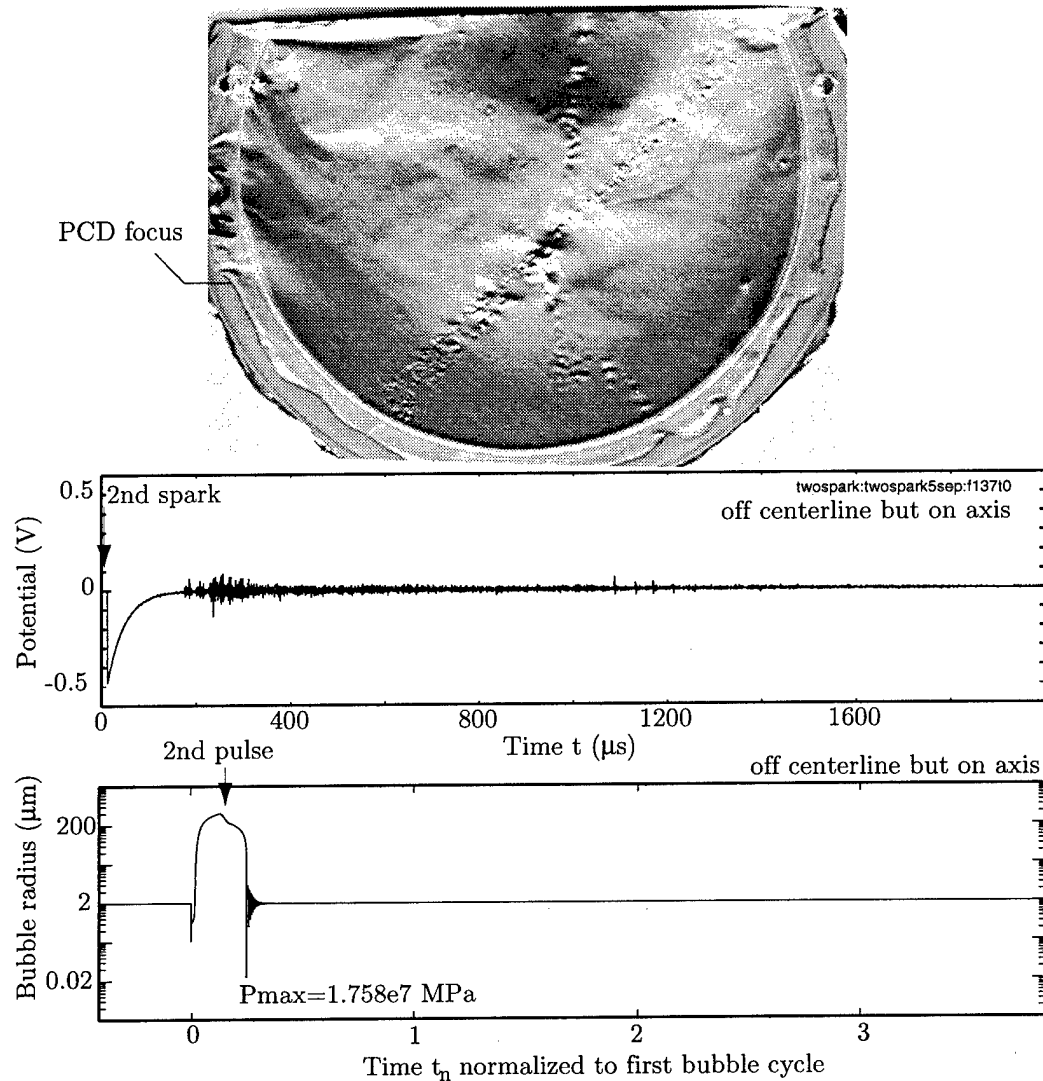


Figure 4.57: Foil detection (a), PCD measurement (b), and numerical calculation (c) of simultaneous pulses. PCD was located 6 mm off axis 1 and on axis 2 behind  $f_2$ . Foil data were corrupted by a delayed additional spark in the first reflector, which made the streak along axis 1 where the simultaneous pulses had not produced pits. No pitting (as measured before the inadvertent pulse), no long bubble cycle, and weak collapse pressures are in agreement.

AS-97-80

simultaneously. The long growth cycle and strong collapse signal were shrunken into one short cycle and one small collapse signal. In the single reflector case, a long bubble cycle was measured, and pitting was recorded. The disappearance of the long bubble cycle supports the argument that the bubbles are stifled.

In the simultaneous dual spark case, at the measuring location, pulses arrived with a short delay between them. The second pulse stifled the growth of the bubble, and one signal was measured. Unresolvable within the one signal are the signal from the first pulse arrival, the signal from the second pulse arrival, and the forced stifled collapse of the bubble. Neither the normal cycle produced by one reflector nor the long cycle caused by pressure doubling was measured. Simply, the one stifled collapse was recorded.

The numerical prediction also shows only a shortened muted bubble cycle. In the model, the 28 MPa pulse was followed 13  $\mu$ s later by the 35 MPa pulse. The pulse amplitudes and the interpulse delay model the pulse sequence measured at the location. The PCD was slightly off axis of the left reflector and to the left of the centerline. The weaker pulse (28 MPa) of the left reflector arrived first, and the stronger pulse (35 MPa) from the right reflector on the axis of the right reflector arrived 13  $\mu$ s later. The result was a stifled collapse where  $P_{\max}$  was reduced by nearly two-thirds. The reduced maximum pressure of  $1.75 \times 10^7$  MPa was below the pitting threshold of  $2.14 \times 10^7$  MPa. No pitting was observed at the location off the centerline. See Fig. 4.44 for examples without the corrupting pit path from the extra spark.

#### 4.6 Pair of rigid reflectors facing each other

The section contains results with simultaneous sparks in two rigid reflectors that were  $180^\circ$  apart. The motivation was that if two reflectors at  $90^\circ$  produced a line of cavitation, would two reflectors at  $180^\circ$  produce a spot of cavitation?

The configuration is shown in Fig. 4.58. The two underwater spark gaps were configured in series. Clean discharge was not obtained. The first spark gap produced two half-amplitude sparks 2-4  $\mu$ s apart, and the second spark gap yielded one full-amplitude spark. We speculate that the first spark arced and partially discharged the capacitor, but the second spark gap had an inherent delay before breaking down

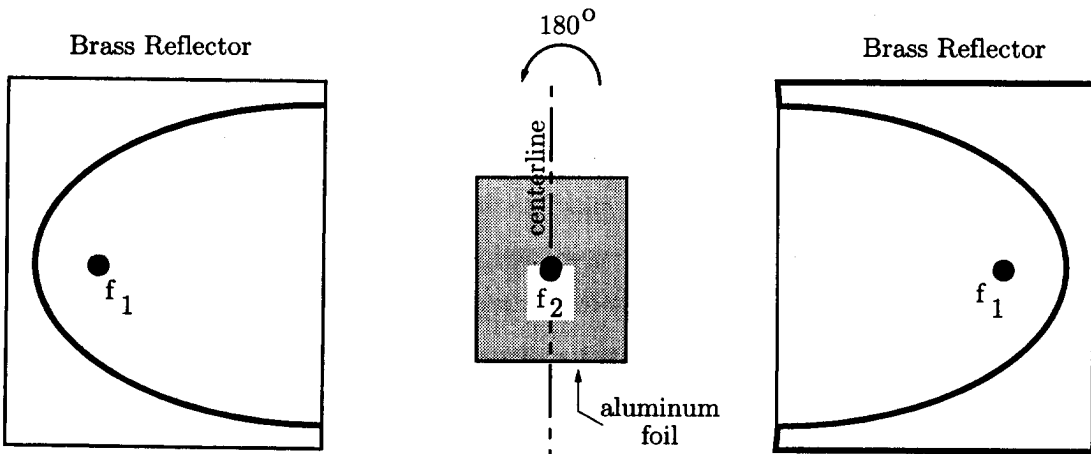


Figure 4.58: One hundred and eighty degree configuration of two rigid reflectors. Foil was placed at  $f_2$ . Spark gaps were connected in series.

AS-97-81

and closing the two-gap circuit. When the spark in the second gap arced, the rest of the capacitor energy passed through both gaps. Hence, one big spark in the second reflector and a second half-amplitude spark in the first reflector resulted.

In future experiments, two independent electrical systems will be used as in the  $90^\circ$  experiments, or the second gap in the series configuration will be modified. One proposed modification is making the gap an exploding wire electrode. In an exploding wire electrode, a thin wire is inserted between the points of the electrode. With sufficient current, the wire explodes, and sound is generated. The wire reduces resistance in the second spark gap, so when the first gap discharges, conduction immediately results in the second. Clean discharge through both gaps may be obtained. Keilman<sup>72</sup> at Applied Physics Laboratories, Seattle, Washington, has constructed an electrode that operates in a manner similar to the exploding wire but without the difficulty of replacing the wire each shot. Keilman's electrode has a fine jet of saline solution between the electrode points. The saline solution has low resistance and substitutes for the wire.

Results presented were recorded without the exploding wire, but nevertheless, show a localized region of intense pitting. With the modifications, we think we can further shrink the region. Figure 4.59(a) contains the long pit stripe produced by the second

reflector with the first reflector blocked. Figure 4.59(b) contains the shortened T-shape section of pitting produced with both reflectors fired simultaneously. Two foils for each case are shown. Much of the long line of pits was canceled with simultaneous firing. The pulses arrived at canceled locations sufficiently far apart to cause stifling. On the centerline, the pulses from the two reflectors superimposed, and pits were deep. The crossbar of the T-shape resulted because superposition intensified collapse off axis as well. The crossbar, however, is only as wide as the effective beam width of the reflectors, in this case  $\sim 1$  cm. The base of the T-shape, we feel, resulted from the unequal discharge of both sparks. The base was on the side of the two small pulses. The strong single pulse from the second reflector followed the weaker first pulse from the first reflector. As discussed in Chapter 2, when the second pulse was much stronger than the first pulse, kicking not stifling resulted (see Fig. 2.10). The single spot to the left of the centerline may also have resulted from unequal discharge and indicates a small region where kicking occurred.

In some instances, the crossbar alone was measured as shown in Fig. 4.60. The result may have been due to small changes in alignment caused by spark jitter. The cavitation field, a slice of which was represented on the foil as a T-shape, had a thumbtack shape in the three dimensions. Slices that included the stem of the tack shape were T-shaped. Slices that missed the stem and cut across only the head of the tack shape recorded only a line normal to the acoustic beams.

Figure 4.60 may also present the measurement of the "cavitation spot" we sought to create. The two sparks may have discharged cleanly, and the pulses canceled each other everywhere except where the tails of the pulses superimposed. Since both discharge and spark jitter are random processes, either misalignment or cancellation explains why only a few lines were measured in the place of T-shapes. The measurement of a lone line is, nevertheless, exciting and encouraging.

The series configuration of the two spark gaps complicated our measurement above by making two sparks in the first reflector. However, the two sparks 2-4  $\mu$ s apart in the first reflector were used with the other reflector blocked to demonstrate another configuration whereby cavitation could be reduced. Figure 4.61 shows an image of a foil treated with the short sequence of two pulses from one reflector. The second pulse

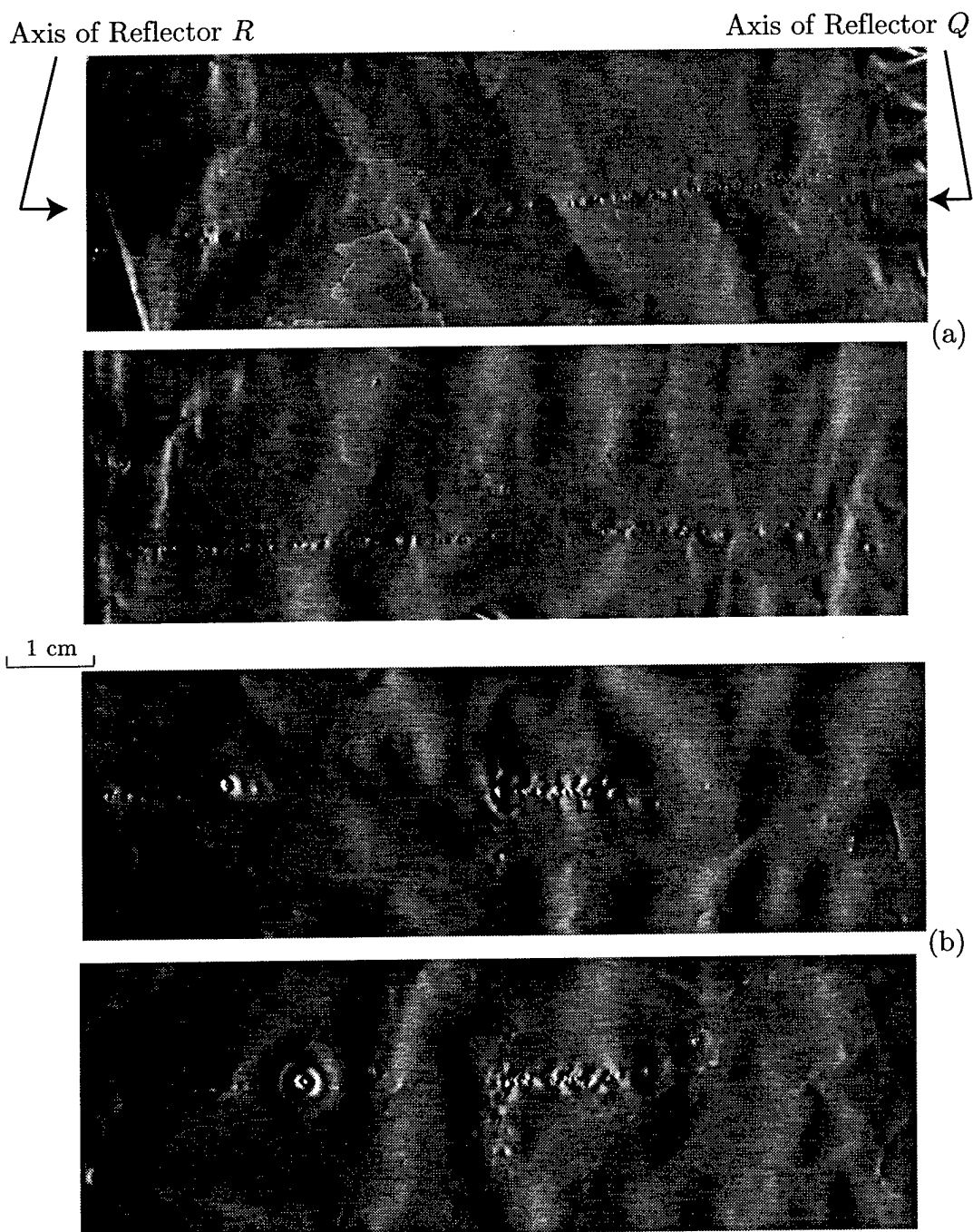


Figure 4.59: Foils pitted: (a) single spark in reflector *Q* and (b) simultaneous sparks in two rigid reflectors (*R* and *Q*) facing each other. The simultaneous sparks cancel most of the long streak of pits seen in (a) and intensify a short region along and across the beams at  $f_2$ .

AS-97-82

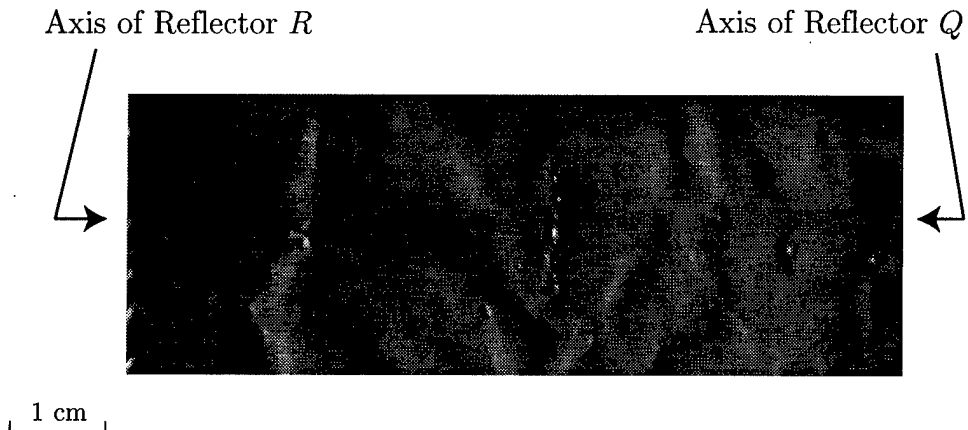


Figure 4.60: Detection of pitting solely normal to the two beam paths of simultaneously fired pulses.

AS-97-83

stifled the cavitation produced by the first, and no pitting was recorded anywhere on the foil.

#### 4.7 Applications-related results

In this section, some results with a modified clinical lithotripter are presented. As in Sec. 4.6, the experiments have direct application to lithotripsy treatment and research. Discussion of applications is included in Chapter 5 but spills over into this section.

##### 4.7.1 In vitro measurement of a modified clinical lithotripter

A pressure-release ellipsoidal shell – reflector  $D$  in Table 3.1 – was inserted in the reflector bowl of the Dornier HM3 lithotripter. Thus, the rigid bowl was transformed into a pressure-release bowl. A photograph of the configuration appears in Fig. 4.62. The balloons on either side of the reflector house the lithotripter's fluoroscopy system used clinically to image the stone. The mask was secured with duct tape. A needle hydrophone in an acrylic baffle is located at  $f_2$  in the photograph. Water was added to the tank after the photograph was taken.

Figure 4.63 shows the waveforms measured with and without reflector  $D$  inserted in the reflector of the Dornier HM3 lithotripter. Without the mask, the unmodified

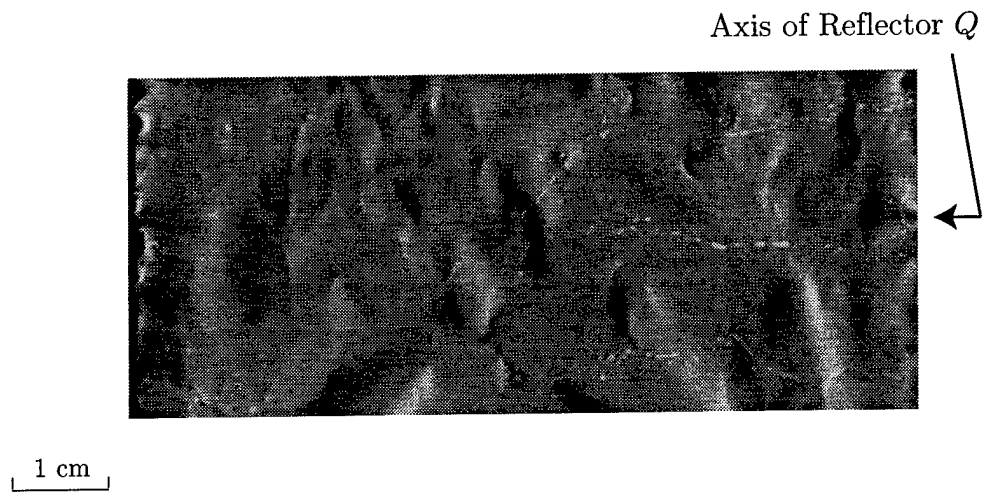


Figure 4.61: No observable pitting produced by two sparks in one bowl and  $\sim 2 - 4 \mu\text{s}$  apart. The second pulse stifles the bubble growth caused by the first.

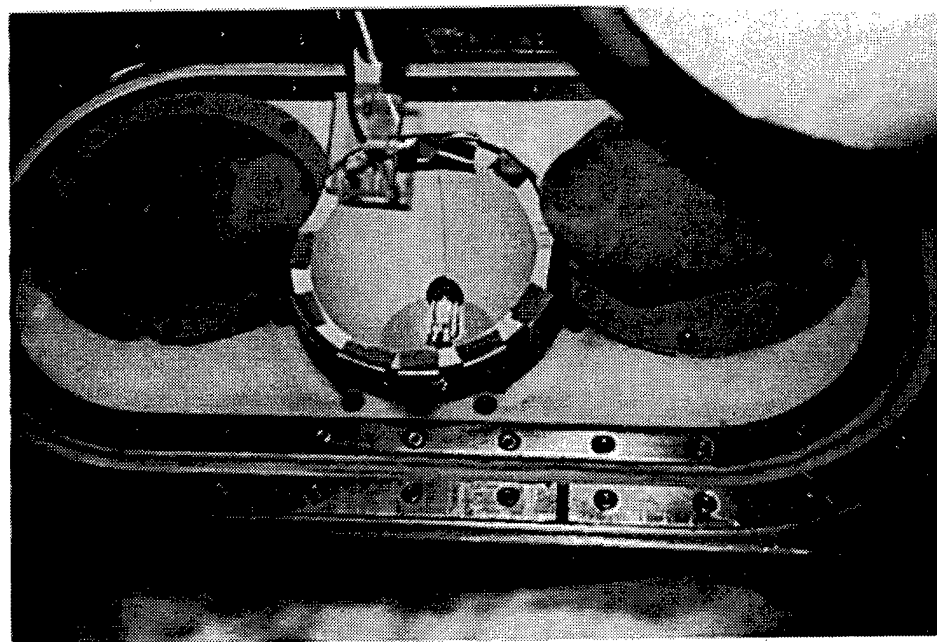


Figure 4.62: Photograph of the pressure-release mask *D* inserted in the reflector of the Dornier HM3 lithotripter.

AS-97-85

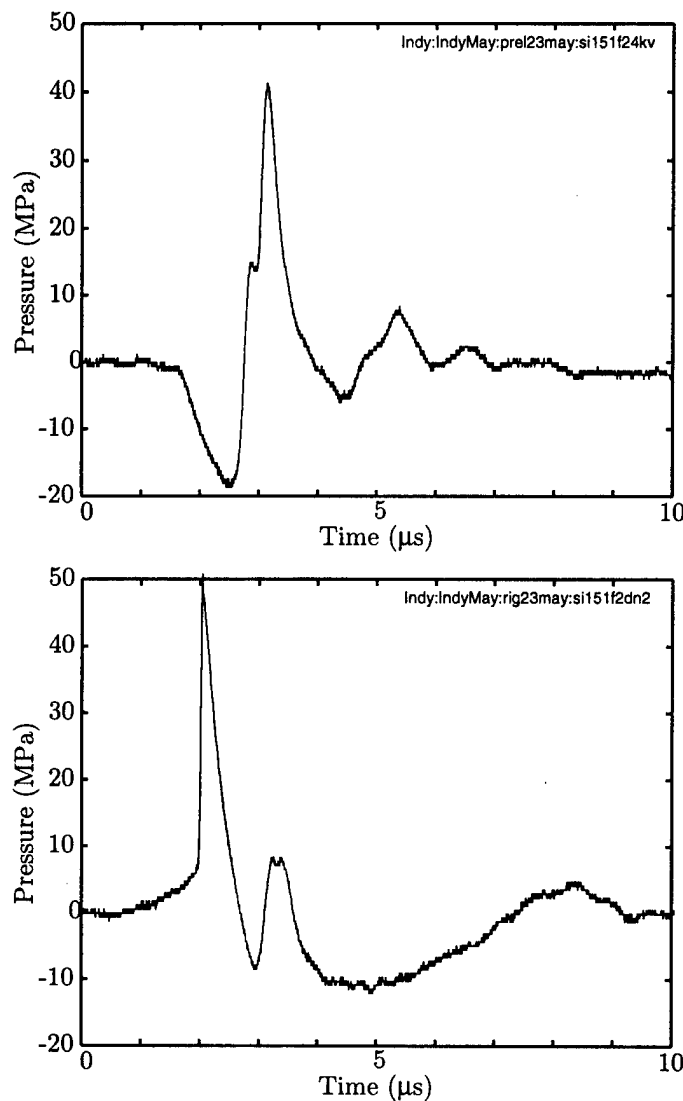


Figure 4.63: Waveform measured with pressure-release masks (a) placed over Dornier HM3 brass reflector and unmodified Dornier HM3 reflector. Both waveforms contain a strong positive phase. The total positive pressure excursion in (a) is greater. Peak negative pressures in (a) are less than -18 MPa.

AS-97-86

reflector produced a wave very similar in shape and amplitude to that with the experimental lithotripter. With mask *D*, the shape was nearly the same as the waveforms measured with the pressure-release reflectors in the experimental lithotripter. The amplitude of the negative-pressure phase with mask *D* was huge,  $< -18$  MPa. Reflection and focusing may have been improved by the solid support of the brass reflector behind the mask. The pressure-release reflectors alone used without the brass support may have deformed when struck by the incident acoustic wave. Deformation could have meant reflections were not as perfectly directed to  $f_2$  in the unsupported case.

The amplitude of the negative-pressure phase measured with the pressure-release mask was 1.5 times larger than with the rigid reflectors. Christopher<sup>62</sup> proposed that the negative phase of the rigid-reflector wave was limited by the tensile strength of water. Lower negative values are possible with the pressure-release-reflector waveform because tensile yield is inversely related to pulse duration. The negative phase of the pressure-release-reflector wave is short, so large negative pressures are not only possible but are measured.

The peak amplitudes of the positive pressure phase in the waveforms in Figs. 4.63(a) and (b) are 42 MPa and 50 MPa, respectively. The positive phases of the waves were very comparable in amplitude and shape. The amplitude is in fact greater with the pressure-release mask than with the rigid reflector when total positive pressure excursion is considered. The pressure in (a) rose from -18 to 42 MPa, which was a 60 MPa positive pressure excursion. In (b), the pressure rose from zero (ambient) to 50 MPa for a total excursion of 50 MPa.

Surface pitting of foil and PCD measurements are not presented for the Dornier HM3 because they did not differ noticeably from the same measurements in the experimental lithotripter. Cavitation was much less intense with the pressure-release reflector than with the rigid reflector.

#### 4.7.2 In vivo measurement of a modified clinical lithotripter

The waveforms produced by the pressure-release mask and the rigid reflector were measured *in vivo*. A hydrophone was surgically implanted in a pig. The pig was then treated in the lithotripter, and waveforms were simultaneously recorded. The

hydrophone was a PVdF membrane on a plastic ring 3 cm in diameter. The experiment was designed and directed by R. O. Cleveland and was described for a rigid reflector by Cleveland *et al.*<sup>64</sup>

The small size of the membrane means that only the first couple microseconds of the waveform are accurate. After that, reflections and membrane waves corrupt the signal. Figure 4.64 shows the rigid-reflector waveform measured *in vivo* behind the pig kidney at  $f_2$ . Figure 4.65 shows the pressure-release-reflector waveform measured *in vivo* behind the pig kidney at  $f_2$ . Both waveforms have retained the same shape measured *in vitro*. Tissue caused attenuation but very little distortion of the waveform. Not enough evidence has been collected to determine if the greater attenuation seen in the pressure-release-reflector waveform in Fig. 4.65 is a general effect of the waveform or a particular effect of the experiment.

#### 4.7.3 In vitro measurement of a partially modified clinical lithotripter

Measurements were made with half a pressure-release ellipsoidal shell inserted in the reflector bowl of a Dornier HM3 lithotripter. The configuration made half the bowl pressure release and left half the bowl rigid. The method provides a means of obtaining a sequence of two pulses with one spark and one reflector. Only pressure-release inserts in a rigid reflector have been tested so far. But inserts and reflectors may be made of either material and used in any combination. This dissertation shows that the acoustic and cavitation fields for these half and half reflectors can be easily estimated.

Figure 4.66 shows a photograph with half of shell  $D$  inserted. The pressure-release insert had smaller dimensions but the same foci as the brass Dornier reflector  $Q_1$ . The major axis of reflector  $D$  was 6 mm shorter, which meant reflections from the pressure-release half arrived at  $f_2$  8  $\mu$ s earlier than reflections from the brass half. As seen in Fig. 4.67, 6  $\mu$ s were measured. The difference was likely due to finite-amplitude acoustics. The shock wave reflected from the rigid reflector travels faster than does the negative pressure pulse from the pressure-release reflector.

The difference in propagation speed of the positive spike produced by the rigid half of the reflector and the negative pulse produced by the pressure-release half of the reflector was calculated. For a finite-amplitude wave, the propagation speed, derived

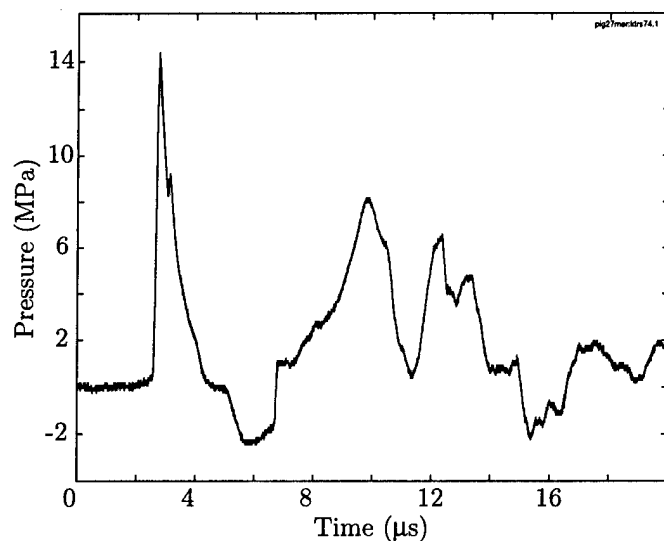


Figure 4.64: With a rigid reflector and 18 kV charging potential, the waveform measured with an encapsulated (ktech) membrane *in vivo* behind the kidney. Peak amplitude of the positive pressure phase is 14.4 MPa, and peak amplitude of the negative pressure phase is -2.5 MPa. The waveform has the same shape as *in vitro* measurements.

AS-97-87

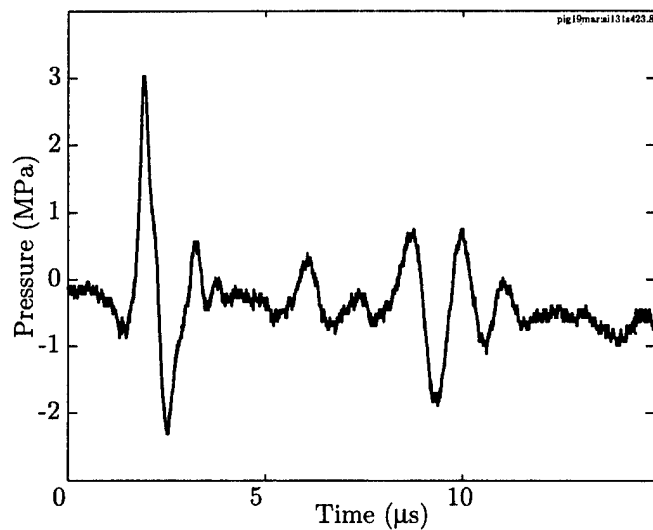


Figure 4.65: With a pressure-release reflector and 18 kV charging potential, the waveform measured with an encapsulated SI membrane *in vivo* behind the kidney. Peak amplitude of the positive pressure phase is 3 MPa, and peak amplitude of the negative pressure phase is -2.3 MPa. The waveform has the same shape as *in vitro* measurements.

AS-97-88

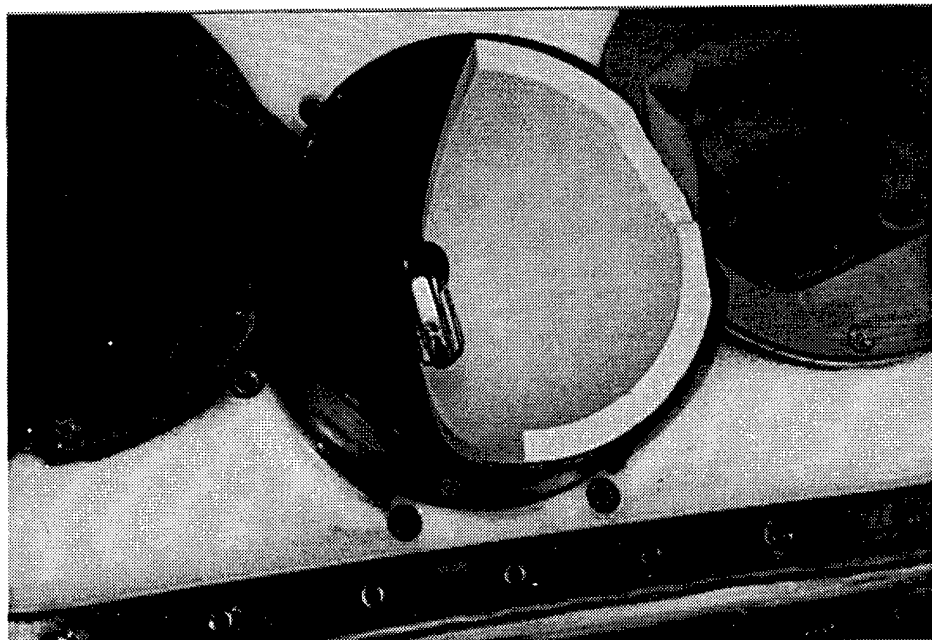


Figure 4.66: Photograph of half of the pressure-release mask *D* inserted in the reflector of the Dornier HM3 lithotripter.

AS-97-89

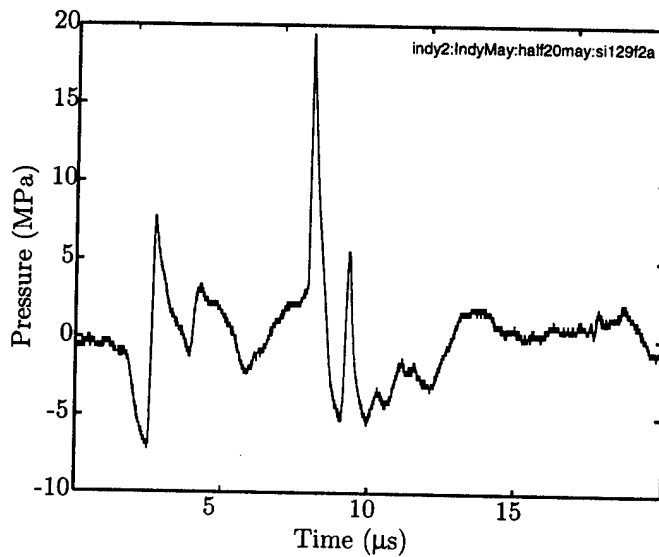


Figure 4.67: Waveform measured with half a pressure-release mask placed within the Dornier HM3 brass reflector. The waveform characteristic of the pressure-release reflector is seen first, followed by that of the rigid reflector. The pressure-release reflector is smaller, so the travel path (time) is shorter.

AS-97-90

from the Poisson solution,<sup>73</sup> is  $c_0 + \frac{\beta p_0}{\rho_0 c_0}$ , where  $\beta$  (=3.5) is the coefficient of nonlinearity in water,  $\rho_0$  is the ambient density of the water,  $c_0$  is the infinitesimal sound speed in water, and  $p_0$  is the peak pressure of the wave. Since the waves grew stronger as they focused,  $p_0$  is hard to define. If we take values 1/10th of the maximum pressures at  $f_2$ , calculate the speed of the negative wave and the positive wave, and multiply by the total path traveled from the spark, we obtain a difference of 6  $\mu\text{s}$  between the arrival of the pulse from the pressure-release reflector and the pulse from the rigid reflector. The difference is 2  $\mu\text{s}$  smaller than that calculated with small signal acoustic theory but is the same difference that was measured.

In Fig. 4.67, the first signal has the shape of a wave from a pressure-release reflector (see Fig. 4.63(a)), and the second has the shape of a wave from a rigid reflector (see Fig. 4.63(b)). The first signal came from the pressure-release mask and the second from the unmasked section of the rigid reflector. Both waves were roughly half amplitude because only half the reflector contributed to each. The second positive spike in the rigid waveform was common with the Dornier lithotripter.

#### 4.7.4 Miscellaneous measurements with the experimental lithotripter

This section contains results measured with the experimental lithotripter in Seattle.

The foil shown in Fig. 4.68 was placed half in and half out of the water. The second focus of the rigid reflector below the foil was at the water's surface. One spark was fired. A small fountain of water squirted from the surface. Cavitation damage to the foil was intense and extensive. The result is a first crack at assessing cavitation near a pressure-release surface, such as near the lungs, for example.

To this point, this dissertation has not addressed the plasma bubble formed at  $f_1$  by the spark at  $f_1$ . The bubble was not of great consequence in our study, but its detection is of scientific interest. However, if the collapse could be intensified and localized at  $f_1$ , the collapse could be a useful source.

The spark heats the water, which as it expands creates the sound pulse and a plasma bubble. The bubble grows very large and collapses nearly 4 ms (4000  $\mu\text{s}$ ) later. Sound radiated by the collapse reflects and is refocused by the reflector at  $f_2$ . Cavitation from the delayed pulse can be detected at  $f_2$ . When two sparks are fired

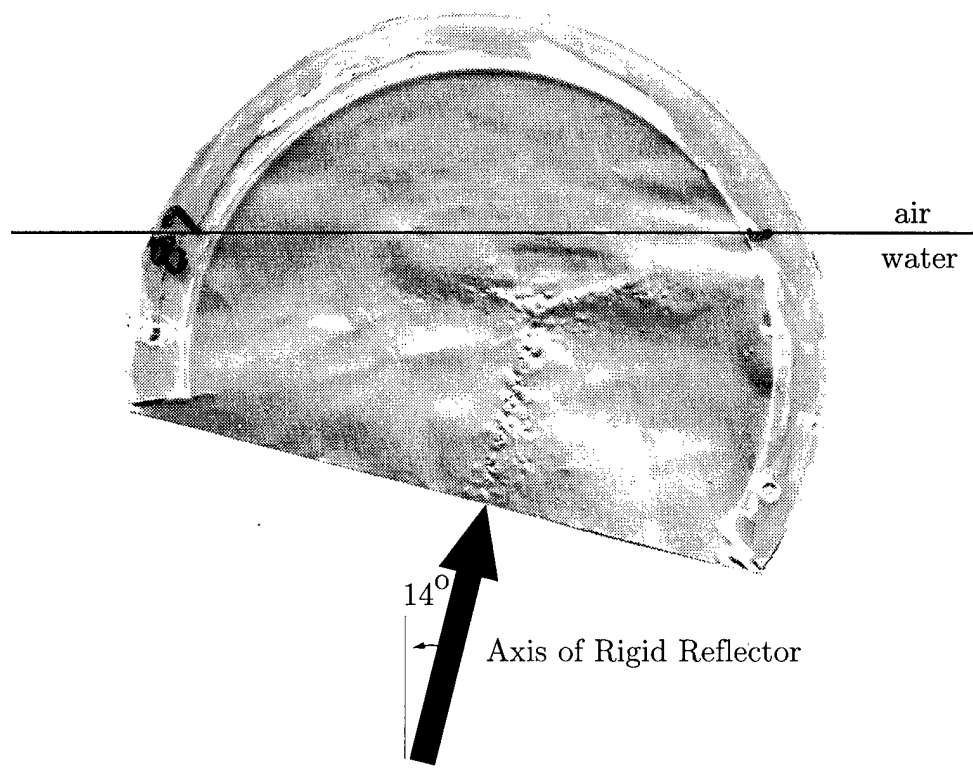


Figure 4.68: Foil placed halfway in the water normal to the water's surface. Increased cavitation damage is observed where splashing occurred at the water-air interface.

AS-97-91

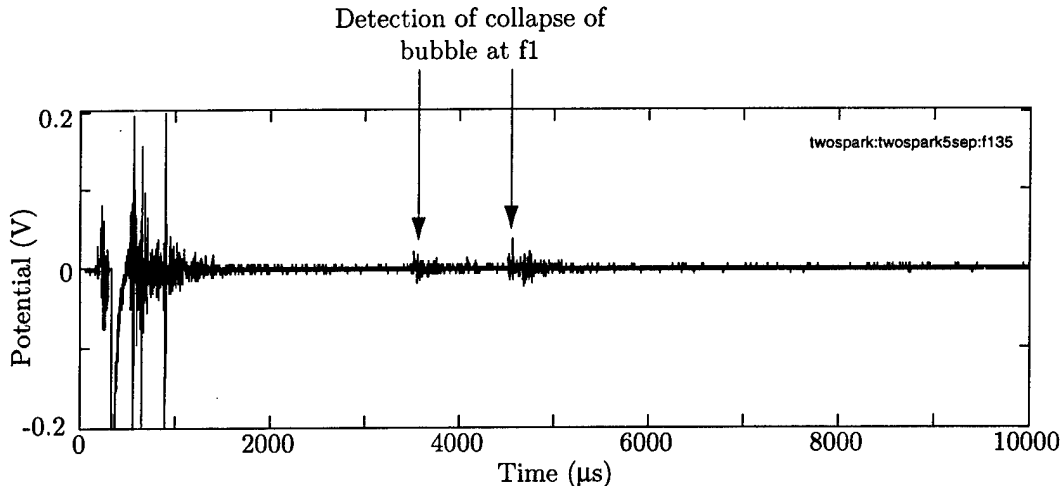


Figure 4.69: PCD detection of collapse of the plasma bubble created at  $f_1$  by the spark. The experimental configuration was two confocal rigid reflectors  $90^\circ$  apart and an interspark delay of  $300 \mu\text{s}$ . The collapse at each  $f_1$  was detected.

**AS-97-92**

in the dual reflector configuration, two collapses, and therefore, two delayed signals are detected. Figure 4.69 shows the PCD detection of two small signals, one for each plasma bubble. The first spark was fired at time zero, and the second spark was fired after a  $300\text{-}\mu\text{s}$  delay. Signals appeared at  $3.5 \text{ ms}$  and  $4.5 \text{ ms}$ . The signals are weak, and no second collapse associated with either was detected.

The potential exists for the plasma bubble to collapse strongly at  $f_1$  and create a strong focused wave. However, translation of the bubble and asymmetries in the collapse weaken the focused reflection of the collapse wave.

## Chapter 5

### Discussion and Applications

In this section, conclusions of the work are summarized, and applications are discussed. The general hypothesis was that cavitation, initiated with one acoustic pulse, could be intensified (“kicked”) or tempered (“stifled”) by the addition of a time-delayed, second acoustic pulse. First, a model based on the Gilmore equation was used to define kicking and stifling and to describe the bubble dynamics involved. Second, experimental measurement techniques (including two separate cavitation detection methods) were developed, and the sound and cavitation fields of our directive sound sources, a spark within a rigid reflector and a spark within a pressure-release reflector, were defined. Third, two reflectors were used in tandem to demonstrate our hypothesis.

#### 5.1 Summary of numerical results

The Gilmore-Akulichev formulation of bubble dynamics was used to numerically demonstrate stifling and kicking of a bubble. More complex waveforms were constructed from simple triangle pulses. Negative and positive pressure phases of one waveform were treated as separate pulses.

Both kicking and stifling were predicted for positive-then-negative bipolar pulses where the positive pressure was less than 50% greater than the negative pressure. Stifling occurred when the second pulse followed shortly after the first pulse. As the bubble began to grow in response to the first pulse, its growth was stifled. The bubble then weakly collapsed. In kicking, the interpulse delay was longer. As the bubble excited by the first pulse collapsed, the second pulse gave the bubble an extra kick that intensified the collapse. When the negative pressure in the bipolar pulse was greater, effects labeled “catching” and “growing” were predicted. These effects were not investigated experimentally, nor were other bipolar waveforms used in the code.

The code also predicted in some cases a “bounce” or second prominent growth and collapse cycle immediately following the collapse. The bounce was never measured.

The proposed explanation was that, in the model, the bubble stays perfectly spherical and stays whole. In the intensity of the final stages of collapse, evidence suggests that real bubbles are no longer spherical and in fact break up into smaller "daughter" bubbles. Our results show excellent agreement between the model and experiment up to the last resolvable stages of collapse.

## 5.2 Summary of experimental results

Much effort was spent defining the acoustic and cavitation fields of an unmodified lithotripter – a spark in a rigid reflector – and contrasting them with the fields of a modification – a pressure-release reflector. Work included definition of a waveform correction to membrane hydrophone deficiencies, demonstration of exceptional agreement between theory and passive cavitation detection when the correction was used, and invention of a new alignment of foil along the lithotripter's axis for measurement of the cavitation field by surface pitting. It was demonstrated numerically and experimentally that the pressure-release reflector, which produced a positive pulse late in the waveform, created mitigated cavitation.

With the basics of single reflectors defined, reflector pairs were used to temper and intensify cavitation. Numerical prediction of pressure within a cavitation bubble and profilometer readings of the size of cavitation-induced pits in aluminum foil showed direct correlation. Simple statistical measures of the foil also were found to correlate with pit depth. Numerically predicted and experimentally measured time histories of pressure radiated by the bubble were in agreement. In all cases, a slightly delayed pulse stifled bubble growth and tempered cavitation; a longer delay and the pulse kicked the collapsing bubble and intensified collapse.

## 5.3 Applications

The basic concepts of stifling and kicking a bubble have numerous applications to lithotripsy. Methods were described and demonstrated that enable the experimenter, or possibly the clinician, to increase or decrease cavitation. Cavitation and stress waves are the two prominent mechanisms in kidney stone comminution. Increased cavitation

therefore could more efficiently break up the stone. At the very least, a way to reduce or increase cavitation allows researchers to assess the role of cavitation.

### **5.3.1 Intensified, tempered and localized cavitation – applications to research and safer lithotripsy**

Methods that mollify or intensify cavitation but do not affect other mechanisms of action in lithotripsy provide tools to assess cavitation's importance as a factor in tissue damage and stone comminution. The same methods, whether implemented with sparks and reflectors as we've implemented them or implemented as modifications or sequences of pulses from other lithotripters, provide tools to improved lithotripsy.

Comparisons were made to a conventional lithotripter – a spark in a rigid reflector. Three methods that reduce cavitation were demonstrated or described. Each employed an acoustic wave that stifled bubble growth and collapse. One was a spark within a pressure-release reflector. A second was two sparks in one rigid reflector with a short ( $< 10 \mu\text{s}$ ) time delay between the sparks. A third was one spark in one reflector where the two halves of the reflector had different dimensions. One method with two variations was demonstrated to intensify cavitation. The method was to use a long delay in a sequence of two pulses to kick the bubble. The variations were use of a pressure-release reflector and a rigid reflector and the use of two rigid reflectors. We speculate that the other mechanisms of action were unaffected in any of the methods because the acoustic pulses were unchanged or, in the case of the pressure-release reflector, changed only slightly. Positive pressure excursion – the factor on which lithotripsy has been shown to depend – was unchanged. See Appendix B for more on the positive pressure excursion of the pressure-release reflector.

The experiment employing the methods as research tools simply consists of comparing effects measured with the modified lithotripters to effects measured with the conventional lithotripter. If effects are less with a modification that yields tempered cavitation, then, cavitation is significant in its effect. If effects increase with the methods that intensify cavitation, the effect's dependence on cavitation is affirmed. If no change is observed with either modification, cavitation is not a significant player in the effect, and other mechanisms caused by the lithotripter pulse are responsible for

the effect.

The two most obvious effects to consider are tissue damage and stone comminution. Tissue damage is undesirable and stone comminution is desirable. Four possible outcomes exist. Outcome number one is that cavitation is not important in either tissue damage or stone cavitation. This outcome would be a new discovery and would reorient a lot of research. Outcome number two is that cavitation is important in tissue damage only. In this outcome, the methods that reduce cavitation not only are useful tools of research but are themselves better lithotripters because they would reduce tissue damage but presumably be equally effective at stone comminution. In the third outcome, cavitation is only important in stone comminution. Here, the method to intensify cavitation would be an improved lithotripter as it intensifies cavitation to break up the stone. The fourth and final outcome is that cavitation is an important factor in both. A wealth of prior albeit indirect evidence points to this outcome. The outcome would define cavitation as the principle direction for lithotripsy research.

A method was also demonstrated that would be an improved lithotripter in the event of the fourth outcome, where both tissue damage and stone comminution are heavily influenced by cavitation. The method was a spark in each of two confocal reflectors and a short time delay between sparks. The method produced a localized region of intensified cavitation within a broad region of mitigated cavitation. Localization resulted because interpulse delay was spatially dependent and was based upon the geometry of the configuration. Pressure doubling occurred when pulses arrived simultaneously – stifling, when they arrived a short time apart, and kicking, when they were farther apart. Cavitation lines were made with reflectors  $90^\circ$  apart. And by making use of the limited beam width of the reflectors, lines were turned into spots with the  $180^\circ$  configuration. Intensified cavitation at the stone and mollified cavitation in the tissue, in the event of outcome four, is the best of both worlds.

### 5.3.2 Applications in progress

Preliminary experiments comparing tissue damage with the pressure-release reflector to damage with the rigid reflector have shown cavitation to be the mechanism responsible for tissue damage in the kidney during lithotripsy. In collaboration with R. Cleveland

and L. Crum (Applied Research Laboratory, Seattle, Washington) and A. Evan and J. McAtee (Indiana University Medical School, Indianapolis, Indiana), we have found that the pressure-release reflector caused no damage to cells in vials or to the kidney of a treated pig. In contrast (see Willis *et al.*<sup>74</sup>), the rigid reflector caused extensive cell damage *in vitro* and hemorrhage in the pig. The result is the first direct evidence linking cavitation and tissue damage.

Human kidney stones have been acquired, but the parallel experiment to determine cavitation's role in stone comminution has not yet begun.

### 5.3.3 General method for application

Although many specific devices were built and demonstrated, many more ways to exploit stifling and kicking exist.

Focused on sparks and reflectors, the work barely touched on the insertion of a mask within the reflector, but this means of implementation has great potential. Using inserts, we minimized the machining necessary and increased the flexibility of our experiment, but half reflectors could also have been used. Rigid masks were not investigated, but their potential application as a tempered-cavitation lithotripter is described above. The mask also presents the possibility of localized cavitation, since off-axis interpulse delays will differ. In combination with an adjustable mask, the potential for a steerable cavitation spot exists.

Although sparks in reflectors were the sources, the general conclusions of this dissertation are relevant to any source. Negative pressure could conceivably be created before positive pressure in a piezoelectric source by swapping the electrical input and output. Instead of initially expanding, the piezoelectric elements would initially contract.

The research determined that the waveform may be manipulated to predictably increase or decrease cavitation. The same elements of the waveform may be kept but the timing altered for larger effect. The finding that waveshape does not change *in vivo* makes predictable control of the waveform even easier.

## Appendix A

### Directivity

A measure of the hydrophone is its directional response. In a focused wavefield, sound was obliquely incident on the hydrophone. As the hydrophone was moved off the focus, distortion of the waveform because of hydrophone directivity became greater and compounded the distortion produced by the membrane wave. Measurement of the directional response provided an estimation of the distortion.

Directivity information played an additional role in *in vivo* measurements where the hydrophone could not be seen inside the pig. Although an alignment procedure was devised, the movements of the pig made it necessary to recognize misalignment and to correct the alignment solely from the shape of the measured waveforms.

Figure A.1 shows the waveforms measured at varying angles between the hydrophone and the reflector axis. Zero and ten degrees are similar; slight misalignment did not have a strong effect. The shock front at  $0^\circ$  was 10 ns and was limited by the hydrophone. The sharp shock front begins to blur at  $10^\circ$  because of integration over the face of the hydrophone's active element. The active element was 0.5 mm in diameter, which is the practical minimum for the a spot size of a PVdF membrane hydrophone. The waveform remained through  $20^\circ$  and  $30^\circ$ , but the amplitude dropped to half. After  $45^\circ$ , the waveforms were severely distorted. The membrane waves played a role in the distortion.

Fig. A.2 shows the average peak amplitude at each angle. Peak pressure without the waveform was not a good measure of the response. The large pressure amplitudes at large angles of incidence were due to hydrophone artifact.

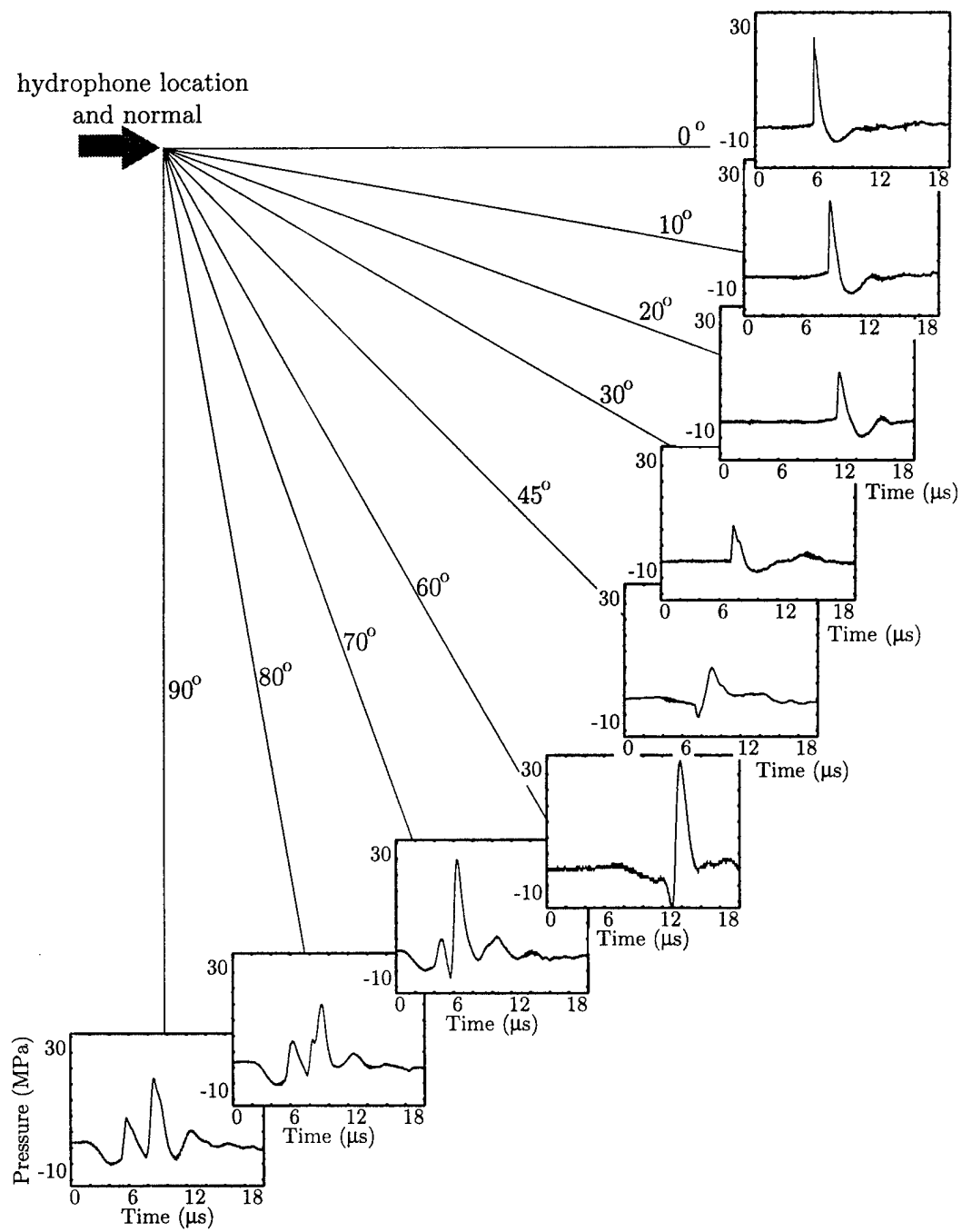


Figure A.1: Distortion of rigid-reflector waveform by hydrophone directivity.

AS-97-93

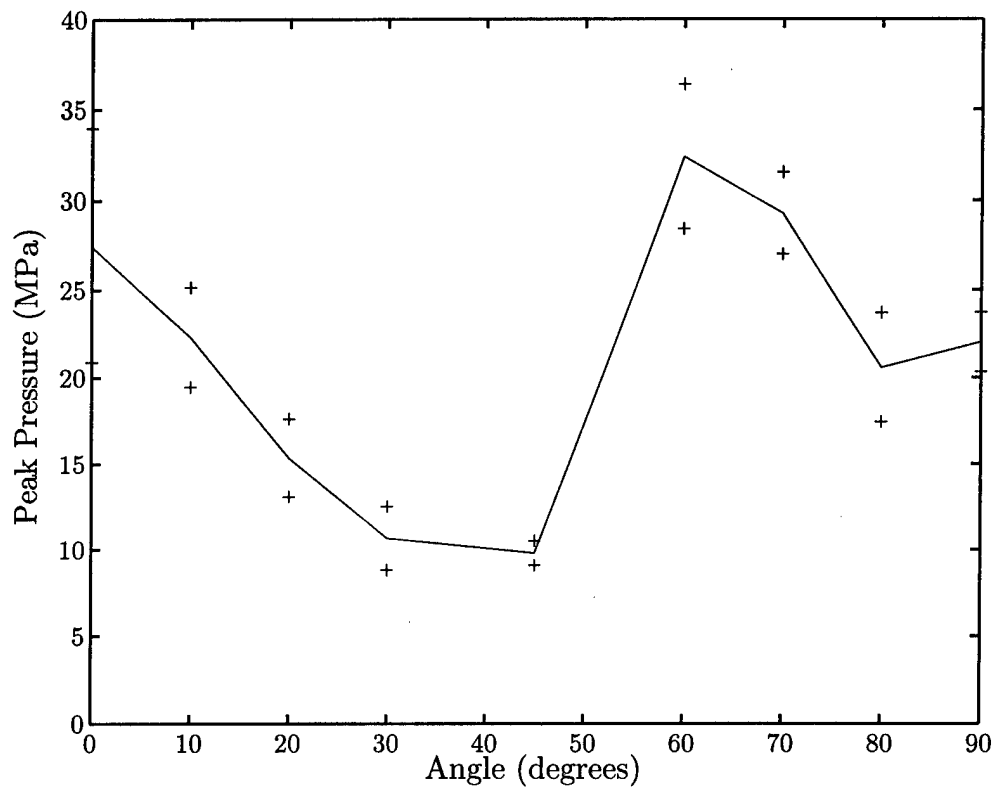


Figure A.2: Peak pressure recorded versus angle between aperture axis and hydrophone normal.

AS-97-94

## Appendix B

### Peak pressure with rigid and pressure-release reflectors

The 60-MPa pressure excursion in the pressure-release waveform in the modified Dornier lithotripter is discussed in Sec. 4. 7. It was also true that the largest pressures measured in the experimental lithotripter were with the pressure-release reflector. Fig. B.1 shows the largest waveform measured with each reflector. The fact that average pressures measured in the rigid and pressure-release reflectors are nearly equal may be indicative of the tight focus in the pressure release reflector. A tight focus that jumps around because of spark jitter will not be detected every time, so the average of many shots will be lower than on the axis of any one shot.

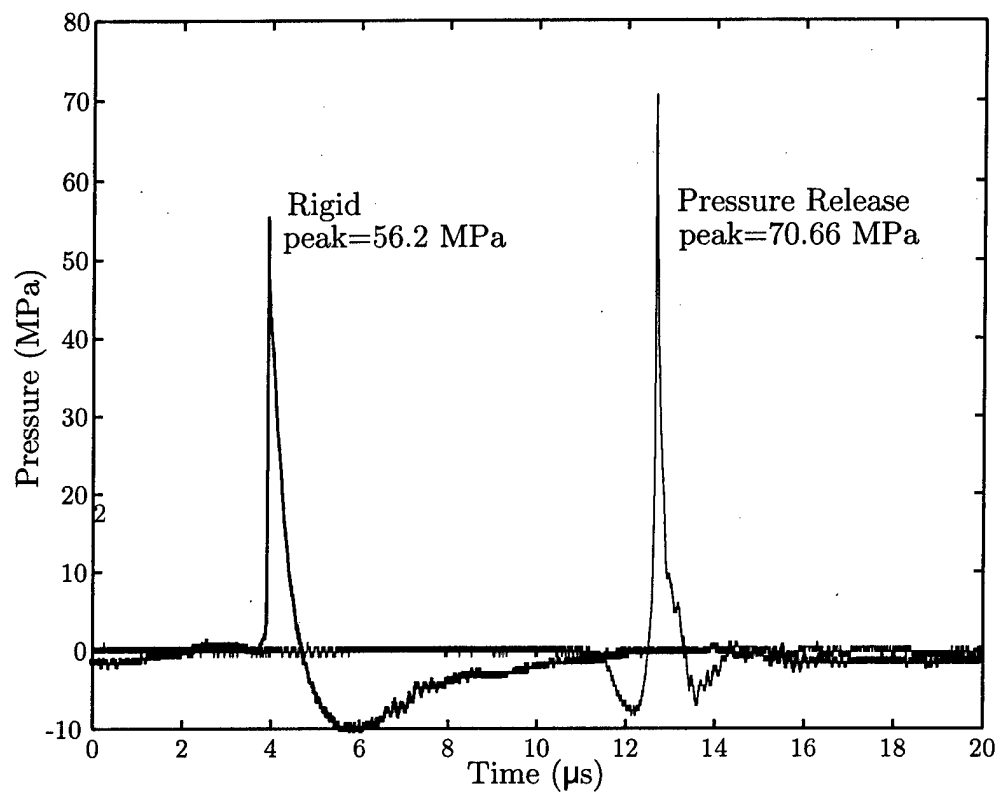


Figure B.1: Highest positive amplitude waveforms recorded in the experimental lithotripter with rigid and pressure-release reflectors.

AS-97-95

## Bibliography

- [1] L. A. Crum, Applied Physics Laboratory, Seattle, Washington, personal communication (1992).
- [2] M. R. Bailey, D. Dalecki, S. Z. Child, C. H. Raeman, D. P. Penney, D. T. Blackstock, and E. L. Carstensen, "Bioeffects of positive and negative acoustic pressures *in vivo*," *J. Acoust. Soc. Am.* **100**(6), 3941-3946 (1996).
- [3] M. Müller, "Focusing of weak spherical shock waves," *Acustica* **64**, 85-93 (1987).
- [4] A. J. Coleman and J. E. Saunders, "A survey of the acoustic output of commercial extracorporeal shock wave lithotripters," *Ultrasound Med. Biol.* **15**, 213-227 (1989).
- [5] C. C. Church, "A theoretical study of cavitation generated by an extracorporeal shock wave lithotripter," *J. Acoust. Soc. Am.* **86**, 215-227 (1989).
- [6] F. R. Gilmore, "The growth or collapse of a spherical bubble in a viscous compressible liquid," Rep#26-4, California Institute of Technology, Pasadena, California, pp. 1-40 (1952).
- [7] V. A. Akulichev, *High-Intensity Ultrasonic Fields*, edited by L. D. Rozenberg (Plenum, New York, 1971), pp. 239-59.
- [8] Z. Ding and S. M. Gracewski, "Response of constrained and unconstrained bubbles to lithotripter shock wave pulses," *J. Acoust. Soc. Am.* **96**(6), 3636-3644 (1994).
- [9] E. L. Carstensen, D. S. Campbell, D. Hoffman, S. Z. Child, and E. J. Aymé-Bellegarda, "Killing of *Drosophila* larvae by the fields of an electrohydraulic lithotripter," *Ultrasound Med. Biol.* **16**(7), 687-698 (1990).

- [10] W. C. Moss, D. B. Clarke, J. W. White, and D. A. Young, "Sonoluminescence and the prospects for table-top micro-thermonuclear fusion," *Phys. Let.* **211**, 69–74 (1996).
- [11] A. J. Coleman, J. E. Saunders, and M. J. Choi, "An experimental shock wave generator for lithotripsy studies," *Phys. Med. Biol.* **34**, 1733–1742 (1989).
- [12] A. J. Coleman, J. E. Saunders, L. A. Crum, and M. Dyson, "Acoustic cavitation generated by an extracorporeal shock wave lithotripter," *Ultrasound Med. Biol.* **13**, 69–76 (1987).
- [13] D. A. Lifshitz, J. C. Williams Jr., B. Sturtevant, B. A. Conners, A. P. Evan, and J. A. McAteer, "Quantization of shock wave cavitation damage *in vitro*," *Ultrasound Med. Biol.*, under revision.
- [14] A. J. Coleman, M. J. Choi, J. E. Saunders, and T. G. Leighton, "Acoustic emission and sonoluminescence due to cavitation at the beam focus of an electrohydraulic shock wave lithotripter," *Ultrasound Med. Biol.* **18**(3), 267–81 (1992).
- [15] A. J. Coleman, M. Whitlock, T. Leighton, and J. E. Saunders, "The spatial distribution of cavitation induced acoustic emission, sonoluminescence and cell lysis in the field of a shock wave lithotripter," *Phys. Med. Biol.* **38**(3), 1545–1560 (1993).
- [16] O. Sapozhnikov, "Focused hydrophone for detection of bubble collapse," *J. Acoust. Soc. Am.*, in preparation.
- [17] H. Poritsky, Proc. First U.S. National Congress in Applied Mathematics (ASME), p. 813 (1952).
- [18] M. J. Choi, A. J. Coleman, and J. E. Saunders, "The influence of fluid properties and pulse amplitude on bubble dynamics in the field of a shock wave lithotripter," *Phys. Med. Biol.* **38**(3), 561–573 (1993).
- [19] A. Prosperetti, "Physics of acoustic cavitation," *Frontiers in Physical Acoustics* (Soc. Italiana di Fisica, Bologna, Italy, 1986), pp. 145–188.

- [20] F. R. Young, *Cavitation* (McGraw-Hill Book Company, London, 1989), pp. 8-36.
- [21] T. G. Leighton, *The Acoustic Bubble* (Academic Press, London, 1994), pp. 302-308.
- [22] R. E. Apfel, *Methods of Experimental Physics*, Vol. 19, *Ultrasonics* (Academic Press, New York, 1981), p. 373.
- [23] C. Herring, Office of Science Research and Development Report 236 (NDRC Report C-4-sr 10-010, Columbia University), 1941.
- [24] L. Trilling, "The collapse and rebound of a gas bubble," *J. Appl. Phys.* **23**(1), 14 (1952).
- [25] H. G. Flynn, *Physics of Acoustic Cavitation in Liquids*, edited by W. P. Mason, Vol. 1B (Academic Press, New York, 1964).
- [26] J. G. Kirkwood and H. A. Bethe, Office of Science Research and Development Report 588 (1942).
- [27] K. Vokurka, "Comparison of Rayleigh's, Herring's, and Gilmore's models for gas bubbles," *Acustica* **59**, 214-219 (1986).
- [28] E. J. Aymé, "Transient cavitation induced by high-amplitude diagnostic ultrasound," Ph.D. Thesis, University of Rochester, Rochester, New York (1988).
- [29] R. Hickling and M. S. Plesset, "Collapse and rebound of a spherical bubble in water," *Phys. Fluids* **7**(1), 7-14 (1964).
- [30] P. A. Thompson, *Compressible-Fluid Dynamics* (Rensselaer Polytechnic Institute, Troy, New York, 1988), p. 102.
- [31] D. A. Sullivan, "Historical review of real-fluid isentropic flow models," *J. Fluids Eng.* **103**, 258-267 (1981).
- [32] D. T. Blackstock, "Nonlinear acoustics (theoretical)," in *American Institute of Physics Handbook*, 3rd ed., edited by D. E. Gray (McGraw, New York, 1972), pp. 3-183 to 3-205.

- [33] M. F. Hamilton, "Fundamentals and applications of nonlinear acoustics," in *Nonlinear Wave Propagation in Mechanics*, edited by T. W. Wright, AMD-Vol. 77, Book H00346 (American Society of Mechanical Engineers, New York, 1986), pp. 1-28.
- [34] A. J. Coleman, J. E. Saunders, R. C. Preston, and D. R. Bacon, "Pressure waveforms generated by a Dornier extracorporeal shock-wave lithotripter," *Ultrasound Med. Biol.* **13**(10), 651-657 (1987).
- [35] L. A. Crum, "Rectified diffusion," *Ultrasonics* **2**, 215-223 (1984).
- [36] A. Eller and H. G. Flynn, "Rectified diffusion during nonlinear pulsations of cavitation bubbles," *J. Acoust. Soc. Am.* **37**, 493-501 (1965).
- [37] H. G. Flynn and C. C. Church, "Transient pulsations of small gas bubbles in water," *J. Acoust. Soc. Am.* **84**(3), 1863-1876 (1988).
- [38] Specifications manual for reference shock wave hydrophone, Sonic Industries, Hatboro, Pennsylvania (1994).
- [39] D. Cathignol, J. L. Mestas, F. Gomez, and P. Lenz, "Influence of water conductivity on the efficiency and the reproducibility of electrohydraulic shock wave generation," *Ultrasound Med. Biol.* **17**(8), 819-828 (1991).
- [40] A. R. Kaiser, C. A. Cain, E. Y. Hwang, J. B. Fowlkes, and R. J. Jeffers, "A cost effective degassing system for use in ultrasonic measurements: the multiple pinhole degassing (MPD) system," *J. Acoust. Soc. Am.* **99**(6), 3857-3859 (1996).
- [41] D. Howard and B. Sturtevant, "In vitro study of the mechanical effects of shock wave lithotripsy," *Ultrasound Med. Biol.*, in preparation.
- [42] M. R. Bailey, "Isolation of a negative-pressure pulse and studies of irregular edge diffraction," M. S. Thesis, The University of Texas at Austin, Austin, Texas (1994).

- [43] D. S. Campbell, H. G. Flynn, D. T. Blackstock, C. Linke, and E. L. Carstensen, "The acoustic fields of the Wolf electrohydraulic lithotripter," *J. Lithotripsy and Stone Disease* **3**(2), 147–156 (1991).
- [44] L. E. Kinsler, A. R. Frey, A. B. Coppens, and J. V. Sanders, *Fundamentals of Acoustics*, 3rd edition (John Wiley & Sons, New York, 1982).
- [45] Specifications sheet for Last-a-Foam, General Plastics Corp., Tacoma, Washington (1996).
- [46] J. A. Ten Cate, "Scattering of sound by sound: nonlinear interaction of collinear and noncollinear sound beams," Ph.D. Thesis, The University of Texas at Austin, Austin, Texas (1992).
- [47] Institute of Electrical and Electronics Engineers (IEEE) Standard 790-1989, Procedure B6.1.
- [48] J. Staudenraus and W. Eisenmenger, "Fibre-optic probe hydrophone for ultrasonic and shock-wave measurements in water," *Ultrasonics* **31**(4), 267–273 (1993).
- [49] R. A. Roy, S. I. Madanshetty, and R. E. Apfel, "An acoustic backscattering technique for the detection of transient cavitation produced by microsecond pulses of ultrasound," *J. Acoust. Soc. Am.* **87**(6), 2451–2458 (1990).
- [50] A. Vogel and W. Lauterborn, "Acoustic transient generation by laser-produced cavitation bubbles near solid boundaries," *J. Acoust. Soc. Am.* **84**(2), 719–731 (1988).
- [51] M. F. Hamilton, "Transient axial solution for the reflection of a spherical wave from a concave ellipsoidal mirror," *J. Acoust. Soc. Am.* **93**(3), 1256–1266 (1993).
- [52] W. M. Wright and D. T. Blackstock, "Experimental study of ellipsoidal focusing of spark-produced N waves in air," *J. Acoust. Soc. Am.* **90**, 2339(A) (1991).
- [53] R. O. Cleveland and M. Averkiou, "Numerical prediction of lithotripter pulses," *J. Acoust. Soc. Am.*, to be submitted.

- [54] Y.-S. Lee and M. F. Hamilton, "Time-domain modeling of pulsed finite-amplitude sound beams," *J. Acoust. Soc. Am.* **97**, 906–917 (1995).
- [55] R. O. Cleveland, "Propagation of sonic booms through a real, stratified atmosphere," Ph. D. dissertation, Department of Mechanical Engineering, The University of Texas at Austin (1995).
- [56] E. A. Zabolotskaya and R. V. Khokhlov, "Quasi-plane waves in the nonlinear acoustics of confined beams," *Sov. Phys.-Acoust.* **15**, 35–40 (1969).
- [57] T. S. Hart and M. F. Hamilton, "Nonlinear effects in focused sound beams," *J. Acoust. Soc. Am.* **84**(4), 1488–1496 (1988).
- [58] D. T. Blackstock, Class notes for courses taught at The University of Texas at Austin, to be published as *Introduction to Physical Acoustics* (1997).
- [59] P. M. Morse, *Vibration and Sound* (Acoustical Society of America, American Institute of Physics, 1981).
- [60] A. D. Pierce, *Acoustics: An Introduction to Its Physical Principles and Applications* (McGraw-Hill, New York, 1981).
- [61] J. Naze Tjøtta and S. Tjøtta, "Nearfield and farfield of pulsed acoustic radiators," *J. Acoust. Soc. Am.* **71**, 824–834 (1982).
- [62] T. Christopher, "Modeling the Dornier HM3 lithotripter," *J. Acoust. Soc. Am.* **96**(5 pt. 1), 3088–3095 (1994).
- [63] A. J. Coleman, M. J. Choi, and J. E. Saunders, "Theoretical predictions of the acoustic pressure generated by shock wave lithotripter," *Ultrasound Med. Biol.* **17**, 245–255 (1991).
- [64] R. O. Cleveland, L. A. Crum, D. Lifshitz, B. A. Connors, and A. P. Evan, "In vivo measurement of lithotripsy shock waves in pigs," *J. Acoust. Soc. Am.* **100** (4 pt. 2), 2617 (1996).

- [65] M. A. Averkiou, L. A. Crum, and M. F. Hamilton, "Focused acoustic pulses of finite amplitude and their influence on cavitation bubble dynamics," *J. Acoust. Soc. Am.* **96** (5 pt.2), 3306 (1994).
- [66] L. J. Gelin, "Self-refraction in the acoustic field of a paraboloidal reflector," Master's thesis, Department of Mechanical Engineering, The University of Texas at Austin (1995).
- [67] C. C. Church, S. Cordrey, and L. A. Crum, "High speed video images of cavitation and stone comminution at the focus of an extracorporeal shock wave lithotripter," *J. Acoust. Soc. Am.*, in preparation.
- [68] K. Jöchle, J. Debus, W. J. Lorenz, and P. Huber, "A new method of quantitative cavitation assessment in the field of a lithotripter," *Ultrasound Med. Biol.* **22**(3), 329–338 (1996).
- [69] L. A. Crum, "Acoustic cavitation," *Proc. Ultrasonics Symp.* **1**, 1–11 (1982).
- [70] S. Kargl, Applied Physics Laboratory, Seattle, Washington, personal communication (1996).
- [71] A. Philippe, M. Delius, C. Scheffczyk, A. Vogel, and W. Lauterborn, "Interaction of lithotripter-generated shock waves with air bubbles," *J. Acoust. Soc. Am.* **93**(5), 2496–2509 (1993).
- [72] G. Keilman, Applied Physics Laboratory, Seattle, Washington, personal communication (1996).
- [73] S. D. Poisson, "Memoir on the theory of sound," *J. L'Ecole Polytech.* **7**, 364–370 (1808).
- [74] L. R. Willis, A. P. Evan, B. A. Conners, G. Reed, N. S. Fineberg, and J. E. Lingeman, "Effects of extracorporeal shock wave lithotripsy to one kidney on bilateral glomerular filtration rate and PAH clearance in minipigs," *J. Urol.*, in press.

This page intentionally left blank.

DISTRIBUTION LIST  
ARL-TR-97-1  
TECHNICAL REPORT  
UNDER GRANT N00014-89-J-1109  
AND ARL:UT IR&D PROGRAM

1-2	DR LOGAN E HARGROVE ONR 331 OFFICE OF NAVAL RESEARCH 800 NORTH QUINCY STREET ARLINGTON VA 22217-5660	15	ANDREW J COLEMAN ST THOMAS HOSPITAL DEPT OF MEDICAL PHYSICS LAMBETH PALACE RD LONDON SE1 7EH ENGLAND
3-4	DEFENSE TECHNICAL INFORMATION CENTER 8725 JOHN J KINGMAN RD SUITE 0944 FORT BELVOIR VA 22060-6218	16	LAWRENCE A CRUM APPLIED PHYSICS LABORATORY UNIVERSITY OF WASHINGTON 1013 NE 40TH STREET SEATTLE WA 98105-6698
Form 298 only	ADMINISTRATIVE GRANTS OFFICER OFFICE OF NAVAL RESEARCH SAN DIEGO REGIONAL OFFICE 4520 EXECUTIVE DRIVE SUITE 300 SAN DIEGO CA 92121-3019	17	DIANE DALECKI UNIV OF ROCHESTER HOPEMAN BUILDING RM 319 ROCHESTER NY 14627
6	DIRECTOR NAVAL RESEARCH LABORATORY ATTN CODE 2667 4555 OVERLOOK AVENUE SW WASHINGTON DC 20375-5326	18	E CARR EVERBACH SWARTHMORE COLLEGE SWARTHMORE PA 19081-1397
7	ROBERT E APFEL YALE UNIV P O BOX 208286 NEW HAVEN CT 06520-8286	19	ANDREW EVAN INDIANA UNIV MEDICAL SCHOOL DEPT OF ANATOMY MS 213A 635 BARNHILL DR INDIANAPOLIS IN 46202-5120
8	W PATRICK ARNOTT ATMOSPHERIC SCIENCES CENTER DESERT RESEARCH INSTITUTE P O BOX 60220 RENO NV 89506	20	STEVEN L GARRETT GRADUATE PROGRAM IN ACOUSTICS PENNNSYLVANIA STATE UNIVERSITY P O BOX 30 STATE COLLEGE PA 16804
9	ANTHONY A ATCHLEY DEPT OF PHYSICS CODE PH/AY NAVAL POSTGRADUATE SCHOOL MONTEREY CA 94943-5000	21	CHRISTY K HOLLAND UNIV OF CINCINNATI DEPT OF RADIOLOGY ML 742 234 GOODMAN STREET CINCINNATI OH 45267-0742
10	HENRY E BASS DEPT OF PHYSICS AND ASTRONOMY UNIVERSITY OF MISSISSIPPI UNIVERSITY MS 38677	22	GLYNN R HOLT BOSTON UNIVERSITY AEROSPACE AND MECH ENGINEERING 110 CUMMINGTON STREET BOSTON MA 02215
11	YVES H BERTHELOT SCHOOL OF MECHANICAL ENGINEERING GEORGIA INSTITUTE OF TECHNOLOGY ATLANTA GA 30332	23	ROBERT M KEOLIAN DEPT OF PHYSICS CODE PH/KN NAVAL POSTGRADUATE SCHOOL MONTEREY CA 93943-5000
12	EDWIN L CARSTENSEN UNIV OF ROCHESTER HOPEMAN BUILDING RM 319 ROCHESTER NY 14627	24	PHILIP L MARSTON DEPT OF PHYSICS WASHINGTON STATE UNIVERSITY PULLMAN WA 99164-2814
13	CHARLES C CHURCH MOLECULAR BIOSYSTEMS INC 10030 BARNES CANYON RD SAN DIEGO CA 92121	25	JULIAN D MAYNARD DEPT OF PHYSICS PENNNSYLVANIA STATE UNIVERSITY UNIVERSITY PARK PA 16802
14	ROBIN O CLEVELAND APPLIED PHYSICS LABORATORY UNIVERSITY OF WASHINGTON 1013 NE 40TH STREET SEATTLE WA 98105-6698		

26	JIM MCATEER INDIANA UNIV MEDICAL SCHOOL DEPT OF ANATOMY MS 213A 635 BARNHILL DR INDIANAPOLIS IN 46202-5120	38	ANDREW COLEMAN MEDICAL PHYSICS DEPARTMENT ST THOMAS HOSPITAL LONDON SE1 7EH UK
27	ALLAN D PIERCE DEPT MECHANICAL & AEROSPACE ENGINEERING BOSTON UNIVERSITY 110 CUMMINGTON STREET BOSTON MA 02215	39	DOMINIQUE CATHIGNOL INSERM UNITE 281 151 COURS ALBERT THOMAS 69424 LYON CEDEX 03 FRANCE
28	ANDREA PROSPERETTI DEPT OF MECHANICAL ENGINEERING JOHNS HOPKINS UNIVERSITY BALTIMORE MD 21218	40-42	MICHAEL R BAILEY APPLIED PHYSICS LABORATORY UNIVERSITY OF WASHINGTON 1013 NE 40TH STREET SEATTLE WA 98105-6698
29	RICHARD RASPET DEPT OF PHYSICS AND ASTRONOMY UNIVERSITY OF MISSISSIPPI UNIVERSITY MS 38677	43	M F HAMILTON ME DEPT
30	RON ROY BOSTON UNIV AEROSPACE & MECH ENGINEERING 110 CUMMINGTON STREET BOSTON MA 02215	44	I J BUSCH-VISHNIAC ME DEPT
31	BRADFORD STURTEVANT CALIFORNIA INSTITUTE OF TECHNOLOGY MAIL CODE 301-46 PASADENA CA 91125	45	E L HIXSON ECE DEPT
32	WAYNE M WRIGHT DEPT OF PHYSICS KALAMAZOO COLLEGE KALAMAZOO MI 49007	46	D T BLACKSTOCK ARL:UT
33	FREDERICK D COTARAS DEFENCE RESEARCH ESTABLISHMENT P O BOX 1012 DARTMOUTH NOVA SCOTIA B2Y 3Z6 CANADA	47	R L ROGERS ARL:UT
34	VERA A KHOKHLOVA DEPARTMENT OF ACOUSTICS PHYSICS FACULTY MOSCOW STATE UNIVERSITY MOSCOW 119899 RUSSIA	48	LIBRARY ARL:UT
35	BRUCE MORTIMER CAPE TECHNIKON P O BOX 652 8000 CAPE TOWN REPUBLIC OF SOUTH AFRICA	49-51	NAD RESERVE ARL:UT
36	CHRISTOPHER L MORFEY INSTITUTE OF SOUND AND VIBRATION RESEARCH UNIVERSITY OF SOUTHAMPTON SOUTHAMPTON SO9 5NH UNITED KINGDOM		
37	OLEG A SAPOZHNIKOV DEPARTMENT OF ACOUSTICS PHYSICS FACULTY MOSCOW STATE UNIVERSITY MOSCOW 119899 RUSSIA		